NANOSTRUCTURED METAL OXIDES FOR HYDROGEN SENSING APPLICATIONS

Thesis submitted by

KAMAL ARORA

In Partial Fulfillment of the Requirements for the Degree of

DOCTOR OF PHILOSOPHY

Under the Supervision of

Dr. NITIN K. PURI
ASSOCIATE PROFESSOR

Department of Applied Physics
Delhi Technological University
Bawana Road, Delhi-110042
India

DECEMBER 2019

DEDICATED TO….

UBIQUITOUS

&

PERENNIAL

SOURCE OF

THE ENERGY

DELHI TECHNOLOGICAL UNIVERSITY

(Govt. of National Capital Territory of Delhi)
Bawana Road, Delhi-110042

CERTIFICATE

This is to certify that the thesis titled ***"Nanostructured metal oxides for hydrogen sensing applications"*** submitted by ***Mr. Kamal Arora*** with registration number ***2K13/Ph.D./AP/11*** to the Delhi Technological University is for the award of the degree of Doctor of Philosophy in Department of Applied Physics. The work embodied in this thesis is a record of bonafide research work carried out by him under the supervision of ***Dr. Nitin K. Puri***, Associate Professor, Department of Applied Physics, Delhi Technological University, Delhi, India. It is further certified that the work embodied in this thesis has neither been partially, nor fully submitted to any other university or institution for the award of any degree or diploma.

Kamal Arora
Candidate
Roll No. 2K13/Ph.D./AP/11

This is to certify that the above statements made by the candidate are correct to the best of our knowledge.

Dr. Nitin K. Puri
Supervisor (Associate Professor)
Department of Applied Physics
Delhi Technological University
Delhi, India

Prof. Rinku Sharma
Head
Department of Applied Physics
Delhi Technological University
Delhi, India

ACKNOWLEDGEMENTS

The duration of my Ph.D. research work can be categorized in five different stages including coursework, literature review, experimentation, discussion and publications. These stages gave me fruitful insights about field of research work, taught me about the proper approach and adaptation of suitable methods to ponder on the existing problems and achieve desired results respectively. Every stage enacted as a mission that could not have been accomplished without the guidance and assistance of foremost my supervisor, subsequently my University, Department, colleagues, friends and family members. Therefore, I would like to acknowledge and pay my heartfelt gratitude to each and everyone for their valuable contribution during this journey.

Firstly, I am forever indebted to my Ph.D. supervisor, Dr. Nitin K. Puri, Associate Professor, Department of Applied Physics, Delhi Technological University for his incessant guidance, motivation and conviction that propelled me to work continuously in spite of several roadblocks and this determination helped me to conclude the research wok on time. I am grateful to Dr. Nitin K. Puri for his credence on my research vision and helping me to acquire the necessary skills as well as tools to convert that vision into reality. He encouraged me to develop ingenuity thinking and supported me to pursue the unconventional proposition which resulted in accomplishing the novel research work.

I am unfeigned obliged to Dr. Saurabh Srivastava, Assistant Professor, Rajkiya Engineering College, Ambedkar nagar (Uttar Pradesh), for his perpetual guidance and training which aided me to pursue, present and report my research work in effective and precise manner. His kind pragmatic nature inspired me to conduct qualitative and productive research work. I will always be grateful to him for providing succour and motivation in times of hardships during my Ph.D. duration like my family member.

The fruitful research work couldn't have been conducted without the consistent assistance from Department of Applied Physics and Delhi Technological University. Hence, I am sincerely grateful to Prof. Yogesh Singh, Hon'ble Vice Chancellor, Delhi Technological University and Prof. Rinku Sharma, Head, Department of Applied Physics for providing research befitting environment and continuous support throughout the period of my doctorate work. I am thankful to Prof. S. C. Sharma for his constant support and guidance during the course of my research work. Also, I want to thank all the faculty members of Department of Applied Physics for their constant assistance. I want to genuinely express my appreciation to University and Departmental staff members for their valuable contribution in the completion of my Ph.D. research work.

I am thankful to Prof. B. D. Malhotra for his valuable guidance and permission to use the fabrication and characterization instruments present in nano bio-electronics laboratory, Department of Biotechnology, Delhi Technological University. Also, I am grateful to Inter-University Accelerator centre (IUAC), New Delhi, India and Advanced Instrumentation Research Facility (AIRF), Jawaharlal Nehru University (JNU), New Delhi, India for providing the necessary characterization instruments utilized in successful completion of this thesis research work.

I want to express my gratitude to Council of Scientific and Industrial Research (CSIR), New Delhi, India and Inter-University Accelerator centre (IUAC), New Delhi, India for providing me with the senior research fellowship (SRF-Direct) (May 2018-April 2020) and project fellowship (UFR-56324), (November 2015-March 2018) respectively, as the source of financial assistance during my Ph.D. duration.

I am ever grateful to my friends and lab members (Nishant Shankwar, Rahul Pandey, Jaya Madan, Vipin Dahiya Deepika Sandil, Ritika Khatri, Kanika Sharma, Nikita Jain, Shine

Augustine, Saurabh Kumar and Suveen Kumar) for providing me motivation and support in difficult times together with cherishing and memorable moments throughout my doctorate years.

Last but not the least; I could not have completed my Ph.D. research work without the unconditional support, wholehearted care and selfless love from my family members. It is impossible to acknowledge their contribution in my life through the medium of words. However, I am and shall always be deeply obliged to my father (Arjun Dass Arora), mother (Pushpa Arora) for their precious blessings and succour in psychological as well as financial adverse times. This milestone wouldn't have been accomplished without the persistent motivational and invigorating words of my fiancée (Akanksha), which aided me in optimistically striving for this achievement. She stood by my side during the contrast phases of this journey like a pillar and provided me the stability to travel steadily on the path. Their unabated belief in my abilities inculcated the much needed confidence in me which backed me to continue my thesis research work at unwavering pace and wrap it up in due time.

(KAMAL ARORA)
New Delhi, India
December 2019

ABSTRACT

Nanostructured Metal Oxides for Hydrogen Sensing Applications

The unique physicochemical properties render it unfeasible to detect hydrogen (H_2) gas using human sensory organs and its flammable nature elevates the need for fabrication of highly sensitive, selective and stable sensors, which can sense wide range concentrations of H_2 at room temperature. However, a sensor should be facile, economical, compact and easily integrable with existing silicon electronics, in order to be employed at industrial level for H_2 sensing applications. **Chapter 1** discuss the structure and mechanism of various available H_2 sensors and outline their traits for sensing applications. Electrochemical and chemiresistive type sensors are found to be best candidate for commercial H_2 sensing applications compared to other existing sensors.

In comparison to exhaustive list of sensing materials, physicochemical and electronic properties of metal oxide (MOX) semiconductors bestow them with favourable characteristics of good sensing material for H_2 sensing application. However, high desorption activation energy of pristine MOX contributes in elevation of operating temperature which makes them unfavourable for H_2 sensing application. Synthesis of nanostructures of MOX, heterostructures with other catalytic active materials and plasmon driven catalysis by radiation exposure, decrease the operating temperature while increasing their sensitivity simultaneously. Based on literature review, the reported work on palladium oxide (PdO) nanostructures till beginning of this thesis research work were limited and they demonstrated good sensitivity for H_2 at high temperature. These results became the scientific motivation behind our research work where we synthesized and examine PdO nanomaterials for H_2 sensing application at room temperature.

Chapter 2 explains various approaches for synthesis of MOX nanostructures and wet chemical synthesis procedure based on bottom up approach is found to be suitable for large scale synthesis of nanomaterials. Sol-gel and hydrothermal synthesis procedures are the most facile and economical methods to obtain homogeneous morphology of nanomaterials comparatively. Setup and working mechanism of x-ray diffraction (XRD), transmission electron microscopy (TEM), scanning electron microscopy (SEM), ultraviolet-visible (UV-Vis) spectroscopy and Fourier transmission spectroscopy instruments, employed in the following chapters for analysis of crystallographic property, size, shape of nanostructures, thin film surface morphology, optical band gap and nature of chemical bonds are demonstrated extensively.

Chapter 3 study the changes in crystallographic properties of PdO nanoparticles are investigated using H_2 in-situ XRD analysis at different low gas pressure (25, 50, 75 and 100 mbar) of H_2 at room temperature. Complete transformation of t-PdO into face centered cubic (fcc) crystal structure of palladium hydride (PdH_x) is observed as pressure rises from 25 to 100 mbar. Also, expansion in lattice parameters corresponding to phase transition takes place as pressure reaches 100 mbar. The results of this study show that pristine PdO nanoparticles are suitable for sensing and storage of H_2 at room temperature.

Chapter 4 includes the research work on amperometric sensing of H_2 gas using PdO nanoparticles thin film as working electrode (WE) and sulphuric acid (H_2SO_4) as proton conducting electrolyte in three electrodes electrochemical cell to detect wide range concentration (10 to 70%) H_2 gas at room temperature. The proposed sensor shows good sensitivity of 0.222 μA/%H_2 with fast response time of 60 seconds and low limit of detection (LOD) as compared to other similar reported amperometric H_2 sensors.

Chapter 5 contains the study on amperometric sensing of H_2 gas using heterostructure of PdO nanoparticles and two dimensional (2D) nanosheets of reduced graphene oxide (rGO) based WE and H_2SO_4 as proton conducting electrolyte in three electrodes electrochemical cell to detect wide range concentration (10 to 80%) H_2 gas at room temperature. The proposed sensor demonstrates sensitivity of 0.462 μA/%H_2 i.e. two folds increase as compared to PdO/ITO WE, with fast response time of 60 seconds and low limit of detection (LOD) as compared to other similar reported amperometric H_2 sensors.

Chapter 6 consists of study on chemiresisitve sensing of H_2 gas using heterostructures of PdO with polyaniline (PANI) conducting polymer matrix as solid state sensing element at room temperature. PdO-PANI nanocomposites based sensing assembly exhibited two folds increase in sensitivity as compared to pristine PANI. Moreover, the magnitude of sensitivity also increases with the percentage concentration of PdO, but the increase is not comprehensive comparatively. The proposed sensor demonstrates enhanced sensitivity, quick response/recovery time of 3 and 4 seconds respectively on comparison with other similar PANI and its nanocomposites based sensors reported in literature.

Chapter 7 consists of elucidated outline of complete research work presented from chapter 1 to chapter 6 correspondingly. It also describes the different course of work which will be approached in future to further enhance the sensitivity of pristine PdO nanomaterials towards H_2 gas at room temperature.

LIST OF FIGURES

LIST OF TABLES

LIST OF PUBLICATIONS

(Included in Ph.D. Thesis)

1. **Kamal Arora**, Deepika Sandil, Gaurav Sharma, Saurabh Srivastava, and Nitin K. Puri. **"Effect of low pressure hydrogen environment on crystallographic properties of PdO nanoparticles."** International Journal of Hydrogen Energy 41, no. 47 **(2016)**: 22155-22161. **(Impact factor: 4.939)**

2. **Kamal Arora** and Nitin K. Puri. **"Electrophoretically deposited nanostructured PdO thin film for room temperature amperometric H_2 sensing."** Vacuum 154 **(2018)**: 302-308. **(Impact factor: 2.906)**

3. **Kamal Arora**, Saurabh Srivastava, Pratima R. Solanki and Nitin K. Puri, **"Electrochemical Hydrogen Gas Sensing Employing Palladium Oxide/Reduced Graphene Oxide (PdO-rGO) Nanocomposites,"** IEEE Sensors Journal, vol. 19, no. 18, pp. 8262-8271, 15 Sept.15, **2019**. **(Impact factor: 3.073)**

4. **Kamal Arora, Nitin K. Puri.** ***"Chemiresistive sensing platform based on PdO-PANI/ITO heterostructure for room temperature hydrogen detection."*** **Materials Chemistry and Physics (2020), 247, 122850. (I.F.= 3.408)**

(Not included in Ph.D. Thesis)

5. Saurabh Srivastava, Vinod Kumar, **Kamal Arora**, Chandan Singh, Md Azahar Ali, Nitin K. Puri, and Bansi D. Malhotra**. "Antibody conjugated metal nanoparticle decorated graphene sheets for a mycotoxin sensor."** RSC Advances 6, no. 61 **(2016)**: 56518-6526. **(Impact factor: 3.119)**

6. Deepika Sandil, Saurabh Kumar, **Kamal Arora**, Saurabh Srivastava, B. D. Malhotra, S. C. Sharma, and Nitin K. Puri. **"Biofunctionalized nanostructured tungsten trioxide based sensor for cardiac biomarker detection**." Materials Letters 186 **(2017)**: 202-205. **(Impact factor: 3.204)**

LIST OF CONFERENCES

1. **Kamal Arora**, Saurabh Srivastava, Nitin K. Puri. **"Room temperature amperometric H_2 sensing using PdO thin film."** **17th International Conference on Thin Films** (ICTF 2017), November 13th – 17th, **2017**, NPL, New Delhi (**Poster presentation).**

2. **Kamal Arora** and Nitin K. Puri. **"PdO/Polyaniline nanocomposite for room temperature hydrogen sensing application." 17th International Meeting on Chemical Sensors** (IMCS 2018), July 15th – 19th, **2018**, Vienna, Austria **(Poster presentation)**.

LIST OF ACRONYMS

SPR	Surface plasmon resonance
AGS	Acoustic gas sensors
QCM	Quartz crystal microbalance
SAW	Surface acoustic waves
IDE	Interdigitated electrodes
WE	Working electrode
CE	Counter electrode
RE	Reference electrode
PTFE	Polytetrafluoroethylene
FEP	Fluorinated ethylene propylene
RT	Room temperature
IL	Ionic liquid
ITO	Indium tin oxide
MOX	Metal oxide
1D	One dimensional
2D	Two dimensional
3D	Three dimensional
UV-Vis	Ultraviolet-visible
PdO	Palladium oxide
XRD	X-ray diffraction
TEM	Transmission electron microscopy
FTIR	Fourier transform infrared spectroscopy
SEM	Scanning electron microscopy
PVD	Physical vapour deposition
CVD	Chemical vapour deposition
CCD	Charged coupled device
HRTEM	High resolution transmission electron microscopy
SAED	Selected area electron diffraction
BSE	Back scattered electron

IR	Infrared
MIR	Mid infrared region
GUI	Graphical user interface
PdH_x	Palladium hydride
t-PdO	Tetragonal palladium oxide
fcc	Face centered cubic
mbar	Millibar
LDL	Lowest detection limit
EPD	Electrophoretic deposition
Ag/AgCl	Silver/silver chloride
D.I.	Deionized
MFC	Mass flow controller
JCPDS	Joint Committee on powder diffraction standards
CV	Cyclic voltammetry
LOD	Limit of detection
CMG	Chemically modified graphene
GO	Graphene oxide
rGO	Reduced graphene oxide
CAS	Chemicals abstract service
RSD	Relative standard deviation
PANI	Polyaniline
ES	Emeraldine salt
EB	Emeraldine base
CSA	Camphor sulphonic acid
APS	Ammonium peroxide sulphate
HCl	Hydrochloric acid

TABLE OF CONTENTS

CHAPTER 1

Introduction and Motivation

Chapter 1 explains about the need for sensitive, stable and selective hydrogen (H_2) sensor which can detect wide range concentration of H_2 at room temperature (RT). All the prevalent H_2 sensors are broadly classified and their operation mechanisms along with their characteristics are discussed extensively. The importance of sensing material together with their traits and criteria for choosing the suitable material for detection of H_2 gas is also reviewed in detail. Amperometric, chemiresistive sensors and metal oxide (MOX) semiconductors are found to be the most sensitive, stable, selective, and explored in contrast with list of other sensors and sensing materials respectively. The barriers in the path of RT sensing of H_2 gas followed by their probable solutions are also described in this chapter. Finally, the motivation for pursuing this research work which outlines the reason for choosing PdO semiconductor as sensing material for sensing of H_2 gas at RT is justified explicitly.

1.1 Need for hydrogen (H_2) sensor

The unique physio-chemical properties of H_2 such as low density, low boiling point, high thermal conductivity, high diffusion coefficient, low minimum ignition energy and high heat of combustion makes it most favourable candidate to substitute various carbon based fuel sources for energy requirements [1]. The energy produced from H_2 is clean and green in nature due to emission of nearly zero pollutants, which has been the cause of major concern in modern world. Therefore, H_2 is used as a fuel, reactant and catalyst in diverse sectors i.e. aerospace, chemical, transportation and refineries to meet the ever growing requirement and expectations of global masses; while preserving and safeguarding the environment [2].

H_2 has high flammability with low ignition energy and a lower explosive limit of 4% concentration, thus there is a need for regular monitoring and sensitive detection mechanism in the industries. However, the colourless, odourless and tasteless characteristics of H_2 gas make it difficult to detect through human sensory organs [3]. Hence, detection of H_2 can only be achieved through observing modifications imparted in the material present in its surrounding. Interaction of the material with H_2 can lead to changes in its temperature, refractive index, electrical properties, mass and other physical properties [4]. These changes can then be transduced into recognizable electrical signal for fast detection and mapping of H_2 gas. This mechanism is the basis of operation for all the varied H_2 sensors available in market today which can be classified as catalytic, thermal conductivity, mechanical, optical, acoustic, electrochemical and chemiresistive or resistance based.

1.1.1 Catalytic H_2 sensor

It works on the principle of heat generation corresponding to change in resistance of material on reaction with combustible gases such as H_2 (figure 1.1) [5].

1.1.1.i Pellistor based catalytic sensor

- It consist of two pellets containing coils of platinum (Pt) attached within it
- Surface of active pellet is coated with catalyst such as palladium (Pd) or Pt
- The surface of inactive compensatory pellet is left unperturbed
- The complete setup is attached to wheat-stone bridge circuit in a closed chamber
- Introduction of current in coils raise their temperature
- Absorption of H_2 followed by reaction with surface oxygen forms water on surface
- The formation of water (H_2O) results in release of heat from surface
- This heat change cause shift in resistance which is measured by bridge circuit

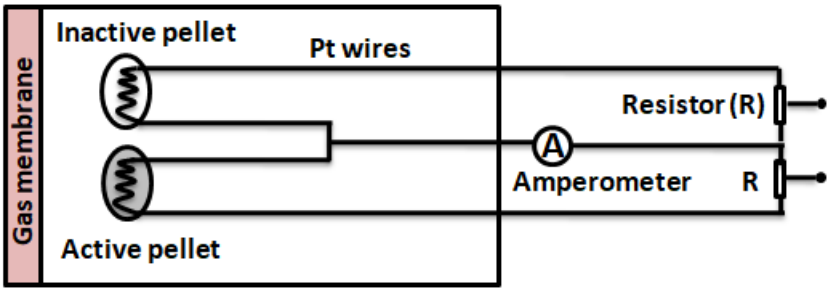

Figure 1.1. Schematic of catalytic H_2 sensor

1.1.1.ii Thermoelectric based catalytic sensor

- The setup is similar to pellistor based catalytic sensor
- It works on principle of Seebeck effect [6]
- Heat generation due to exothermic reaction with H_2 generates electrical signal
- Signal occurs in form of potential difference between two points of coil

1.1.2 Thermal conductivity H_2 sensor

The principle of its working is based on transduction of rate of heat transfer from hot body to surrounding in form of electrical signal (figure 1.2) [7].

1.1.2.i Pellistor based thermal conductivity sensor

- The setup is similar to catalytic sensor
- Only difference is enclosing one pellet in a separate chamber containing reference gas
- Zero heat transfer on exposing both pellets with reference gas
- Heat transfer takes place on exposure of synthesized pellet with H_2
- Direction of heat transfer depends on interaction of pellet with target gases
- The magnitude of signal depends on rate and magnitude of heat transfer

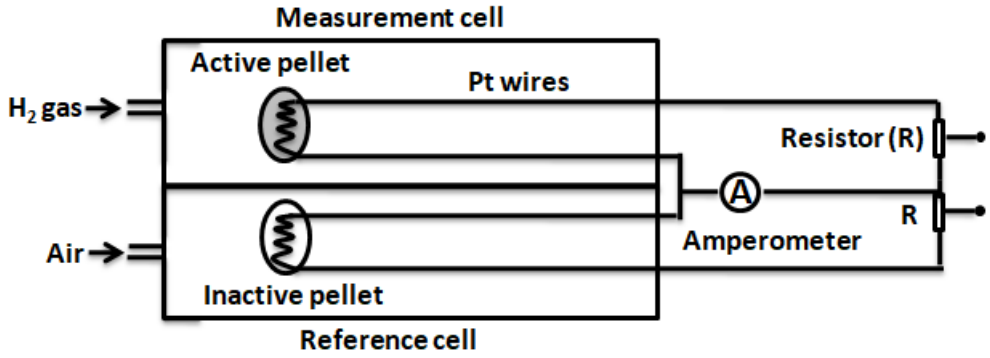

Figure 1.2. Schematic of thermal conductivity based H_2 sensor

1.1.3 Mechanical H_2 sensor

- The setup consist of cantilever coated with Pd or Pt thin film
- Interaction of Pd with H_2 leads to expansion of its structure (figure 1.3)
- However, cantilever material resist the expansion yielding stress
- Induced stress is transduced in the form of bending of cantilever [8]
- The magnitude of bending depends on the concentration of H_2

1.1.4 Optical H_2 sensor

- The setup consist of optical fiber with cladding coated with Pd or Pt layer
- The optical path of incident light is analyzed using interferometry

- H_2 gas is introduced inside the fiber leading to expansion of Pd layer [9]
- Expansion of layer modifies the optical path of travelling light (figure 1.4)
- The change in optical path length is measured to detect concentration of H_2

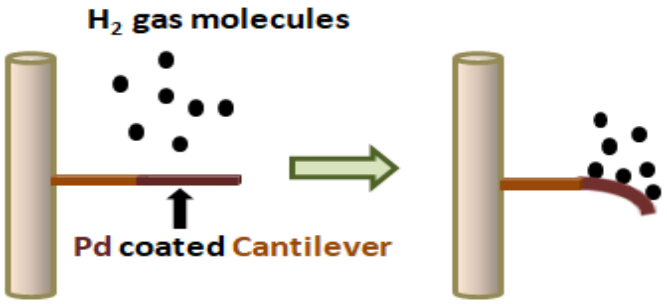

Figure 1.3. Schematic of mechanical H_2 sensor

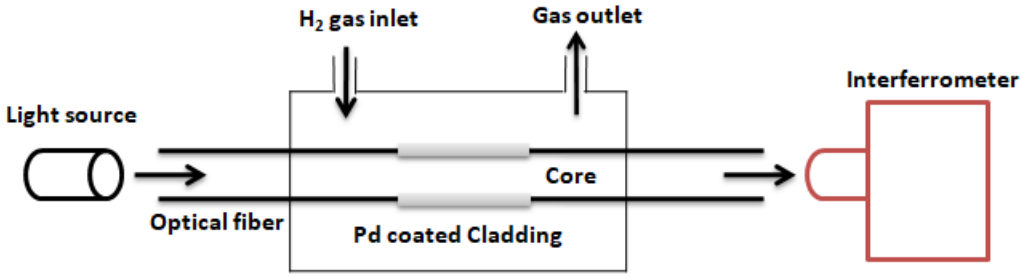

Figure 1.4. Schematic of optical H_2 sensor

1.1.4.i Surface Plasmon resonance (SPR) H_2 sensor

- Surface plasmons are electromagnetic waves propagating parallel to materials surface
- Prism or grating coupler are used to generate surface plasmons [10]
- SPR active materials such as gold, silver, Pd etc. can only be used
- However, due to high reactivity of Pd with H_2, it is used as active material in SPR
- Interaction with H_2 leads to modification of refractive index
- The change is measured in terms of resonant wavelength or resonant frequency

1.1.5 Acoustic H_2 gas sensor (AGS)

It works on the principle of modification in characteristics of acoustic waves propagating on surface of piezoelectric materials, due to absorption of H_2 gas molecules on surface or bulk of the material (figure 1.5).

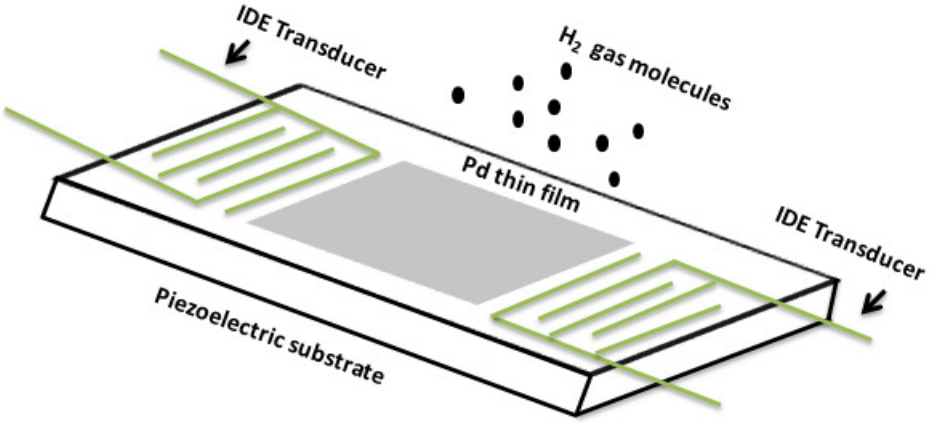

Figure 1.5. Schematic of acoustic H_2 sensor

1.1.5.i Quartz crystal microbalance (QCM) H_2 sensor

- It consist of two electrodes deposited on either side of H_2-philic material
- The material is coated on quartz disk substrate
- Application of potential across electrodes leads to resonation of material [11]
- Vibration of material at resonant frequency yields in deformation of material
- Resonant frequency is dependent on the concentration of H_2 molecules on surface

1.1.5.ii Surface acoustic wave (SAW) H_2 sensor

- SAW sensor contains a H_2-philic material coated on piezoelectric substrate
- Interdigitated electrode (IDE) transducers are deposited on either sides of material
- One side transducer converts electrical signal to Rayleigh or SA waves [12]
- SA waves propagate on surface of material and collected by other side transducer

- Thereafter, transducer converts these propagated waves back to electrical signal
- The magnitude of signal depends on the concentration of H_2 molecules on surface

Although, these H_2 sensors shows facile and robust detection of H_2 gas at room temperature (RT) with low power consumption; nevertheless their disadvantages outweigh their positive traits and makes them undesirable for large scale production and application. The disadvantages of above explained H_2 sensors are as follows [4]:

- Slow response characteristics
- Poor sensitivity to low concentration of H_2 gas
- Susceptibility to interference from other gases
- Susceptibility to H_2 induced structural damages and aging effects
- Susceptibility to irreversible poisoning by environmental contaminants
- High cost of fabrication

However, electrochemical and chemiresistive H_2 sensors are found to be economical and sensitive at low concentration of H_2 gas with fast response characteristics comparatively.

1.1.6 Electrochemical H_2 sensor

- The setup consists of electrochemical cell attached to potentiostat/galvanostat
- Electrochemical cell contains two electrodes dipped in proton conducting electrolyte
- Working electrode (WE) is made up of H_2-philic material and serves as a anode
- Counter electrodes (CE) is generally made of Pt and works as a cathode [13]
- Pt is used extensively as CE due to low solubility of H_2 as compared to Pd
- Redox reaction between electrodes contributes to change in electrical properties
- Increase or decrease in electrical parameters depends on analyte concentration
- It is categorized in two types i.e. amperometric and potentiometric H_2 sensors

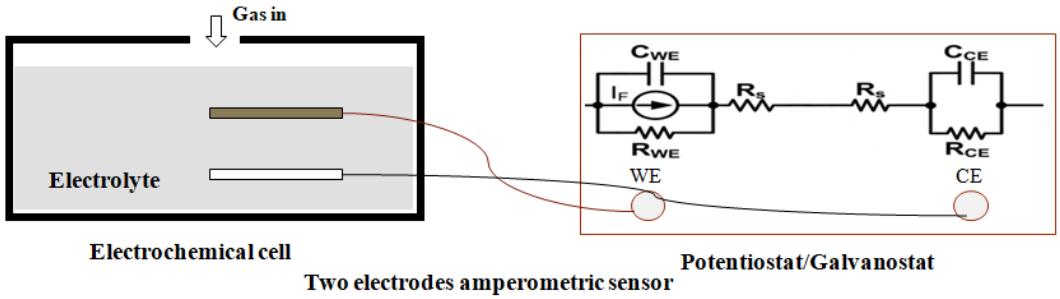

Two electrodes amperometric sensor

WE is working electrode (sensing element) , CE is counter electrode, C_{WE} is working electrode capacitance in pico Faraday (pF), R_s is electrolyte resistance in ohms (Ω), C_{CE} is counter electrode capacitance (pF) and I_F is the circuit current micro Amperes (μA)

Figure 1.6. Schematic of two electrodes electrochemical H_2 sensor

1.1.6.i Amperometric H_2 sensor

This type of electrochemical sensor works on the principal of change in the concentration of electrons at constant applied potential, because of redox reaction between electrodes inside the electrochemical cell (figure 1.6). The signal is recorded as a rate of change in electrochemical current or amperometry, with the modification in concentration of analyte or H^+ ions within proton conducting electrolyte. The signal of this sensor depends on the concentration of H_2 gas diffusing inside the electrolyte and the amount of H^+ ions reaching the electrode-electrolyte surface to participate in the redox reaction [14].

The sensor can be operated in two electrochemical kinetic limiting conditions i.e. diffusion kinetic control and electrode kinetic control. When the rate of diffusion (r_d) is much greater than rate of electrode reaction (r_r) ($r_d >> r_r$), the amount of H^+ ions reaching the electrode-electrolyte surface is larger than the amount consumed for electrochemical reaction by the electrodes. This results in saturation of electrolyte and creates a barrier towards incoming H^+ ions at the electrodes surface affecting the sensor signal. The response of amperometric sensor is governed by electrodes kinetic control and the limiting current (i_{lim}) can be evaluated using Faraday's law and equation 1.1;

$$i_{lim} = nFkAC\ e^{(\frac{znFE}{RT})}$$ **(Equation 1.1)**

Where, n is number of electrons per molecule, F is Faraday constant i.e. (9.648 x 10^4 coulombs/mol), k is standard rate constant, A is area of electrodes (m^2), C is concentration of analyte (mol/m^3), z is transfer coefficient, E is potential between electrodes (volts), R is gas constant i.e. (8.3145 Joules mol^{-1} $Kelvin^{-1}$) and T is temperature (Kelvin).

As it is observed in equation 1.1, the limiting current is also dependent on the size of electrodes, thus modification and degradation of electrodes with time leads to decay in response of the amperometric sensor. This instability of sensor can be mitigated by operating under diffusion kinetic control i.e. ($r_r >> r_d$), the rate of diffusion is slower than the rate of analyte reaction on electrodes surface which leads to an assumption that every molecule of analyte diffusing inside electrolyte through porous gas permeable membrane is consumed in redox reaction at electrode surface. This operating condition gives maximum, stable and optimum response of amperometric sensor with high resolution between different concentrations of analyte. The limiting current is governed by Fick's law (equation 1.2) and is calculated using modified Faraday's (i.e. combination of Faraday and Fick's law) equation 1.3;

$$i_{lim} = k\ [C]$$ **(Equation 1.2)**

$$i_{lim} = 2QAD\frac{\partial C}{\partial x}$$ **(Equation 1.3)**

Where, Q is electronic charge (1.6 x 10^{-19} coulombs) A is the area of diffusion barrier (m^2), x is thickness of membrane (m) and D is diffusion coefficient (m^2/seconds).

1.1.6.ii Potentiometric H_2 sensor

The operating principal of this type of electrochemical sensor is analyzing the change in electrochemical thermodynamic potential between electrodes by assuming thermal equilibrium between redox reactions resulting in near zero current. The signal of the sensor is governed by Nernst equation (equation 1.3) and depends on the concentration of analyte within proton conducting electrolyte [13].

$$E = E^0 + \frac{RT}{nF} \ln A \qquad \textbf{(Equation 1.4)}$$

Where, E^0 is standard electrochemical potential of electrodes (in volts) and A is chemical activity of analytes.

1.1.6.iii Favourable electrochemical H_2 sensor

Amperometric Sensor	**Potentiometric Sensor**
Linear and accurate dynamic range of response [15]	Logarithmic response with low accuracy (deviation from Nernstian behaviour)
Sensitivity can enhanced by modifying electrode structure	Independent of physical characteristics of electrodes
High sensitivity even for low concentration	Low sensitivity comparatively
Mechanism can be easily explained by chemical reaction	Several chemical reactions leads to observed signal [13]

Thus, it can be inferred that amperometric sensor gives more sensitive, stable and selective response towards diffused H_2 gas compared to potentiometric sensor. However, there are following drawbacks attached to two electrodes amperometric sensor [16]:

- Shift in constant thermodynamic electrochemical potential during redox reaction
- Diffusion of other gases along with H_2 lead to cross sensitivity

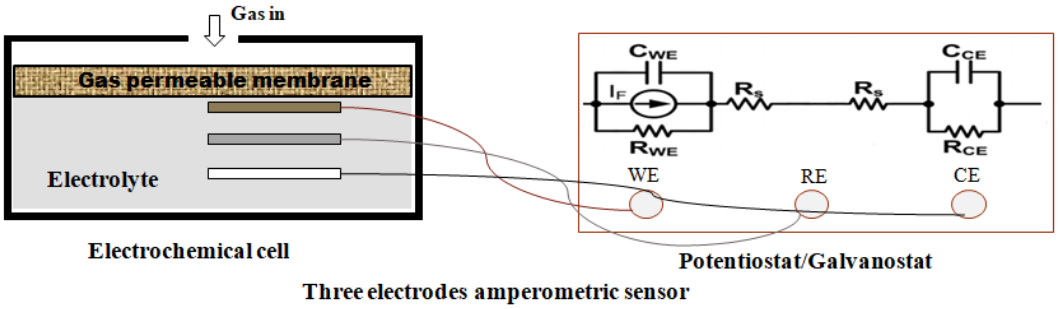

Three electrodes amperometric sensor

WE is working electrode (sensing element) , RE is reference electrode, CE is counter electrode [Platinum (Pt)], C_{WE} is working electrode capacitance in pico Faraday (pF), R_s is electrolyte resistance in ohms (Ω), C_{CE} is counter electrode capacitance in micro Faraday (μF) and I_F is the circuit current micro Amperes (μA)

Figure 1.7. Schematic of three electrodes electrochemical H_2 sensor

It results in low sensitivity and selectivity of amperometric sensor with inaccurate sensing signal. These drawbacks can be resolved by employing following methods;

1. **Three electrode amperometric sensor:** A third electrode or reference electrode (RE) is used to maintain the constant thermodynamic potential of electrochemical cell throughout the redox reactions. However, just inclusion of RE does not solve the problem as the material used for fabrication of RE should be non-reactive towards H_2 gas molecule, thus Silver (Ag)/ Silver chloride (AgCl) based RE are used the most by researchers. Nevertheless, Ag/AgCl can react with the contaminants present in the electrolyte which leads to removal of chloride ions (Cl^-) from RE. It results in degradation of RE with time and affect the sensing response of amperometric sensor. Therefore, RE is coated with proton conducting membrane of Nafion (sulfonated tetrafluoroethylene based fluoropolymer-copolymer) which protects the RE from other interferants present in the surrounding (figure 1.7).
2. **H_2 selective gas permeable membrane:** Various polymeric and inorganic porous H_2 selective gas permeable membranes, such as Teflon, polytetrafluoroethylene (PTFE), fluorinated ethylene propylene (FEP) etc., are used in amperometric H_2 sensor for

effective diffusion of H_2 gas in proton conducting electrolyte compared to other gases and zero permeability for aqueous electrolytes.

1.1.6.iv Proton conducting electrolytes

Various electrolytes are used for dissolving H_2 gas molecules are thereafter transporting corresponding H^+ ions towards electrodes for initiating redox reactions [13]. These electrolytes are known as proton conducting electrolytes and they can be classified on basis of their state as:

1. Liquid electrolyte

Sulphuric acid (H_2SO_4) and potassium hydroxide (KOH) are the inorganic acid and basic solutions used as proton conducting liquid electrolyte along with biologically compatible materials such as hydrogenase.

Advantages:

- High solubility of H_2 molecules and good conductivity for H^+ ions at RT
- Sensing response is independent of relative humidity (RH) in the surrounding

Disadvantages:

- Drying, spilling and leakage of electrolyte with time results in aging of sensor
- Corrosion of electrodes due to reaction with its material
- Formation of water molecules in liquid electrolyte decrease the sensitivity of sensor

2. Solid electrolyte

Various conducting polymers, hydrogels, solid state metal oxides, ceramics and perovskites are used as proton conducting electrolyte in amperometric H_2 sensor.

Advantages:

- Long term stability and high sensitivity
- Fast response characteristics
- Mitigates the problem of corrosion of electrodes

Disadvantages:

- Low mobility and conductivity for H^+ ions at RT
- Sensing response interfered by RH resulting in inaccurate sensing signal at RT
- Requires high temperature for conductivity and transportation of H^+ ions
- Proton conductivity is function of operating temperature

3. Ionic liquid (IL) electrolyte

These are the materials which exist in liquid state only when the temperature is less than 100 ^{0}C. Most commonly used IL electrolyte in amperometric H_2 sensors are mixture of cations such as imidazolium, pyridinium, phosphonium, pyrrolidinium, tetraalkylphosphonium, tetraalkylammonium and trialkylsulfonium combined with anions such as tetrafluoroborate hexafluorophosphate, trifluorotris(pentafluoroethyl)phosphate, thiocyanate, dicyanamide, ethyl sulfate, and bis(trifluoromethylsulfonyl)amide [17].

Advantages:

- They contains all the good qualities of both liquid as well as solid electrolytes
- Hygroscopic in nature

Disadvantages:

- Less conductivity and mobility as compared to concentrated aqueous electrolytes
- Slower response time

- High viscosity

Hence, it can be concluded that irrespective of above explained drawbacks, liquid electrolytes are the most suitable candidate for sensitive and selective amperometric sensing of H_2 gas at RT.

1.1.7 Chemiresistive H_2 sensor

The operational principle of this type of sensor is based on change in resistance or resistivity of material on solid state interaction with H_2 gas molecule. The setup of chemiresistive H_2 sensor contains a sensing element connected to multimeter or source meter to record the changes in electrical properties of target material (figure 1.8). The chemiresistive sensing element consists of a solid substrate i.e. glass, silicon (Si), copper (Cu), indium tin oxide (ITO) layered glass etc. coated with material thin film, above which interdigitated electrodes (IDE) are deposited for attaining the electrical connection. The interaction of material with H_2 occurs via two process of adsorption i.e. physisorption followed by chemisorptions [18].

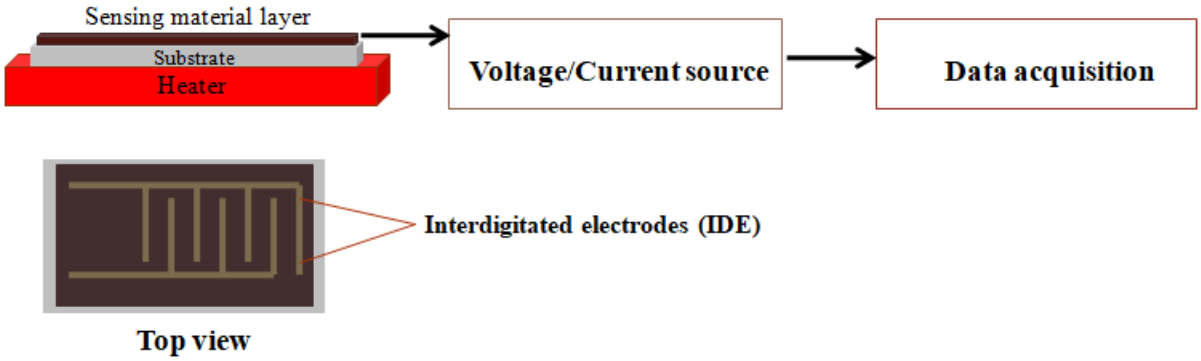

Figure 1.8. Schematic of chemiresistive H_2 sensor

Physisoprtion is an exothermic process which results in association of dissociated H^+ ions on the surface of materials using weak Van der Waal's bonds. The process of physisorption is followed by formation of strong chemical covalent bond between adsorbed H^+ ions and other

ions present on the surface of material which results in transfer of electrons, this process is endothermic in nature and require high temperature for the recovery of material to its original form.

Advantages

- High sensitivity [4]
- Wide operating temperature change
- Low cost of fabrication and production
- Easily integrated in existing electronic circuits
- Long term stability

Disadvantages

- Response characteristics and operating temperature dependent on sensing material
- Usually requires high operating temperature
- Not suitable for flammable gases such as H_2
- Poor selectivity
- Sensing signal interfered from RH and other environmental gases
- Poisoning by other contaminant gases present in atmosphere
- Requires sealed vacuum chamber for effective operation

1.2 Choice of sensing materials

Sensing materials play a significant role in sensing of H_2 gas in all the above explained sensors. The sensing signal, response characteristics and operating temperature of H_2 sensors depend on the surface, electrical, physical and chemical properties of materials [19]. Varied materials have been used till date for H_2 sensing applications and can be broadly categorized as:

- Solid electrolytes
- Polymers
- Ionic membranes
- Ionic salts
- Metals
- Semiconductors

The best suitable sensing material for H_2 sensors should have the following characteristics:

- Low density of surface states
- Wide band gap
- Low activation energy for adsorption of H_2 gas
- Optimally high activation energy for desorption of H_2 gas
- High catalytic ability towards H_2
- Low concentration of point defects or zero self conductivity
- High thermal and chemical stability
- Low volatility
- Long term stability
- Ease of synthesis and fabrication
- Should be easily integrated within existing silicon based electronic circuits

Metals and semiconductors are the only materials which have been extensively researched for electrochemical and chemiresistive H_2 sensing application. Nonetheless, Bulk metals have very low band gap, high conductivity, low thermal and chemical stability. However, reducing their size to nano-dimension mitigates these problems and makes them suitable for H_2 sensing application. Nano-sized Copper (Cu), Gold (Au), Silver (Ag), Palladium (Pd) and Platinum (Pt) based sensing elements have been reported in literature for their H_2 sensing

application. But, Pd and Pt are the only noble metals which are explored the most compared to others, due to their high reactivity and catalytic ability via process of spillover effect [20-22]. Nevertheless, pristine metals get irreversibly poisoned from sulfur (S), arsenic (As), lead (Pb), iron (Fe), phosphorus (P) etc., which act as environmental contaminants [23]. Also, interaction of these metals with H_2 leads to expansion of their structure which results in development of cracks because of hydrogen embrittlement and delamination of their thin film deposited on the rigid substrate [24].

There are two classes of semiconductors i.e. covalent and ionic semiconductors. Silicon (Si), germanium (Ge) and gallium arsenide (GaAs) belong to the category of covalent semiconductors. Ionic semiconductors are further divided into two types, standard ionic semiconductors such as zinc sulfide (ZnS), cadmium sulfide (CdS) etc. and metal oxide semiconductors such as tin oxide (SnO_2), zinc oxide (ZnO) etc.

It is observed that irrespective of their size, only metal oxide (MOX) semiconductors contain all the best traits of sensing material and thus are the most favorable choice for H_2 sensing application compared to other materials discussed in above paragraphs of section 1,2 [25].

1.2.1 Metal oxide (MOX) semiconductors

MOX semiconductors are subdivided into three categories depending on their valence electronic configuration into pre-transition MOX, transition MOX and post-transition MOX [19]. It is found that only transition MOX and post transition MOX are suitable for H_2 sensing application.

i. Pre-transition MOX

- Valence orbital belongs to s and p-orbital symmetry

- Magnesium oxide (MgO), Aluminium oxide (Al_2O_3) etc. belongs to this category
- Large band gap ($E_g \geq 6$ eV)
- Very high resistance
- Good isolators and not suitable for sensing application

ii. Transition MOX

- Valence orbital belongs to d-orbital symmetry (d^n)
- Elements with ($1 \leq n < 10$) falls in this category
- More than one preferred oxidation state possible

Advantages

- Comparatively low operating temperature
- Can be reduced as well as oxidized
- High catalytic activity

Disadvantages

- Small and narrow band gap ($1 \text{ eV} \leq Eg < 3 \text{ eV}$)
- Structural instability
- Higher electroconductivity

iii. Post-transition MOX

- Elements with (n=0) and (n = 10) falls in this category
- Only one preferred oxidation state possible
- Zinc oxide (ZnO), tin oxide (SnO_2) etc. belongs to this category

Advantages

- Wide band gap ($3 \text{ eV} \leq Eg \leq 6 \text{ eV}$)
- Structural stability

- Low electroconductivity

Disadvantages

- High operating temperature
- Can only be reduced not oxidized
- Low catalytic activity

It can be concluded from above discussion that although post transition MOX shows maximum sensing response in comparison to transition MOX, but they have high activation energy for physisorption which results in long recovery time and thus sensors based on post transition MOX require high temperature for their operation. Hence, pristine bulk post transition MOX semiconductors are not suitable for sensing of H_2 gas due to its flammable nature.

1.2.2 Ways to achieve room temperature sensing

There are three major ways to reduce the operating temperature and enhance the sensing characteristics of MOX semiconductors based H_2 sensors.

1. Nanostructured MOX

It has been observed that reducing the size of bulk MOX to nano dimensions increases their sensing response while decreasing their recovery time and thus enabling H_2 sensors to operate at room temperature; because of additional surface and quantum size effects. Surface effects of nanomaterials include high surface to volume ratio due to decrease in grain size which results in significant modification of space charge region, enhancing the sensitivity of sensors. Quantum size effects include confinement of nanomaterials in 2-dimension (nanosheets, etc.), 1 dimension (nanorods, etc.) and 0-dimension (quantum dots), it is observed that quantum confinement of nanomaterial reduces the concentration of point

defects in their structure, increase their electronic band gap and renders them with specific adsorption and catalytic properties [26].

Various research work have been published in literature demonstrating low temperature H_2 sensitivity of nanostructures of transition MOX semiconductors such as Titanium oxide (TiO_2), Tungsten oxide (WO_3), Molybdenum oxide (MoO_3), Nickel oxide (NiO), Vanadium oxide (VO_2), Niobium oxide (Nb_2O_5), etc. [27-32] and post transition MOX such as Tin oxide (SnO_2), Zinc oxide (ZnO), etc., based sensing materials [33-34] .

2. Heterostructure materials

The material containing physical interface between two different materials (A & B) are known as heterostructure and the interface is known as heterojunction. Heterostructures are categorized in following three ways;

- Simple mixture of two materials A and B (denoted by A-B)
- Addition of material A over surface of material B (denoted by A@B)
- Well defined partition between layers of material A and B (denoted by A/B)

It has been observed that synthesis of heterostructure of two different MOX, MOX with nobel metal and MOX with carbon nanostructure enhances the sensing characteristics and decrease the recovery time of heterostructure material which results in room temperature operation of chemiresistive H_2 sensors. This enhancement in sensing properties is due to lowering of activation energy, increase in catalytic capability, increase in surface area for adsorption and synergistic surface reactions between interfaces [35]. The mechanism of sensing by heterostructures is governed by shifting of Fermi level followed by charge carriers depletion and separation yielding a potential barrier between interface i.e. schottky barrier. Researchers have reported extensive studies on enhanced response characteristics and low temperature sensitivity of H_2 gas for sensing elements based on heterostructures of MOX

semiconductors such as TiO_2/NiO, ZnO@SnO_2, MoO_3-SnO_2, cobalt oxide (Co_3O_4)-SnO_2, etc. [36-39]; heterostructures of MOX with noble metals such as Pt-SnO_2, Pd/V_2O_5, Cu@ZnO, Pt-Au@ZnO, Pd/WO_3, Pt@ZnO, Co-TiO_2 etc. [40-46], and heterostructures of MOX with cabon nanostructures such as In_2O_3/graphene, SnO_2/reduced graphene oxide (rGO), ZnO/graphene, TiO_2-polyaniline (PANI), etc., respectively [47-50].

3. Plasmon driven catalysis

High activation energy for desorption of H_2 in MOX semiconductors yields large recovery time for the sensors, thus high temperatures are applied as external stimulus for breaking the chemisorbed intermediate hydroxyl complex species from the surface of MOX. However, different external stimuli such as electromagnetic radiation i.e. ultraviolet-visible (UV-Vis) light illumination treatment post H_2 exposure have been reported to enable RT chemiresisitive H_2 sensing MOX nanomaterials [51].

Nicola cattabiani et. al showed enhanced sensitivity and fast response characteristics of Ag-SnO_2 nanowires towards H_2 gas at RT on illumination with UV-Vis light post exposure [52]. Similarly, Gopal K. Mor et. al reported self cleaning reversible sensing mechanism of TiO_2 nanotubes for H_2 gas with fast recovery time at RT due to photocatalytic oxidation on being exposed to UV radiation [53]. Thereafter, Sipra Choudhary et. al also demonstrated fast recovery and good sensitivity of palladium oxide (PdO) nanoparticles for H_2 gas at room temperature under UV illumination [54].

1.3 Motivation for the research work

Although, much research work have been reported in literature regarding H_2 sensing using various MOX nanostructures and their heterostructures at RT. Nonetheless, till the year 2015 i.e. beginning of this thesis research work, there were only two research studies reported in literature regarding H_2 gas sensing ability of pristine palladium oxide (PdO) nanomaterial.

- In the year 2010, Y. T. Lee et. al demonstrated solid state H_2 gas sensing using PdO thin film at RT [55]. The findings of this first study shows that,
  - Interaction of PdO with H_2 gas results in its reduction to Pd
  - However, sensing mechanism is observed to be irreversible in nature
- In the year 2015, Y. J. Chiang et. al reported a mechanistic study on solid state H_2 sensing by PdO nanoflakes thin film at different operating temperature intervals [56]. The results of this work confirmed the observations of first study and demonstrated that:
  - There is a instant reduction of PdO to Pd in presence of H_2 gas at RT
  - The reduction process results in formation of Pd nanoislands on PdO surface
  - Adjacently, dissociation of H_2 into H^+ ions takes place followed by its adsorption
  - Interaction of PdO layer with H^+ results in increased resistance of nanoflakes film
  - Absorption of H_2 in Pd increase electron scattering center, decreasing the conductivity
  - The response of the sensor remains irreversible in the interval of RT- 150 ^{0}C
  - Sensing mechanism becomes reversible only at high temperatures (150-200 ^{0}C)
  - The detailed discussion about this work is explained in section 3.1 of chapter 3

Thus, it can be inferred that although pristine PdO nanomaterial is not suitable for chemiresistive sensing of H_2 gas due to high operating temperature. However, PdO nanomaterial displays high catalytic activity and low activation energy for adsorption of H_2 similar to Pd nanomaterial. Moreover, the presence of uniform coating of oxide layer on the surface of PdO protects it from contamination and damage by atmospheric contaminants. Hence, PdO can be substituted for Pd as catalytic material for enhancing the sensitivity and

response characteristics of other MOX semiconductors towards H_2 gas [57-60]. As already discussed in section 1.1 and 1.2.1, amperometric sensors employing proton conducting liquid electrolyte and chemiresitive sensors using nanostructures and heterostructures of MOX sensing materials enable sensing of H_2 gas at RT respectively. This motivated us to begin our study with examination of detailed interaction mechanism between PdO nanoparticles and H_2 gas molecules, by observing the modifications in crystallographic structure and properties of PdO in presence of ambient H_2 environment at RT (Chapter 3). Furthermore, PdO nanoparticles and its heterostructures are synthesized and applied as sensing material in amperometric and chemiresisitive sensors to achieve enhanced sensitivity for wide range H_2 gas concentration at RT (Chapter 4 to 6 respectively).

1.4 References

[1] Q. Zhao*, et al.*, "Batch fabrication of nanogap electrodes arrays with controllable cracking for hydrogen sensing," *Sensors and Actuators B: Chemical,* vol. 270, pp. 475-481, 2018.

[2] J. H. Kim*, et al.*, "Aerogel sheet of carbon nanotubes decorated with palladium nanoparticles for hydrogen gas sensing," *International Journal of Hydrogen Energy,* vol. 43, pp. 6456-6461, 2018.

[3] J.-H. Kim*, et al.*, "Improving the hydrogen sensing properties of SnO2 nanowire-based conductometric sensors by Pd-decoration," *Sensors and Actuators B: Chemical,* vol. 285, pp. 358-367, 2019.

[4] T. Hübert*, et al.*, "Hydrogen sensors–a review," *Sensors and Actuators B: Chemical,* vol. 157, pp. 329-352, 2011.

[5] E.-B. Lee*, et al.*, "Micromachined catalytic combustible hydrogen gas sensor," *Sensors and Actuators B: Chemical,* vol. 153, pp. 392-397, 2011.

[6] M. Nishibori*, et al.*, "Thermoelectric hydrogen sensors using Si and SiGe thin films with a catalytic combustor," *Journal of the Ceramic Society of Japan,* vol. 118, pp. 188-192, 2010.

[7] A. Harley-Trochimczyk*, et al.*, "Catalytic hydrogen sensing using microheated platinum nanoparticle-loaded graphene aerogel," *Sensors and Actuators B: Chemical,* vol. 206, pp. 399-406, 2015.

[8] H. P. Lang*, et al.*, "Nanomechanical cantilever array sensors," in *Springer Handbook of Nanotechnology*, ed: Springer, 2017, pp. 457-485.

[9] H. Song*, et al.*, "Optical fiber hydrogen sensor based on an annealing-stimulated Pd–Y thin film," *Sensors and Actuators B: Chemical,* vol. 216, pp. 11-16, 2015.

[10] R. Tabassum and B. D. Gupta, "Surface plasmon resonance-based fiber-optic hydrogen gas sensor utilizing palladium supported zinc oxide multilayers and their nanocomposite," *Applied optics,* vol. 54, pp. 1032-1040, 2015.

[11] O. Abuzalat*, et al.*, "High-Performance, Room Temperature Hydrogen Sensing With a Cu-BTC/Polyaniline Nanocomposite Film on a Quartz Crystal Microbalance," *IEEE Sensors Journal,* vol. 19, pp. 4789-4795, 2019.

[12] W. Wang*, et al.*, "Development of a Pd/Cu nanowires coated SAW hydrogen gas sensor with fast response and recovery," *Sensors and Actuators B: Chemical,* vol. 287, pp. 157-164, 2019.

[13] G. Korotcenkov*, et al.*, "Review of electrochemical hydrogen sensors," *Chemical reviews,* vol. 109, pp. 1402-1433, 2009.

[14] J. R. Stetter and J. Li, "Amperometric gas sensors a review," *Chemical reviews,* vol. 108, pp. 352-366, 2008.

[15] R. Baron and J. Saffell, "Amperometric gas sensors as a low cost emerging technology platform for air quality monitoring applications: A review," *ACS sensors,* vol. 2, pp. 1553-1566, 2017.

[16] Y. Chao*, et al.*, "Amperometric sensor for selective and stable hydrogen measurement," *Sensors and Actuators B: Chemical,* vol. 106, pp. 784-790, 2005.

[17] M. J. Shiddiky and A. A. Torriero, "Application of ionic liquids in electrochemical sensing systems," *Biosensors and Bioelectronics,* vol. 26, pp. 1775-1787, 2011.

[18] J. Huang and Q. Wan, "Gas sensors based on semiconducting metal oxide one-dimensional nanostructures," *Sensors,* vol. 9, pp. 9903-9924, 2009.

[19] G. Korotcenkov, "Metal oxides for solid-state gas sensors: What determines our choice?," *Materials Science and Engineering: B,* vol. 139, pp. 1-23, 2007.

[20] Y. Fukai, *The metal-hydrogen system: basic bulk properties* vol. 21: Springer Science & Business Media, 2006.

[21] R. M. Penner, "A nose for hydrogen gas: fast, sensitive H2 sensors using electrodeposited nanomaterials," *Accounts of chemical research,* vol. 50, pp. 1902-1910, 2017.

[22] H.-J. Cho*, et al.*, "Pt-Functionalized PdO Nanowires for Room Temperature Hydrogen Gas Sensors," *ACS sensors,* vol. 3, pp. 2152-2158, 2018.

[23] M. Khanuja*, et al.*, "Concentration-specific hydrogen sensing behavior in monosized Pd nanoparticle layers," *Nanotechnology,* vol. 20, p. 015502, 2008.

[24] J. Song and W. Curtin, "A nanoscale mechanism of hydrogen embrittlement in metals," *Acta Materialia,* vol. 59, pp. 1557-1569, 2011.

[25] V. Aroutiounian, "Metal oxide hydrogen, oxygen, and carbon monoxide sensors for hydrogen setups and cells," *International Journal of Hydrogen Energy,* vol. 32, pp. 1145-1158, 2007.

[26] E. Roduner, "Size matters: why nanomaterials are different," *Chemical Society Reviews,* vol. 35, pp. 583-592, 2006.

[27] C. S. Rout*, et al.*, "Room temperature hydrogen and hydrocarbon sensors based on single nanowires of metal oxides," *Journal of Physics D: Applied Physics,* vol. 40, p. 2777, 2007.

[28] Z. Li*, et al.*, "Resistive-type hydrogen gas sensor based on TiO2: A review," *International Journal of Hydrogen Energy,* vol. 43, pp. 21114-21132, 2018.

[29] Z. Wang*, et al.*, "Fast and highly-sensitive hydrogen sensing of Nb2O5 nanowires at room temperature," *International Journal of Hydrogen Energy,* vol. 37, pp. 4526-4532, 2012.

[30] S. Yang*, et al.*, "Highly responsive room-temperature hydrogen sensing of α-MoO3 nanoribbon membranes," *ACS applied materials & interfaces,* vol. 7, pp. 9247-9253, 2015.

[31] M. Kandyla*, et al.*, "Nanocomposite NiO: Pd hydrogen sensors with sub-ppm detection limit and low operating temperature," *Materials Letters,* vol. 119, pp. 51-55, 2014.

[32] E. Strelcov*, et al.*, "Gas sensor based on metal− insulator transition in VO2 nanowire thermistor," *Nano letters,* vol. 9, pp. 2322-2326, 2009.

[33] J. Hassan*, et al.*, "A high-sensitivity room-temperature hydrogen gas sensor based on oblique and vertical ZnO nanorod arrays," *Sensors and Actuators B: Chemical,* vol. 176, pp. 360-367, 2013.

[34] G. Liu*, et al.*, "Remarkably Enhanced Room-Temperature Hydrogen Sensing of SnO2 Nanoflowers via Vacuum Annealing Treatment," *Sensors,* vol. 18, p. 949, 2018.

[35] D. R. Miller*, et al.*, "Nanoscale metal oxide-based heterojunctions for gas sensing: a review," *Sensors and Actuators B: Chemical,* vol. 204, pp. 250-272, 2014.

[36] I. Kosc*, et al.*, "Sputtered TiO2 thin films with NiO additives for hydrogen detection," *Applied Surface Science,* vol. 269, pp. 110-115, 2013.

[37] L. Tien*, et al.*, "Detection of hydrogen with SnO2-coated ZnO nanorods," *Applied Surface Science,* vol. 253, pp. 4748-4752, 2007.

[38] Z. Ansari*, et al.*, "Effect of MoO3 doping and grain size on SnO2-enhancement of sensitivity and selectivity for CO and H2 gas sensing," *Sensors and Actuators B: Chemical,* vol. 87, pp. 105-114, 2002.

[39] U.-S. Choi*, et al.*, "Sensing properties of Au-loaded SnO2–Co3O4 composites to CO and H2," *Sensors and Actuators B: Chemical,* vol. 107, pp. 397-401, 2005.

[40] L. Bizhou*, et al.*, "Facile synthesis and remarkable hydrogen sensing performance of Pt-loaded SnO2 hollow microspheres," *Materials Research Bulletin,* vol. 106, pp. 403-408, 2018.

[41] A. Sanger*, et al.*, "A fast response/recovery of hydrophobic Pd/V2O5 thin films for hydrogen gas sensing," *Sensors and Actuators B: Chemical,* vol. 236, pp. 16-26, 2016.

[42] R. K. Malik*, et al.*, "Hydrogen sensing properties of copper-doped zinc oxide thin films," *IEEE Sensors Journal,* vol. 15, pp. 7021-7028, 2015.

[43] F. Fan*, et al.*, "Hydrogen sensing properties of Pt-Au bimetallic nanoparticles loaded on ZnO nanorods," *Sensors and Actuators B: Chemical,* vol. 241, pp. 895-903, 2017.

[44] B. Liu*, et al.*, "Improved room-temperature hydrogen sensing performance of directly formed Pd/WO3 nanocomposite," *Sensors and Actuators B: Chemical,* vol. 193, pp. 28-34, 2014.

[45] L. Tien*, et al.*, "Hydrogen sensing at room temperature with Pt-coated ZnO thin films and nanorods," *Applied Physics Letters,* vol. 87, p. 222106, 2005.

[46] Z. Li*, et al.*, "Low-cost fabrication of highly sensitive room temperature hydrogen sensor based on ordered mesoporous Co-doped TiO2 structure," *Applied Physics Letters,* vol. 111, p. 032104, 2017.

[47] M. Mansha*, et al.*, "Synthesis of In2O3/graphene heterostructure and their hydrogen gas sensing properties," *Ceramics International,* vol. 42, pp. 11490-11495, 2016.

[48] P. A. Russo*, et al.*, "Room-temperature hydrogen sensing with heteronanostructures based on reduced graphene oxide and tin oxide," *Angewandte Chemie International Edition,* vol. 51, pp. 11053-11057, 2012.

[49] K. Anand*, et al.*, "Hydrogen sensor based on graphene/ZnO nanocomposite," *Sensors and Actuators B: Chemical,* vol. 195, pp. 409-415, 2014.

[50] S. Srivastava*, et al.*, "Synthesis and characterization of TiO2 doped polyaniline composites for hydrogen gas sensing," *International Journal of Hydrogen Energy,* vol. 36, pp. 6343-6355, 2011.

[51] Z. Li*, et al.*, "Advances in designs and mechanisms of semiconducting metal oxide nanostructures for high-precision gas sensors operated at room temperature," *Materials Horizons,* vol. 6, pp. 470-506, 2019.

[52] N. Cattabiani*, et al.*, "Tin oxide nanowires decorated with Ag nanoparticles for visible light-enhanced hydrogen sensing at room temperature: bridging conductometric gas sensing and plasmon-driven catalysis," *The Journal of Physical Chemistry C,* vol. 122, pp. 5026-5031, 2018.

[53] G. K. Mor*, et al.*, "A room-temperature TiO 2-nanotube hydrogen sensor able to self-clean photoactively from environmental contamination," *Journal of Materials Research,* vol. 19, pp. 628-634, 2004.

[54] S. Choudhury*, et al.*, "Nanostructured PdO thin film from Langmuir–Blodgett precursor for room-temperature H2 gas sensing," *ACS applied materials & interfaces,* vol. 8, pp. 16997-17003, 2016.

[55] Y. T. Lee*, et al.*, "Hydrogen gas sensing properties of PdO thin films with nano-sized cracks," *Nanotechnology,* vol. 21, p. 165503, 2010.

[56] Y.-J. Chiang*, et al.*, "A mechanistic study of hydrogen gas sensing by PdO nanoflake thin films at temperatures below 250° C," *Physical Chemistry Chemical Physics,* vol. 17, pp. 3039-3049, 2015.

[57] M. Jiao*, et al.*, "On-chip growth of patterned ZnO nanorod sensors with PdO decoration for enhancement of hydrogen-sensing performance," *International Journal of Hydrogen Energy,* vol. 42, pp. 16294-16304, 2017.

[58] F. Annanouch*, et al.*, "p-Type PdO nanoparticles supported on n-type WO3 nanoneedles for hydrogen sensing," *Thin Solid Films,* vol. 618, pp. 238-245, 2016.

[59] S. Kabcum*, et al.*, "Ultra-responsive hydrogen gas sensors based on PdO nanoparticle-decorated WO3 nanorods synthesized by precipitation and impregnation methods," *Sensors and Actuators B: Chemical,* vol. 226, pp. 76-89, 2016.

[60] J. H. Lee*, et al.*, "Sputtered PdO decorated TiO2 sensing layer for a hydrogen gas sensor," *Journal of Nanomaterials,* vol. 2018, 2018.

CHAPTER 2

Synthesis and Characterization techniques

Different approaches for synthesis of metal oxide (MOX) semiconductor nanostructures, corresponding methods for fabrication of their thin film based sensing elements and characterization tools for analysis of their physicochemical properties have been explored extensively in chapter 2. Wet chemical synthesis procedures based on liquid-solid transformation, are observed to be more favourable for synthesis of nanomaterials as compared to physical methods, which follows solid-solid and gas-solid transformation. The chemical synthesis procedures are facile, economical and more efficient in production of uniform and homogeneous nanostructures in bulk quantities comparatively. X-ray diffraction (XRD) measurements, transmission electron microscopy (TEM), ultraviolet-visible (UV-Vis) absorption spectroscopy, Fourier transform infrared (FTIR) transmission spectroscopy and scanning electron microscopy (SEM) are employed to analyze crystal structure, size, geometry, optical band gap, bonding nature, inter-bonding interaction and surface morphology of synthesized materials to validate the successful formation of desired nanostructures.

2.1 Synthesis of metal oxides (MOX) nanostructures

The choice of synthesis process plays an important role in controlling the size and shape of MOX nanomaterials. The synthesis of nanostructures is categorized in two approaches:

2.1.1 Top down approach

The method of obtaining nanostructures from their bulk counterparts comes under this category. The approach involves solid-solid and gas-solid transformations from bulk to nanomaterials and it can be realized using physical methods employing the process of grinding crushing and decomposition [57].

Following methods adopt top down approach:

- Ball milling
- Electric or Plasma arcing
- Electric, magnetic or laser sputtering
- Vapour deposition techniques
    - Physics vapour deposition (PVD)
    - Chemical vapour deposition (CVD)

2.1.1.i Disadvantages

- No control over geometry
- Requires sophisticated apparatus and vacuum condition
- High cost of operations
- Unsuitable for synthesis of uniform and homogeneous nanostructures
- Defects and imperfection results in degradation of properties

2.1.2 Bottom up approach

This approach involves preparation of desired nanostructures through interaction of atoms and molecules, resulting in formation of clusters of material through accumulation [58]. The interactions are based on liquid-solid transformation and consist of following chemical methods:

- Co-precipitation
- Sol-gel
- Microemulsions
- Solvothermal or hydrothermal
- Template or surface derived

The wet chemical methods are extensively employed by researchers for synthesis of varied nanostructures of MOX in contrast to physical methods because of following advantages [59];

2.1.2.i Advantages

- Enables control over size and geometry
- Allow uniform and homogeneous fabrication
- Yields good quality nanostructures in bulk quantities
- More facile and economical in operation

2.1.3 Mechanism of growth

The growth of nanostructures using bottom down approach undergoes step by step process involving nucleation, coarsening and agglomeration. All these steps occur simultaneously in order to synthesize nanostructure of MOX material (figure 2.1). Nucleation is the primary step which plants the seed for development of structures. Whereas the size and shape of these nanostructures are governed by secondary processes such as coarsening and agglomeration.

i. Nucleation

It is the first step of synthesis involving transition from existing precursor phase into thermodynamically unstable new phase forming a nucleus which ultimately grows irreversibly into minute grains or particles of desired material [60].

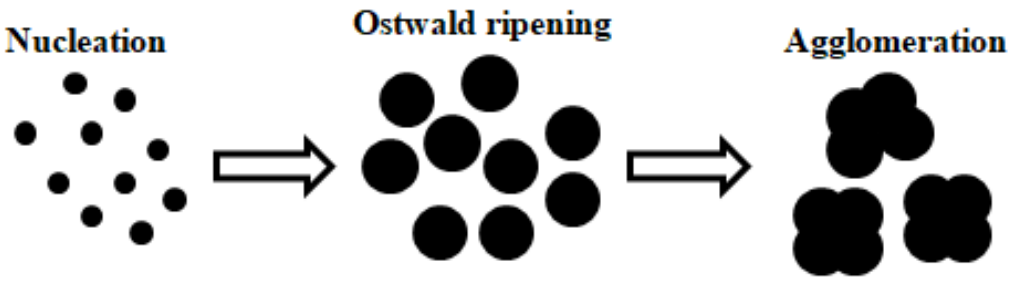

Figure 2.1. Schematic of nanostructures growth mechanism

ii. Ostwald ripening/coarsening

As observed by Wilhelm Ostwald in 1896, the smaller grains obtained during nucleation process precipitates to form thermodynamically stable bigger particles within the chemical solution. The process involves dissolution of small grains followed their diffusion in solvent and ultimately their accumulation to form bigger grain [61].

iii. Agglomeration

The bigger grains or particles obtained during the ripening process have high surface energy, which makes them to collide with each other and force them to join with each other to create thermodynamically equilibrated cluster of materials [62].

2.1.4 Co-precipitation

- Metallic salt precursors are dissolved in aqueous or inorganic solutions [63]
- Inorganic bases are added in the solution to initiate the precipitation (figure 2.2)

- Chemical reactions yield intermediate oxo-hydroxide and hydroxyl complex species
- The solution is filtered, washed and calcined to obtain powder of MOX nanomaterials

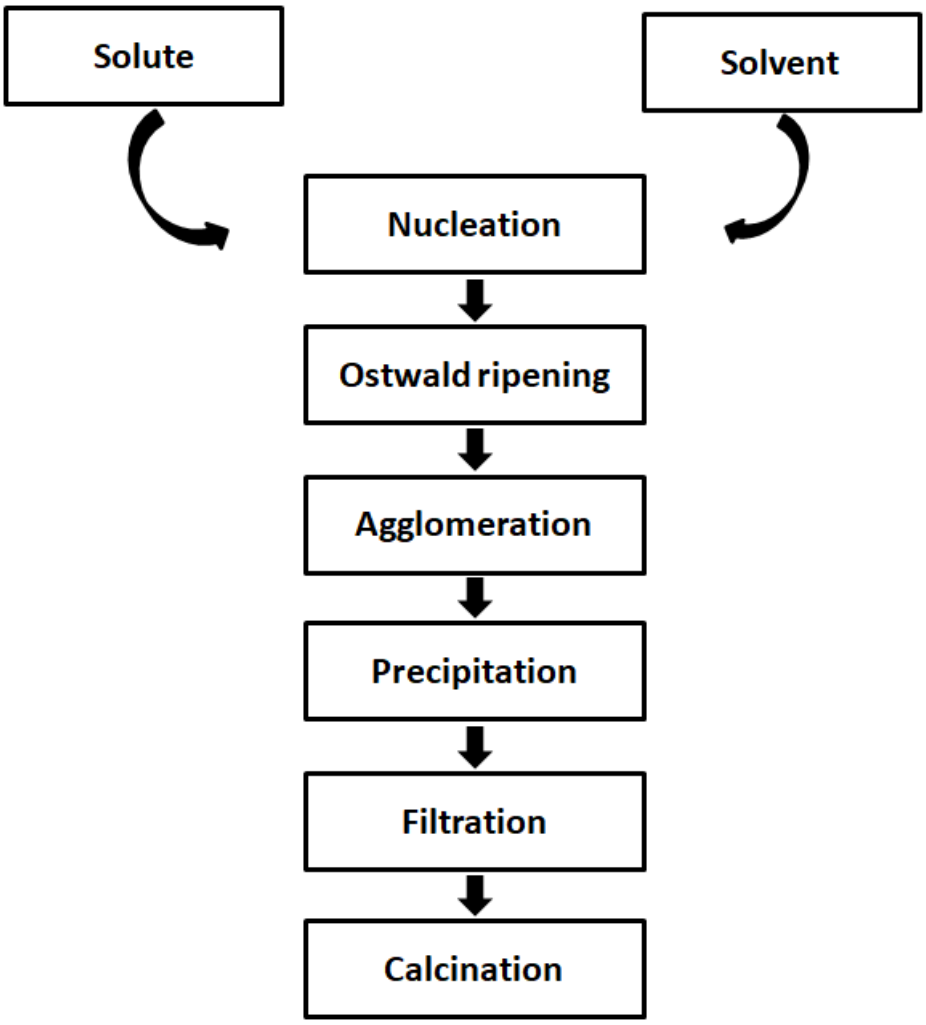

Figure 2.2. Co-precipitation procedure

2.1.4.i Advantages

- Facile and fast preparation
- Control over size and composition of nanostructures
- Low temperature operation
- Allow modifications in surface state and homogeneity of nanostructures

2.1.4.ii Disadvantages

- Not suitable for uncharged precursor species

- Precipitation of impurities within the product
- Unfavourable for precursors having different precipitation rates
- No reproducibility at large scale production

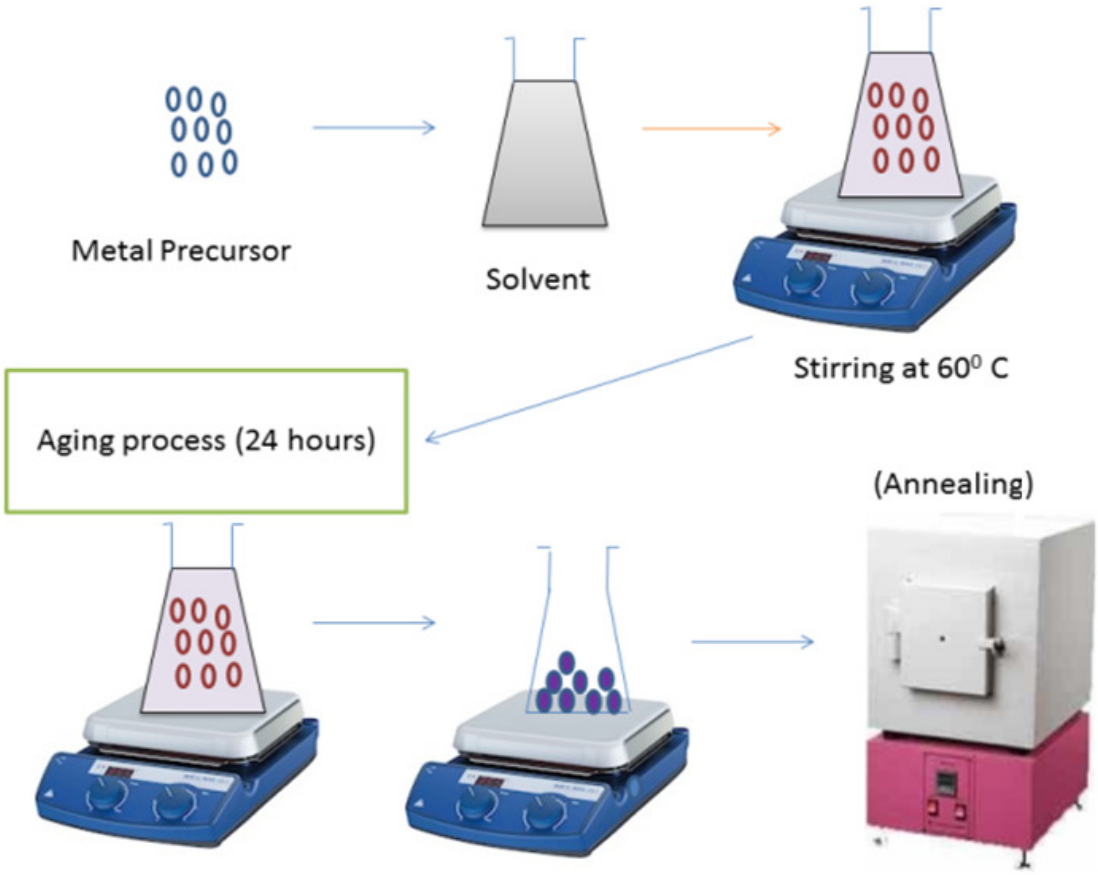

Figure 2.3. Sol-gel synthesis procedures

2.1.5 Sol-gel synthesis

- Hydrolysis of metal precursors in organic solvents (figure 2.3)
- Chemical reactions results in formation of oxo-hydroxide and hydroxyl groups
- Condensation of solution yields MOX network structure [64]
- Resultant solution is allowed to age for some time to achieve polymerization
- Polymerization of hydroxyl group leads to gelation of solution
- Filtration, washing and calcinations of gel gives powder of MOX nanomaterial

2.1.5.i Advantages

- Formation of homogeneous final product
- High purity of products compared to that with co-precipitation method
- Allow control over composition of material
- Synthesis at low temperature

2.1.5.ii Disadvantages

- Longer reaction time

2.1.6 Microemulsion synthesis

- Metal precursors and oil based surfactants are dissolved in aqueous solution
- Exchange of reactants result in intermediate oxo-hydroxide species via precipitation
- The process of precipitation is followed by nucleation and agglomeration of particles
- Precipitate is filtered, washed and dried to obtain MOX nanostructure powder
- The particles of MOX nanostructures are stabilized by surfactants (figure 2.4)

2.1.6.i Advantages

- Ease of preparation
- Thermodynamically stable
- Minimal agglomeration results in uniform and homogeneous geometry
- Control over particle size and composition [65]

2.1.6.ii Disadvantages

- Requires high concentration of surfactants to achieve emulsions
- Changes in environmental factors and pH influence the stability
- Low solubility of materials with high melting point

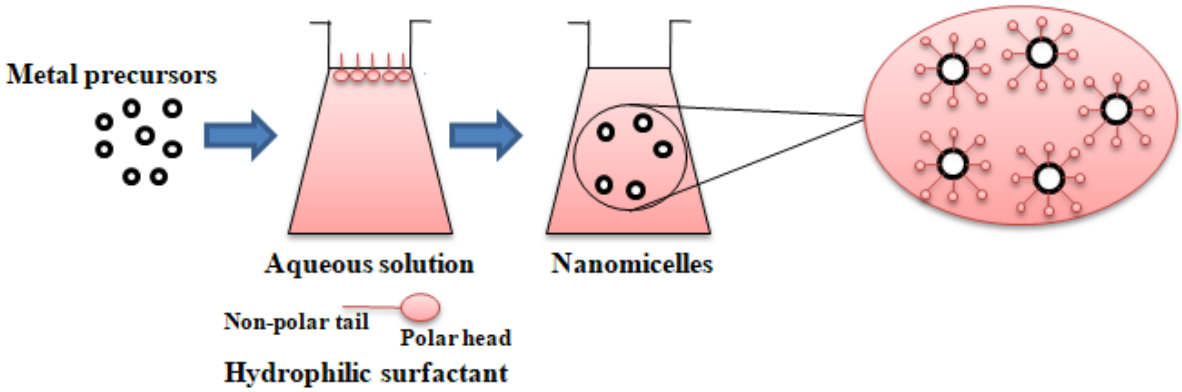

Figure 2.4. Microemulsion synthesis procedure

2.1.7 Solvothermal or hydrothermal techniques

- Reactants and surfactants are dissolved in organic solvents to form uniform solution
- Chemical reactions results in formation of intermediate oxo-hydroxide species [59]
- Solution is transferred in sealed vessel for treatment at high temperature and pressure
- Temperature gradient in vessel leads to fabrication of hot and cold ends (figure 2.5)
- Production and growth of seeds at hot and cold end respectively yields nanostructure
- Final precipitate is filtered, washed and dried to obtain powder of MOX nanostructure
- Addition of surfactant mitigates the particles agglomeration and control the geometry

2.1.7.i Advantages

- Increased solubility of reactants due to high temperature and pressure
- Comprehensive increases in chemical activity of reactants
- Easy production of intermediate or metastable states
- Accurate control over size, shape and distribution of nanostructures

2.1.7.ii Disadvantages

- Require costly apparatus of autoclave
- Risky and unsafe due to operation at high temperatures

- Reaction process is invisible to the user

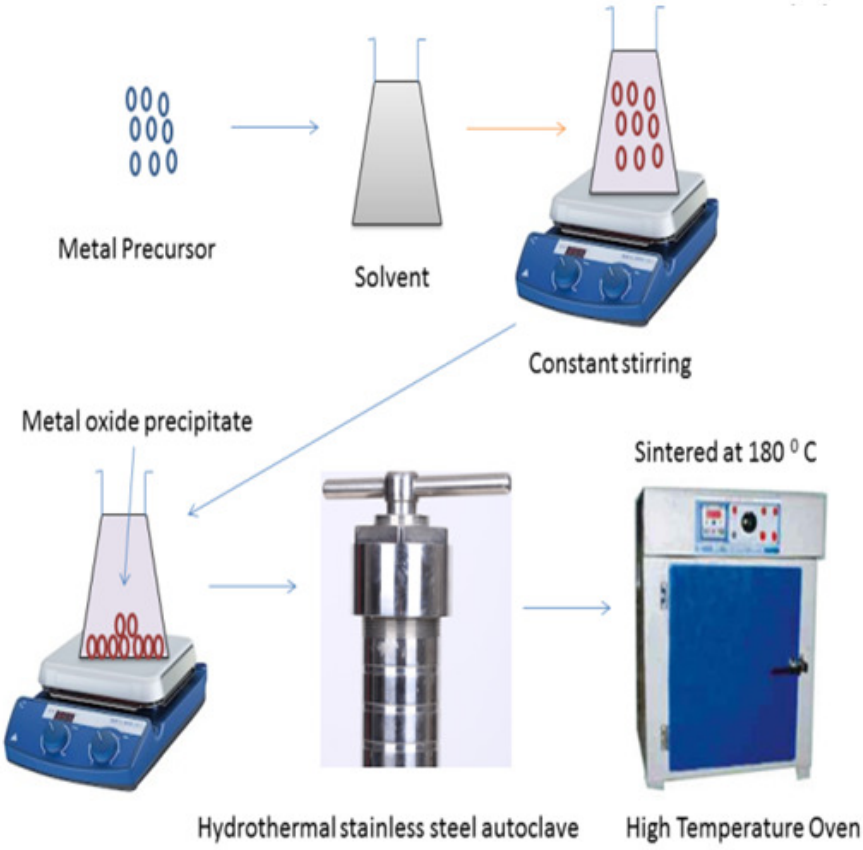

Figure 2.5. Solvothermal or hydrothermal synthesis procedure

2.1.8 Template or surface derived techniques

This technique is used to create desired structures of MOX using already successfully fabricated nanostructures of porous material as a skeleton or building blocks. The particles of MOX arrange themselves as per the exposed skeleton of nanostructures in uniform and homogeneous manner [66]. Thereafter, the template nanomaterial is separated and removed using dissolution methods which yield the pristine nanostructures of MOX materials (figure 2.6).

2.1.8.i Advantages

- Ease of fabrication

- Uniform and homogeneous nanostructures deposited on desired surface
- No agglomeration within the nanostructures
- Synthesis of nanostructures and thin film deposition can be achieved simultaneously

2.1.8.ii Disadvantages

- Complicated synthesis procedure
- Slow rate of synthesis due to prolonged nucleation period
- Dissolution of template by calcination enhance the cost and results in contamination

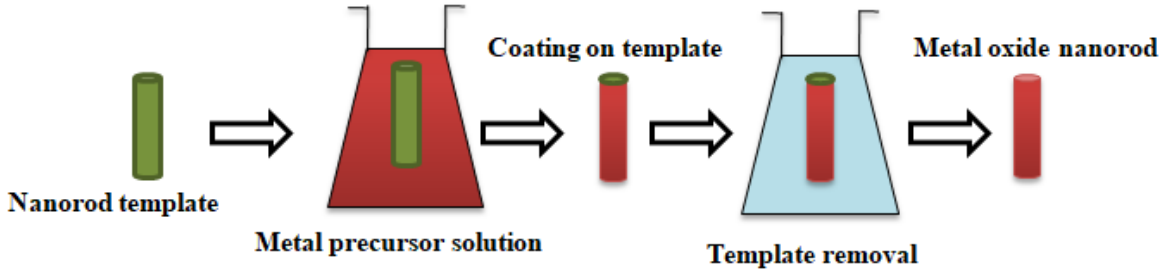

Figure 2.6. Template derived synthesis procedure

2.2 Thin film fabrication

The sensing element used in gas sensors consist of thin films of nanostructured MOX coated on substrates with metallic electrodes deposited on surface of film for securing electrical connection. The shape, uniformity and homogeneity of film play a crucial role in enhancing the sensitivity of sensing element. These characteristics depend on deposition technique employed for fabrication of thin film and their parameters [67]. The types of substrate rely on the integrability with existing electronic circuits and operation parameters. Quartz glass substrate is more favourable for operating sensing element at high temperatures and pressures. The economical and facile deposition processes used extensively for coating thin film of nanomaterials synthesized using wet chemical synthesis method are as follows:

2.2.1 Spin coating technique

The equipment consist of substrate holder known as chuck, rotation motor with maximum capability of 20000 rotation per minute (rpm), turbo molecular vacuum pump with achievable pressure of 10^{-2} torr. The setup is automated by interfacing with microcontroller which enables the user to choose desired rotation speed and time. The model of the instrument used for thin film fabrication in the work reported in chapter 6 is Metrex spin coating unit, available in nanomaterials research laboratory, department of applied physics, Delhi technological university, Delhi, India [figure 2.7.(b)].

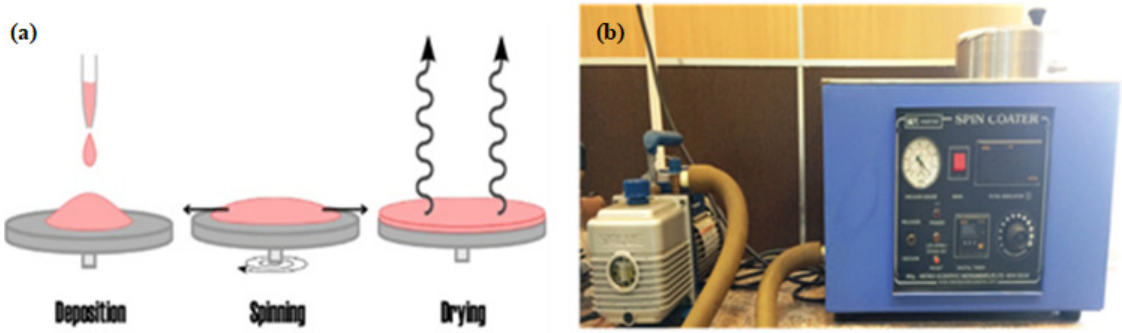

Figure 2.7. (a) Schematic of spin coating mechanism (b) Equipment image

2.2.1.i Working

The substrate is placed on circular disk of chuck and fixed under effect of vacuum to restrict its displacement. Homogeneous solution of powder and aqueous or organic solvent is prepared. A drop of solution is placed on the substrate and it is rotated at desired rpm and time. The molecules of the solution experience centrifugal force which pulls the liquid outwards towards the circumference of the disk and spread the solution uniformly on the surface of substrate [68]. Thereafter, the substrate is dried to evaporate extra solvent and obtain the layer of thin film on substrate [figure 2.7.(a)].

2.2.1.i Disadvantages

- Require optimum viscosity of analyte solution
- Applicable only for homogenous solution
- Wastage of chemical solution

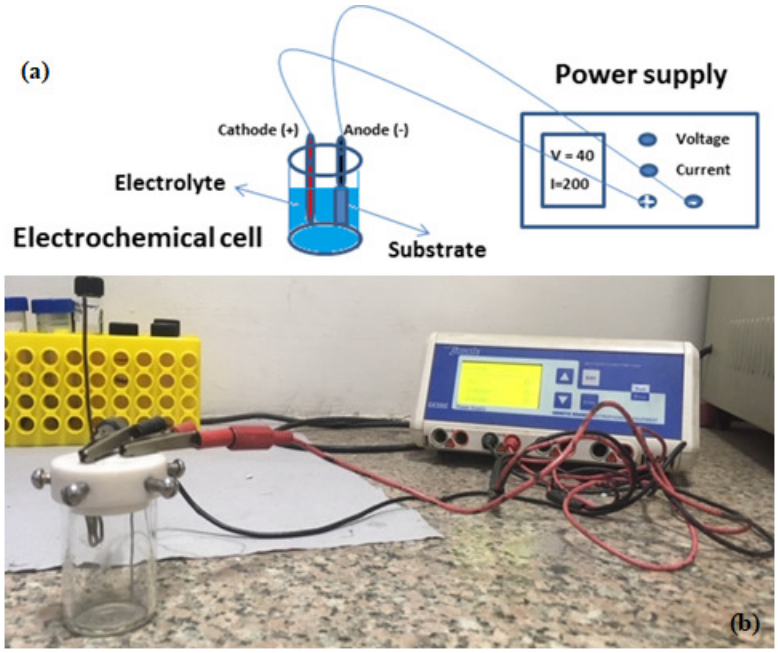

Figure 2.8. (a) Schematic of electrophoretic deposition system (b) Equipment image

2.2.2 Electrophoretic deposition method

This method requires conducting substrates for thin film deposition such as indium tin oxide (ITO) layered glass substrate. It consist of electrochemical cell assembly containing conducting substrate as anode and platinum (Pt) rod as cathode dipped in conducting electrolyte solution attached to voltage power supply. The model used for fabrication of nanostructures thin film in research work reported in chapter 4 and 5 is genetix 300c with power supply range (0-300 V), available in nano bio-electronics research laboratory, department of biotechnology, Delhi technological university, Delhi, India [figure 2.8.(b)].

2.2.2.i Working

The electrolyte is formed by solution of nanomaterial powder in aqueous or organic solvent, homogeneously dispersed by ultrasonication treatment. Small quantity of dispersant such as Magnesium Nitrate Hexahydrate [$Mg(NO_3)_2.6H_2O$] is added in resultant solution to increases the ionic conductivity. ITO substrate and Pt rod is dipped in conducting solution present inside cell as anode and cathode respectively. Electrochemical cell is made up of 30 ml glass beaker sealed using Teflon disk containing inlets for placement of electrodes. The electrodes are attached with power supply using crocodile connectors and suitable voltage i.e. deposition voltage is applied for certain time i.e. deposition time in order to create potential difference between electrodes for movement of corresponding ions to participate in redox reaction [figure 2.8.(a)]. The cations reaching the anode settle on ITO substrate and form a thin film layer of synthesized nanomaterials. The thickness of layer depends on magnitude of deposition voltage, deposition time, homogeneity and conductivity of dispersed solution [69].

2.2.2.ii Disadvantages

- Require conducting substrates for thin film deposition
- Applicable for homogeneously dispersed conducting solution
- Addition of dispersant may result in impurities
- High cost of operation
- Time consuming

2.3 Characterization methods

The properties of MOX nanostructures such as crystallographic nature, size, shape, electronic band gap, surface morphology and bonding arrangements, synthesized using bottom up approach is evaluated using x-ray diffraction (XRD) measurements, transmission electron

microscopy (TEM), scanning electron microscopy (SEM), ultraviolet-visible (UV-Vis) spectroscopy and Fourier transform infrared (FTIR) spectroscopy respectively.

2.3.1 X-ray diffraction analysis

X-rays are electromagnetic waves with very small wavelength in order of 1 Å as compared to visible light spectrum. Thus, diffraction phenomenon demonstrated by x-ray cannot be measured with the help of plane diffraction grating. William Bragg pointed out that the crystals have regular and periodic arrangement of atom; therefore the crystal can be used as a natural 3-dimensional (3D) grating (figure 2.9) [70].

When x-ray falls on the atomic arrangement of the crystal, then each atom of the lattice act as a scattering centre and scatters the x-ray falling on them. On the other hand, x-ray passing in between the atoms is allowed to transmit without any interference. This phenomenon leads to superimposition of two rays travelling close to each other as demonstrated in figure. The path difference between two rays is equal to integral amount of x-ray wavelength (equation 2.1).

$$Path\ difference\ (\Delta) = n\lambda \qquad \textbf{(Equation 2.1)}$$

$$\Delta = 2d \sin\theta \qquad \textbf{(Equation 2.2)}$$

$$2d \sin\theta = n\lambda \qquad \textbf{(Equation 2.3)}$$

For first order diffraction, $\sin\theta \leq 1$, which implies $\lambda \leq 2$Å;

Hence, visible light cannot be employed for observing the crystal diffraction pattern as the wavelength of visible light is much larger. Moreover, diffraction pattern can be observed only an at specific diffraction angle which satisfies the Bragg's diffraction law.

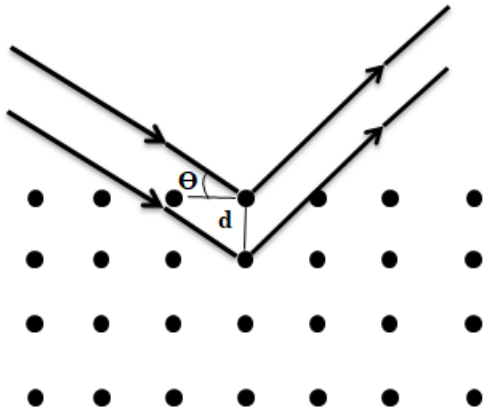

Figure 2.9. Schematic of x-ray diffraction from lattice structure

2.3.1.i XRD instrument

The model of XRD instrument used during the course of research work is Bruker (U.S.) D8 advance, available in advanced instrumentation facility, department of applied physics, Delhi technological university (DTU), Delhi, India [figure 2.10.(c)]. The setup consist of movable Cu-($K_{\alpha 1}$) source for emission of x-ray spectrum of wavelength 1.54 Å, fixed sample holder assembly and a high speed energy dispersive compound silicon strip based LYNXEYE XE-T detector with automatic adjustable window that can measure pattern in angular range of 0.15^0 to 90^0 [figure 2.10.(b)].

2.3.1.ii Mechanism

The method used for analyzing XRD pattern is based on Debye Scherrer technique in which analyzed sample is in powder form which constitutes tiny crystals known as crystallites. These crystallites are randomly oriented and form all possible angles with the atomic planes. The advantage of this method is that the various orders in the pattern can be recorded at the same time. When the monochromatic x-ray is incident on the powder kept in the capillary tube, the ray are diffracted from the crystal planes in conical form while satisfying the

Bragg's law [75]. The diffracted rays are collected by detector which converts the incoming x-ray energy into electrical signal of proportional size and data is recorded in term of diffraction angle and intensity of signal [figure 2.10.(a)].

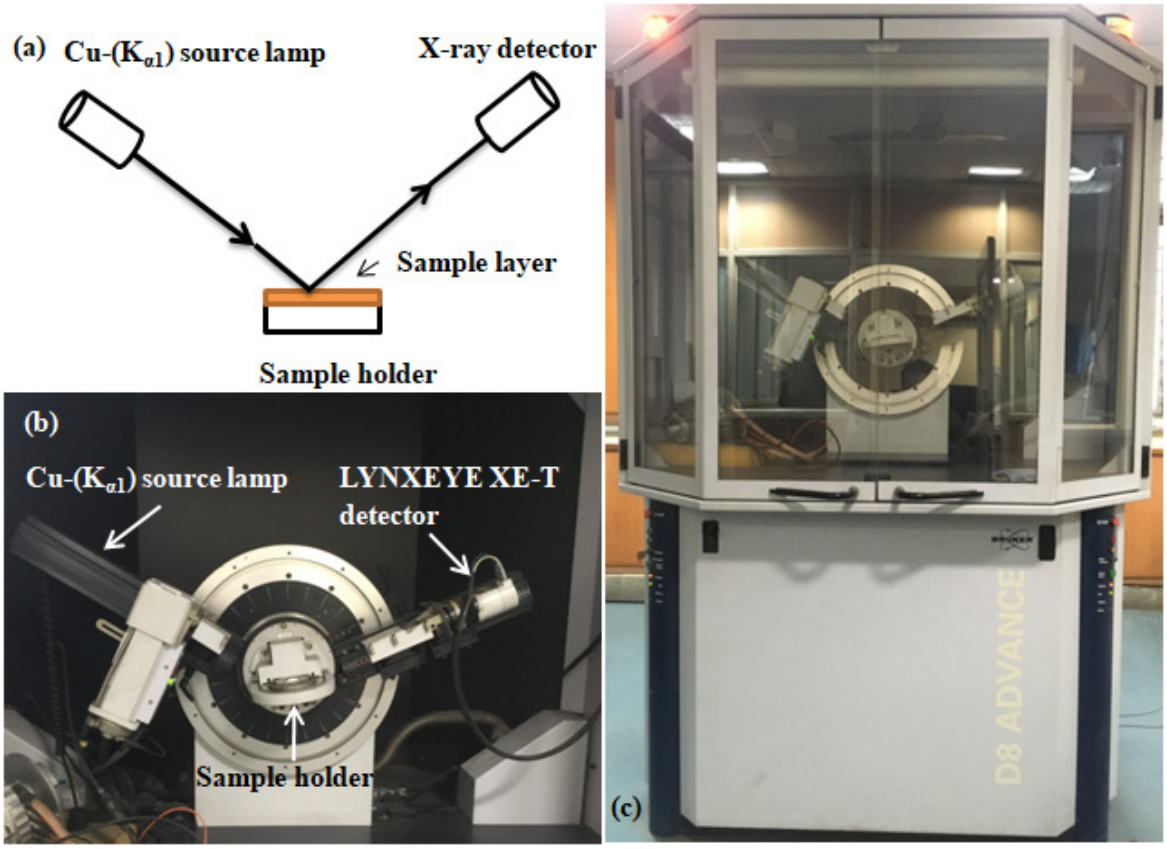

Figure 2.10. (a) Schematic (b) Image of diffraction setup and (c) Instrument image

2.3.2 Transmission electron microscopy (TEM)

It is impossible to visualize the size and shape of nanostructures using optical microscopy instruments because their dimension is comprehensively smaller than the wavelength of visible spectrum. This resulted in invention of electron microscopy which is based on scattering and transmission phenomenon of electron beam from the surface of nanostructures. The microscopy based on scattering of electron beam is useful only to study the surface morphology, whereas internal geometry can be analyzed only if the beam is allowed to pass

through the structure. Transmission electron microscopy is the form of electron microscopy which works on principle of analysis of transmitted electron beam from the structure of nanomaterials.

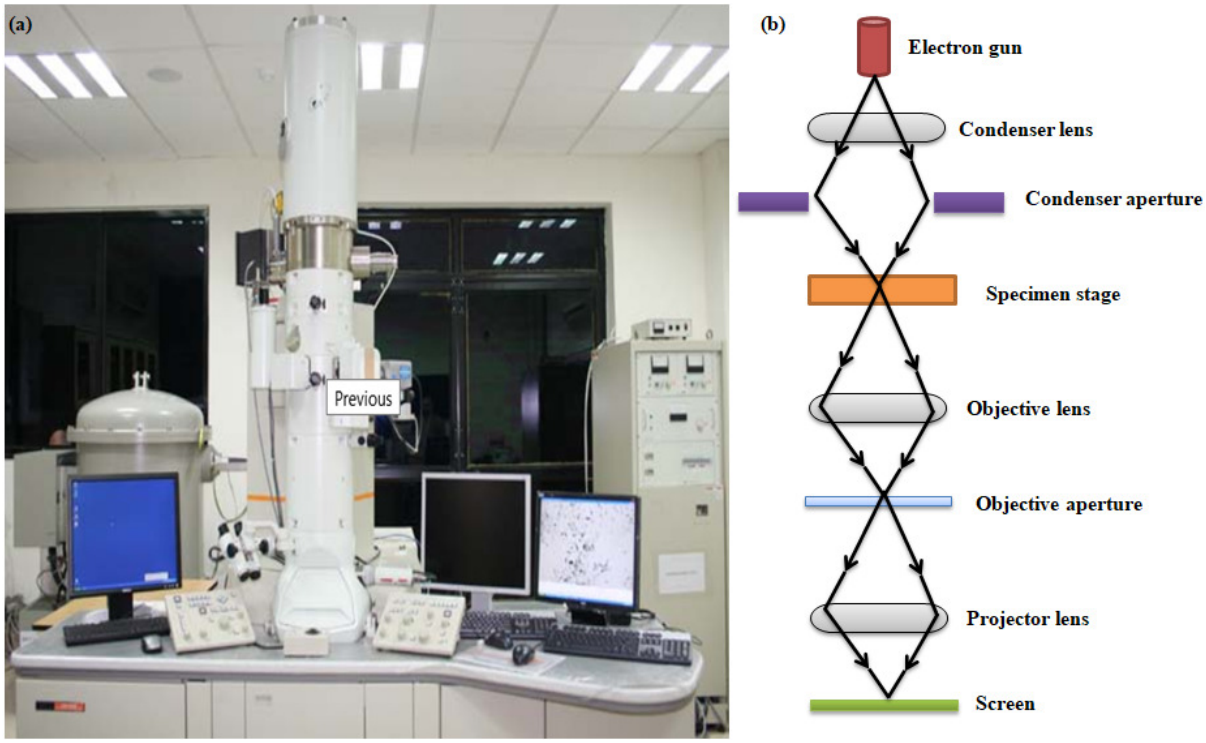

Figure 2.11. (a) Instrument image and (b) Schematic of transmission electron microscopy

2.3.2.i TEM instrument

The model of TEM instrument used in the research work presented in chapter 3 to 6, is JEOL (Japan) JEM-2100F, available in advanced instrumentation research facility (AIRF), Jawahar lal university (JNU) and university science instrumentation centre, university of Delhi, Delhi, India. The setup consist of schottky field emission gun for generating high energy beam of electrons, cryo-pole piece based electromagnetic condenser lenses for focussing of beam, automated specimen stage for holding conducting copper grid coated with sample and Gatan interline charged couple device (CCD) camera to convert the electric charge into pixels of

image [figure 2.11.(a)]. The complete setup of TEM is placed in high vacuum chamber and is interfaced with graphical user interface (GUI) data acquisition system.

2.3.2.ii Mechanism

Powder of MOX nanostructures are dispersed in suitable aqueous or organic solvent through ultrasonication treatment. The dispersed solution is collected in microtip using pipette and is dropped on conducting side of carbon coated copper (Cu) grids. These grids are placed in specimen stage of TEM and introduced inside TEM setup [figure 2.11.(b)].

Electron beams originating from electron gun falls on the specimen stage and interacts with the sample resulting in scattering of beam. There are two types of scattering which takes place i.e. elastic and inelastic. Elastic scattering takes place due to arrangement of atoms in the crystal of nanostructures and it yields spot pattern because of coherence in electron beam scattering. On the other hand, inelastic scattering gives rise to absorption or emission of beam which is specific to the compound or chemical structure of nanomaterials [76]. The transmitted electron beam is transferred to CCD detector through objective condenser lens and corresponding image is recorded.

The contrast of the image depends on two different mechanisms:

(a). Bright field image: The transmitted beam is used for the imaging and diffracted beam is eliminated by introducing suitable aperture below the back of objective condenser lens.

(b). Dark field image: The diffracted beam is used for imaging in this mode by using a movable aperture or by shifting the incident beam keeping the aperture intact.

The resolution of TEM image should be equivalent to wavelength of electrons which is of the order of picometer. However, the resolution of resultant image is not of similar order due to incoherent nature of electron beam. Point resolution of the image can be enhanced by

increasing the accelerating voltage of field emission gun because as the voltage increases, the wavelength of electrons decreases. The images acquired in this mode are known as high resolution TEM (HRTEM) image and they are used to analyze the interplanar spacing of crystal planes of nanostructures.

Since, the dimensions of the nanostructures are larger than the wavelength of electrons. Thus they act as a diffraction grating for incoming electrons and scatter the electrons depending on the crystal structure at different angles while satisfying Bragg's law. Whereas, transmitted electrons are allowed to pass through the sample, resulting in formation of monochromatic spots on dark backgrounds corresponding to reciprocal lattice of crystal planes. This phenomenon is used to confirm the results of XRD analysis and the image is known as selected area electron diffraction (SAED) image.

2.3.3 Scanning electron microscopy (SEM)

The characteristic of nanostructure surface is observed using scanning electron microscopy by analyzing the surface scattered electrons which consist of secondary electrons and back scattered electrons (BSE).

2.3.3.i SEM instrument

The model of the instrument used to study surface morphology of nanostructures described in the research work discussed in upcoming chapters is TESCAN (Czech Republic) MIRA II LMH, available in inter-university accelerator centre (IUAC), Delhi, India. The setup consist of schottky field emitter electron gun for producing high energy beam of electrons, electron lenses which produce magnetic fields to focus the beam on desired area, two pairs of scan coils for moving the electron beam across the specimen in two dimensions using magnetic field, motorized sample stage, solid state detector for analyzing secondary electrons and Everhart Thornley (ET) detector for detection of BSE. Complete setup is enclosed within

high vacuum sealed chamber and is connected with GUI data acquisition system [figure 2.12.(a)].

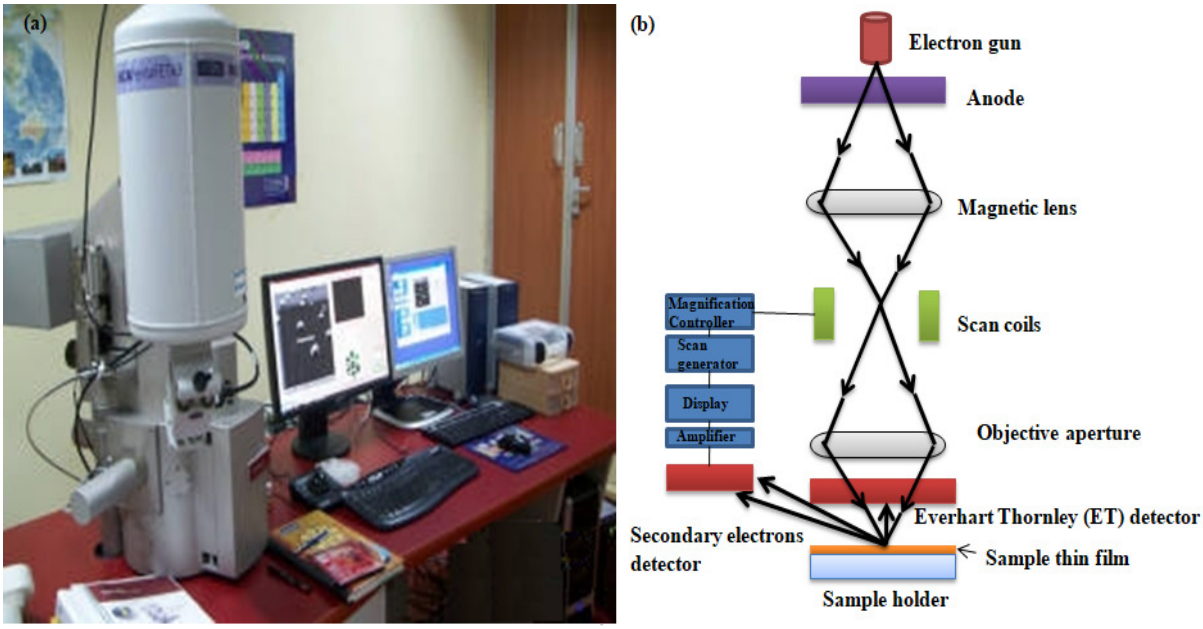

Figure 2.12. (a) Instrument image and (b) Schematic of scanning electron microscopy

2.3.3.ii Mechanism

Thin film of MOX nanostructures on solid substrate or powder form distributed over conducting carbon tape is used as sample for SEM analysis. The electron beam is swapped across the sample resulting in their interaction with the elements of nanomaterials. The interaction of electrons takes place in form their scattering from the surface yielding secondary and back scattered electrons [17]. Secondary electrons are generated in entire volume of interaction, but they escape only from few surface layers and they are slow in nature with energy less than 50 eV. Back scattered electrons are elastically scattered from surface and penetrates more deeply as compared to secondary electron as their energy is greater than 50 eV. Elements with high atomic number produce more number of back scatter electrons as compared to low atomic number elements and thus appear as bright spots in SEM image. Hence, different chemical composition of elements on surface can be visualized

using contrast in images formed by BSE. The bright and dark contrasting image of surface corresponds to concentration of back scattered electrons and intensity of signal is proportional to concentration of secondary electrons [figure 2.12.(b)].

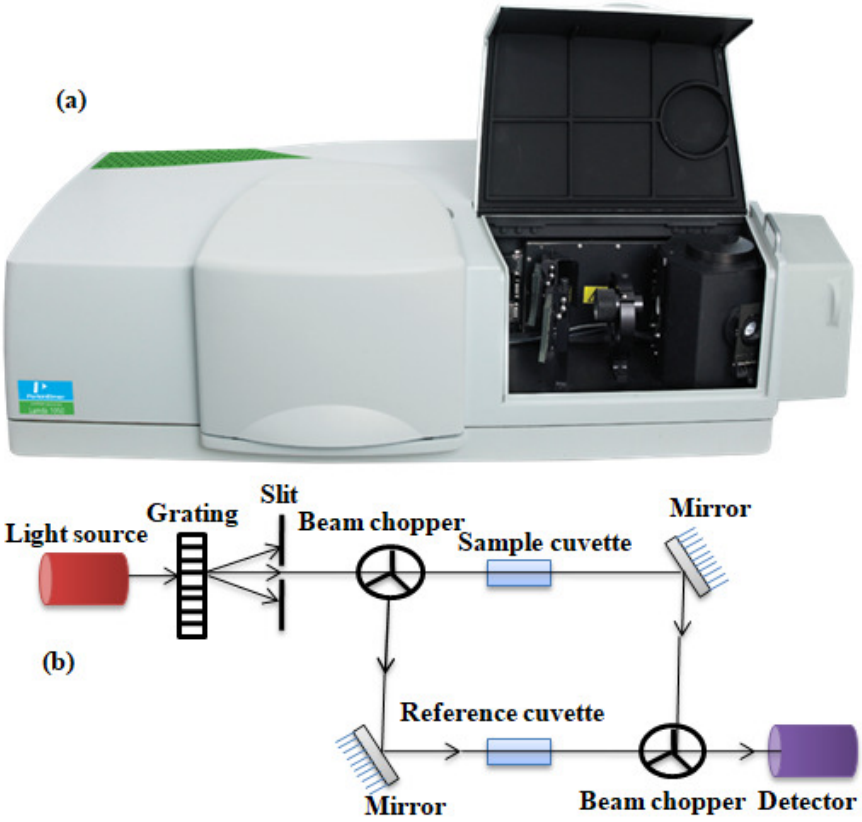

Figure 2.13. (a) Instrument image and (b) Schematic of ultraviolet-visible (UV-Vis) absorption spectroscopy

2.3.4 Ultraviolet-visible (UV-Vis) absorption spectroscopy

It is also referred to as absorption or reflectance spectroscopy. The light used in this spectroscopy lies in UV region (100-1000 nm) which contains visible and adjacent region of spectrum. There is electronic transition in atomic structure of nanostructured materials on absorption of this electromagnetic spectrum. This spectroscopy is widely used in analytical chemistry for detection of transition metal ions, highly conjugated organic compounds and biological macromolecules.

2.3.4.i UV-Vis spectrophotometer instrument

The model of the instrument used for studying the electronic transition of nanostructures is Perkin Elmer (U.S.) lambda 950 UV-Vis spectrophotometer; available in nano bio-electronics laboratory, department of biotechnology, Delhi technological university, Delhi, India. The setup is a double beam instrument consisting of deuterium and tungsten halogen light sources for emission of UV-Vis and near infrared (NIR) radiation, sample holder made up of rectangular quartz glass tube known as cuvette, diffraction grating monochromator for passing of selected radiation, chopper for splitting into two beams and photomultiplier detector for transducing radiation energy into electrical signal [figure 2.13.(a)].

2.3.4.ii Mechanism

Radiation of wavelength (175-3300 nm) emitted from source lamps are entered through grating monochromator that allows only UV-Vis radiation of wavelength (175-900 nm) to pass through chopper and get split in two beams. One beam is used to analyze the reference while other beam passes through the sample. Initially, two cuvettes are filled with same solvent as used for formation of solution with nanostructure powder solute. The cuvettes are placed in instrument to measure and record the reference beam reaching the detector window. Thereafter, one of the cuvette is refilled with dispersed nanostructure solution and placed with other solvent cuvette to analyze the difference between reference and sample beam. The chopper blocks one beam at a time and the detector adjusts itself between sample and reference beam. The intensity of beam varies after passing through the analyte solution due to absorption of some wavelengths in incident spectrum of radiation [figure 2.13.(b)] [18].

According to Beer-Lambert's law, the absorbance of a solution is directly proportional to concentration of the absorber or analyte in the solution and pathlength of beam. For fixed pathlength, UV-Vis spectrometry can also be used to detect the concentration of the analyte

in solution. The spectrophotometer measures the intensity of beam (I) passing through sample and compares it to the intensity of reference beam. The ratio I_0/I is known as absorbance (A), which is usually expressed in terms of percentage and is calculated as

$$A = \log_{10} \frac{I_0}{I}$$

Where I_0 is the intensity of reference beam and I is intensity of beam after passing through sample.

2.3.4.iii Optical band gap

The concentrations of electrons are higher in ground state (valence band) as compared to excited state (conduction band) and it has been observed that on exposure of suitable radiation from electromagnetic spectrum, there is transition of electrons from ground to excited state on absorption of this radiation i.e. direct optical transition. On the other hand, if electrons excite to intermediate (metastable) energy state before finally transitioning to excited state, such transitions are known as indirect optical transition. However, the energy of incident radiation should be equal or greater than the energy difference between two states i.e. band gap energy and there is no change in concentration of charge carriers [19]. This phenomenon is used to evaluate the band gap of synthesized MOX semiconductors using optical spectroscopy as demonstrated by Jan Tauc in 1966. Tauc plot is used to analyze the optical band (i.e. Tauc gap) between semiconductors and it is given by equation 2.2;

$$\alpha h\upsilon = C(h\upsilon - E_g)^n \qquad \textbf{(Equation 2.2)}$$

Where α is absorption coefficient, h is planck's constant, E_g is band gap, n is transition parameter (i.e. n is non-negative integers for indirect and proper fraction for direct transitions respectively) and C is proportionality constant.

The intercept of curve on x-axis of Tauc plot [$(\alpha h\upsilon)^{1/n}$ versus $h\upsilon$] gives the magnitude of optical band gap (E_g) for either type of transitions respectively.

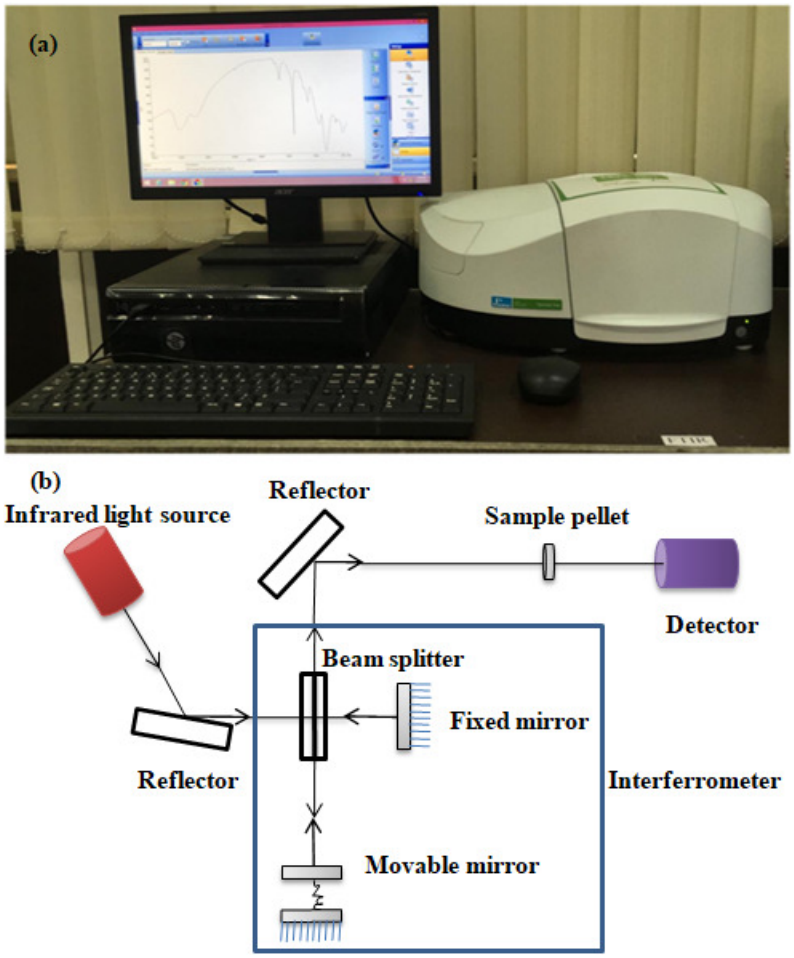

Figure 2.14. (a) Instrument image and (b) Schematic of Fourier transform infrared transmission spectroscopy

2.3.5 Fourier transform infrared (FTIR) spectroscopy

The materials are formed of different chemical elements joined together by a strong covalent bond i.e. molecules and the nature of bonds depends on the electronic configuration of atomic elements. The bonds are in constant kinematics such as vibration, stretching, rotation etc. within the structure of material and their energy lies in ground state. When infrared radiation of electromagnetic spectrum is incident on these materials, there is a molecular transition to the excited state after absorption of energy. Thereafter, the radiation with wavelength

equivalent to the energy gap which falls in the mid infrared region (MIR) of spectrum (4000-400 cm^{-1}) is emitted on relaxation of molecules back to ground state. Hence, infrared (IR) spectroscopy is used to observe the nature of bonds and inter-bonds interaction in the synthesized nanostructures. Conventional IR spectroscopy is slow in nature as it works on dispersed beam and uses grating monochromator which acquire data point by point for each wavelength, whereas FTIR spectroscopy employs interferometer which analyze absorption or transmission of radiation for several wavelengths at a time. The functioning of FTIR spectrometer is to obtain the interferogram, digitalize it, perform Fourier transform and project the resultant spectrum in terms of wavenumber and intensity of electrical signal, using GUI data output system [20].

2.3.5.i FTIR spectroscopy instrument

The model used for analyzing the nature and type of bonds along with inter-bonds interaction between molecules of MOX nanostructures as depicted in the research work presented in chapter 5 and 6 respectively is Perkin Elmer (U.S.) Spectrum two L160000A series, available in nanomaterials research laboratory, department of applied physics, Delhi technological university, Delhi, India. The setup consist of source lamp made up of Nernst filament which emit MIR region radiation, Michelson interferometer for generating interferogram encoded form of MIR radiation, sample holder assembly, $LiTaO_3$ (lithium tantalate) MIR detector for converting the incoming MIR radiation into electrical signal and spectrum 10 software for converting encoded signal into graphical form [figure 2.14.(a)].

2.3.5.ii Mechanism

When MIR radiation emitted by source lamp is incident on interferometer, it is splitted into two beams which pass through optical assembly and recombine at beam splitter resulting in optically interfered beam consisting of all MIR wavelengths encoded in single beam i.e.

interferogram. This interferogram is passed through the sample which absorb corresponding wavelength of radiation, transit to excited state and thereafter return back to ground state by emitting energy gap characteristics wavelength radiation. The output interferogram is collected by MIR detector which converts the beam into electrical signal. These signals are decoded using Fourier transform mathematical technique by corresponding computer software and projected in terms of spectrum, plotting transmittance in relation with wavenumber [figure 2.14.(b)].

2.4 References

[1] S. K. Kulkarni, *Nanotechnology: principles and practices*: Springer, 2014.

[2] G. A. Ozin and A. Arsenault, *Nanochemistry: a chemical approach to nanomaterials*: Royal Society of Chemistry, 2015.

[3] A. Nikam*, et al.*, "Wet chemical synthesis of metal oxide nanoparticles: A review," *CrystEngComm,* vol. 20, pp. 5091-5107, 2018.

[4] M. I. Vesselinov, *Crystal growth for beginners: fundamentals of nucleation, crystal growth and epitaxy*: World scientific, 2016.

[5] L. Koao*, et al.*, "Properties of flower-like ZnO nanostructures synthesized using the chemical bath deposition," *Materials science in semiconductor processing,* vol. 27, pp. 33-40, 2014.

[6] M. A. Ashraf*, et al.*, "Effects of size and aggregation/agglomeration of nanoparticles on the interfacial/interphase properties and tensile strength of polymer nanocomposites," *Nanoscale research letters,* vol. 13, p. 214, 2018.

[7] L. D'Souza and R. Richards, "Synthesis of metal-oxide nanoparticles: liquid–solid transformations," *Synthesis, properties, and applications of oxide nanomaterials. Hoboken, New Jersey: John Wiley & Sons, Inc,* pp. 81-117, 2007.

[8] A. Feinle*, et al.*, "Sol–gel synthesis of monolithic materials with hierarchical porosity," *Chemical Society Reviews,* vol. 45, pp. 3377-3399, 2016.

[9] B. Richard*, et al.*, "Nanoparticle size control in microemulsion synthesis," *Langmuir,* vol. 33, pp. 4748-4757, 2017.

[10] Y. Xie*, et al.*, "Review of research on template methods in preparation of nanomaterials," *Journal of Nanomaterials,* vol. 2016, p. 11, 2016.

[11] M. Patil*, et al.*, "Study of various synthesis techniques of nanomaterials," in *AIP Conference Proceedings*, 2018, p. 030238.

[12] Y. Zhang*, et al.*, "Rapid and Selective Deposition of Patterned Thin Films on Heterogeneous Substrates via Spin Coating," *ACS applied materials & interfaces,* 2019.

[13] P. Amrollahi*, et al.*, "Electrophoretic deposition (EPD): Fundamentals and applications from nano-to micro-scale structures," *Handbook of Nanoelectrochemistry: Electrochemical Synthesis Methods, Properties and Characterization Techniques,* pp. 1-27, 2016.

[14] B. Cullity, "Elements of x ray diffraction–scholar's choice edition," *Scholar's Choice,* pp. 103-105, 2015.
[15] M. A. Wahab, *Solid state physics: structure and properties of materials*: Alpha Science Int'l Ltd., 2005.
[16] L. Reimer, *Transmission electron microscopy: physics of image formation and microanalysis* vol. 36: Springer, 2013.
[17] J. I. Goldstein*, et al.*, *Scanning electron microscopy and X-ray microanalysis*: Springer, 2017.
[18] R. Karoui, "Spectroscopic Technique: Fluorescence and Ultraviolet-Visible (UV-Vis) Spectroscopies," in *Modern techniques for food authentication*, ed: Elsevier, 2018, pp. 219-252.
[19] N. Sangiorgi*, et al.*, "Spectrophotometric method for optical band gap and electronic transitions determination of semiconductor materials," *Optical Materials,* vol. 64, pp. 18-25, 2017.
[20] B. C. Smith, *Fundamentals of Fourier transform infrared spectroscopy*: CRC press, 2011.

CHAPTER 3

Effect of low pressure hydrogen environment on crystallographic properties of PdO nanoparticles

In this chapter, we demonstrate the change in crystallographic structure of tetragonal palladium oxide in presence of low pressure (25, 50, 75 and 100 mbar) H_2 environment at room temperature. Nanoparticles of palladium oxide (PdO) are synthesized using sol-gel chemical method. X-ray diffraction (XRD) analysis, transmission electron microscopy (TEM), ultraviolet-visible (UV-Vis) spectroscopy and scanning electron microscopy (SEM) are used to study the crystallographic structure, size of nanoparticles, optical band gap and surface morphology of PdO nanoparticles. Complete transformation of PdO to palladium hydride (PdH_x) crystal structure is observed as the pressure rises from 25 to 100 mbar. Also, there is phase transition in PdH_x crystal structure along with lattice expansion as H_2 pressure reaches 100 mbar.

The work presented in this chapter is published as:

"Effect of low pressure hydrogen environment on crystallographic properties of PdO nanoparticles"

International Journal of Hydrogen Energy, 41(2016), 22155-22161

3.1 Introduction

Palladium oxide (PdO) is a p-type transition metal oxide electroactive semiconductor with band gap ranging from 1.5 eV to 2 eV, which belongs to platinum (Pt) group metals. Only, platinum oxide (PtO_2) and di-Rhodium trioxide (Rh_2O_3) are semiconducting in nature whereas Rhodium dioxide (RhO_2), Ruthenium dioxide (RuO_2) and Iridium dioxide (IrO_2) are metallic conductors. The members of this group consist of either d^6 or d^8 electronic configuration. PdO contains d^8 valence electronic configuration with activation energy ranging from 0.04 eV to 0.1 eV [1].

Cations and anions of tetragonal (t) unit of PdO are surrounded by four opposite charge ions with oxygen ions (O^{2-}) being tetrahedrally coordinated with palladium ions [2]. At temperatures above 800 ^{0}C, PdO decomposes to yield palladium (Pd) metallic structure [3]. The detailed mechanism explaining interaction of H_2 with PdO nanomaterial is conducted in temperature range of 25 ^{0}C to 250 ^{0}C. It is observed that reduction of PdO to Pd occurs in presence of H_2 which thereafter dissociate itself into H-atoms at room temperature (RT), but reoxidation of Pd doesn't takes place till temperature reaches 150 ^{0}C. Thus, pristine PdO based sensing element is not favourable for RT H_2 sensing application due to long recovery time. Oxygen ionosorption model is used to explain the reaction between PdO and H_2 till surrounding temperature is less than 150 ^{0}C. However, as the operating temperature rises above 150 ^{0}C, reoxidation of Pd to PdO takes place easily in absence of H_2 molecule leading to fast response and recovery time. The interaction of H_2 with PdO can be explained using different reaction models for two different temperature intervals. Oxygen ionosorption, hydroxylation model govern the interaction of H^+ ions on surface of PdO whereas oxygen vacancy model dominates above 200 ^{0}C. The combined reactions involved in these mechanism are suggested by Mars-Van-Krevlen redox mechanism [4]. Additionally, XPS

spectroscopy study of PdO nanomaterials shows decrease of curve area under Pd^{2+} peaks and increase of area under Pd^{0} peaks, confirming the reduction of PdO to Pd in presence of H_2 gas at RT [5]. After reduction of PdO, dissociated H-atoms are adsorbed on to the surface of Pd resulting in hydrogenation of Pd surface. Rate of hydrogenation of Pd is directly proportional to square root of H_2 environmental pressure and corresponding H_2 concentration at room temperature. It has been observed that maximum hydrogenation can be achieved at room temperature for high H_2 concentrations even at low H_2 pressure [6]. However, higher pressure is required to achieve optimum hydrogenation at low concentration and elevated temperature because of less availability of H-atoms required for PdH_x formation, due to decrease in their sticking coefficient. Also, as compared to bulk Pd, the amount of hydrogenation increases as the size of Pd structure reduces to nano dimensions.

At low concentration, $0< H/Pd$ atomic ratio (x) <0.015, adsorption of H-atoms onto Pd surface occur followed by diffusion and storage near subsurface region (0.7 nm to 1.1 nm) between grain boundaries; resulting in formation of solid solution phase of (Pd-H) known as α-phase [7]. As the H_2 concentration rises, x becomes greater than critical concentration value (α_{max}) ~0.015, H-atoms diffuses inside the octahedral interstitial sites of face centered cubic (fcc) structure of Pd which results in transition to new saturated crystal phase of PdH_x known as β-PdH_x. Both the phases of PdH_x coexist simultaneously till $0.015<x<0.6$; thereafter, as $x>0.6$, complete transition to β-phase takes place inside PdH_x crystal network [8-9]. Additionally, there is 6% expansion in lattice structure on (α- β) phase transition of PdH_x which increases continuously with H_2 concentration. Modification and transformation of crystallographic and lattice structure of PdO nanoparticles in presence of low pressure (25, 50, 75 and 100 mbar) H_2 environment have been studied using in-situ X-ray spectroscopy in this chapter. PdO nanoparticles are synthesized using sol-gel chemical method and their 10 mm thick pellet is fabricated using hydraulic press process.

3.2 Experimental Section

3.2.1 Synthesis, characterization and experimental procedure

0.1 M solution of palladium chloride ($PdCl_2$), hydrochloric acid (HCl) and ethanol (C_2H_5OH) is prepared by dissolving requisite quantities of each chemical. The chemicals used during the synthesis procedure are 99.9% pure and belongs to AR grade. The reaction mechanism can be explained by following chemical equations (equations 3.1 & 3.2).

$$PdCl_2 + 3\ C_2H_5OH + HCl \rightarrow Pd(OH)_2 + 3\ C_2H_5Cl + H_2O \quad \textbf{(Equation 3.1)}$$

$$Pd(OH)_2 \rightarrow PdO + H_2O \quad \textbf{(Equation 3.2)}$$

The brown colored solution is allowed to age for 24 hours in order for the reaction to complete successfully. Thereafter, solution is filtered, washed with ethanol and D.I. water several time to bring pH of solution to 7. Powder of the synthesized sample is obtained by heating the precipitate obtained at 60 ^{0}C for 24 hours. The obtained powder is divided into three classes (‘a’, ‘b’ & ‘c’) and annealed at three different temperatures (600 ^{0}C, 800 ^{0}C and 1000 ^{0}C) for 2 hours respectively. The crystal structure, optical band gap, size and surface morphology of synthesized samples are analyzed using X-ray diffraction (XRD) spectroscopy, ultra-violet (UV-Vis) transmission spectroscopy, Transmission electron microscopy (TEM) and scanning electron microscopy (SEM).

The favourable synthesized sample is employed as 10 mm thick pellet in a in-situ XRD spectroscopic instrument and studied for crystal structure changes and lattice modifications in presence of different low pressure (25, 50, 75 and 100 mbar) H_2 environmental pressure at room temperature.

3.3 Results and discussions

3.3.1 X-ray diffraction (XRD) analysis

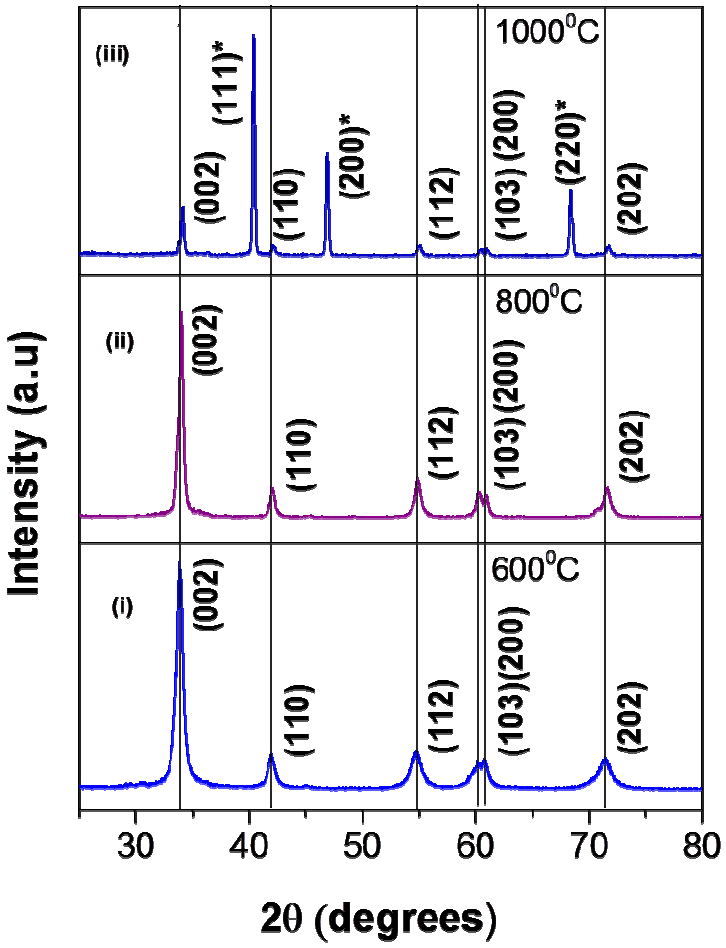

Figure 3.1. XRD plot of (i) sample 'a', (ii) sample 'b' & (iii) sample 'c'

Crystal structure and lattice parameters of Sample 'a', 'b' and 'c' are analyzed using XRD study in figure 3.1.(i-iii) respectively. The intense peaks visible in XRD plot correspond to (002), (110), (112), (103), (200) and (202) planes, verified by comparing the intensity peaks with the published data (CAS number: 88-2335 & 88-2434), which indicates the formation of tetragonal crystal structure of palladium oxide (t-PdO). There is an apparent right shift in intensity peaks towards higher diffraction angle and becomes narrower as annealing temperature increases from 600 ^{0}C to 1000 ^{0}C due to increase in crystallanity and reduction

of oxygenated species. The decrease in broadness and splitting of peaks can be observed lucidly in figure 3.1.(ii) as compared to figure 3.1.(i) reflecting good crystalline behaviour of sample 'b'. The presence of three additional peaks along with standard peaks of t-PdO at 40^0, 46^0 and 68^0 belongs to (111)*, (200)* and (220)* planes of (fcc) Pd respectively [figure 3.1.(iii)]. Reduction of t-PdO to fcc Pd is evident at temperatures above 800 ^{0}C. The rate of formation of PdO is proportional to rate of decomposition in Pd crystal at 1000 ^{0}C which explain the presence of intensity peaks of both t-PdO and fcc Pd crystal in sample 'c' [10]. The size of crystallites in t-PdO crystal structure if found to be 24.02 nm using Debye Scherrer equation (equation 3.3) [11],

$$t = \frac{0.9\lambda}{\beta cos\theta} \qquad \textbf{(Equation 3.3)}$$

where, t represent crystallite size, λ is wavelength, β is the FWHM (Full width half maxima) and θ is the angle having maximum intensity.

3.3.2 Transmission electron microscopy (TEM)

Size, structure and crystallinity of sample 'a', 'b' and 'c' is analyzed using transmission electron microscopy (TEM) and selected area electron diffraction (SAED) images (figure 3.2).

SAED images confirm the formation of tetragonal crystal structure of PdO nanoparticles in all the synthesized sample and their Bragg reflection planes with interplanar spacing are also evaluated [12]. TEM image of sample 'a' shows the group of small particles forming cluster of size ranging from 20 to 50 nm [figure 3.2.(i.a)]. On the other hand, SAED image shows fainted ring like structure corresponding to highly favoured (101) plane which reflects the

amorphous nature of sample ‘a’ [figure 3.2.(ii.a)]. 10 to 125 nm agglomerated yet distinguishable particles are visible in TEM image of sample ‘b and corresponding SAED

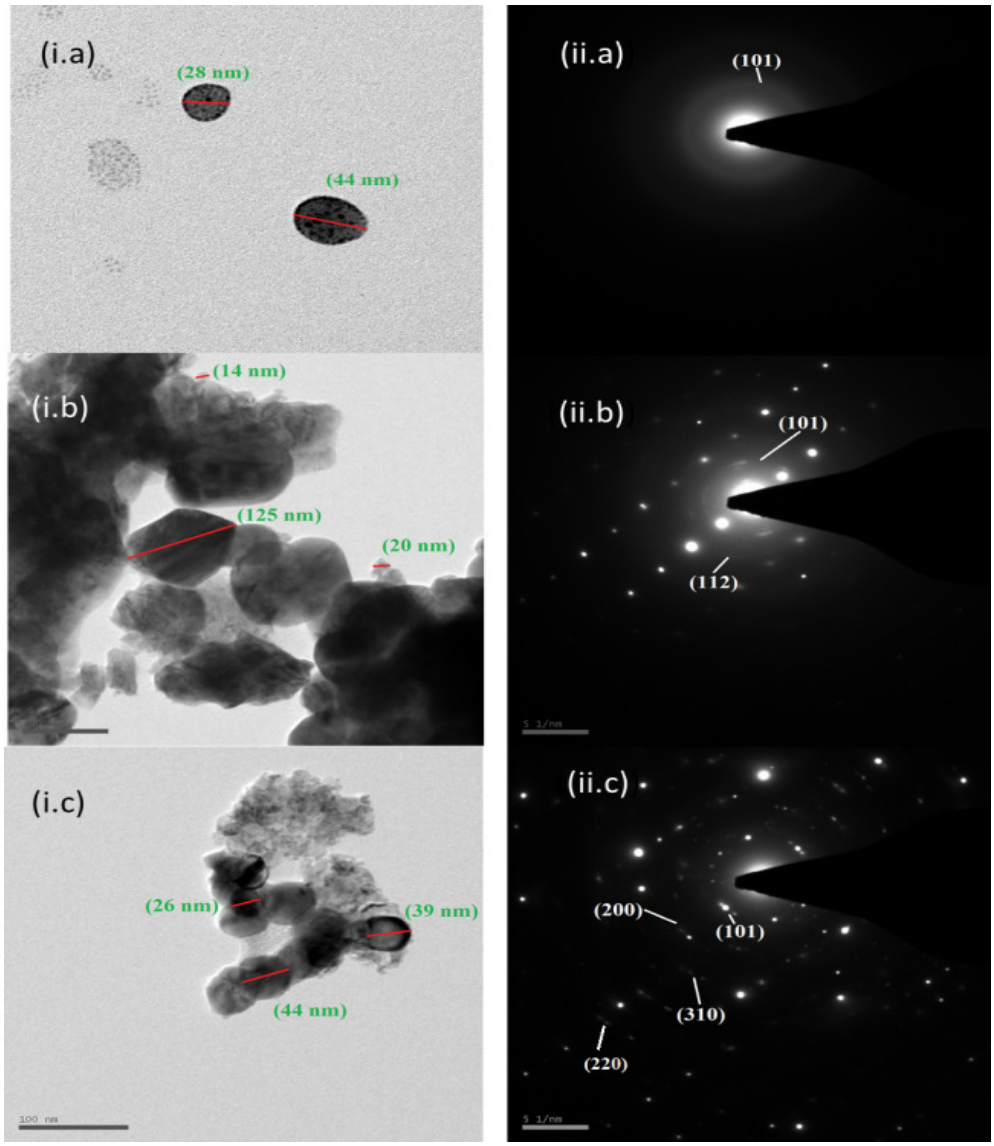

Figure 3.2. (i) TEM images, (ii) SAED images of Sample ‘a’, Sample ‘b’ and Sample ‘c’

image confirms the formation of tetragonal crystalline structure of PdO, which coincides with the observations of XRD analysis [figure 3.2.(i.b) and 3.2.(ii.b)]. Also, Figure 3.2(ii.b) shows the presence of mostly single crystals in tetragonal crystal structure of PdO nanoparticles.

Sporadic ring like structure are formed by various bright dots present in SAED image of sample ‘c’, which displays presence of both single as well as poly-crystals in tetragonal

crystal structure of PdO nanoparticles in sample 'c' [figure 3.2.(ii.c)]. Presence of dotted rings in SAED image of sample 'c' corresponding to (200) and (220) of fcc Pd crystal structure shows mixture of Pd and PdO crystal structure in synthesized sample. Also, it proves that reduction of PdO takes place at temperature above 800 ^{0}C which also validates the reported result of published research work. Sample 'c' contains indistinguishable highly agglomerated nanoparticles with 20-50 nm size forming rod like structure [figure 3.2.(i.c)]. Hence, through detailed characterization analysis, it is concluded that sample 'b is more favourable among other synthesized samples for in-situ x-ray spectroscopy analysis in presence of low pressure H_2 environment at room temperature.

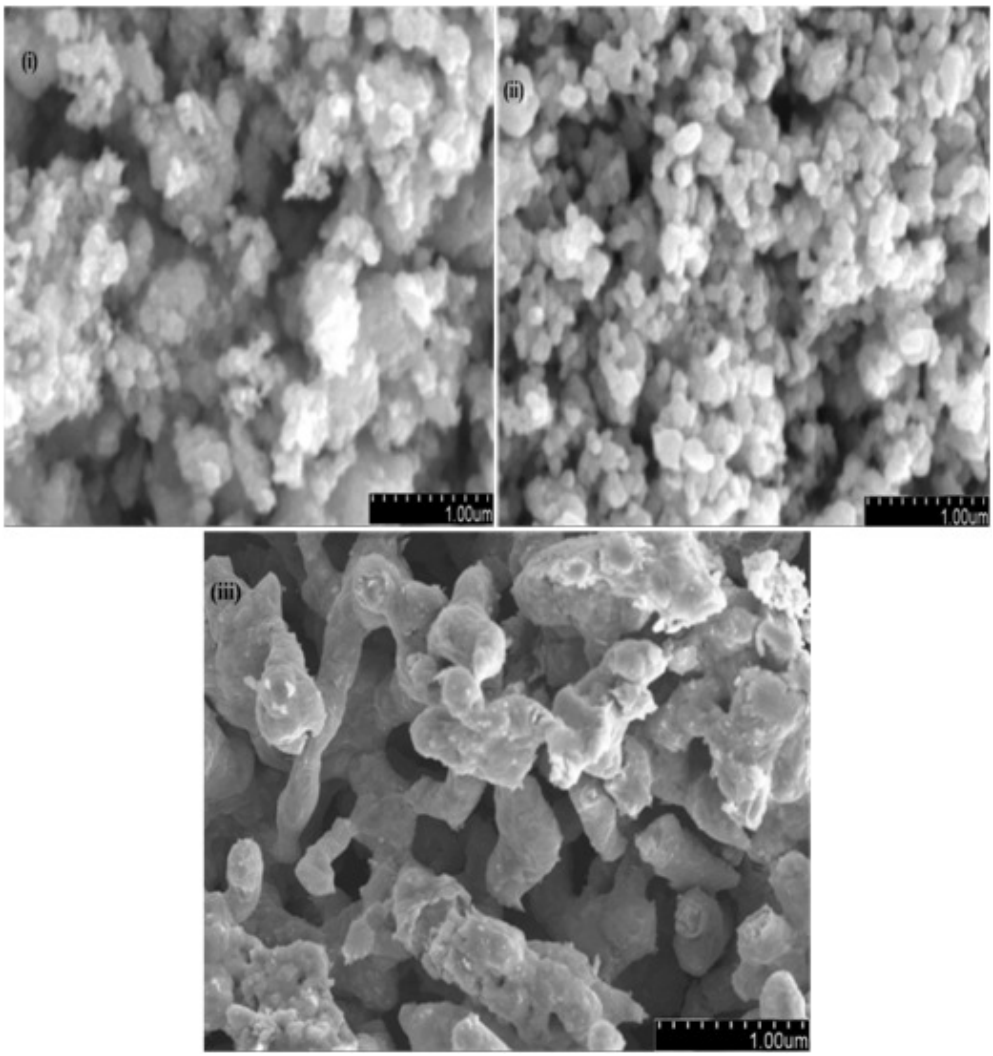

Figure 3.3. SEM images of (i) sample 'a', (ii) sample 'b', (iii) sample 'c

3.3.3 Scanning electron microscopy (SEM)

SEM images of samples 'a', 'b' and 'c are visible in figure 3.3.(i-iii). Agglomeration of particles results in undefined particles shape and boundaries in sample 'a' [figure 3.3.(i)]. Sample 'b' SEM image shows uniform distribution of particles with defined shape and boundaries with the presence of voids on the surface [figure 3.3.(ii)].

Interconnected rod like structure can be seen in SEM image of sample 'c' with indistinguishable boundaries and presence of individual particles [figure 3.3.(iii)]. Surface of sample 'a' contains non-uniform deposition of indistinguishable particles shape and boundaries, whereas sample 'c' surface consist of thick randomly oriented rod like structure with no presence of uniformly distributed particles. Consequently, sample 'b' is more favourable to be used as test material in in-situ XRD spectroscopic studies.

3.3.4 Ultraviolet-visible (UV-Vis) transmission spectroscopy

UV-Vis transmission spectroscopy of PdO nanoparticles shows strong transmission in far ultraviolet region of electromagnetic spectrum at 186 nm as presented in figure 3.4.(i). Figure 3.4.(ii) represents the Tauc plot of PdO nanoparticles and the direct band gap is evaluated to be 1.84 eV using relation mathematically formulated by equation 3.4, and the calculated value also coincides with already reported value lying in range of (1.5-2 eV) [1-2, 13].

$$\alpha h\nu = \left(h\nu - E_g\right)^{\frac{1}{n}} \qquad \textbf{(Equation 3.4)}$$

where α is absorption coefficient, h is planck's constant, ν is photon frequency and E_g is band gap of the semiconductor.

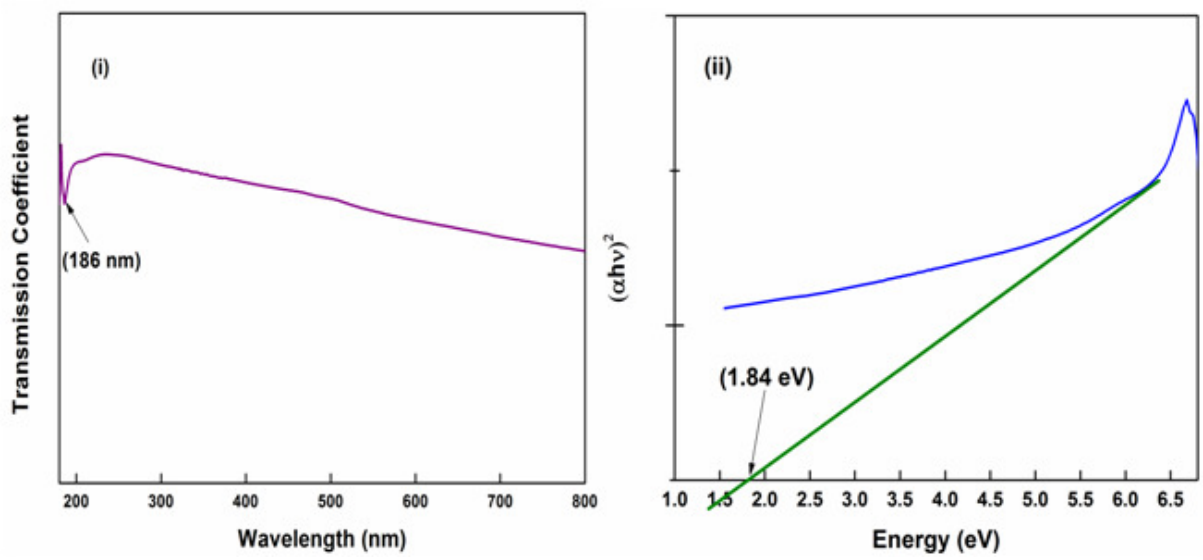

Figure 3.4. (i) UV-Vis transmission spectra and (ii) Band gap estimated from Tauc plot

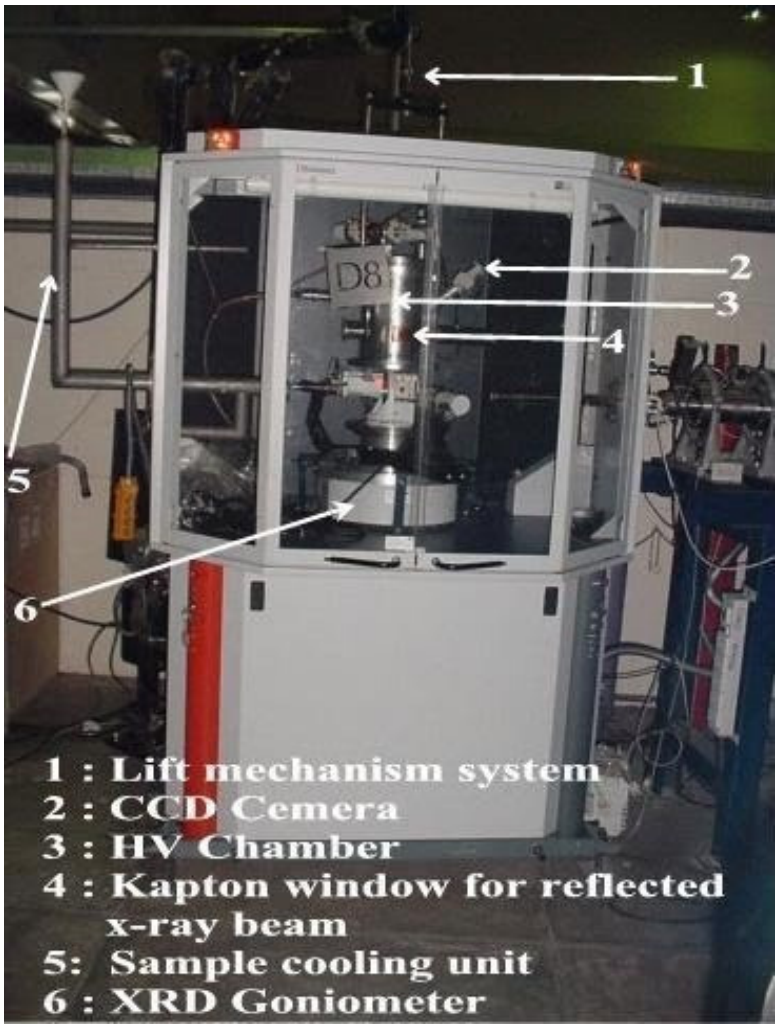

Figure 3.5. In-situ XRD analysis equipment, courtesy: Inter University Accelerator Centre

3.3.5 In-situ XRD experimental analysis

PdO nanoparticles synthesized in sample 'b' are transformed in a 10 mm pellet using hydraulic press pressure method. The pellet is introduced inside vacuum chamber of in-situ XRD observation equipment and vacuum pressure of 0 mbar is achieved using rotary pump (figure 3.5) at room temperature. XRD graph of pristine sample is obtained in 0 mbar chamber pressure for Cu-K_α source with wavelength of 1.54 Å. Thereafter, 100 % H_2 gas is introduced inside the chamber at different low pressure (25, 50, 75 and 100 mbar) and XRD plot of the sample is obtained in tandem. It is observed that as the vacuum pressure of 0 mbar is maintained [figure 3.6.(i)], the obtained XRD plot correspond to t-PdO crystal structure but as environmental pressure of 25 mbar is achieved by filling H_2 gas in chamber [figure 3.6.(ii)], new intensity peaks [(111)*, (101)*, (110*), (200)* and (211)*] matching fcc PdH_x crystal structure start to rise and peaks [(100), (002), (110), (112), (103), (200) & (202)] belonging to t-PdO crystal structure become less intense compared to graph obtained at 0 mbar. As the pressure escalates from 25 to 75 mbar, fcc PdH_x XRD intensity peaks become highly intense and prominent while t-PdO crystal intensity peaks become minute and indistinguishable [figure 3.6.(ii), (iii) and (iv)]. At 100 mbar H_2 pressure, acquired XRD plot contains all the peaks of fcc PdH_x cystal structure and peaks representing t-PdO crystal structure vanishes comprehensively except that for (002) plane [figure 3.6.(v)]. This suggest conversion and thereby transformation of synthesizes sample from t-PdO crystal structure into fcc PdH_X with increase in the environmental pressure of H_2 gas.

Reduction of PdO in presence of H_2 takes place at 25 mbar and room temperature, building nano-islands of Pd by removing oxygen (O^{2-}) ions. Adjacently, dissociation of H_2 to H-atoms takes place which get adsorbed on the surface and diffused within sub-surface region of material, leading to formation of solid solution of Pd-H, i.e. α-phase of PdH_x with increase in

pressure from 25 to 50 mbar. As the pressure increases to 75 and 100 mbar, the concentration of H-atoms around reduced PdO-Pd composite material also increases, H-atoms start diffusing within the fcc lattice structure of Pd inside the octahedral interstitial sites forming more saturated phase of PdH_x crystal structure known as β-phase.

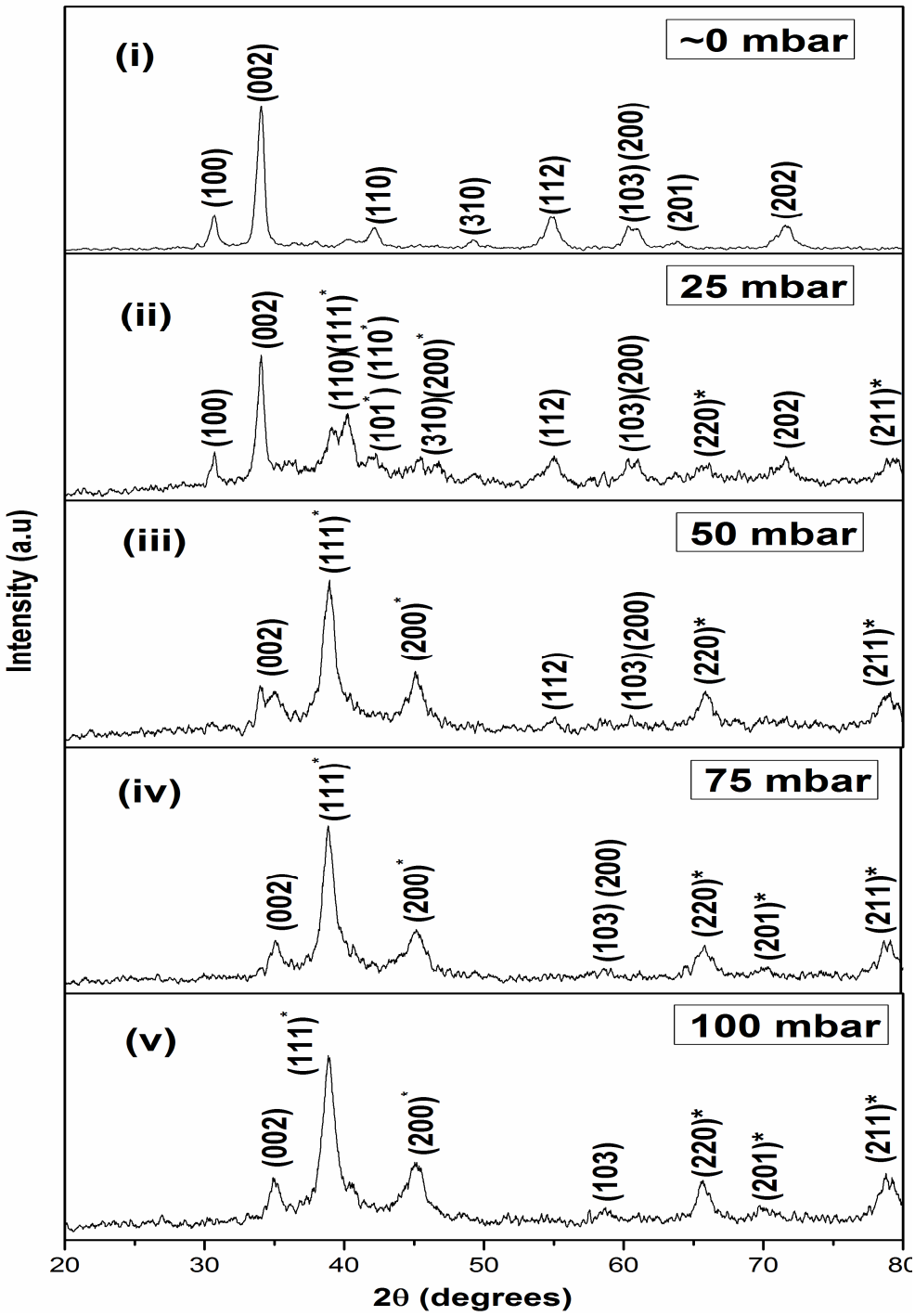

Figure 3.6. XRD graph of sample b at (i) 0 mbar (ii) 25 mbar (iii) 50 mbar (iv) 75 mbar (v) 100 mbar hydrogen pressure

3.3.6 Effect of H_2 pressure on lattice constants

PdO nanoparticles have tetragonal crystal structure with x, y and z as longitudinal and transverse 3D lattice parameters respectively, the relation between these parameters for tetragonal arrangements is given by (x=y≠z) [14]. The evaluated transverse and longitudinal lattice parameters of t-PdO without H_2 gas are found to be approx. (4.01± 0.002) Å and (3.06± 0.0005) Å respectively. With increase in H_2 environmental pressure from 25 to 100 mbar, there is slight decrease in longitudinal axes of lattice from (3.06± 0.0005) Å to (3.03± 0.0009) Å from 25 mbar to 75 mbar pressure attributed to slight contraction of lattice due to surrounding H-atoms, whereas they face sharp increase to (4.06 ± 0.004) as pressure reaches 100 mbar, while transverse axis remains unperturbed (figure 3.7).

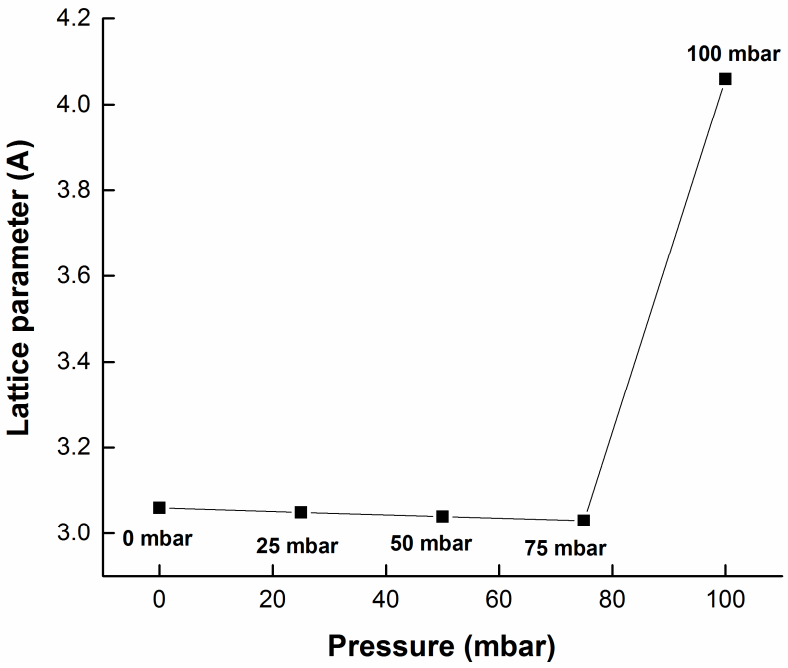

Figure 3.7. Effect of hydrogen gas environment pressure on lattice constants

The expansion of PdO nanoparticles lattice in presence of large concentration of H_2 gas at room temperature influence the electrical properties of material because lattice expansion results in decrease in interparticles gap which minimize the electron mobility barrier and

hence enhance the conductivity of the PdO nanomaterials [15]. Whereas, volume expansion and decrease in resistivity forms the H_2 sensing mechanism for Pd nanoclusters based sensing material [9]. The results of the study suggest that PdO nanoparticles is a favourable candidate to substitute Pd nanoparticles for hydrogen sensing and storage applications.

3.4 Conclusion

PdO nanoparticles are synthesized using simple and facile sol-gel chemical method. The prepared material is annealed under three different annealing temperatures (600, 800 and 1000 ^{0}C). XRD and TEM analysis confirms the formation of tetragonal crystal structure of PdO nanoparticles (t-PdO) in all three treated samples, but sample annealed at 800 ^{0}C displays good crystalline behaviour and particle geometry. SEM study shows uniform homogeneous deposition of distinguishable nanoparticles on surface of sample annealed at 800 ^{0}C. UV-Vis transmission spectroscopy and corresponding Tauc plot shows electronic band to be lying in the ultraviolet region and is evaluated to be 1.8 eV which coincides with reported data. Pellet of PdO nanoparticles are studied for modification in crystal and lattice structure under the presence of low pressure hydrogen environment (25, 50, 75 and 100 mbar) using in-situ XRD study. Transformation of t-PdO nanoparticles into fcc PdH_x nanoparticles takes place as pressure rises from 25 to 100 mbar along with α to β phase transition and significant expansion in lattice parameters of PdH_x nanoaparticles. The findings of this research work shows similar behaviour of PdO nanoparticles compared to Pd nanoparticles at room temperature. Hence, PdO nanoparticles are suitable substitute as solid state material for H_2 sensing and storage applications in ambient environment.

3.5 References

[1] D. Rogers*, et al.*, "Crystal growth and semiconductivity of palladium oxide," *Journal of Solid State Chemistry,* vol. 3, pp. 314-316, 1971.

[2] P. Nilsson, "Optical properties of PdO in the range of 0.5-5.4 eV," *Journal of Physics C: Solid State Physics,* vol. 12, p. 1423, 1979.
[3] C.-J. Huang*, et al.*, "Growth and photoresponse study of PdO nanoflakes reactive-sputter deposited on SiO 2," *Journal of Applied Physics,* vol. 108, p. 053105, 2010.
[4] Y.-J. Chiang*, et al.*, "A mechanistic study of hydrogen gas sensing by PdO nanoflake thin films at temperatures below 250° C," *Physical Chemistry Chemical Physics,* vol. 17, pp. 3039-3049, 2015.
[5] Y. K. Kim*, et al.*, "Colorimetric hydrogen gas sensor based on PdO/metal oxides hybrid nanoparticles," *Talanta,* vol. 188, pp. 356-364, 2018.
[6] M. Khanuja*, et al.*, "Hydrogen induced lattice expansion and crystallinity degradation in palladium nanoparticles: Effect of hydrogen concentration, pressure, and temperature," *Journal of Applied Physics,* vol. 106, p. 093515, 2009.
[7] M. Yamauchi*, et al.*, "Nanosize effects on hydrogen storage in palladium," *The Journal of Physical Chemistry C,* vol. 112, pp. 3294-3299, 2008.
[8] D. Narehood*, et al.*, "X-ray diffraction and H-storage in ultra-small palladium particles," *International Journal of Hydrogen Energy,* vol. 34, pp. 952-960, 2009.
[9] M. Suleiman*, et al.*, "Phase transition and lattice expansion during hydrogen loading of nanometer sized palladium clusters," *Journal of alloys and compounds,* vol. 356, pp. 644-648, 2003.
[10] H. Gabasch*, et al.*, "In situ XPS study of Pd (1 1 1) oxidation at elevated pressure, Part 2: Palladium oxidation in the 10− 1 mbar range," *Surface science,* vol. 600, pp. 2980-2989, 2006.
[11] B. D. Cullity and S. R. Stock, *Elements of X-ray Diffraction* vol. 3: Prentice hall New Jersey, 2001.
[12] M. A. Wahab, *Solid state physics: structure and properties of materials*: Alpha Science Int'l Ltd., 2005.
[13] S. Choudhury*, et al.*, "Nanostructured PdO thin film from Langmuir–Blodgett precursor for room-temperature H2 gas sensing," *ACS applied materials & interfaces,* vol. 8, pp. 16997-17003, 2016.
[14] J. Okazaki*, et al.*, "In situ high-temperature X-ray diffraction study of thin palladium/α-alumina composite membranes and their hydrogen permeation properties," Journal of Membrane Science, vol. 335, pp. 126-132, 2009.
[15] A. Gurlo and D. R. Clarke, "High-Sensitivity Hydrogen Detection: Hydrogen-Induced Swelling of Multiple Cracked Palladium Films on Compliant Substrates," Angewandte Chemie International Edition, vol. 50, pp. 10130-10132, 2011.

CHAPTER 4

Electrophoretically deposited nanostructured PdO thin film for room temperature amperometric H_2 sensing

Palladium oxide (PdO) nanoparticles are synthesized using facile and economical hydrothermal sol-gel chemical method. Electrophoretic process has been used to deposit uniform thin films of PdO nanoparticles on ITO coated glass substrates at 10 V to 35 V deposition potential respectively. X-ray diffraction analysis (XRD) and transmission electron microscopy (TEM) is used to study the crystal structure, shape and size of nanoparticles. Surface morphology of PdO thin film deposited at various deposition voltage is analyzed using scanning electron microscopy (SEM). Ultraviolet-visible (UV-Vis) absorption spectroscopy is employed to study the electronic band gap of PdO nanoparticles. Working electrode (WE) based on PdO thin film deposited over ITO (PdO/ITO) is used for amperometric sensing of wide concentrations (10-70%) of hydrogen gas at room temperature through potentiostat/galvanostat Autolab instrument. The sensing response of electrophoretically deposited PdO/ITO working electrodes at different potential is also studied. The proposed amperometric sensor displays good sensitivity of 0.222 μA/%H_2 with a response time of 60 seconds compared to other similar reported sensors.

The work presented in this chapter is published as:

"Electrophoretically deposited nanostructured PdO thin film for room temperature amperometric H_2 sensing"

Vacuum, 154(2018), 302-308.

4.1 Introduction

The physical and chemical properties of H_2 make it difficult to detect it through sensory organs. Also, the lowest detection limit (LDL) is set to be 4% after which it becomes flammable in nature. A wide percentage (1% - 99%) concentration of H_2 is used for various industrial and scientific purposes such as fuel cells, nuclear reactors, nickel hydride (Ni-H) batteries and refineries applications [1]. However, among all the types of available H_2 sensors, only electrochemical sensors show stable and selective response with wide detection range.

The structural properties and working mechanism of different types of electrochemical sensors along with their advantages and disadvantages have been discussed in detail in chapter 1.

Facile and economical electrophoretic deposition (EPD) process is more favourable for uniform deposition of homogeneous thin film of metal oxides and their composites with other 2D nanomaterials on conductive substrates compared to other conventional methods because it offers control for the selecting desired shape of the substrate [2]. The thickness and surface morphology of the fabricated film can be amended by varying the deposition potential and deposition time of the EPD process. Also, the homogeneity, uniformity and particles geometry of deposited film depends not only on processing parameters, but also on the properties of liquid colloidal suspension used i.e. dielectric constant, viscosity, conductivity and stability of colloidal suspension [3-4]. Hence, desired characteristics of thin film can be achieved using EPD method by modifying one or the other parameters

PdO nanoparticles deposited over ITO layer coated glass substrate (PdO/ITO) is used as working electrode (WE) in indigenously fabricated electrochemical cell for amperometric sensing study of wide range (10% to 70%) H_2 concentration at room temperature.

4.2 Experimental work

4.2.1 Synthesis, characterization and experimental procedure

All the chemicals are bought from Sigma Aldrich and Fisher scientific and they belong to 99.9% pure AR grade. Palladium chloride ($PdCl_2$), 25 ml ethanol (C_2H_5OH) and 12 Molar (M) 5 ml hydrochloric acid (HCl) are mixed together to form a homogeneous brown colored 0.1 M solution by continuous stirring for 30 minutes. The obtained solution is kept unperturbed for 24 hours to age the solution and complete the reaction. Thereafter, solution is placed in Teflon based hydrothermal vessel to be thermally treated at 200 ^{0}C for 2 hours. The resultant precipitate is filtered, washed with D.I. water, 0.1 M HCl and consequently dried at 60 ^{0}C for 24 hours which yield brown colored complex powder. The sample is annealed at 600 ^{0}C for 2 hours to remove chloride and organic impurities in its powder yield oxidized black powder.

Crystallographic properties, material recognition, size, shape of nanoparticles and electronic band gap of synthesized sample is observed using x-ray diffraction (XRD) spectroscopy, transmission electron microscopy (TEM) and ultraviolet-visible (UV-Vis) absorption spectroscopy. The results of these studies indicate formation of tetragonal PdO nanoparticles with spherical size of 20 to 80 nm with band gap of 1.9 eV.

4.2.1.i Fabrication of working electrode (WE)

Nanoparticles of t-PdO is casted in form of several thin films on to the (5 mm x 10 mm) ITO layered glass substrates (PdO/ITO) using electrophoretic deposition method for various deposition potential (10, 15, 20, 25, 30 and 35 Volts) at deposition time of 2 minutes. The EPD setup consists of electrochemical cell made up of 20 ml glass beaker containing (4 cm x 1 mm) platinum (Pt) cylindrical rod based anode and substrate as cathode placed at separation of 1 cm. The electrochemical cell is attached to indigenously fabricated microcontroller based

programmable source meter instrument which provides constant potential and current for EPD process.

The electrolyte used during this electrochemical process is made up of dispersed solution of 0.1 g PdO powder and 10 mL of ethanol. The conductivity and mobility of the dispersed ions are enhanced by adding 100 µL of (0.1 M) magnesium nitrate [$Mg(NO_3)_2.6H_2O$] in the electrolyte. Several thin films of PdO nanoparticles with 1µm thickness are uniformly coated on ITO substrates at different EPD potential (10, 15, 20, 25, 30 and 35 V) respectively. The surface morphology and homogeneity of all fabricated films are analyzed using scanning electron microscopy (SEM) and it is observed that PdO/ITO deposited at 30 V is most suitable among other films to be used as WE for amperometric sensing H_2 gas.

4.2.1.ii Amperometric gas sensing setup

The schematic of amperometric gas sensing setup is depicted in figure 4.1, which consist of two elements i.e. indigenously fabricated electrochemical cell and Potentiostat/galvanostat Autolab. The fabricated cell contains three electrodes placed 1 cm apart being dipped in 0.5 M sulphuric acid (H_2SO_4) solution as liquid electrolyte which is enclosed within a 30 ml glass beaker with gas and electrodes inlets and outlets for carrying out the redox electrochemical reactions.

Three electrodes of electrochemical cell are counter electrode (CE), made up of (4 cm x 1 mm) Platinum (Pt) cylindrical rod, Reference electrode (RE), made up of Nafion coated (5 cm x 3 mm) silver/silver chloride (Ag/AgCl) cylindrical rod and WE made up of sensing (PdO/ITO) thin film element. Pt has low oxygen reduction over-potential along with less hydrogen solubility in comparison to palladium (Pd) [5]. Ag/AgCl has zero electrochemical redox potential which enables the cell to maintain zero potential shift and stay stable throughout the reaction between the WE and CE. Nafion polymer coating of electrode protect

them from interacting with other impurities present in electrolyte and allow only hydrogen ions to diffuse [5]. The chloridization of AgCl is carried out by dipping Ag rod inside Iron chloride ($FeCl_3$)/0.1 M HCl solution for 24 hours. Thereafter, rod is washed with D.I water and dipped in saturated AgCl solution to remove traces of $FeCl_3$. This process results in forming of uniform gray black layer on the electrode. Subsequently, Ag/AgCl electrode is dipped in and out of 5% Nafion 117 polymer solution to obtain homogeneous coating of Nafion on electrode [6-7].

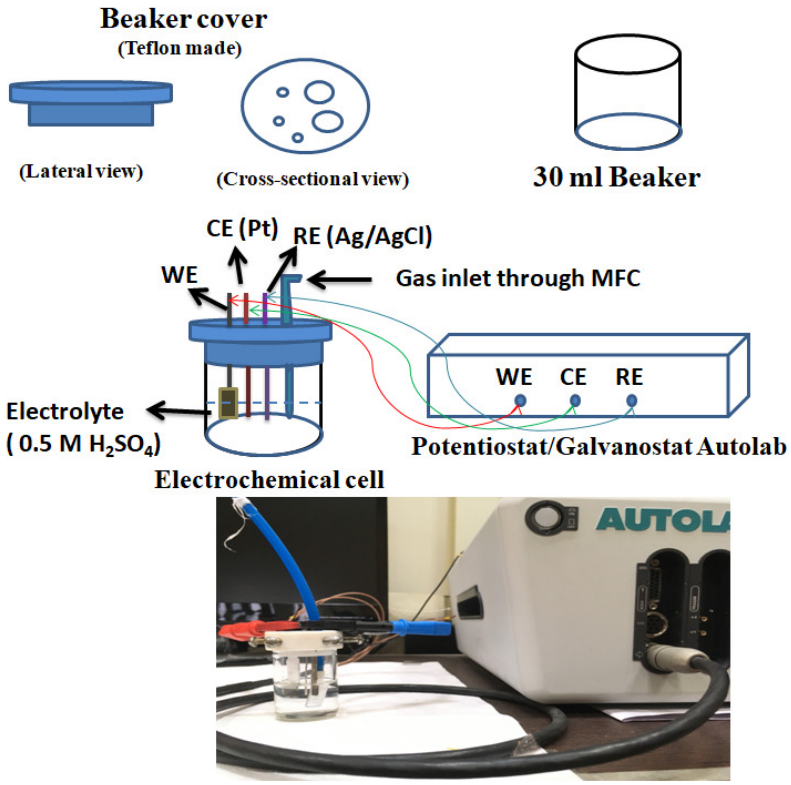

Figure 4.1. Amperometric gas sensing setup

PdO/ITO based working electrode is used as sensing material in electrochemical cell to detect H_2 gas through amperometric measurements. The sensing setup is connected to potentiostat/galvanostat Autolab using crocodile connectors to analyze relation between response current and time of gas flow. The gas inlet of electrochemical cell is attached to the Alicat scientific MC standard series gas mix mass flow controller (MFC) using Teflon pipes.

4.3. Results and Discussions

4.3.1 X-ray diffraction (XRD) analysis

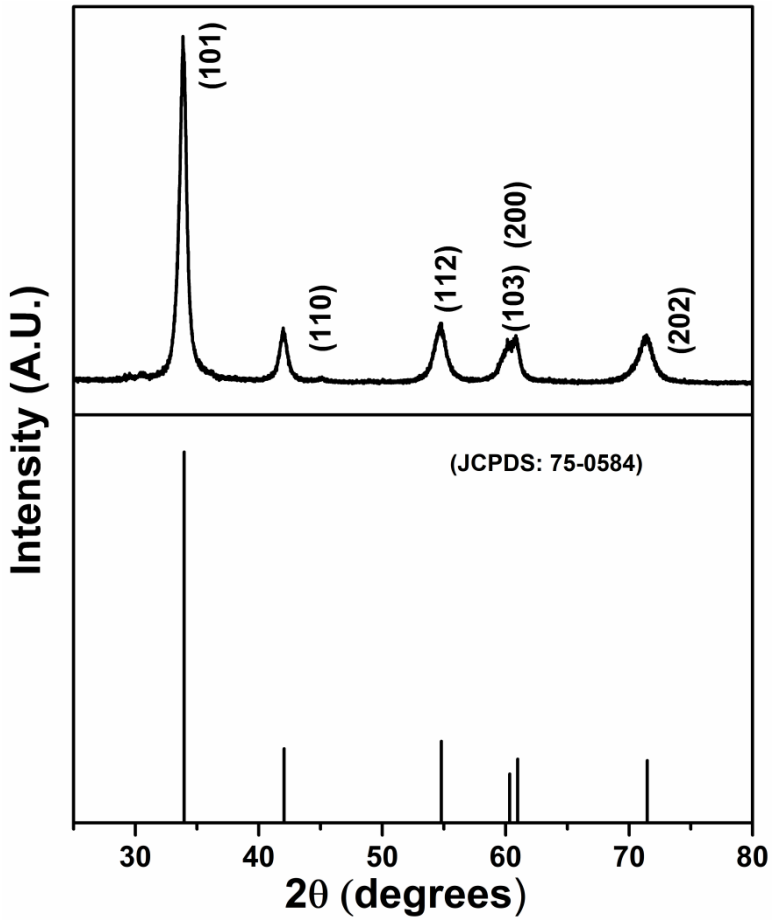

Figure 4.2. XRD plot of PdO nanoparticles

Figure 4.2 represent the XRD study of synthesized powder sample prepared through hydrothermal route. On comparison with reported JCPDS data (CAS number: 750584), it is inferred that all the intensity peaks in graph represents the tetragonal crystal structure of PdO nanoparticles (t-PdO). Highly intense peaks at 33.8^0 belongs to (101) plane, but other moderate intense peaks at highly intense peak at 42^o, 54.7^o, 60.12^o, 61^o and 71.3^o represent (110), (112), (103), (200) and (202) of t-PdO respectively. The average crystallite size of t-PdO is calculated to be equal to 14 nm (equation 3.4) (refer section 3.3.1) [8].

4.3.2 Transmission electron microscopy (TEM)

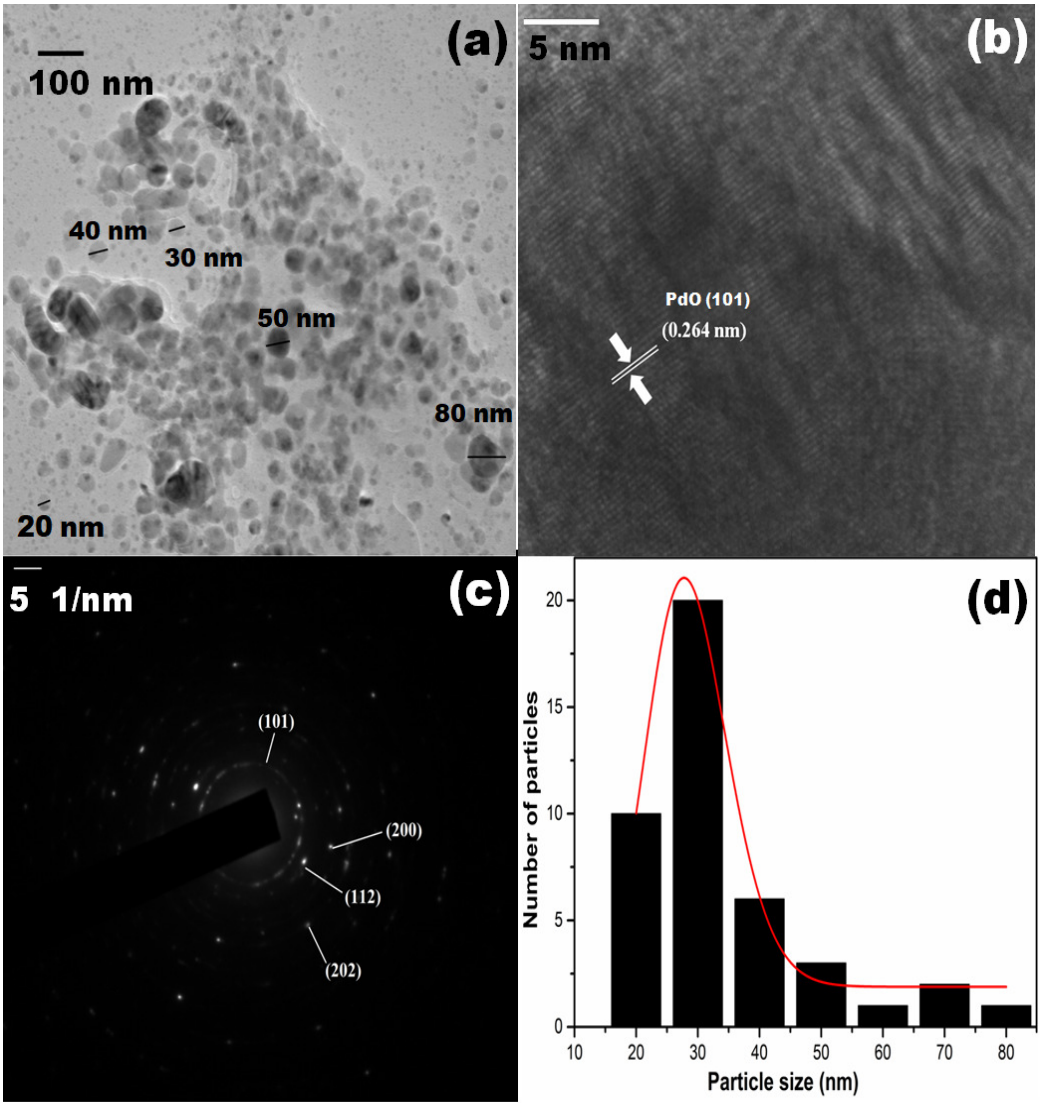

Figure 4.3. (a) TEM image (b) HRTEM image (c) SAED image (d) Particle size distribution

TEM image shows presence of nanoparticles with size 20 to 80 nm in the synthesized sample [figure 4.3.(a)]. The density of nanoparticles with size 20 to 40 nm is observed to be higher compared to other size nanoparticles [figure 4.3.(d)]. HRTEM validates the findings of XRD results by confirming the formation of t-PdO with crystallographic interplanar spacing of 0.264 nm representing (101) plane [figure 4.3.(b)], whereas SAED image shows concentric rings formed by polycrystalline dots corresponding (101), (112), (200) and (202) planes of t-PdO nanoparticles [figure 4.3.(c)].

4.3.3 Ultraviolet-visible (UV-Vis) absorption spectroscopy

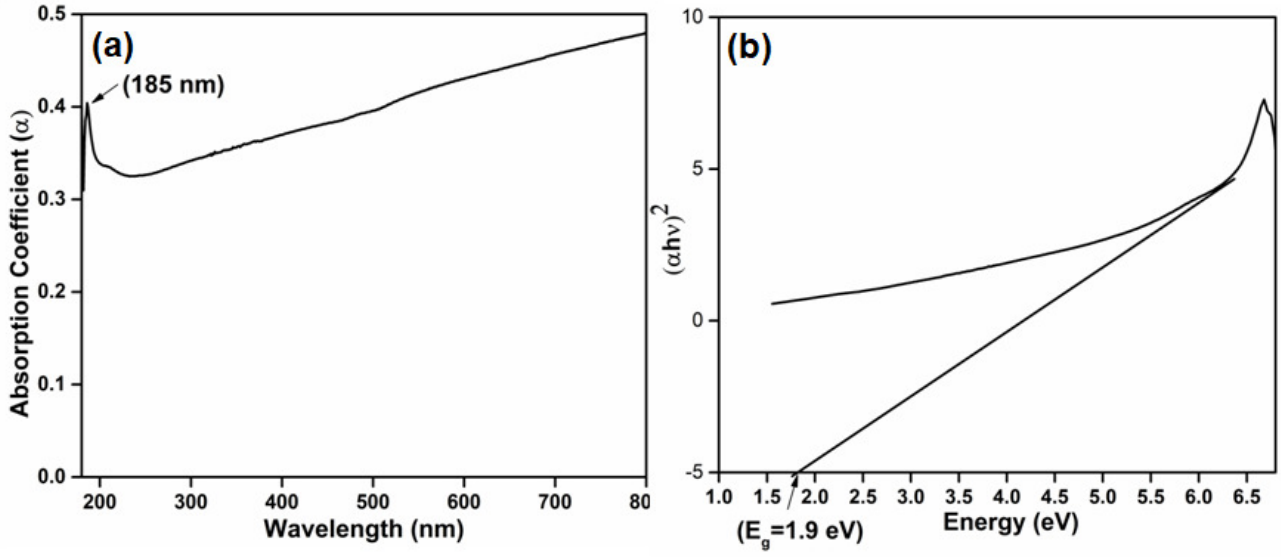

Figure 4.4. (a) UV-Vis absorption spectra (b) Tauc plot

UV-Vis absorption spectra of PdO nanoparticles displays strong absorption peaks in ultraviolet region electromagnetic spectrum at 185 nm [figure 4.4.(a)] [9]. Direct band gap of 1.9 eV is calculated from the Tauc plot consisting of $(\alpha h\nu)^2$ versus hν (energy) on vertical and horizontal axis respectively [Fig. 4.4.(b)] using equation 5 (refer section 3.3.4), where α is absorption coefficient, h is Planck's constant and ν is frequency of radiation.

4.3.4 Scanning electron microscopy (SEM)

PdO nanoparticles thin films deposited on ITO layered glass substrates (PdO/ITO) on different electrophoretic deposition potential (10, 15, 20, 25, 30 and 35 volts) respectively with deposition time of 2 minutes are studied for determining the surface morphology using scanning electron microscopy (figure 4.5). There is random, sparse and separated distribution of particles on surface of film deposited at 10 V [figure 4.5.(a)]. On increasing deposition

potential of electrophoretically deposited film to 30 V, the density of particles increase and separation between particles on the surface of decrease. Also, rise in potential results to increase in concentration of nanoparticles available for deposition which results in nanojoining of particles eventually leading to agglomeration of nanoparticles [10].

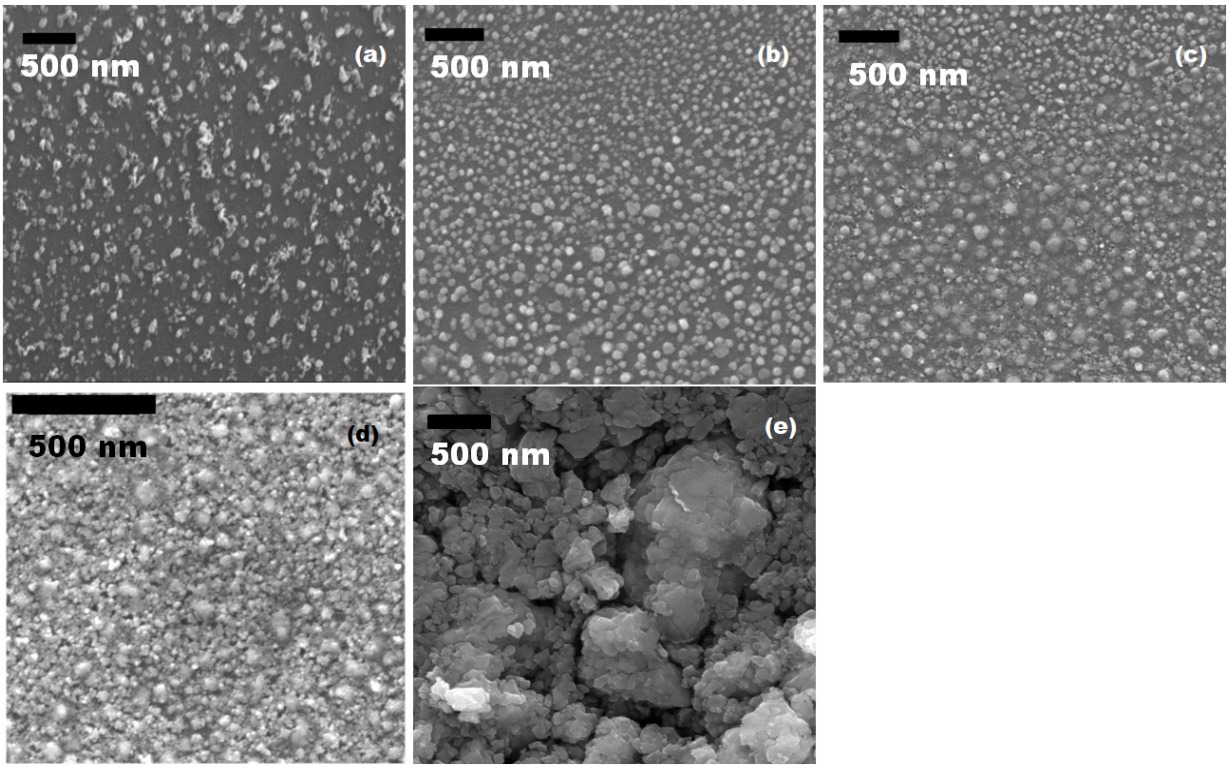

Figure 4.5. SEM images of working electrodes deposited at Electrophoresis deposition potential of (a) 10 V, (b) 20 V, (c) 25 V, (d) 30 V and (e) 35 V

Higher surface uniformity with reduced number of gaps between particles is observed on surface of thin film deposited at 30 V, due to aggregation of nanoparticles [figure 4.5.(d)]. The uniform surface morphology and presence of small voids with no visible cracks on the surface of the thin film deposited at 30 V makes it suitable to be used as WE in amperometric sensing application compared to other deposited thin films.

Large nanoclusters are formed by excessive agglomeration of nanoparticles in thin film deposited at 35 V which yield non-uniformity and heterogeneity on the surface morphology

[figure 4.5.(e)]. There is considerable effect of electrophoretic deposition potential on the size of nanoparticles on the surface of thin film. Smaller particles appear on surface of film deposited at 10 V; however particles size increase comprehensively on increasing the potential to 30 V. The disparity in particles size on thin film surface deposited at different electrophoretic deposition potential is a result of recrystallization of Pd^{2+} ions in the electrolyte solution. Moreover, electrochemical reaction takes place during electrophoresis process which result in reduction of Pd^{2+} ions into Pd atoms which thereby attached themselves to nanoparticles present on the surface of WE [11].

4.3.5 Amperometric H_2 gas sensing study

The cyclic voltammetry (CV) study is performed on PdO nanoparticles present in PdO/ITO WE dipped in 0.5 M sulphuric acid (H_2SO_4) liquid electrolyte to confirm its non-participating catalytic behavior in an electrochemical reaction (figure 4.6). It can be seen that PdO re-oxidation happens during anodic sweep with maximum oxidation current at 0.62 mV, on the other hand reduction of PdO takes place in the cathodic sweep with maximum reduction current at 0.15 mV. This study validates the redox catalytic behavior of PdO and also coincides with the published research work [12-13].

The amperometric H_2 gas sensing study is carried out at 25 ^{0}C by allowing various percentage (10 to 70%) concentration of H_2 gas to flow into Teflon sealed electrochemical sensing setup at flow rate of 80 mL/min through mass flow controller (MFC) for a time period of 5 minutes (figure 4.1). H_2 gas selective polymer membrane Fluorinated ethylene propylene (FEP) is covered on the gas inlet in sensing setup to restrict other impurities present with target gas to flow inside the cell during the amperometric process [6].

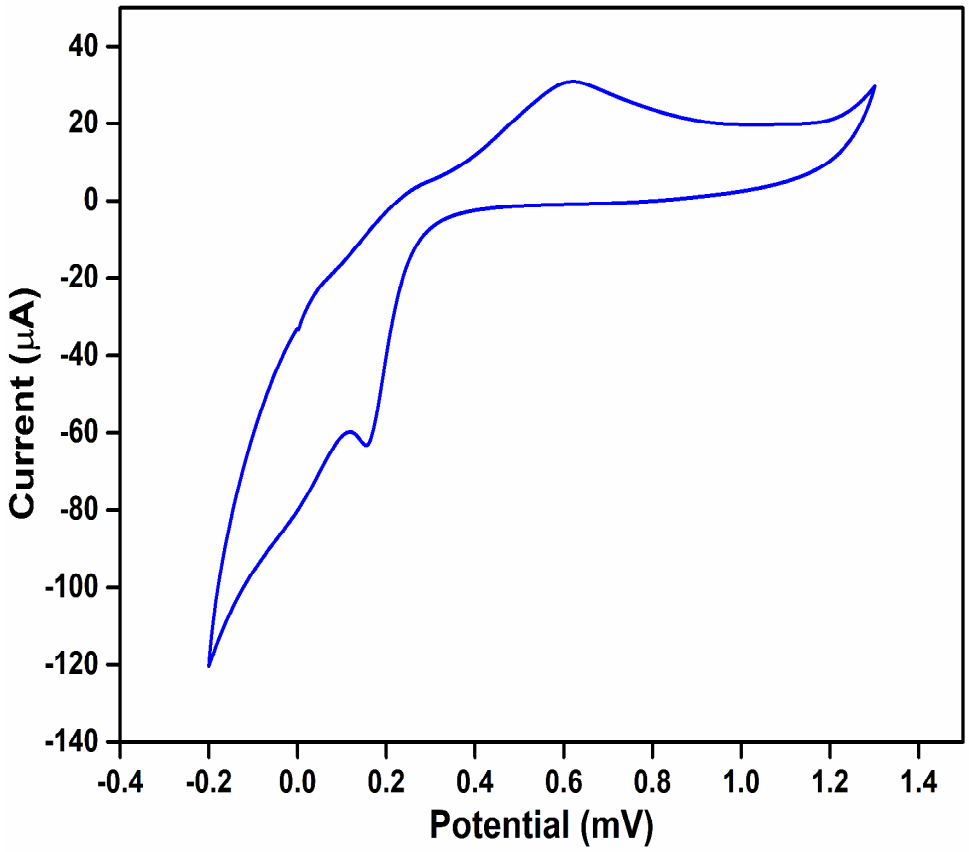

Figure 4.6. Cyclic voltammetry study of PdO thin film

The indigenously fabricated electrochemical cell is connected to potentiostat/galvanostat Autolab instrument and a constant potential of 1 V is applied across the electrodes. PdO/ITO based WE shows quick rise in response current for steady state response time (t_{90}) after which it saturates to constant value and eventually decays back to baseline position as H_2 gas is removed from the cell. The response is plotted as curve depicting relation between current (μA) with time (seconds) (figure 4.7).

4.3.5.i Sensing Mechanism

The possible redox reactions explaining this electrochemical mechanism can be explained using follows equations (equations 4.1 to 4.4) [13],

(Before Hydrogen gas flow)

$PdO + H_2O \leftrightarrows PdO_2 + 2H^+ + 2e^-$ **[Equation 4.1]**

$2PdO_2 \leftrightarrows 2PdO + O_2$ **[Equation 4.2]**

(After Hydrogen gas flow)

$PdO + H_2O + H_2 \leftrightarrows PdO_2 + 4H^+ + 4e^-$ **[Equation 4.3]**

$2PdO_2 + 4H^+ + 4e^- \leftrightarrows 2PdO + 2H_2O$ **[Equation 4.4]**

The free electrons generated from electrochemical redox reactions get transferred from WE to CE, participating in increasing the current of the electrical circuit. The response current increases on increasing the percentage concentration of target gas.

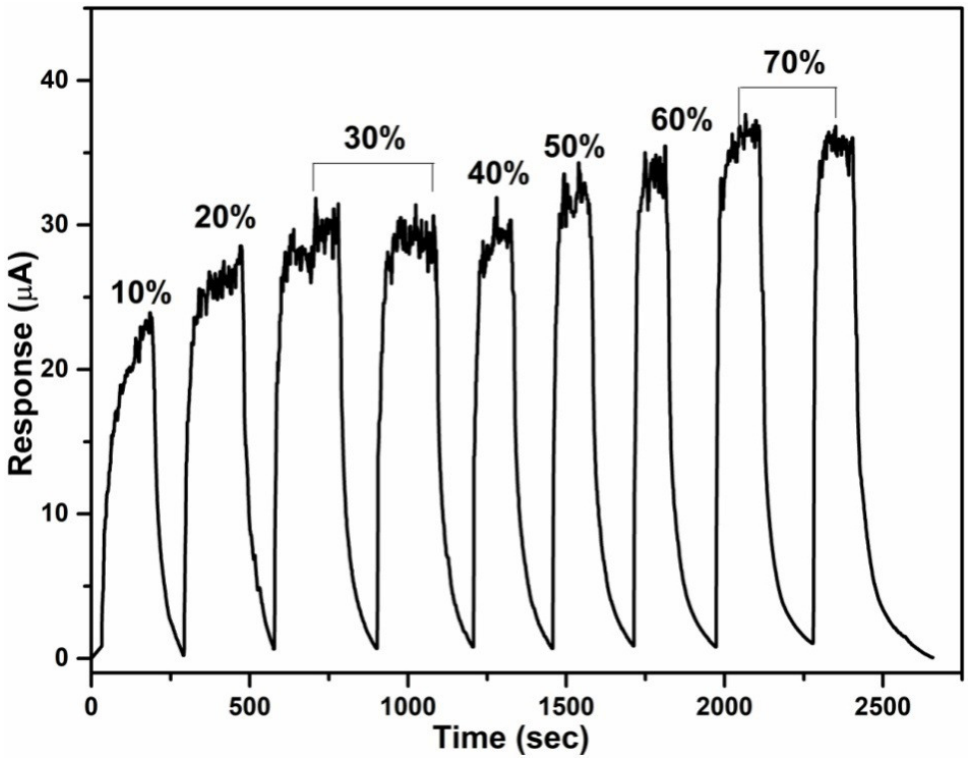

Figure 4.7. Response curve

4.3.5.ii Amperometric sensor performance

The sensing response of PdO/ITO based WE towards 10 to 70 % H_2 is linearly calibrated and displays good sensitivity (S) of (0.222±0.008) μA/%H_2 with variance of 0.98602 (figure 4.8).

The calibration is realized through linear fitting of sensitivity curve using linear regression equation y=24.59 + 0.222x, where x is H_2 gas concentration percentage and y is response current (μA) respectively. The proposed sensor has 0.1% H_2 limit of detection (LOD), which is defined as (3S/N), where S is standard deviation and N is the slope of the curve. The fabricated amperometric sensor shows steady state response time (t_{90}) of 60 seconds with fast recovery time for 10 to 70 % concentrations of H_2 gas.

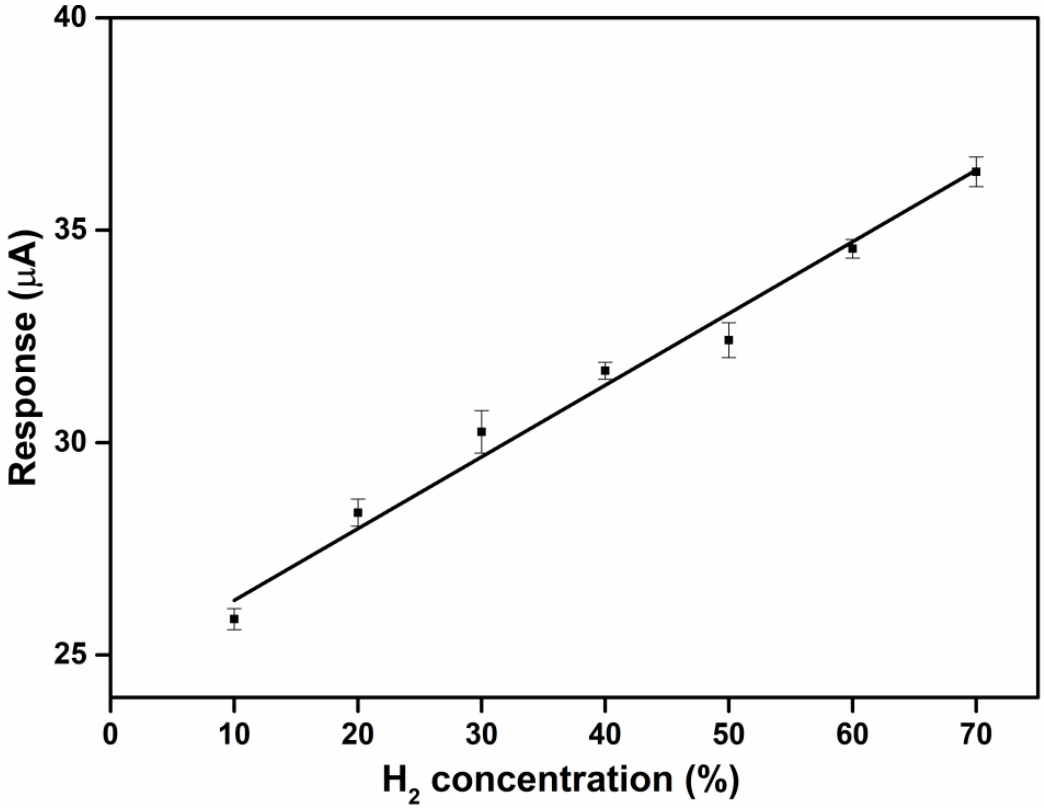

Figure 4.8. Calibration plot of response curve

4.3.5.iii Effect of deposition voltage on sensing response

It has been observed that PdO/ITO thin films deposited at different electrophoretic potential (10, 15, 20, 25, 30 and 35 Volts) shows changes in response current towards amperometric sensing for 10, 20 and 30 % H_2 (figure 4.9). There is a linear increase in the response current as deposition potential rises from 10 to 30 V, but it drops as the potential reaches 35 V.

Enhanced nanoparticles density and uniformity of thin films surface attributes to increase in sensitivity from 10 V to 30 V. Formation of interstitial sites and voids due to aggregation of particles occurs in thin film deposited at 30 V, which favours the adsorption capability of WE and thus increase in response current (figure 4.8).

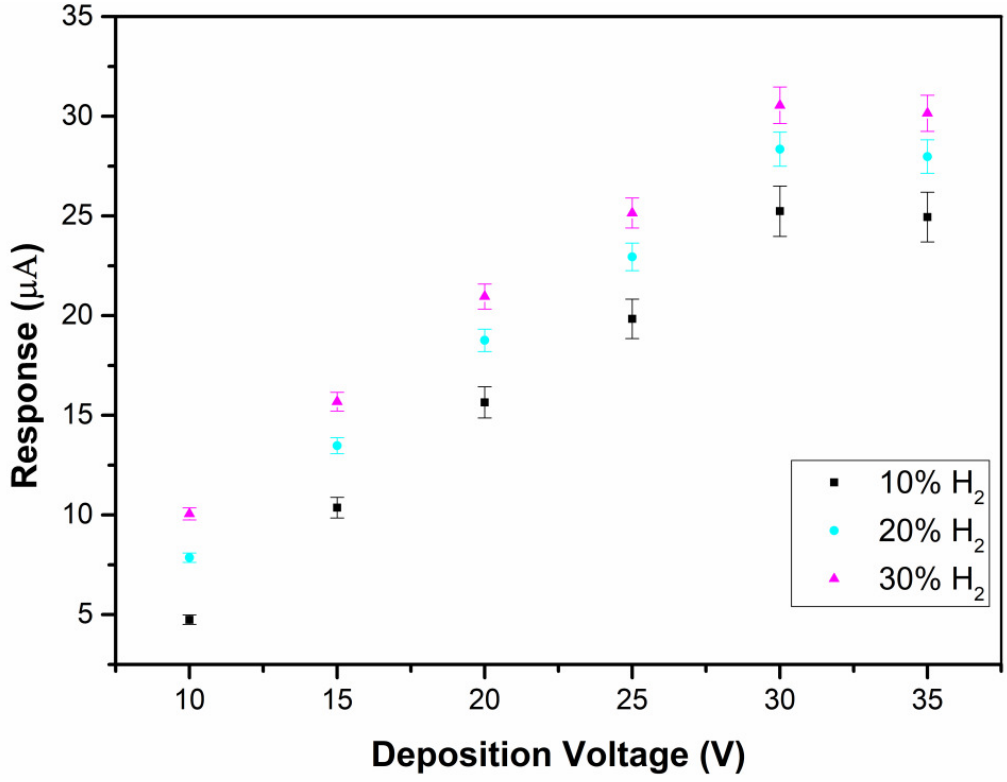

Figure 4.9. Relationship between Sensing response and deposition potential

PdO/ITO WE deposited at 35 V shows decrease in response current due to rapid rate of deposition, which hinders the homogeneity and uniformity of thin film by forming large size nanoclusters on its surface [14-15]. Moreover, higher deposition voltage results in enhanced packing density of deposited particles which leads to low porosity and unavailability of voids on surface of the PdO thin film [15].

The comparison of proposed room temperature amperometric H_2 sensor with other similar reported sensors published in literature are presented in table 4.1.

Gas	Sensing Electrode	Electrolyte	LOD (%H_2)	References
H_2	Pt/Carbon	5M H_2SO_4	-	[16]
H_2	Gold	9M H_2SO_4	-	[17]
H_2	Pt-Ag/AgCl	1M H_2SO_4	<1%	[18]
H_2-Air	Pt-Ag/AgCl	H_2SO_4	<0.2%	[6]
H_2-Nitrogen	Pt-Ag/AgCl	H_2SO_4	<0.4%	[6]
H_2-Ar	**PdO**	**0.5M H_2SO_4**	**<0.2%**	**Present work**

Table 4.1. Amperometric H_2 sensors based on liquid electrolytes

4.4 Conclusions

PdO nanoparticles of size 20 to 80 nm have been synthesized using facile and economical hydrothermal chemical process. The crystal structure of synthesized nanoparticles is studied using XRD measurements and is found to be tetragonal in nature. SAED and HRTEM images confirm the finding observed in XRD plot of PdO nanoparticles. The synthesized nanoparticles have a direct band gap of 1.9 eV as evaluated using UV-Vis absorption spectroscopy. Thin films of PdO nanoparticles are deposited on ITO glass substrate (PdO/ITO) using electrophoresis method at different deposition potential. PdO/ITO thin films are used as working electrodes in indigeneously fabricated electrochemical sensing setup for amperometric sensing of wide range (10 to 70 %) concentrations of H_2 gas at room temperature. Catalytic property of PdO nanoparticles is analyzed using CV study and it is found that PdO exhibit redox behavior towards electrochemical H_2 sensing at room

temperature. PdO/ITO working electrode fabricated at 30 V electrophoretic deposition potential shows higher sensitivity of 0.222 μA/%H_2 compared to other deposited electrodes. The amperometric sensor display steady state response of 60 seconds with fast recovery time and 0.1% H_2 limit of detection. The results of this study show wide range detection of H_2 gas at room temperature for the fabricated amperometric sensor. Nanostructures and composites of PdO nanoparticles can be studied further for enhancing the sensitivity and selectivity of the proposed sensor.

4.5 References

[1] M. Khanuja*, et al.*, "Concentration-specific hydrogen sensing behavior in monosized Pd nanoparticle layers," *Nanotechnology,* vol. 20, p. 015502, 2008.

[2] S. Srivastava*, et al.*, "Electrophoretically deposited reduced graphene oxide platform for food toxin detection," *Nanoscale,* vol. 5, pp. 3043-3051, 2013.

[3] L. Besra and M. Liu, "A review on fundamentals and applications of electrophoretic deposition (EPD)," *Progress in materials science,* vol. 52, pp. 1-61, 2007.

[4] P. Sarkar and P. S. Nicholson, "Electrophoretic deposition (EPD): mechanisms, kinetics, and application to ceramics," *Journal of the American Ceramic Society,* vol. 79, pp. 1987-2002, 1996.

[5] G. Korotcenkov*, et al.*, "Review of electrochemical hydrogen sensors," *Chemical reviews,* vol. 109, pp. 1402-1433, 2009.

[6] Y. Chao*, et al.*, "Amperometric sensor for selective and stable hydrogen measurement," *Sensors and Actuators B: Chemical,* vol. 106, pp. 784-790, 2005.

[7] S. Yao and M. Wang, "Electrochemical sensor for dissolved carbon dioxide measurement," *Journal of the electrochemical society,* vol. 149, pp. H28-H32, 2002.

[8] B. D. Cullity and S. R. Stock, *Elements of X-ray Diffraction* vol. 3: Prentice hall New Jersey, 2001.

[9] P. Nilsson, "Optical properties of PdO in the range of 0.5-5.4 eV," *Journal of Physics C: Solid State Physics,* vol. 12, p. 1423, 1979.

[10] X.-Y. Zhang*, et al.*, "Silver nanoplate aggregation based multifunctional black metal absorbers for localization, photothermic harnessing enhancement and omnidirectional light antireflection," *Journal of Materials Chemistry C,* vol. 6, pp. 989-999, 2018.

[11] S.-Q. Zhu*, et al.*, "Gold nanoparticle thin films fabricated by electrophoretic deposition method for highly sensitive SERS application," *Nanoscale research letters,* vol. 7, p. 613, 2012.

[12] T. C. Wen and C. C. Hu, "Cyclic Voltammetric Investigation of PdO-Coated Titanium Electrode in H 2 SO 4," *Journal of the electrochemical society,* vol. 140, pp. 988-995, 1993.

[13] C. C. Hu and T. C. Wen, "Voltammetric Investigation of Hydrogen Sorption/Desorption at/within Oxide-Derived Pd Electrodes in NaOH and H 2 SO 4," *Journal of the electrochemical society,* vol. 141, pp. 2996-3001, 1994.

[14] S. K. Dondapati*, et al.*, "Controlled electrophoretic deposition of multifunctional nanomodules for bioelectrochemical applications," *Biosensors and Bioelectronics,* vol. 24, pp. 55-59, 2008.

[15] R. Zhang*, et al.*, "Electrochemical Sensor Coating Based on Electrophoretic Deposition of Au-Doped Self-Assembled Nanoparticles," *ACS applied materials & interfaces,* vol. 10, pp. 5926-5932, 2018.

[16] V. Nikolova*, et al.*, "Tungsten carbide-based electrochemical sensors for hydrogen determination in gas mixtures," *Journal of applied electrochemistry,* vol. 30, pp. 705-710, 2000.

[17] K. Okamura*, et al.*, "Electrochemical gas sensor using a novel gas permeable electrode modified by ion implantation," *Surface and Coatings Technology,* vol. 201, pp. 8116-8119, 2007.

[18] Y. C. Liu*, et al.*, "Nafion Based Hydrogen Sensors: Pt/Nafion Electrodes Prepared by Takenata-Torikai Method and Modified with Polypyrrole," *Electroanalysis: An International Journal Devoted to Fundamental and Practical Aspects of Electroanalysis,* vol. 14, pp. 556-558, 2002.

CHAPTER 5

Electrochemical Hydrogen Gas Sensing Employing Palladium Oxide-Reduced Graphene Oxide (PdO-rGO) Nanocomposites

Nanocomposites of palladium oxide-reduced graphene oxide (PdO-rGO) have been synthesized using modified Hummer's and wet chemical methods. Crystallographic properties, shape, size, bonding information and band gap of composites are analyzed using x-ray diffraction (XRD) analysis, transmission electron microscopy (TEM), Fourier transform infrared (FTIR) transmission spectroscopy and ultraviolet-visible (UV-Vis) absorption spectroscopy. 30 to 35 nm sized nanoparticles are embedded within 2-dimensional (2D) sheets structure of rGO which aids in enhancing the surface area of composite for adsorption of hydrogen (H_2) gas. Thin film of PdO-rGO is deposited on ITO glass substrate using electrophoretic deposition (EPD) process. PdO-rGO/ITO is used as working electrode (WE) in electrochemical cell for amperometric sensing of H_2 gas. The response of proposed electrochemical H_2 sensor is recorded in terms of amperometric relation for 10 to 80 % concentration of H_2 using potentiostat/galvanostat autolab at room temperature. The sensitivity of H_2 sensor is found to be 0.462μA/% H_2, i.e. double to that observed for PdO/ITO based WE in previous chapter. The fabricated amperometric sensor is also found to be selective, stable and reproducible in nature towards H_2.

The work presented in this chapter is published as:

"Electrochemical Hydrogen Gas Sensing Employing Palladium Oxide/Reduced Graphene Oxide (PdO-rGO) Nanocomposites"

IEEE Sensors Journal, 19(2019), 8262 - 8271.

5.1 Introduction

Composites of two or more dissimilar nanomaterials lead to formation of heterostructures and interface between these nanomaterials is known as heterojunctions. It has been observed that fabrication of nanocomposite results in comprehensive enhancement in gas sensing capability of heterostructured materials. These synergistic effects of nanocomposites are attributed to various factors which include band bending due to Fermi level shifting, separation of charge carriers, modification of depletion layer, increase in potential barrier of interface, lowering of activation energy, targeted catalytic activity, synergistic effect of surface reactions, alteration in grain structures, increase in surface area and increase in adsorption rate of gas molecules [1].

Two dimensional (2D) nanomaterials exhibit unique properties compared to other nanostructures such as 0D, 1D, 3D and bulk material. Charge carriers of 2D nanomaterials are confined along the thickness of material and permitted to move only along the plane. The electronic and physical properties of 2D nanomaterials can be manipulated by modifying the thickness of 2D nanomaterials which is not possible in 0, 1 and 3D nanostructures. Narrow thickness and large planar area yields large surface area which makes them suitable for gas sensing applications. Also, 2D nanomaterials are sensitive to external stimuli and thus can be easily doped and modified with other desired materials [2]. 2D graphene has outstanding physical, chemical and electrical properties over other allotropes of carbon, which made them most researched material for catalytic and electrochemical activities. Graphene has high theoretical surface area of 2600 $m^2 g^{-1}$ compared to other nanomaterials and double to that of other carbon nanostructures. Pristine graphene is not sensitive towards adsorption based sensing applications as they do not have free surface bonds required for its functionalization and modification. However, graphene extracted from chemical synthesis process known as

chemically modified graphene (CMG) i.e. graphene oxide (GO) and reduced graphene oxide (rGO) have impurities and defects present on the surface and within its 2D sheet like structure which makes them more suitable for catalytic and sensing application compared to pure graphene [3]. Chemically modified graphene (CMG) can be synthesized at large scale using economical and facile chemical method. The presence of large number of oxygenated functional groups imparts GO with insulating nature and poor electrochemical properties. Transformation of GO to rGO is essential to attain the conductivity similar to that of graphene for its use in electrochemical applications. rGO has high electron mobility, good conductivity and large surface area due to presence of free localized π electrons, high surface to volume ratio and large number of surface defects. [4]. Doping of rGO with noble metals such as palladium (Pd) or platinum (Pt) and forming their heterostructure with electroactive materials can significantly enhance their catalytic activity which makes them favourable candidate for sensing and storage applications [5-6].

Heterostructure of PdO with rGO has not been studied before for amperometric sensing of H_2 gas using proton conducting liquid electrolyte. Hence, nanocomposite of PdO and rGO are synthesized using modified hummer's wet chemical route. PdO-rGO nanocomposite is deposited over ITO layer coated glass substrate (PdO-rGO/ITO) and it is used as working electrode (WE) in indigenously fabricated electrochemical cell for amperometric sensing study of wide range (10% to 80%) H_2 concentration at room temperature.

5.2 Experimental work

5.2.1 Synthesis of graphene oxide (GO)

99.9% purity AR grade chemicals have been used to synthesize GO, rGO and PdO-rGO nanocomposites. Marcabo et. al suggested economical improved Hummer's method for

synthesis of GO at large scale chemically. 9:1 ratio concentrated solution of Phosphoric acid (H_3PO_4) and sulphuric acid (H_2SO_4) is prepared in a conical flask followed by addition of 2 g graphite powder. 12 g Potassium permanganate ($KMnO_4$) is mixed with resultant solution dropwise through continuous stirring for 12 hours at 50 ^{0}C, as the equation becomes highly exothermic in nature. The temperature of final solution is cooled down by adding ice together and thereafter 2 mL H_2O_2 is mixed with the solution. The obtained brown solution is filtered and washed with hydrochloric acid (HCl) and deionized (D.I.) water several times to bring the pH of solution to 7. At last, solution is heated at 70^0 C for 24 hours to flakes of GO [7].

5.2.2 Synthesis of reduced graphene oxide (rGO)

Reduction of GO is achieved using hydrazine hydrate ($N_2H_4.H_2O$) as moderate reducing agent as demonstrated by Park et. al. in their published research work. 1mg/ml solution of GO is obtained in D.I. water by stirring it for 1 hour at room temperature. $N_2H_4.H_2O$ is added in GO solution with a (1:1) ratio through continuous stirring for 12 hours. The black solution obtained through above process is filtered, washed with D.I. water and dried at 70 ^{0}C to obtain powder form rGO [8].

5.2.3 Synthesis of PdO-rGO nanocomposite

Nanocomposites of PdO with synthesized rGO is obtained using in-situ wet chemical method by dissolving palladium chloride ($PdCl_2$) in ethanol (C_2H_5OH) with concentration of (1µg/ml) keeping their molar ratio at (1:1). The resultant solution is continuously stirred for 1 hour to obtain homogeneous solution. The solution is left unperturbed to age for 24 hours and thereafter it is filtered, washed with D.I. water and heated at 80 ^{0}C for 24 hours to yield brown powder of PdO-rGO nanocomposite. The powder is annealed at 600 ^{0}C for 2 hours to

obtain crystalline form of nanocomposite and elimination of organic and chloride ions impurities. The crystallographic structure, shape, size of nanocomposite, bonding information , intra-bond interaction, surface morphology of thin films and band gap of semiconducting nanocomposite is analyzed using x-ray diffraction (XRD) spectroscopy, transmission electron microscopy (TEM), Fourier transform infrared spectroscopy, ultraviolet-visible (UV-Vis) absorption spectroscopy and scanning electron microscopy (SEM).

5.2.4 Fabrication of working electrode (WE)

Thin film of PdO-rGO nanocomposite is fabricated on (5 mm x 10 mm) ITO coated glass substrate using electrophoretic deposition process at potential of 40 volts with 2 minutes deposition time. PdO-rGO/ITO based working electrodes (WE) are used in same electrochemical sensing setup described in chapter 4 for amperometric sensing of H_2 gas at room temperature (refer section 4.2.1.ii).

5.3 Results and discussions

5.3.1 X-ray Diffraction analysis (XRD)

Figure 5.1.(a), (b) and (c) represent the XRD plot of GO, rGO and PdO-rGO nanocomposite respectively. XRD intensity graph of GO consist of characteristic intensity peaks at 11.01^0 corresponding to (002) plane, XRD plot of rGO shows shifted broad amorphous peak at 23.78^0 which confirm the successful reduction of GO and figure 5.1.(c) contains intensity peaks of both rGO and t-PdO, showing synthesis of nanocomposite. These results have been validated by comparing with the published JCPDS data (CAS number: 750200 and 850624). The intensity peak of rGO has diminished to larger extent whereas the peaks of PdO have become more intense in nature. This is due to interaction of PdO

nanoparticles with surface bonds of rGO reducing the concentration of free surface states required for growth of 2D rGO structure;

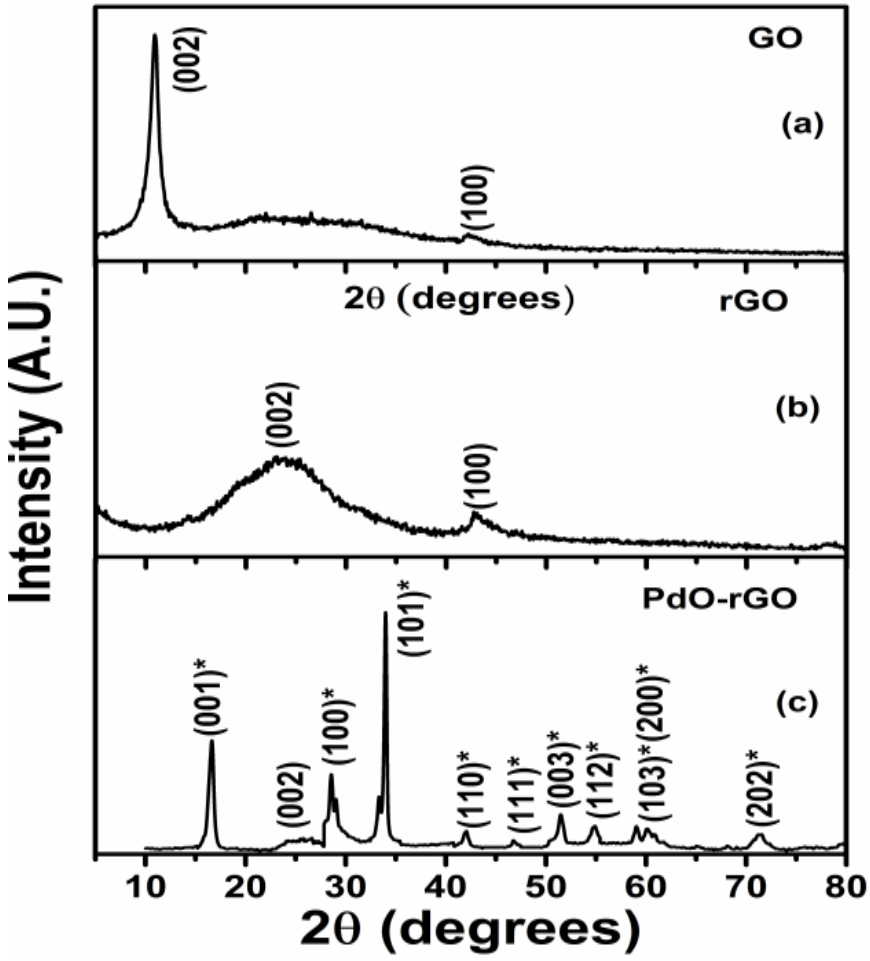

Figure 5.1. XRD plot of (a) GO, (b) rGO, (c) PdO-rGO nanocomposite

However, the crystallanity of PdO remains unperturbed by the presence of rGO. The average crystallite size of t-PdO and number of rGO layers in nanocomposite sample is calculated to be 23.72 nm and three, by using equation 3.4 (refer to section 3.3.1) and 5.1 respectively [9-10]. The interplanar spacing of GO and rGO for characteristics (002) plane is found to be 8.02 Å and 3.74 Å correspondingly.

$$2d\sin\theta = n\lambda \qquad \textbf{[Equation 5.1]}$$

d is interplanar spacing, θ is diffraction angle, n is order of diffraction and λ is wavelength

5.3.2 Transmission electron microscopy (TEM)

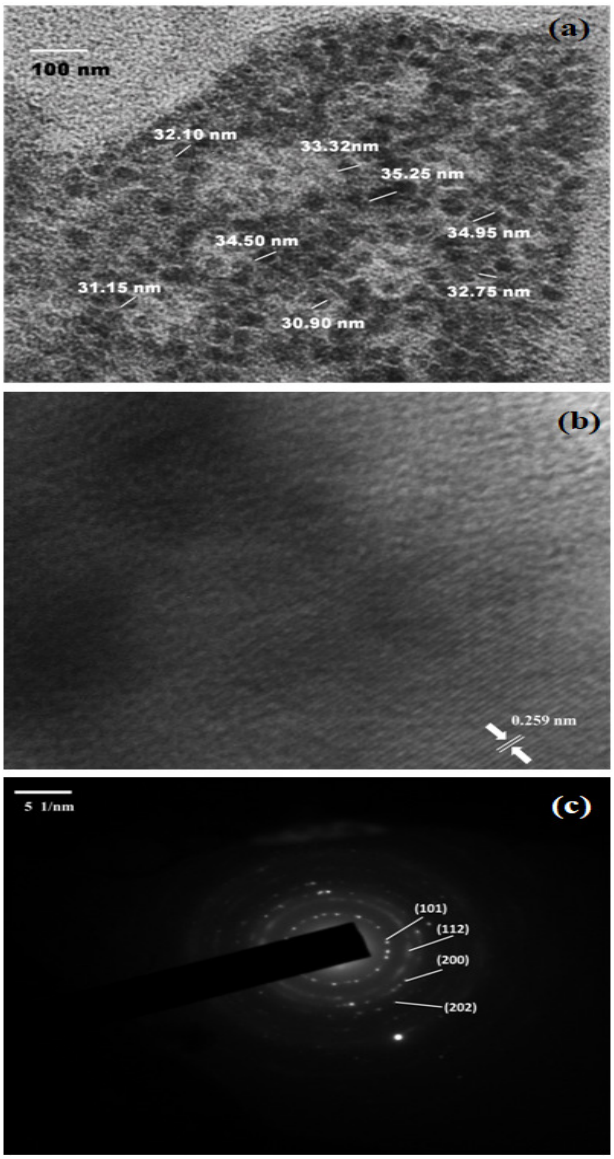

Figure 5.2. (a) TEM image, (b) HRTEM image, (c) SAED image of PdO-rGO nanocomposite

TEM image [figure 5.2.(a)] of nanocomposite shows 30-35 nm size PdO nanoparticles (dark circular spots) embedded on the surface of 2D nanosheets (bright background) of rGO. The synthesized nanoparticles have well defined particle shape as well as boundaries. HRTEM and SAED images confirm the results demonstrated by XRD analysis

about formation of nanocomposite of rGO with tetragonal crystal structure PdO nanoparticles and interplanar spacing of t-PdO is evaluated to be 0.225 nm which corresponds to characteristic (101) plane [figure 5.2.(b) and figure 5.2.(c)]. SAED image of nanocomposite contains fused ring like geometry along with bright dots forming circular pattern suggesting formation of polycrystalline t-PdO structure and amorphous rGO sheets.

5.3.3 Fourier Transform Infrared (FTIR) transmission spectroscopy

FTIR spectra of GO, rGO and PdO-rGO nanocomposite are depicted in figure 5.3.(a), (b) and (c) respectivelty. FTIR spectrum of GO consist of transmission peaks at 1061.55 cm^{-1}, 1628.87 cm^{-1}, 1735.41 cm^{-1} and 3445.87 cm^{-1} which arises due to presence -C-O- stretching, -C–O–H- deformation, C=O stretching of -COOH- group and -O-H- functional groups correspondingly [11].

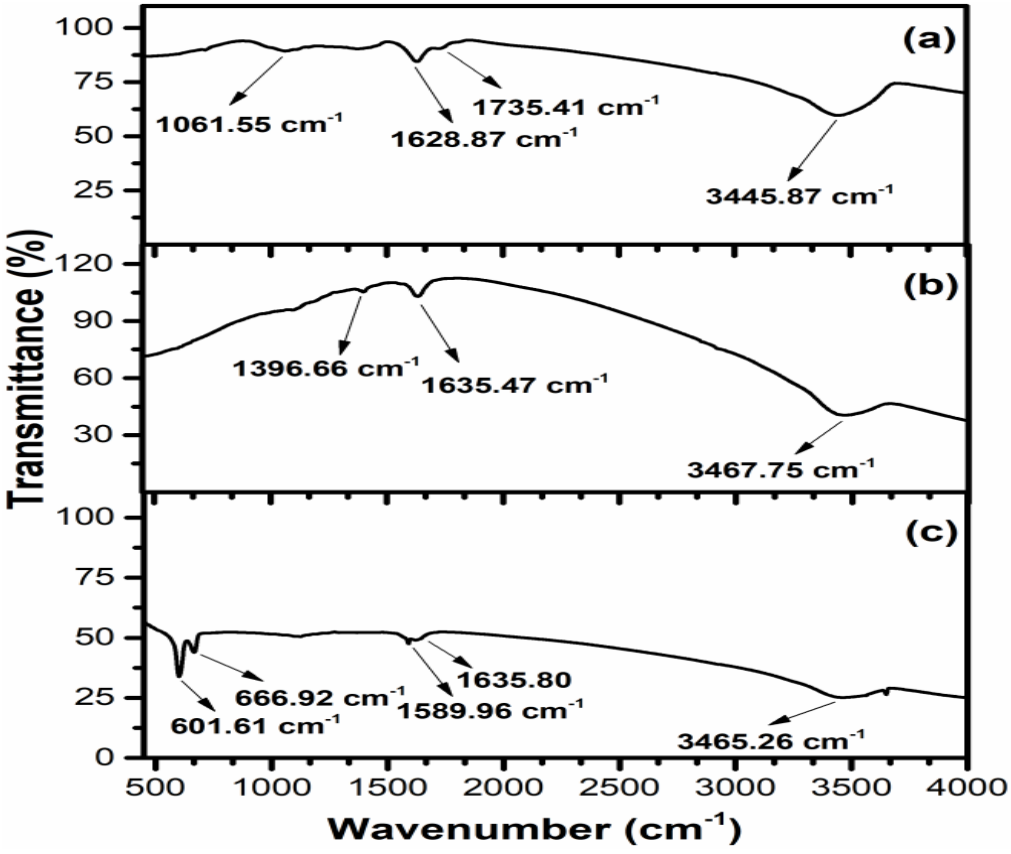

Figure 5.3. FTIR spectroscopy plot of (a) GO, (b) rGO, (c) PdO-rGO nanocomposite

It is observed that peaks corresponding to oxygenated functional groups of GO have reduced in intensity comprehensively on its reduction to rGO. The presence of peak at 1396.66 cm^{-1} in rGO FTIR spectrum is attributed to graphene sheets skeletal vibrations [figure 5.3.(c)] [12]. FTIR spectrum of PdO-rGO nanocomposite contains all the peaks visible in rGO spectrum along with new peaks at 601.61 cm^{-1} and 666.92 cm^{-1} which occur due to vibrational interaction between -Pd-O- and -Pd-C- bonds respectively. There is a red shift of transmission peaks to 1589.96 cm^{-1}, 1635.80 cm^{-1} and 3465.26 cm^{-1} along with the splitting due to inter-bond interaction of PdO, carboxylic and hydroxyl groups of 2D rGO nanosheets.

5.3.4 Ultraviolet Visible (UV-Vis) absorption spectroscopy

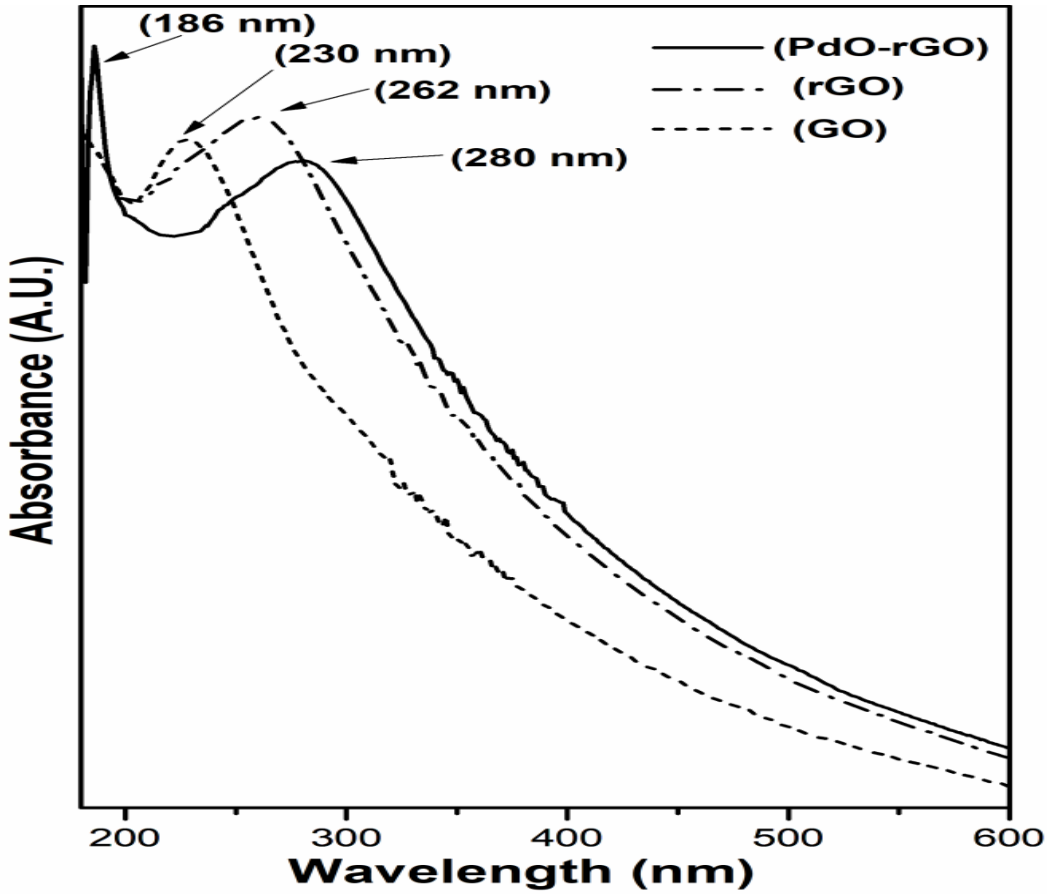

Figure 5.4. UV-Vis absorption spectra of GO, rGO and PdO-rGO nanocomposite

Figure 5.4 shows the UV-Vis spectra of GO, rGO and PdO-rGO nanocomposite respectively. The absorption peak at 230 nm corresponds to π-π^* transition of C-C bond present in GO structure which undergoes right shift towards higher wavelength of 262 nm. This red shift is due to elimination of oxygenated functional groups which increase the number of π electrons in rGO sheet structure and restoration of sp^2 C-C conjugated structure [13]. The absorption peak shift rightward further to 280 nm along with rise in new peak at 186 nm on mixing PdO and rGO together confirming the successful fabrication of PdO-rGO nanocomposite [14-15]. Figure 5.5.(a), (b) and (c) represent the Tauc plot of GO, rGO and PdO-rGO respectively. It is observed that band gap of GO which is evaluated using equation 5 (refer section 3.3.4) to be 3.75 eV, reduces to 2.92 eV on reduction of GO to rGO and further decrease to 2.71 eV on synthesis of PdO-rGO nanocomposite. All the calculated values coincides with the published data [16-17].

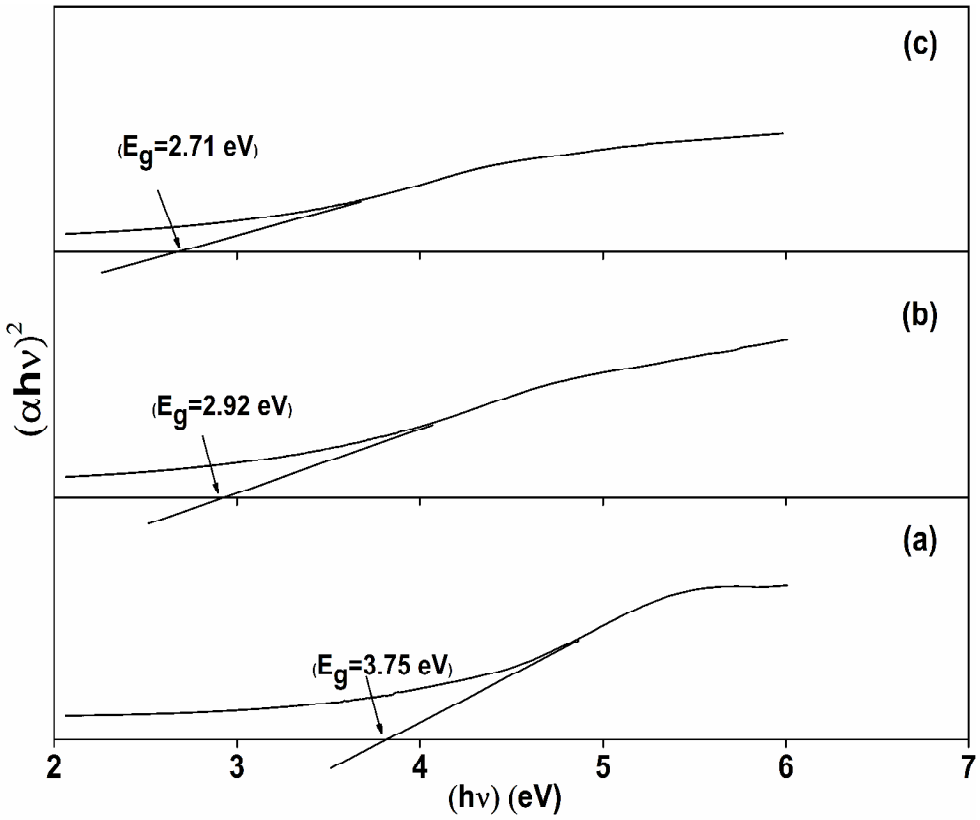

Figure 5.5. Tauc plot of (a) GO, (b) rGO and (c) PdO-rGO

5.3.5 Scanning electron microscopy (SEM)

Surface morphology of PdO-rGO nanocomposite thin film is depicted in figure 5.6. The dark grey area in image shows uniformly aggregated and randomly blended stacked multiple 2D nanosheets of rGO. The rGO sheets are covered with bright cluster of spots representing agglomerated PdO nanoparticles. There is uniform distribution of accumulated nanoparticles with undefined boundaries on surface of wrinkled 2D rGO nanosheets which are folded at the edges. The size and shape of nanoparticles are not visible on surface of thin film, but they have been analyzed using TEM analysis of nanocomposite sample.

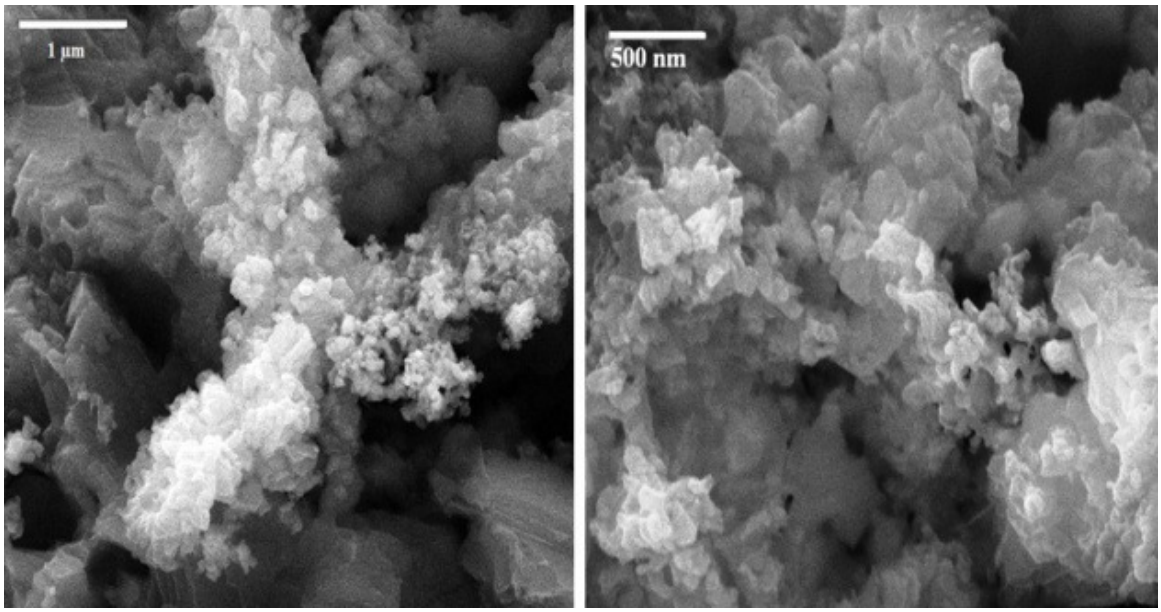

Figure 5.6. Scanning electron microscopy (SEM) images of PdO-rGO nanocomposite thin film

5.3.6 Electrochemical H_2 amperometric sensing study

The amperometric sensing study is performed on wide percentage concentration of H_2 gas ranging from 10-80% in dry air at room temperature. H_2 gas is allowed to pass into indigenously fabricated electrochemical cell at a flow rate of 60 ml/min through mass flow

controller (MFC) for a time of 5 minutes keeping the same variables and parameters as defined already in our previous work reported in chapter 4 (refer section 4.3.5)

PdO/ITO WE shows good catalytic behaviour towards H^+ ions in proton conducting H_2SO_4 electrolyte. The catalytic behaviour of PdO-rGO nanocomposite is also analyzed similarly using cyclic voltammetry (CV) study, both in presence and absence of hydrogen gas (figure 5.7). It has been observed that CV plot of PdO-rGO/ITO WE follows similar pattern with or without H_2 gas, but a considerable increase in oxidation and reduction current is found as a result of redox reactions contributing in increasing the concentration of electrons. However, there is right shift in oxidation cathodic cycle from 0.65 mV to 0.72 mV along with reduction anodic cycle from 0.10 mV to 0.12 mV respectively which is a result of increasing concentration of H^+ ions at electrode-electrolyte interface, that create a barrier for other incoming H^+ ions shielding them from participating in electrochemical reactions.

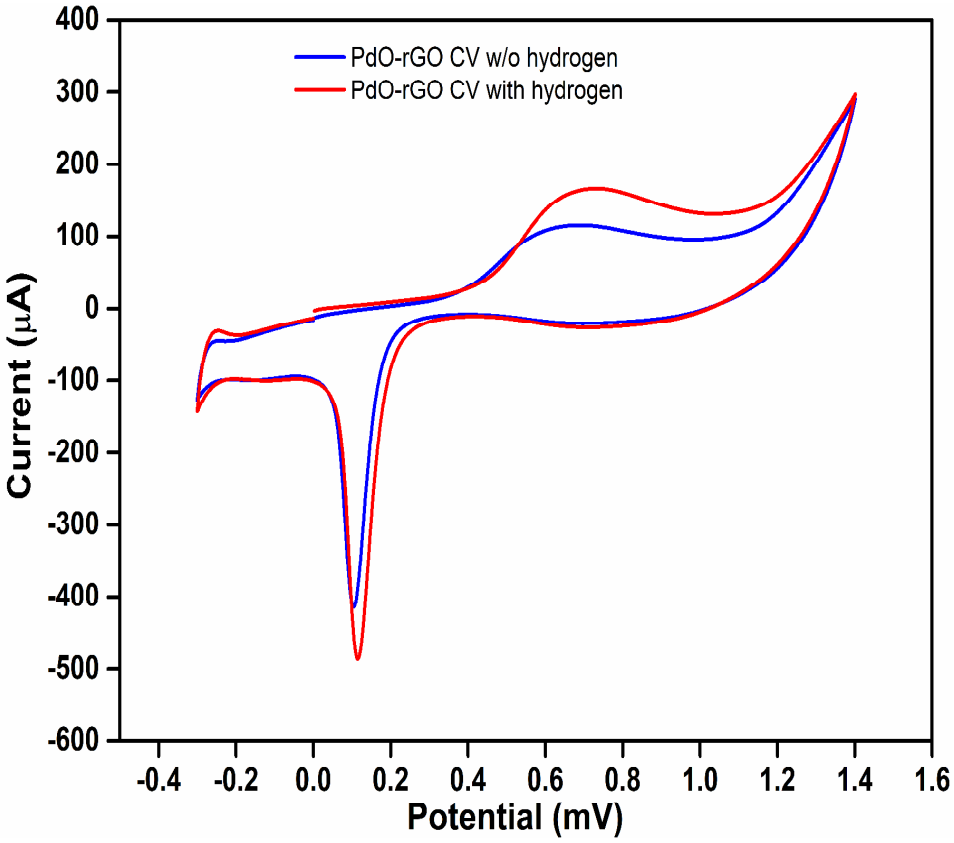

Figure 5.7. Cyclic voltammetry study of PdO-rGO nanocomposite thin film

Thus, PdO-rGO nanocomposite also shows electrochemical catalytic activity towards H^+ ions as similar to PdO nanoparticles at room temperature in proton conducting electrolyte and will shows good electrochemical sensing signal for amperometric H_2 sensing application. The amperometric signal of PdO-rGO nanocomposite for 10-80% H_2 gas is plotted in response curve depicted in figure 5.8. There is a comprehensive increase in electrochemical current as H_2 gas is introduced in the circuit which rises appreciably with increasing concentration of H_2 gas. However, the steep increase in sensing signal is not observed at concentrations greater than 50% because of saturation of WE with H^+ ions as amperometric sensing is diffusion limited process. PdO-rGO/ITO WE shows fast sensing response towards H_2 gas at room temperature, with a steady state current (t_{90}) response of 60 seconds and 0.13% H_2 LOD.

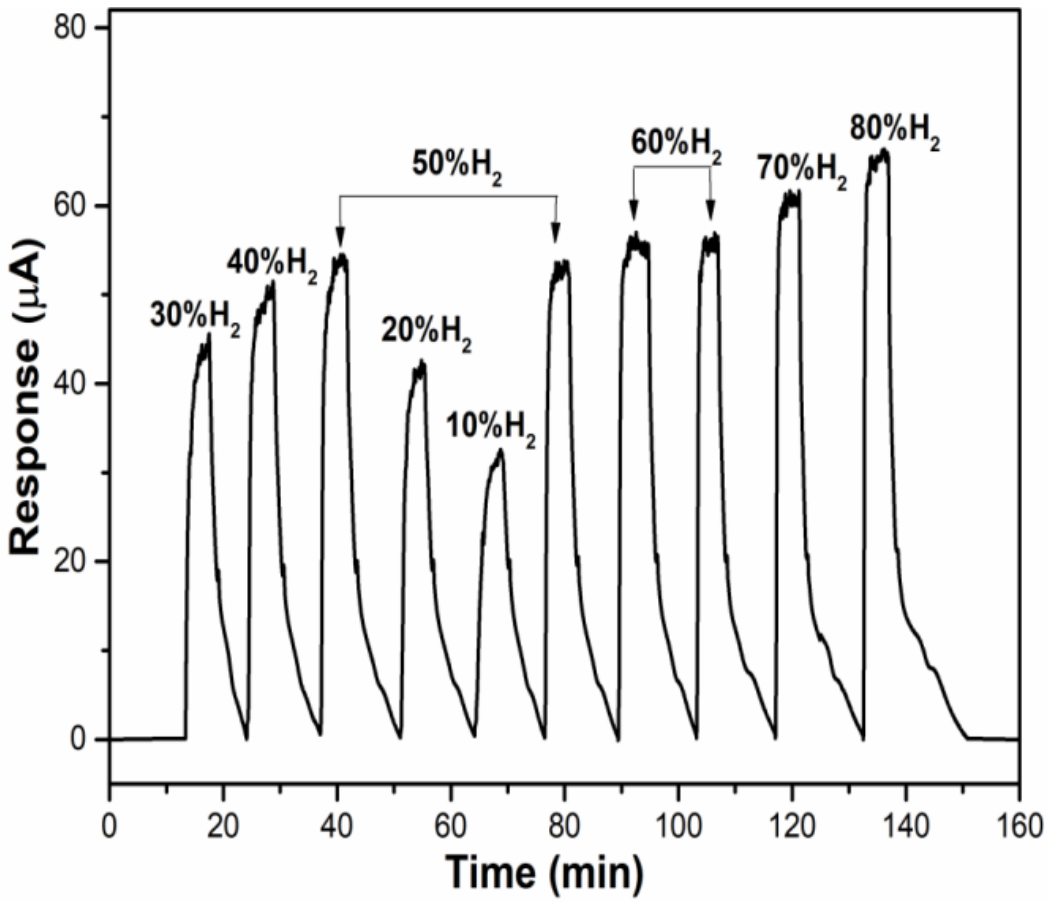

Figure 5.8. Response curve for different percentage concentration of H_2 gas

The sensitivity of the proposed WE in indigenously fabricated electrochemical cell is obtained using linearly calibrated response calibration curve (figure 5.9) and is found to be (0.462 ± 0.023) μA/%(H_2) with a variance of 0.98229, i.e. double the sensitivity of PdO/ITO based WE used in our last research work. The fitting of curve is achieved using regression equation $y=29.38 + 0.462x$, where x and y represent the H_2 gas concentration (%) and the amperometric signal (μA) respectively. The mechanism of electrochemical response for PdO-rGO nanocomposite is similar to the pristine PdO nanoparticles and can be explained using equations 5 to 8, as described in chapter 4 (refer section 4.3.5.i). Hence, rGO offers large surface area for adsorption of incoming H^+ ions and also provides a conducting medium for fast transport of incoming electrons in electrochemical circuit, leading to enhanced sensing response of proposed amperometric sensor.

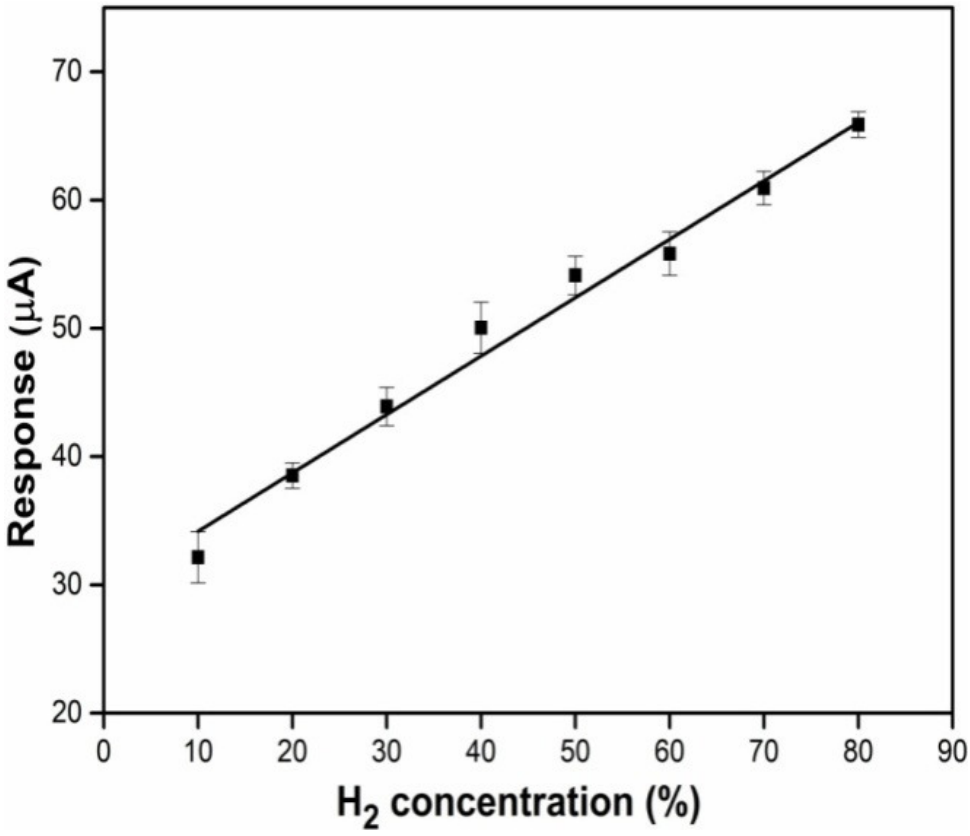

Figure 5.9. Calibration plot of response current (μA) vs H_2 concentration (%)

5.3.7 Selectivity study

Figure 5.10 shows the amperometric sensing response of PdO-rGO/ITO WE towards 80% concentration of Methane (CH_4), Carbon dioxide (CO_2) and Sulphur dioxide (SO_2) gas and compared with that for H_2 gas using same experimental parameters. The sensing signal for H_2 gas is found to be comprehensively large as compared to other test gases. The fabricated WE produce sensing current for CH_4, CO_2 and SO_2 too, which suggest possible interference on sensing signal in presence of these gases. However, the magnitude of response current is significantly small and thus it can be inferred that PdO-rGO nanocomposite is highly selective towards electrochemical sensing of H_2 gas at room temperature.

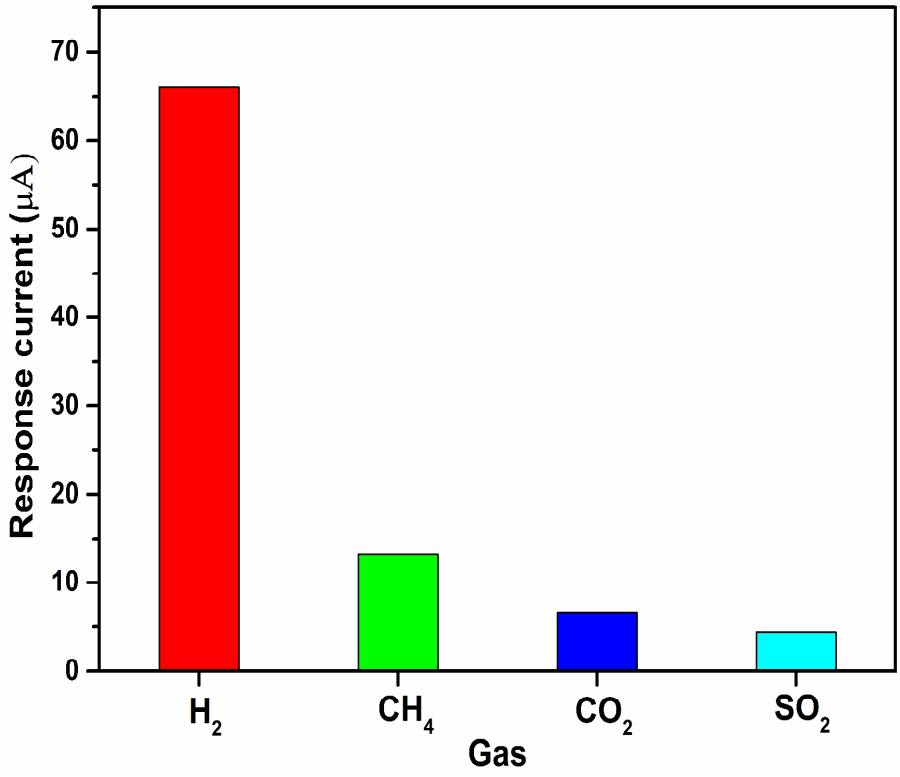

Figure 5.10. Response of PdO-rGO nanocomposite based amperometric sensor to various gases

The interaction of SO_2 can be explained using the following step by step process which involves diffusion or dissolution of SO_2 molecules to sulphite ions (SO_4^{2-}), transfer of these

ions towards the surface of WE followed by its diffusion, oxidation of SO_4^{2-} ions on the surface of WE together with simultaneous reduction of protons which are released during dissolution of SO_2 at counter electrode (CE) and restore the ionic content of electrochemical reaction. The mechanism of the interaction can be explained from equations 5.2 to 5.4;

$$SO_2 + 2H_2O \rightarrow SO_4^{2-} + 4H^+ + 2e^- \quad \textbf{[Equation 5.2]}$$

$$PdO + SO_4^{2-} + 2H^+ \leftrightarrow PdSO_4 + H_2O \quad \textbf{[Equation 5.3]}$$

$$\frac{1}{2}O_2 + 2H^+ + 2e^- \rightarrow H_2O \quad \textbf{[Equation 5.4]}$$

PdO-rGO/ITO WE interacts with CO_2 gas in presence of proton conducting electrolyte H_2SO_4 using the following processes which include ionization of H_2SO_4 to release H^+ ions followed by transportation of H^+ ions and CO_2 molecules towards WE surface, absorption of CO_2 molecules by WE followed by its oxidation at nanocomposite surface and instantaneous reduction of protons at CE to restore the ionic content of the system and can be explained using equations 5.5 and 5.6 [18-20].

$$PdO + CO_2 + 2H^+ \leftrightarrow PdCO_3 + H_2O + 2e^- \quad \textbf{[Equation 5.5]}$$

$$\frac{1}{2}O_2 + 2H^+ + 2e^- \rightarrow H_2O \quad \textbf{[Equation 5.6]}$$

5.3.8 Stability study

The sensing signal of PdO-rGO/ITO WE is measured for 60 days and recorded in stability curve depicted in figure 5.11. There is no significant variation in response current in interval of 60 days. The magnitude of current observed on first day is 65.89 μA which reduces to 63.42 μA on last day. Hence, proposed WE is found to be very stable for electrochemical sensing of H_2 gas at room temperature.

5.3.9 Reproducibility study

Figure 5.12 shows the reproducibility of PdO-rGO/ITO WE towards amperometric sensing of H_2 gas by recording the sensing signal of four electrodes fabricated using same sets of electrophoretic deposition parameters as described in experimental section of this chapter. It can be seen in the figure that there is no considerable difference between the signal of all four electrodes and relative standard deviation (RSD) is calculated to be 3.31%, which indicates good reproducibility and precision of fabricated electrodes.

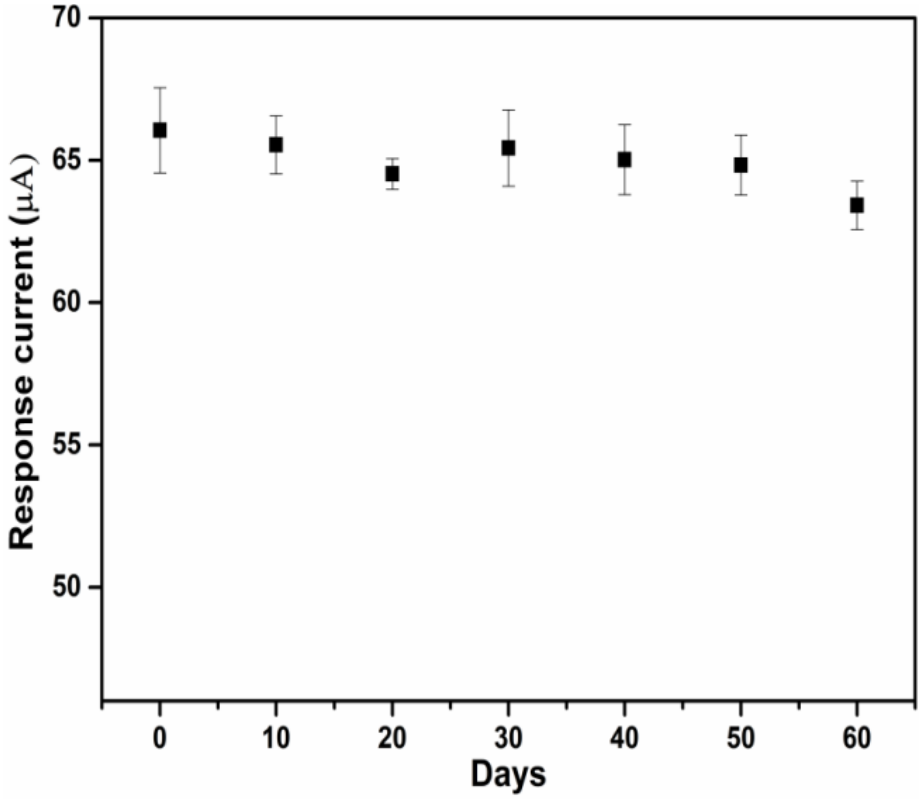

Figure 5.11. Stability study of working electrode

The proposed amperometric H_2 sensing setup employing PdO-rGO nanocomposites as sensing material displays enhanced sensitivity and limit of detection as compared to other similar reported sensors in table 5.1. Also, it demonstrates two folds increase in sensitivity as compared to PdO/ITO WE based amperometric H_2 sensor as discussed in chapter 4.

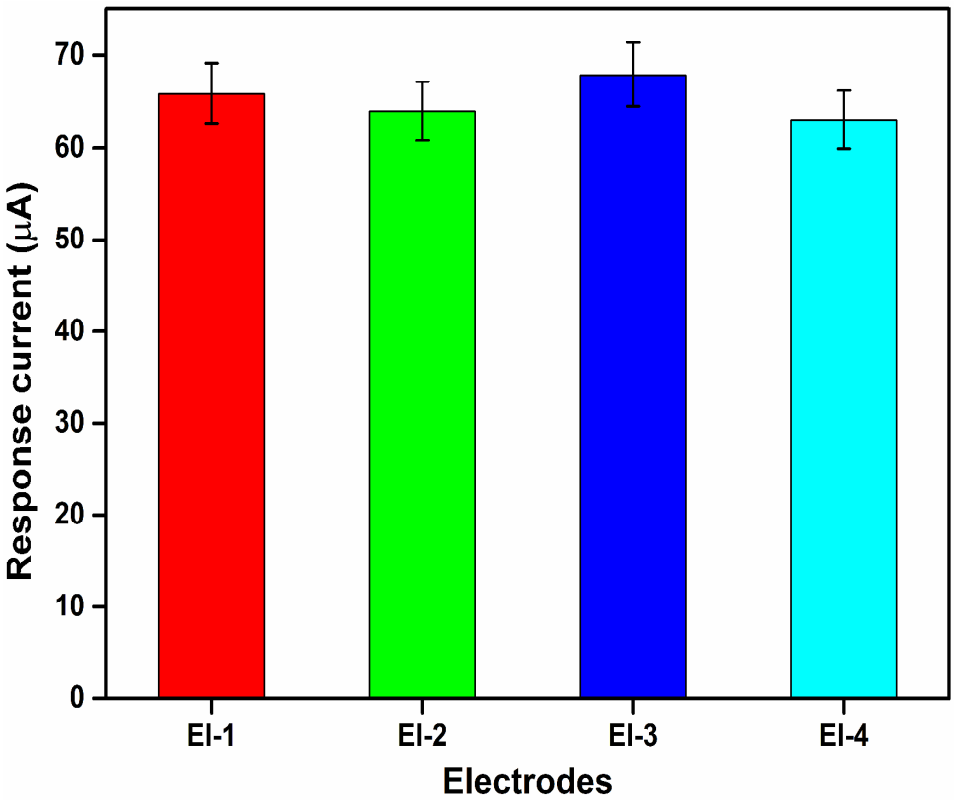

Figure 5.12. Reproducibility study of working electrodes

Gas Analyte	Working Electrode	Liquid Electrolyte	Limit of Detection (%H_2)	Sensitivity (μA/% or (ppm)H_2)	References
H_2	Pt/Carbon	5M H_2SO_4	-	-	[21]
H_2	Gold	9M H_2SO_4	-	-	[22]
H_2	Pt-Ag/AgCl	1M H_2SO_4	<1%	0.0305	[23]
H_2-Air	Pt-Nafion	1 M H_2SO_4	<0.2%	0.008	[24]
H_2-Ar	PdO/ITO	0.5M H_2SO_4	<0.2%	0.222	[25]
H_2-Ar	**PdO-rGO/ITO**	**0.5 M H_2SO_4**	**<0.2%**	**0.462**	**Present work**

Table 5.1. Liquid electrolyte based amperometric hydrogen sensors

5.4 Conclusions

This chapter discusses about synthesis and fabrication of PdO-rGO heterostructure and its enhanced sensitivity towards H_2 gas compared to pristine PdO nanoparticles using amperometric sensing study at room temperature. GO, rGO and PdO-rGO nanocomposite sample are synthesized using improved modified Hummer's and in-situ wet chemical

method. 30-35 nm size PdO nanoparticles with tetragonal crystal structure are found to be embedded within 2D nanosheets of rGO using XRD study and TEM images. FTIR transmission spectroscopy also confirms the successful synthesis of nancomposites using economical and facile chemical process. The band gap of heterostructure is evaluated using UV-Vis absorption spectroscopy and found to be less than that of GO and rGO comparatively. Thin film of PdO-rGO nanocomposite is deposited on ITO glass substrate using electrophoretic deposition process and analysis of its surface morphology using SEM images shows uniform deposition of nanocomposite with surface defects which makes it suitable for H_2 sensing application. PdO-rGO/ITO is used as working electrode (WE) for amperometric sensing of 10 to 70% concentration of H_2 gas. The proposed sensor is found to be highly sensitive, stable, selective and reproducible towards electrochemical H_2 gas sensing at room temperature. The sensitivity is found to be double to that of PdO/ITO WE which is studied in the previous chapter. PdO-rGO nanocomposite based amperometric sensor shows good response signal and fast response characteristics as compared to similar sensors reported in literature.

5.5 References

[1] D. R. Miller*, et al.*, "Nanoscale metal oxide-based heterojunctions for gas sensing: a review," *Sensors and Actuators B: Chemical,* vol. 204, pp. 250-272, 2014.

[2] A. H. Khan*, et al.*, "Two-dimensional (2D) nanomaterials towards electrochemical nanoarchitectonics in energy-related applications," *Bulletin of the Chemical Society of Japan,* vol. 90, pp. 627-648, 2017.

[3] D. R. Dreyer*, et al.*, "The chemistry of graphene oxide," *Chemical Society Reviews,* vol. 39, pp. 228-240, 2010.

[4] S. Stankovich*, et al.*, "Synthesis of graphene-based nanosheets via chemical reduction of exfoliated graphite oxide," *carbon,* vol. 45, pp. 1558-1565, 2007.

[5] A. Esfandiar*, et al.*, "The decoration of TiO 2/reduced graphene oxide by Pd and Pt nanoparticles for hydrogen gas sensing," *International Journal of Hydrogen Energy,* vol. 37, pp. 15423-15432, 2012.

[6] P. A. Russo*, et al.*, "Room-Temperature Hydrogen Sensing with Heteronanostructures Based on Reduced Graphene Oxide and Tin Oxide," *Angewandte Chemie International Edition,* vol. 51, pp. 11053-11057, 2012.

[7] D. C. Marcano*, et al.*, "Improved synthesis of graphene oxide," 2010.

[8] S. Park*, et al.*, "Hydrazine-reduction of graphite-and graphene oxide," *carbon,* vol. 49, pp. 3019-3023, 2011.

[9] B. D. Cullity and J. W. Weymouth, "Elements of X-ray Diffraction," *American Journal of Physics,* vol. 25, pp. 394-395, 1957.

[10] S. Srivastava*, et al.*, "Electrophoretically deposited reduced graphene oxide platform for food toxin detection," *Nanoscale,* vol. 5, pp. 3043-3051, 2013.

[11] M. E. Uddin*, et al.*, "Preparation and properties of reduced graphene oxide/polyacrylonitrile nanocomposites using polyvinyl phenol," *Composites Part B: Engineering,* vol. 80, pp. 238-245, 2015.

[12] D.-T. Phan and G.-S. Chung, "P–n junction characteristics of graphene oxide and reduced graphene oxide on n-type Si (111)," *Journal of Physics and Chemistry of Solids,* vol. 74, pp. 1509-1514, 2013.

[13] A. K. Das*, et al.*, "Iodide-mediated room temperature reduction of graphene oxide: a rapid chemical route for the synthesis of a bifunctional electrocatalyst," *Journal of Materials Chemistry A,* vol. 2, pp. 1332-1340, 2014.

[14] S. Gurunathan*, et al.*, "Oxidative stress-mediated antibacterial activity of graphene oxide and reduced graphene oxide in Pseudomonas aeruginosa," *International journal of nanomedicine,* vol. 7, p. 5901, 2012.

[15] K. Arora*, et al.*, "Effect of low pressure hydrogen environment on crystallographic properties of PdO nanoparticles," *International Journal of Hydrogen Energy,* vol. 41, pp. 22155-22161, 2016.

[16] M. Velasco-Soto*, et al.*, "Selective band gap manipulation of graphene oxide by its reduction with mild reagents," *carbon,* vol. 93, pp. 967-973, 2015.

[17] Y. Shen*, et al.*, "Evolution of the band-gap and optical properties of graphene oxide with controllable reduction level," *carbon,* vol. 62, pp. 157-164, 2013.

[18] Z. Cao*, et al.*, "The properties and applications of amperometric gas sensors," *Electroanalysis,* vol. 4, pp. 253-266, 1992.

[19] J. W. Fergus, "A review of electrolyte and electrode materials for high temperature electrochemical CO2 and SO2 gas sensors," *Sensors and Actuators B: Chemical,* vol. 134, pp. 1034-1041, 2008.

[20] J. Currie*, et al.*, "Micromachined thin film solid state electrochemical CO2, NO2 and SO2 gas sensors," *Sensors and Actuators B: Chemical,* vol. 59, pp. 235-241, 1999.

[21] V. Nikolova*, et al.*, "Tungsten carbide-based electrochemical sensors for hydrogen determination in gas mixtures," *Journal of applied electrochemistry,* vol. 30, pp. 705-710, 2000.

[22] K. Okamura*, et al.*, "Electrochemical gas sensor using a novel gas permeable electrode modified by ion implantation," *Surface and Coatings Technology,* vol. 201, pp. 8116-8119, 2007.

[23] Y. C. Liu*, et al.*, "Nafion Based Hydrogen Sensors: Pt/Nafion Electrodes Prepared by Takenata-Torikai Method and Modified with Polypyrrole," *Electroanalysis,* vol. 14, pp. 556-558, 2002.

[24] F. Opekar, "Detection of hydrogen in air with a detector containing a nafion membrane metallized on both sides," *Journal of electroanalytical chemistry and interfacial electrochemistry,* vol. 260, pp. 451-455, 1989.

[25] K. Arora and N. K. Puri, "Electrophoretically deposited nanostructured PdO thin film for room temperature amperometric H2 sensing," Vacuum, vol. 154, pp. 302-308, 2018.

CHAPTER 6

Chemiresistive sensing platform based on PdO-PANI/ITO heterostructure for room temperature hydrogen detection

Pristine PANI, 5 wt% and 10 wt% Palladium oxide (PdO)-polyaniline (PANI) nanocomposites are fabricated using one pot in-situ wet chemical oxidative polymerization method. Thin films of PANI and PdO-PANI nanocomposites are deposited on ITO glass substrate using spin coating process. The crystallographic properties, shape, size, bonding information, optical transitions of nanocomposites and surface morphology of their thin films are studied using x-ray diffraction (XRD) analysis, transmission electron microscopy (TEM), Fourier transform infrared (FTIR) transmission spectroscopy, ultraviolet-visible (UV-Vis) absorption spectroscopy and scanning electron microscopy (SEM). Sensing elements based on PANI/ITO and PdO-PANI/ITO heterostructure is used for chemiresistive sensing of (1, 3, 10 and 20) % concentration of H_2 gas at room temperature. The ohmic contacts are achieved using direct contact of Molybdenum (Mo) metallic electrodes with ITO layer, eliminating the requirement of expensive interdigitated electrodes (IDE). Sensitivity of heterostructure based sensing element demonstrates two fold increase in sensitivity compared to pristine PANI for all concentrations of H_2. The proposed chemiresisitve sensor shows high response with fast response characteristics in contrast with other similar sensors reported in literature.

The work presented in this chapter is published as:

"Chemiresistive sensing platform based on PdO-PANI/ITO heterostructure for room temperature hydrogen detection."

Materials Chemistry and Physics (2020), 247, 122850.

6.1 Introduction

Amperometric sensors employing proton conducting liquid electrolyte enable safe detection of high concentrations of H_2 gas at room temperature; but leakage, drying and contamination of electrolyte along with slow response characteristics restrict the sensing performance for long period of time. However, solid state chemiresistive sensor demonstrates long term stability with fast response time compared to amperometric sensor. As described in chapter 1, metal oxides are most favourable among other materials for sensing of H_2 gas; but it requires high temperature for its operation, which is not suitable for H_2 as it highly flammable in nature.

Chemical sensors based on polymers have high potential of single molecule sensitivity at room temperature which can be attributed due to the fact that these sensors have high surface to volume ratio, compact architecture, low weight, less power consumption, faster response and the ability to be integrated within the existing electronic system comparatively [1].

However, in general pure polymers have low conductivity and hence cannot be directly used as active material in sensor system, but their conductivity can be enhanced significantly by doping with catalytic materials. Additionally, charging the back-bone of polymers after removing their electronic carriers either by chemical or electrochemical oxidation process also contributes in increasing the conductivity of polymers. Nevertheless, a new class of materials known as conducting polymers has paved the path for polymers to be used in electronic, electromagnetic, energy storage and sensing applications. These conducting polymers have chemical structure similar to the polymers with their electrical properties matching with that of metal; hence they can also be termed as organic conducting polymer materials [2].

Polypyrrole was the first among the conducting polymer family to be used in gas sensing applications, but it exhibited poor sensing characteristics and incomplete reversibility of sensor response [1]. However, Polyaniline (PANI) showed unique promising properties which can be exploited as sensing material, the level of doping in PANI can be manipulated through acid/base, doping/dedoping process. These characteristics of PANI allow it to be present in various oxidation states. The level of reduction in PANI nitrogen chain categorizes it in three form i.e. fully reduced or leucoemeraldine form, partially reduced or emeraldine form and completely oxidized or pernigraniline form (figure 6.1). The most applicable form of PANI is its emeraldine salt form which consist of both amine (-NH-), imine (-N=) nitrogen and polarons for effective charge transport equally in its polymer chain [2].

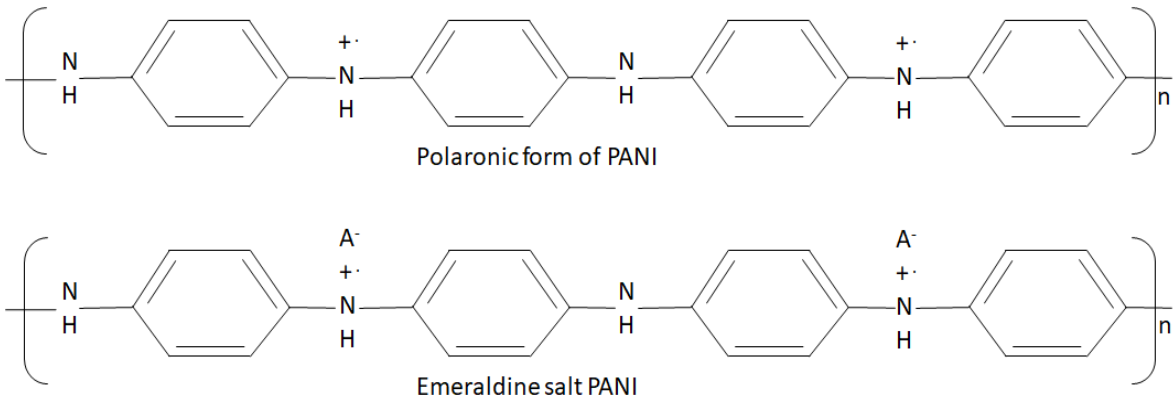

Figure 6.1. Polaronic and emeraldine salt form of PANI

Various studies demonstrate that composites of PANI with other materials including wide band gap metal oxides and hydrogen-philic palladium (Pd) and platinum (Pt) show enhanced sensing response and characteristics of chemiresistive H_2 sensors in contrast to pristine PANI (table 3).

Heterostructure of PANI with PdO has not been studied before for chemiresistive sensing of H_2 gas. Hence, 5 wt% and 10 wt% PdO-PANI nanocomposites deposited over indium tin

oxide (ITO) layered glass substrate, forming PdO-PANI/ITO heterojunction are used as sensing platform for sensing 1, 3, 10 and 20 % concentration of H_2 gas at room temperature. Direct contact assembly of proposed sensor eliminates the need for expensive IDE based probe system.

6.2 Experimental work

6.2.1 Synthesis of pristine PANI and PdO-PANI nanocomposite

Oxidative polymerization and in-situ wet chemical oxidative polymerization process have been used for the synthesis of emeraldine salt (ES) form of PANI and its composite with PdO. Solutions of aniline and oxidizing agent ammonium peroxide sulfate (APS) are dissolved in 1 M hydrochloric acid (HCl) solution with 0.1 molar concentration simultaneously with similar solution of dispersed PdO nanoparticles having 5 wt% and 10 wt% of aniline in 1 M HCl by continuous stirring for 2 hours and ultrasonication treatment for 1 hour respectively. Thereafter, aniline and PdO solution is added dropwise with APS solution through continuous stirring for 2 hours by maintaining 0-5 ^{0}C temperature until dark green colored solution is obtained. The resultant solution is kept overnight to complete the leftover reaction and settle the precipitate of samples. Finally, the precipitate is filtered, washed with 1 M HCl solution and D.I. water respectively to bring its pH value to 7, followed by its drying at 60 ^{0}C for 24 hours to obtain powder of PANI (ES), 5 wt% and 10 wt% PdO-PANI (ES).

6.2.2 Fabrication of sensing element

Emeraldine form of PANI is found to be insoluble in most organic solvents such as ethanol, methanol, propanol and chloroform. Thus, PANI is transformed into emeraldine base (EB)

form by dissolving it in 0.1 M ammonia solution by continuous mixing for 6 hours. The obtained dark blue precipitate is then filtered and washed with 1 M HCl and D.I. water adjacent with drying at 60 ^{0}C for 24 hours. The resultant (EB) powder is protonated with 10-camphor sulphonic acid (CSA) to obtain protonated PANI (EB), 5 wt% and 10 wt% PdO-PANI (EB), denoted as pristine PANI and PdO-PANI nancomposites respectively in this chapter [3].

Thin films of pristine PANI, 5 wt% and 10 wt% PdO-PANI nanocomposites are deposited over (10 mm x 10 mm) ITO substrate using spin coating process through following process. Uniform solution (0.3 g/30 ml) of Pristine PANI and its nanocomposites with PdO in chloroform are obtained by continuous stirring for 4 days. The resultant solution is distributed on substrate while covering its 10 mm^2 surface area by spinning it at a speed of 2000 rpm for 20 seconds respectively. PANI/ITO, 5 wt% and 10 wt% PdO-PANI/ITO heterostructures are employed as sensing element in proposed chemiresistive sensing setup. Direct contacts are obtained by placing the metallic probes on bare ITO surface of fabricated sensing element (figure 6.3).

6.2.3 Characterization procedure

The crystallinity of pristine PANI and PdO-PANI nanocomposite has been studied using PANalytical X'pert PRO x-ray diffractometer. Perkin Elmer FTIR spectrometer is used to observe the type of bonds and their inter-bond interactions. The electronic transition corresponding to ultraviolet-visible (UV-Vis) spectrum is analyzed using Perkin Elmer UV-Visible (UV-Vis) spectrometer. The morphology including uniformity and shape of nanocomposite structure on thin film surface is observed using Zeiss EVO 40 scanning electron microscope.

6.2.4 Gas sensing setup, device schematic and configuration

The indigenously constructed chemiresisitve gas sensing setup is made up of stainless steel (SS) vacuum chamber which is connected to oil based rotary vacuum pump that can help achieve a vacuum pressure of 10^{-2} Torr. The chamber is also attached with one ALICAT mass flow controller (MFC) for maintaining flow rate of H_2 gas mixture and a seven star MFC to maintain flow rate of dry air throughout the observation duration. The components of SS chamber consist of flexibly adjustable spring pressure contact probe system, two Cu cylindrical easily bendable pipes and 10 cm copper (Cu) circular disk substrate holder; The sensing element placed on substrate holder can be heated till temperature of 400 ^{0}C using heating element made up of Tungsten (W) rod connected by programmable microcontroller (figure 6.2).

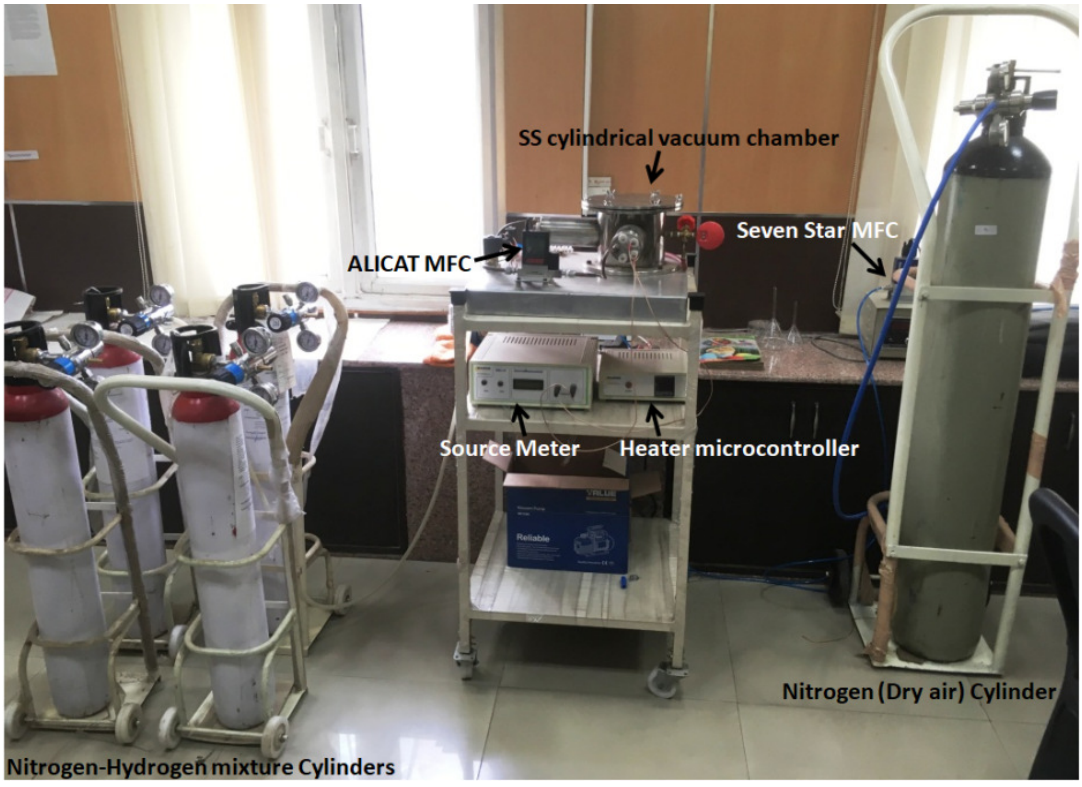

Figure 6.2. Resistance based gas sensing setup

The two metallic probes are constructed from 2 cm long, 1µm thin pins of Molybdenum (Mo) that are attached to the source meter for applying effective constant

current. The contacts are obtained by placing Mo pins in direct contact with bare ITO of heterojunction sensing element (figure 6.3). The sensing response is recorded in terms of rate of resistance change, current and voltage with gas flow time by a software self-coded using LabVIEW.

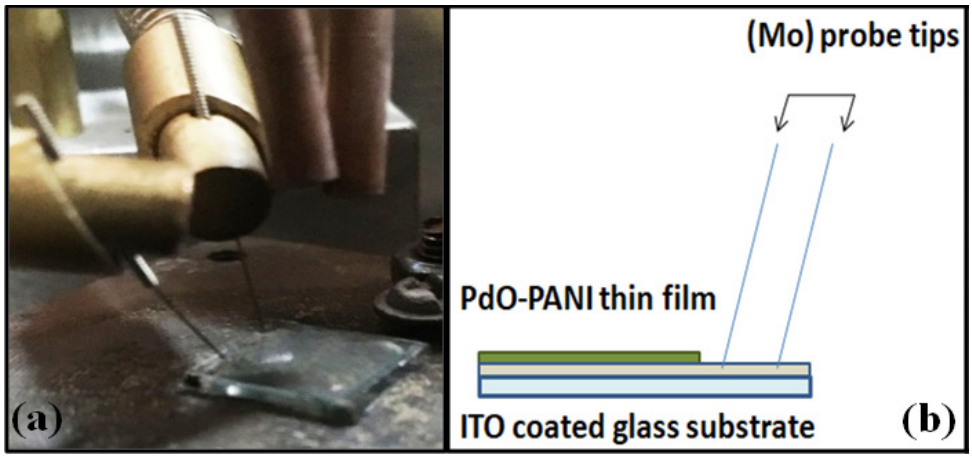

Figure 6.3. Probes contact (a) Front view, (b) Side view schematic

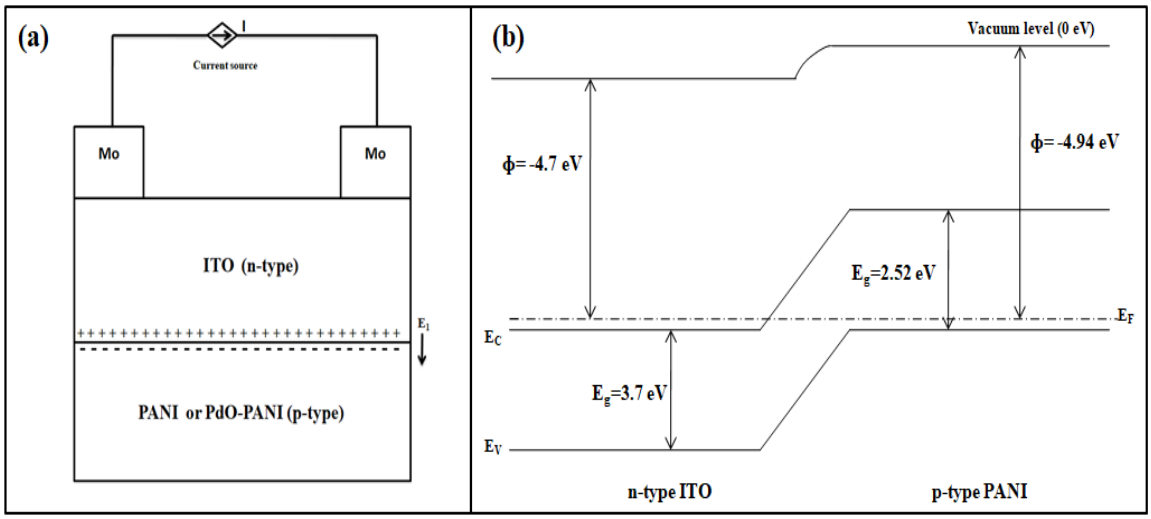

Figure 6.4. (a) Device schematic and (b) Band diagram of CSA doped PANI/ITO heterojunction

Figure 6.4.(a) displays the schematic of sensing device consisting of assembly of Mo contacts on bare n-type ITO interfaced with p-type PANI or PdO-PANI nancomposites yielding PANI/ITO and PdO-PANI/ITO heterojunction. CSA doped PANI has a work function (Φ) of

4.941±0.035 eV with band gap (E_g) of 2.52 eV [4]; Φ and E_g of ITO is found to be 4.7 eV and 3.7 eV respectively. The electronic band gap diagram shows heterojunction between p-type PANI or PdO-PANI and ITO that leads to shifting of Fermi level and construction of potential or schottky barrier at the junction as $\Phi_{PANI/PdO\text{-}PANI} > \Phi_{ITO}$ [figure 6.4.(b)] [5]. However, the interface between Mo and n-type ITO results in ohmic contact between them as Φ_{Mo} is 4.5 eV and $\Phi_{ITO} > \Phi_{Mo}$.

6.3 Results and Discussions

6.3.1 X-ray Diffraction (XRD) study

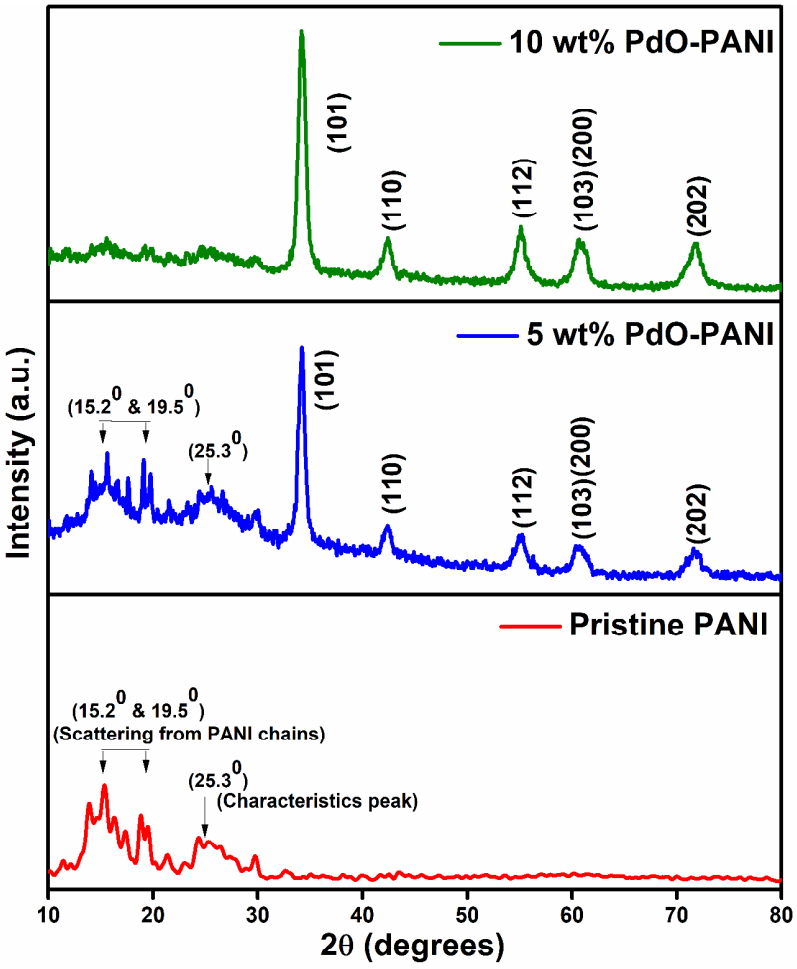

Figure 6.5. X-ray diffraction plot

Figure 6.5 represents the XRD plot of pristine PANI, 5 wt%, and 10 wt% PdO-PANI composites. XRD graph of CSA protonated PANI (EB) or prisitine PANI contains characteristics broad peaks at 15.2^0, 19.5^0 and 25.3^0 which belongs to (110) and (003) planes respectively on comparison with published data (JCPDS no. 531717). Scattering within interplanar spacing of PANI conjugated chains results in intensity peaks at 15.2^0 and 19.5^0, whereas periodicity characteristics of PANI results in low intensity peak at 25.3^0.

XRD graph of 5 wt% and 10 wt% PdO-PANI nanocomposite contains diffraction peaks of both pristine PANI as well as PdO showing successful fabrication of heterostructure. The intense peaks observed in XRD plot of composites at 42.2^0, 55.1^0, 60^0, 61^0 and 72^0 correspond to (101), (110), (112), (103), (200) and (202) planes of tetragonal crystal structure of PdO respectively. The intensity of peaks of pristine PANI decrease and eventually diminish as the percentage concentration of PdO increases from 5 wt% to 10 wt%, this is due to interaction of PdO nanoparticles with polarons present in polymer structure which inhibits the growth of PANI chains and restrict its crystalline behaviour [6] [7]. On the other hand, the intensity of t-PdO peaks increase, which shows that crystallinity of PdO remains unperturbed by PANI conjugates chain structure [3]. Debye Scherrer equation is used to calculate the average crystallite size of t-PdO and it is found to be 6.702 nm [equation 3.4] (refer section 3.3.1)

6.3.2 Transmission electron microscopy (TEM)

TEM image of pristine PANI displays transparent sheet like structure with the presence of dark thin lines which attributes to formation of nanofibers matrix [figure 6.6.(a)], whereas TEM image of 10 wt% PdO-PANI nanocomposite shows the presence of black dots embedded within the transparent sheet matrix suggesting successful fabrication of nanocomposites [figure 6.6.(b)]. [3, 8-9].

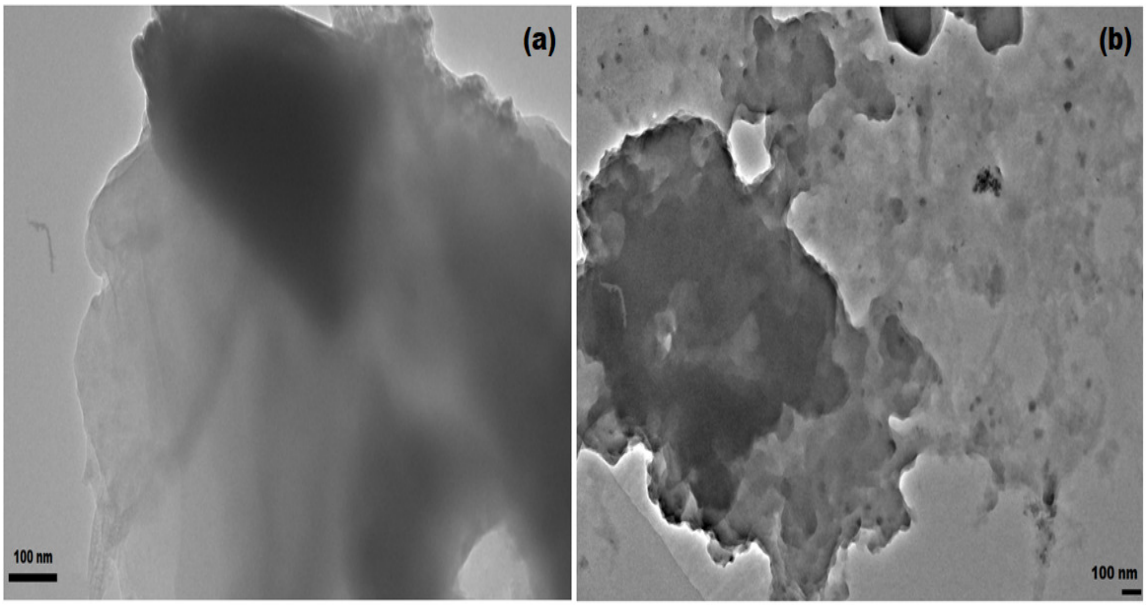

Figure 6.6. TEM image of (a) Pristine PANI, (b) 10 wt% PdO-PANI nanocomposite

6.3.3 Ultraviolet-visible (UV-Vis) absorption Spectroscopy

Figure 6.7 reprsents the UV-Vis absorption spectra of pristine PANI, 5 wt% PdO-PANI and 10 wt% PdO-PANI nanocomposites which are uniformly dispersed in solution of chloroform. π-π^* bond interactions, polaron-π^* and π-polaron transitions results in presence of absorption peaks at 348 nm, 430 nm and 769 nm in pristine PANI spectra correspondingly which reflects its good conductivity [10]. It is observed that intensity of obtained peaks decrease significantly along with shifting towards higher wavelength as the percentage concentration of PdO nanoparticles increase from 5 wt% to 10 wt%; it is because of change in polaron density within PANI chains due to interaction of PdO nanoparticles with PANI aromatic structure [6].

6.3.4 Fourier transform infrared (FT-IR) transmission spectroscopy

Figure 6.8 depicts the FTIR transmission spectra of pristine PANI, 5 wt% and 10 wt% PdO-PANI nanocomposites. The transmission peaks observed in spectrum of pristine PANI at 1049 cm^{-1}, 1173 cm^{-1} , 1003 cm^{-1}, 1384 cm^{-1}, 1635 cm^{-1},1738 cm^{-1}, 2885 cm^{-1} and 2960 cm^{-1}

belongs to quinoid unit of pristine PANI, in-plane bending vibrations of C-H resulting from protonation of PANI (EB), C-C bond of benzene ring, C=C bonds of benzenoid ring, C-N imine stretching vibrations, NH_2^+ and N-H bond of aromatic amines respectively [11].

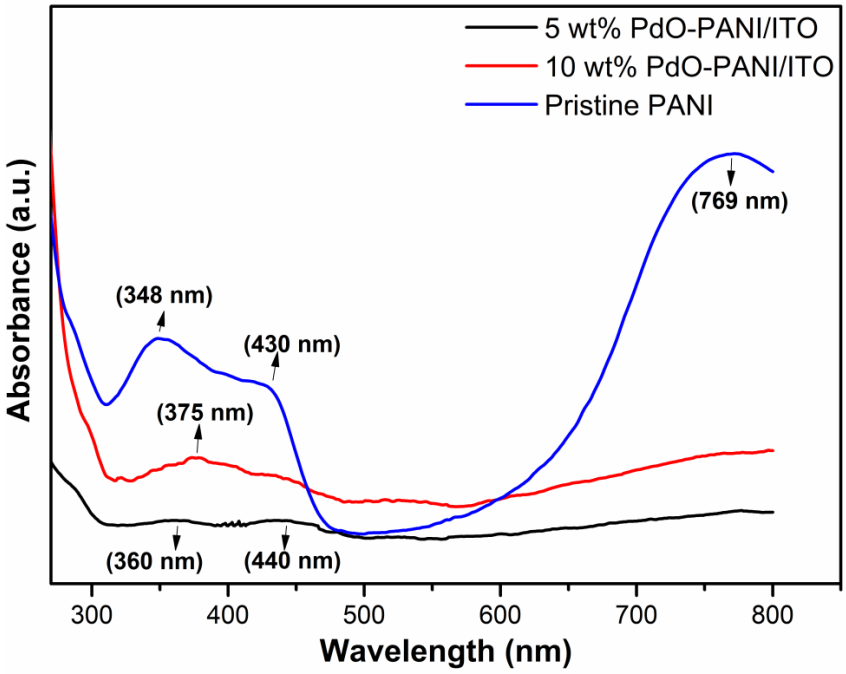

Figure 6.7. UV-Vis absorption spectra

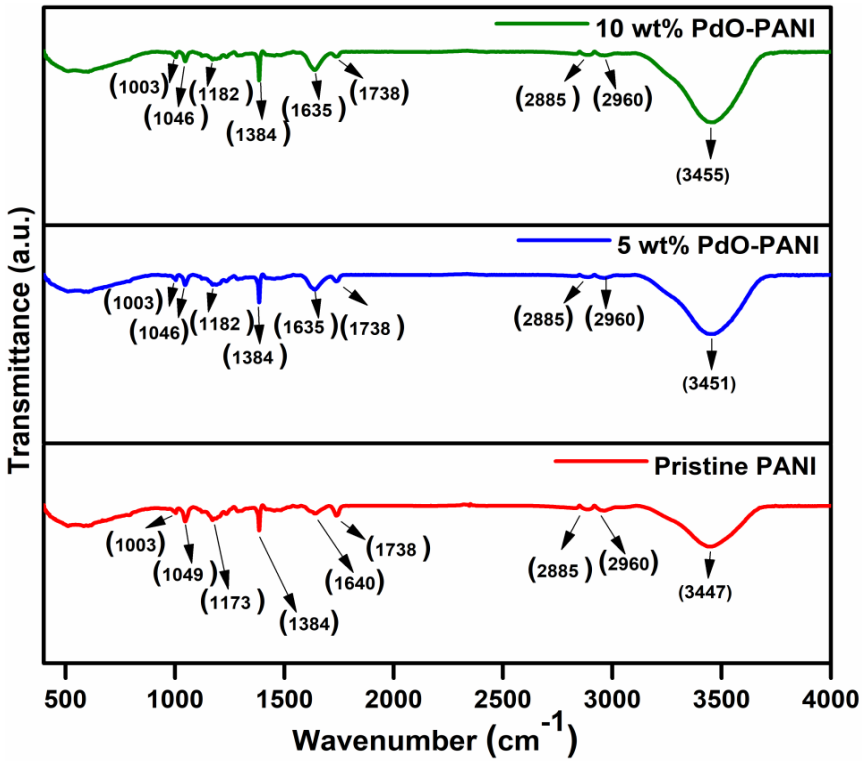

Figure 6.8. FT-IR transmission spectra

Formation of heterostructure with PdO does not yield any new transmission peaks in FTIR spectra of nanocomposites, but significant increase in intensity together with shifting of transmission peaks is found as the percentage concentration of PdO nanoparticles increase from 5 wt% to 10 wt% in PdO-PANI nanocomposites. These changes in FTIR spectra of nanocomposites is due to uniform distribution of PdO nanoparticles in PANI aromatic structure [12].

6.3.5 Scanning electron microscopy (SEM)

Figure 6.9 represents the SEM images showing thin film surface of pristine PANI/ITO, 5 wt% PdO-PANI/ITO and 10 wt% PdO-PANI/ITO respectively. Non-uniform shape and size nano-flakes like structure are homogeneously distributed on the surface of pristine PANI thin film [figure 6.9.(a)]. The size of flakes decrease as the percentage concentration of PdO increases from 5 wt% to 10 wt% due to aggregation of PdO nanoparticles within PANI matrix resulting in improved capacitance of thin film [figure 6.9.(b) and (c)] [12].

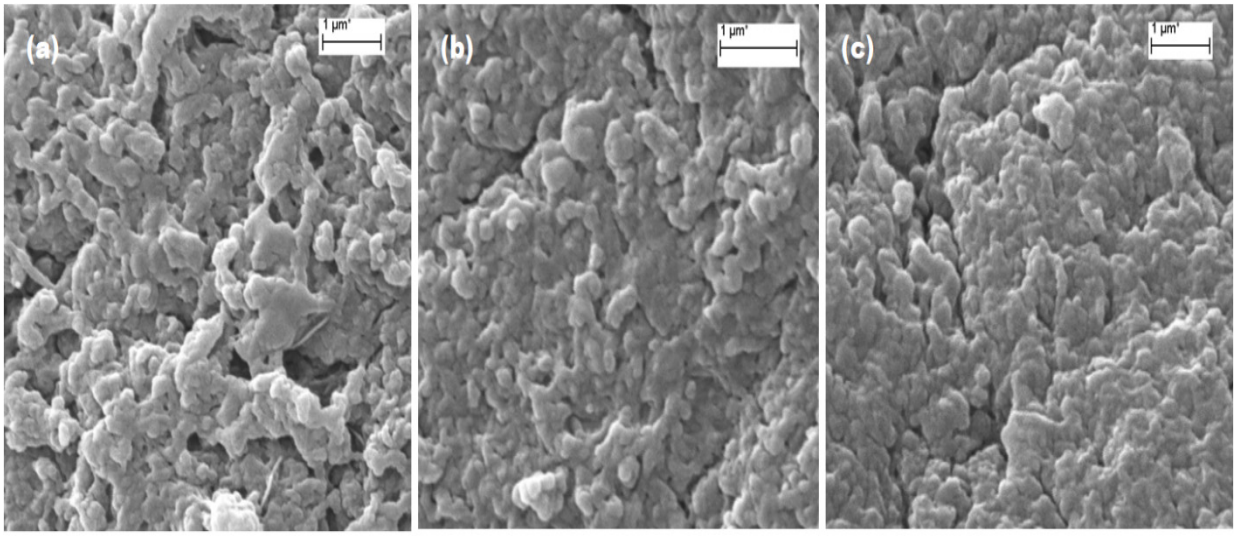

Figure 6.9. SEM images of thin film (a) Pristine PANI, (b) 5 wt% PdO-PANI and (c) 10 wt% PdO-PANI

There is presence of lumps and holes on surface of thin film which act as surface defects and will help in adsorption of H_2. However, the concentration of surface defects decrease with

increasing concentration of PdO in nanocomposite because of stacking of nanoflakes with nanoparticles on the surface of thin films. Also, increasing concentration of PdO in nanocomposite yields network of rod-like structures on thin films surface which enhances the surface area and porosity of thin films. Hence, sensing element based on PdO-PANI nanocomposites thin film will be more favourable for H_2 sensing application [3].

6.3.6 Chemiresistive H_2 gas sensing study

Various percentages (1, 3, 10 and 20 %) concentration of H_2 gas mixture in dry air is introduced in the sensing chamber of gas sensing setup (figure 6.2) at flow rate of 200 (standard cubic centimeter per minute) sccm for a observation time of 20 seconds. The response of PANI/ITO, 5 wt% and 10 wt% PdO-PANI/ITO heterojunction towards H_2 gas is recorded in graphical form as change in resistance (ΔR) (Ohms) with time (t) (seconds) at a temperature of 28 ^{0}C [figure 6.10.(a), (b) and (c)].. The sensitivity (S) of proposed chemiresistive sensor is evaluated using equations 6.1 and 6.2 respectively

$$\Delta R = R_g - R_a \qquad \textbf{[Equation 6.1]}$$

$$S = \frac{\Delta R}{R_a} \qquad \textbf{[Equation 6.2]}$$

Where, R_g, R_a are the values of sensing element resistance in presence of H_2 gas and dry air respectively.

6.3.7 Sensing response

The sensing response of PANI/ITO, 5 wt% and 10 wt% PdO-PANI/ITO for 1%, 3%, 10% and 20% H_2 concentration at room temperature is presented in figure 6.11.(a), (b), (c) and (d)

respectively. It is observed that resistance of all sensing elements attain a constant base resistance (R_a) value in presence of dry air. On introduction of H_2 gas in the sensing chamber, the value of resistance rises swiftly and reaches a maximum value (R_g) after which it gets

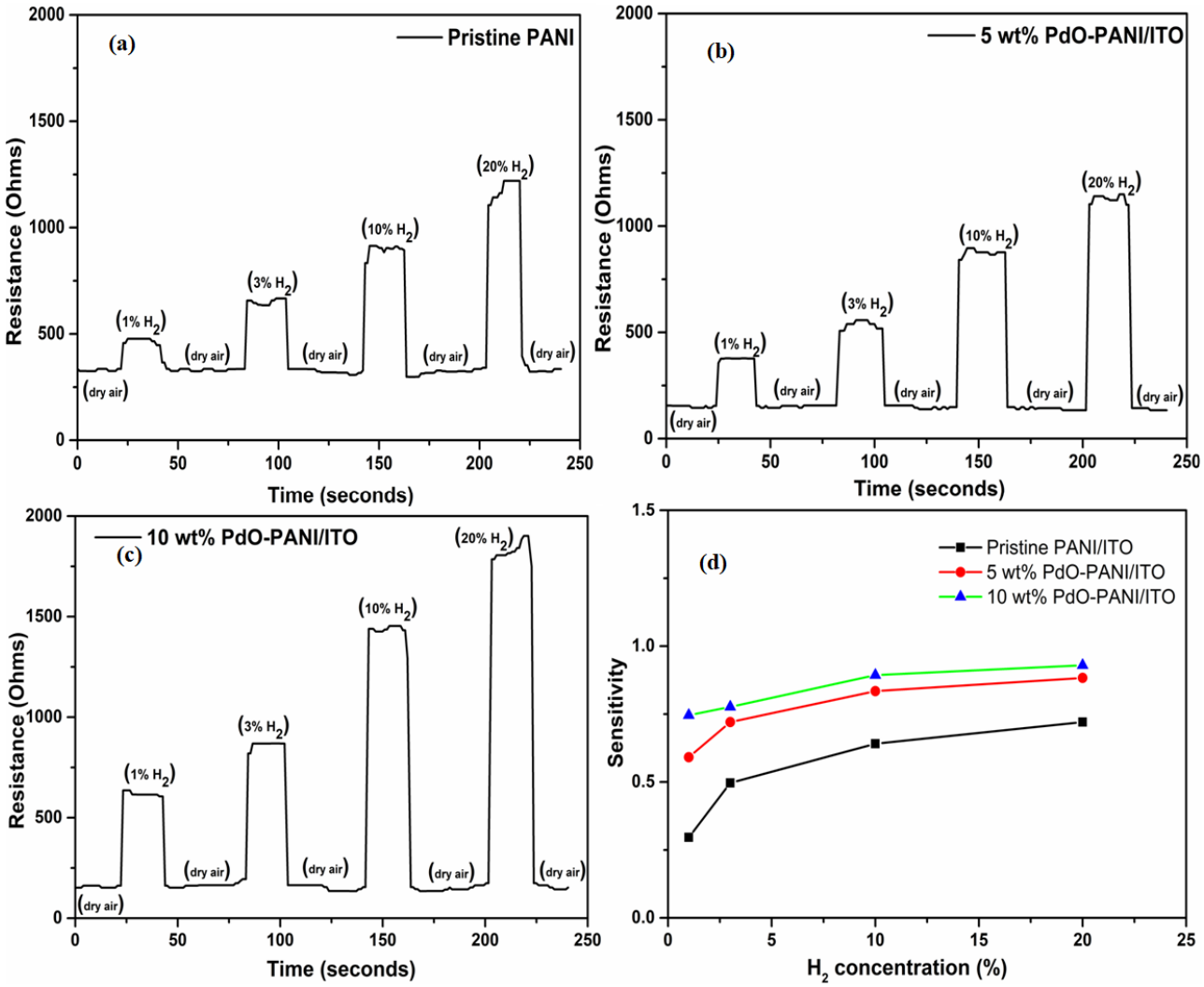

Figure 6.10. Sensing response (a) Pristine PANI/ITO, (b) 5 wt% PdO-PANI/ITO, (c) 10 wt% PdO-PANI/ITO and (d) Sensitivity comparison plot

constant for entire duration of gas flow. The value of R_g falls back to R_a as soon as H_2 gas is withdrawn from the chamber, displaying pulsed sensing characteristics of heterostructure sensing elements. There is a comprehensive increase in value of R_g with increasing concentration of H_2 gas. Also, the value of R_a decrease considerably for PdO-PANI/ITO heterostructure as compared to pristine PANI/ITO. The reduction in value of base resistance

is because of increasing conductivity of p-type nanocomposite due to rise in concentration of charge carriers with corresponding decay in schottky barrier at the heterojunction. Due to very small barrier height and saturation of heterojunction with charge carriers, no further decrease in value of R_a is observed on increasing the percentage concentration of PdO from 5 wt% to 10 wt% in nanocomposites [13].

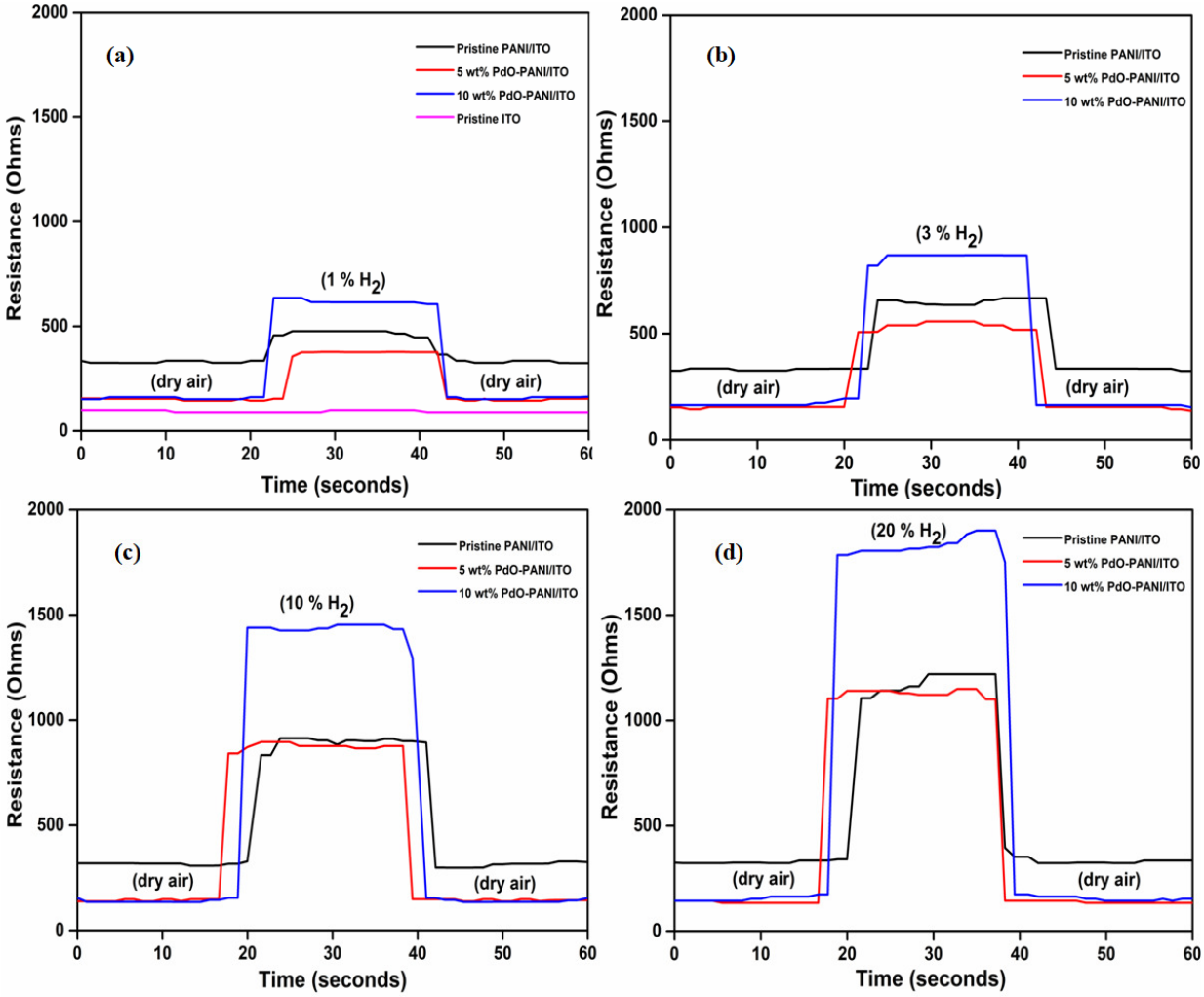

Figure 6.11. Sensing response comparison of Pristine PANI/ITO, 5 wt% and 10 wt% PdO-PANI/ITO towards (a) 1% H_2, (b) 3% H_2, (c) 10% H_2 and (d) 20% H_2

The increase in ΔR value is insignificant for 5 wt% PdO-PANI/ITO as compared to PANI/ITO, but there is a large increase in its value for 10 wt% PdO-PANI/ITO sensing element [figure 6.11]. There is a comprehensive rise in charge carrier depletion, space charge region separation and schottky barrier height at the heterojunction, which contributes in

combination for high sensing response of 10 wt% PdO-PANI nanocomposite based sensing element.

Figure 6.10.(d) shows the sensitivity comparison plot of PANI/ITO, 5 wt% and 10 wt% PdO-PANI/ITO for 1, 3, 10 and 20 % H_2 concentration respectively. It is observed that the sensitivity of fabricated sensing elements show increase in sensitivity with concentration of H_2 gas. However, this increase is considerably large in nanocomposites based sensing element compared to pristine PANI. It is attributed to rise in concentration of electrons reaching the heterojunction from the p-side of heterostructure, which results in rise of schottky barrier.

Nonetheless, the comprehensive increase in sensitivity is not observed with increasing concentration of PdO nanoparticles in PdO-PANI nanocomposites due to significant decrease in polaron density which helps in transport of incoming electrons towards heterojunction [3]. The significant increase in sensitivity of 5 wt% PdO-PANI compared to pristine PANI for similar H_2 concentrations is because of electronic and chemical sensitization of PANI by PdO, which lead to increases in density of H^+ ions and electrons on surface of p-type nanocomposite yielding wider potential barrier. But the similar increasing pattern of sensitivity is not observed for 10 wt% PdO-PANI due to saturation of PANI matrix by reduction in concentration of available amine units and hence decrease in polar density.

6.3.8 Sensing mechanism

The mechanism of sensing is combined effect of charge carrier separation and depletion, chemical sensitization of PANI matrix by PdO nanoparticles, protonation of amine-imine sites of PANI conjugated structure, formation of schottky barrier at heterojunction and Fermi level mediated charge transfer.

There is a dissociation of H_2 gas into H^+ ions on interaction with polarons of emeraldine form of PANI. This process is followed by release of two electrons, partial protonation of imine (-N=) units and substitution on semiquinone amine nitrogen ($-NH^+-$) sites, which results in new N-H bonds on PANI conjugated structure. Thereafter, protonated PANI reverts back to its emeraldine form through transfer of charges followed by ejection of H^+ ions [14].

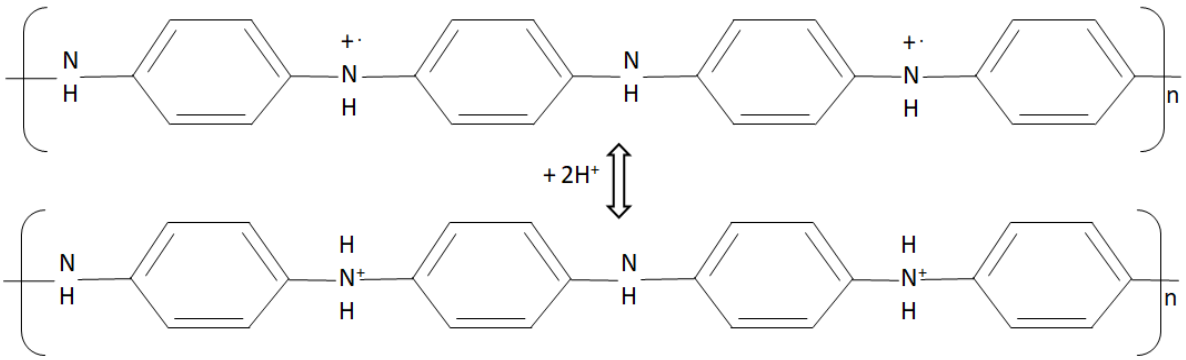

Figure 6.12. Hydrogenation of polaronic form

The rate of H_2 dissociation into H^+ ions is enhanced in the presence of PdO nanoparticles which reduce to Pd in presence of H_2 gas molecules. The diffusion of H^+ ions in octahedral interstitial sites of face centred cubic (fcc) Pd crystal results in formation of palladium hydride (PdH_x), which act as scattering center for incoming electrons on surface of nanocomposites, reducing their mobility [15-16]. Also, the concentration of physisorbed H^+ ions increases within PANI matrix by process of spillover effect in presence of PdO nanoparticles. The increase in electron concentration diffusing through p-side of heterostructure with increasing H_2 concentration, results in enhanced schottky barrier width at nanocomposite/ITO heterojunction (figure 6.3), thereby increasing the resistance of sensing element. Moreover, interaction of H^+ ions with semiquinone amine ($-NH^+-$) present in PANI chain results in increasing concentration of protonated amine ($-NH_2^+-$) which offers intrachain barrier towards conduction of electrons from surface of nanocomposite towards heterojunction (figure 6.12) [17].

Room temperature chemiresistive sensing of H_2 gas using proposed heterostructure displays high sensing response with quick response characteristics of 3-4 seconds in comparison to other similar reported sensors (table 6.1). Nevertheless, no change in response and recovery time of proposed sensor is observed on using either pristine PANI or PdO-PANI based sensing element.

S.No.	Sensing element	H_2 concentration	Response	Response time (seconds)	Recovery time (seconds)	Reference
1.	**PdO-PANI/ITO**	**1 %**	**1.75**	**3**	**4**	**Present work**
2.	Ag-SnO_2/PANI	500 ppm	1.9	16	24	[18]
3.	Pd-rGO doped PANI	1 %	1.25	20	50	[15]
4.	SnO_2/PANI	1000 ppm	1.5	3	4	[19]
5.	PANI/anatase TiO_2	0.8 %	1.63	83	130	[11]
6.	PANI/rutile TiO_2	0.8 %	1.54	152	170	[20]
7.	TiO_2:SnO_2/PANI	0.8 %	1.25	75	117	[6]

Table 6.1. Solid state H_2 sensors based on various PANI nanocomposites

6.4 Conclusions

Economical and facile oxidative polymerization and in-situ wet chemical polymerization method is used to synthesize pristine PANI, 5 wt%, and 10 wt% PdO-PANI nanocomposites. X-ray diffraction (XRD) analysis, transmission electron microscopy (TEM), ultraviolet-visible (UV-Vis) absorption spectroscopy and Fourier transform infrared (FTIR) transmission spectroscopy shows successful synthesis of PdO-PANI nanocomposites containing 2-9 nm

size PdO nanoparticles with tetragonal crystal structure uniformly distributed within emeraldine PANI matrix. Spin coating method is used to deposit thin films of synthesized sample on ITO coated glass substrate resulting in formation of PANI/ITO and PdO-PANI/ITO heterostructure. Pristine PANI/ITO, 5 wt% and 10 wt% PdO-PANI/ITO are used as sensing element for chemiresistive sensing of 1, 3, 10 and 20 % H_2 gas concentration in presence of dry air at room temperature. The contacts are established directly with ITO surface without using expensive interdigitated electodes. Two folds increase in sensitivity is observed for PdO-PANI nanocomposites based sensing element in contrast to pristine PANI. Additionally, there is a considerable increase in sensitivity with the increasing percentage concentration of H_2 gas. The maximum sensing response is achieved for 10 wt% PdO-PANI/ITO based sensor as compared to 5 wt% PdO-PANI/ITO heterostructure. The proposed chemiresistive sensor demonstrates high sensing response with fast response and recovery time of 3 and 4 seconds respectively on comparison with other similar sensors published in literature.

6.5 References

[1] D. Nicolas-Debarnot and F. Poncin-Epaillard, "Polyaniline as a new sensitive layer for gas sensors," *Analytica chimica acta,* vol. 475, pp. 1-15, 2003.

[2] A. Sadek*, et al.*, "A room temperature polyaniline nanofiber hydrogen gas sensor," in *SENSORS, 2005 IEEE*, 2005, p. 4 pp.

[3] S. Srivastava*, et al.*, "Synthesis and characterization of TiO2 doped polyaniline composites for hydrogen gas sensing," *International Journal of Hydrogen Energy,* vol. 36, pp. 6343-6355, 2011.

[4] J. D. Fowler*, et al.*, "Hydrogen detection by polyaniline nanofibers on gold and platinum electrodes," *The Journal of Physical Chemistry C,* vol. 113, pp. 6444-6449, 2009.

[5] A. Bera*, et al.*, "Flexible diode of polyaniline/ITO heterojunction on PET substrate," *Applied Surface Science,* vol. 418, pp. 264-269, 2017.

[6] S. Nasirian and H. M. Moghaddam, "Polyaniline assisted by TiO2: SnO2 nanoparticles as a hydrogen gas sensor at environmental conditions," *Applied Surface Science,* vol. 328, pp. 395-404, 2015.

[7] S. Kotresh*, et al.*, "Polyaniline-Titanium dioxide composite as humidity sensor at room temperature," *Наносистемы: физика, химия, математика,* vol. 7, 2016.

[8] R. Li*, et al.*, "Carbon-Based Polyaniline Nanocomposites for Supercapacitors," in *Carbon-Based Polymer Nanocomposites for Environmental and Energy Applications*, ed: Elsevier, 2018, pp. 489-535.

[9] T. Sen*, et al.*, "Synthesis and sensing applications of polyaniline nanocomposites: a review," *RSC advances,* vol. 6, pp. 42196-42222, 2016.

[10] C.-L. Zhu*, et al.*, "Synthesis of core/shell metal oxide/polyaniline nanocomposites and hollow polyaniline capsules," *Nanotechnology,* vol. 18, p. 275604, 2007.

[11] S. Nasirian and H. M. Moghaddam, "Hydrogen gas sensing based on polyaniline/anatase titania nanocomposite," *International Journal of Hydrogen Energy,* vol. 39, pp. 630-642, 2014.

[12] A. Mostafaei and A. Zolriasatein, "Synthesis and characterization of conducting polyaniline nanocomposites containing ZnO nanorods," *Progress in Natural Science: Materials International,* vol. 22, pp. 273-280, 2012.

[13] B. G. Streetman and S. Banerjee, *Solid state electronic devices*: Prentice-Hall of India, 2001.

[14] I. Fratoddi*, et al.*, "Chemiresistive polyaniline-based gas sensors: A mini review," *Sensors and Actuators B: Chemical,* vol. 220, pp. 534-548, 2015.

[15] Y. Zou*, et al.*, "Doping composite of polyaniline and reduced graphene oxide with palladium nanoparticles for room-temperature hydrogen-gas sensing," *International Journal of Hydrogen Energy,* vol. 41, pp. 5396-5404, 2016.

[16] Y. T. Lee*, et al.*, "Hydrogen gas sensing properties of PdO thin films with nano-sized cracks," *Nanotechnology,* vol. 21, p. 165503, 2010.

[17] A. Ray*, et al.*, "Polyaniline: protonation/deprotonation of amine and imine sites," *Synthetic Metals,* vol. 29, pp. 151-156, 1989.

[18] S. B. Kondawar*, et al.*, "Ag-SnO2/Polyaniline composite nanofibers for low operating temperature hydrogen gas sensor," *Journal of Materials NanoScience,* vol. 4, pp. 13-18, 2017.

[19] H. J. Sharma*, et al.*, "Electrospun SnO 2/polyaniline composite nanofibers based low temperature hydrogen gas sensor," *Fibers and Polymers,* vol. 16, pp. 1527-1532, 2015.

[20] H. M. Moghaddam and S. Nasirian, "Hydrogen gas sensing feature of polyaniline/titania (rutile) nanocomposite at environmental conditions," *Applied Surface Science,* vol. 317, pp. 117-124, 2014.

CHAPTER 7

Outline and Future scope of work

7.1 Summary of research work

Chapter 1 describes various H_2 sensors available commercially and describe their working mechanism along with their characteristics. Out of all H_2 sensors, only electrochemical and chemiresistive based sensors are found to be stable, economical and integrable within existing silicon electronics. Various type of materials are used to fabricate the sensing element for H_2 gas sensing application; however, metal and metal oxide (MOX) semiconductor are the only class of materials which contains all the essential physicochemical and electronic properties of a good sensing material. It has been observed that structure of pristine metals get damaged from absorption of H_2, due to hydrogen embrittlement and are easily poisoned by environmental impurities such as sulphur, arsenic etc. compounds. Although, MOX semiconductor are less volatile and more stable in nature, but the sensing element constructed from MOX have high operation temperature which makes them unsuitable for room temperature (RT) sensing application. Moreover, Chapter 1 explains about different processes which include nanostructuring of bulk material, heterostructuring with catalytically active material and Plasmon driven catalysis for H_2 desorption, to minimize the operating temperature of MOX semiconductor based H_2 sensors. Extensive research on various MOX nanomaterials have been reported in literature, but only two research works studying palladium oxide (PdO) nanoparticles were reported at the onset of thesis research work till 2015. They demonstrated good sensing response of PdO nanoparticles towards H_2 gas at high temperature. Hence, this motivated us to study sensing response of nanostructures and heterostructures of PdO in presence of H_2 gas at RT.

Chapter 2 explores varied approaches for synthesis of MOX nanostructures and concluded that wet chemical synthesis methods based on bottom up approach are facile, economical and controllable synthesis procedures comparatively. All the wet chemical methods are explained extensively along with their corresponding traits and it is observed that sol-gel and hydrothermal synthesis procedures are most suitable for homogeneous formation of MOX nanomaterials. Thin film fabrication methods favourable for deposition of nanostructures synthesized using wet chemical procedure such as spin coating and electrophoretic deposition techniques are described in this chapter. The characterization instruments such as x-ray diffraction (XRD) measurement, transmission electron microscopy (TEM), Fourier transform infrared (FTIR) spectroscopy, ultraviolet-visible (UV-Vis) spectroscopy and scanning electron microscopy (SEM) have also been discussed broadly including their setup details, working and operation mechanism. These techniques are employed for observing crystal geometry, physical appearance, characteristics of molecular bond, optical band gap of synthesized MOX nanomaterials and their thin film surface morphology in the following chapters.

Chapter 3 discusses about the effect of hydrogen (H_2) on crystal and lattice structure of palladium oxide (PdO) p-type semiconductor at various low pressure (25, 50, 75 and 100) millibar (mbar) gas in the surroundings. The findings of this study are as follows:

- Target sample of PdO is successfully synthesized using wet chemical sol-gel synthesis method at annealing temperature of 800 ^{0}C
- X-ray diffraction (XRD) analysis and transmission electron microscopy (TEM) confirm the formation of tetragonal (t) PdO crystal structure with size 10-125 nm
- Scanning electron microscopy study shows uniform and homogeneous surface morphology of sample
- Pellet of t-PdO is used to conduct the H_2 in-situ XRD experimental investigation

- The study shows formation of face centered cubic (fcc) palladium hydride (PdH_x) within t-PdO crystal structure in presence of H_2 gas at 25 mbar pressure
- The intensity of peaks corresponding to PdH_x increases whereas that for t-PdO decreases as pressure rises from 25 to 50 mbar
- Complete transformation of crystal structure into fcc PdH_x as pressure reaches 75 mbar
- Plot between H_2 pressure and lattice parameters shows lattice expansion on further increase in pressure from 75 to 100 mbar
- The comprehensive lattice expansion indicates phase transition in transformed PdH_x crystal structure at 100 mbar
- Synthesized PdO nanoparticles shows similar behavior towards H_2 as Pd nanoparticles at room temperature (RT)
- Hence, synthesized PdO nanoparticles are suitable for H_2 sensing applications at RT

In **chapter 4**, amperometric sensing of H_2 gas is performed using PdO thin film based working electrode (WE) sensing element. Wide range concentrations (10 to 70%) percent of H_2 gas is introduced in indigenously developed electrochemical gas sensing setup and corresponding sensing response is recorded at room temperature. The work presented in this chapter can be summarized as follows:

- PdO nanoparticles are synthesized using economical solvothermal or hydrothermal synthesis technique
- XRD study and TEM analysis validates the formation of t-PdO crystal structure with particles size ranging from 30-80 nm
- Thin films of PdO nanoparticles are deposited on ITO coated glass substrates using electrophoretic deposition method at different deposition potential (10, 15, 20, 25, 30 and 35 V) respectively

- Scanning electron microscopy (SEM) shows PdO thin films deposited at 30 V have uniform and homogeneous geometry comparatively
- PdO thin film/ITO deposited at 30 V is used as WE for amperometric H_2 gas sensing
- Cyclic voltammetry (CV) study validates redox catalytic behavior of PdO thin film towards H^+ ions
- Sensor shows good sensitivity of 0.222 μA/% H_2 and steady state response of 60 seconds
- PdO/ITO WE deposited at 30 V shows maximum sensing response signal as compared to other deposited thin films
- Proposed amperometric H_2 sensor based on PdO/ITO WE shows good sensitivity and limit of detection (LOD) compared to other similar reported sensor

As explored in chapter 2, heterostructure nanomaterials demonstrate good physicochemical and electrical properties. Moreover, they show enhanced H_2 sensitivity at room temperature with good selectivity and stability as compared to pristine nanomaterials. Hence, thin film heterostructure of PdO nanoparticles with two dimensional (2D) reduced graphene oxide (rGO) nanosheets is employed as WE to enhance the amperometric sensitivity of indigeneously developed electrochemical sensing arrangement towards wide range concentration (10 to 80 %) of H_2 gas at room temperature. The observations of this research work are reported in **chapter 5** and can be summarized as follows:

- PdO-rGO nanocomposites are synthesized using improved Hummer's and sol-gel wet chemical method
- 30-35 nm size tetragonal (t) PdO nanoparticles are observed to be embedded within rGO nanosheets using XRD analysis and TEM observations
- Thin film of PdO-rGO nanocomposites are deposited on ITO coated glass substrates using electrophoretic deposition method at deposition potential of 40 V

- Amperometric H_2 sensing is performed using PdO-rGO nanocomposite thin film based WE
- CV study confirms the redox catalytic behavior of PdO-rGO nanocomposite thin film based WE towards H^+ ions
- Sensor shows enhanced sensitivity of 0.462 μA/% H_2 and steady state response of 60 seconds
- Two folds increase in sensitivity is observed for PdO-rGO/ITO WE as compared to PdO/ITO WE (discussed in chapter 4) towards amperometric H_2 detection
- PdO-rGO thin film WE shows good selectivity, stability and reproducibility towards H_2 gas amperometric sensing
- Proposed amperometric H_2 sensor based on PdO-rGO/ITO WE shows good sensitivity and LOD compared to other similar reported sensor

Chemiresistive solid state sensing requires high temperature for their operation and thus is not suitable for sensing of H_2 gas due to its high flammability. Conducting polymer such as polyaniline (PANI) has displayed good sensitivity toward H_2 gas at room temperature. Therefore, heterostructure consisting of PdO nanoparticles distributed within PANI conjugated chain structure can be synthesized to enhance the sensitivity towards H_2 gas compared to other reported pristine PANI based sensors. Hence, PdO-PANI heterostructure nanomaterial based solid state sensing element has been used for chemiresistive sensing of (1, 3, 10 and 20%) concentrations of H_2 gas at room temperature. The results of this work are presented in **chapter 6** and are also summarized below;

- Pristine PANI, 5 wt% and 10 wt% PdO-PANI nanocomposites are synthesized using wet chemical oxidative polymerization method
- XRD analysis and FTIR spectroscopy confirms the formation of PdO-PANI nanocomposite with uniform deposition of 2-9 nm size PdO particles in PANI matrix

- Thin films of pristine PANI and nanocomposites are deposited on ITO coated glass substrate forming PANI/ITO and PdO-PANI/ITO heterojunction respectively
- PANI/ITO, 5wt% and 10 wt% PdO-PANI/ITO are employed as sensing element with direct metallic contacts without using expensive interdigitated electrodes (IDE)
- Proposed chemiresisitve H_2 sensing device forms a schottky barrier at PANI/ITO and PdO-PANI/ITO (p-n) semiconductor heterojunction
- PdO-PANI/ITO based solid state sensing device demonstrates two folds increase in sensitivity for H_2 gas as compared to PANI/ITO
- Proposed sensing device assembly exhibits fast response time of 3 seconds and quick recovery time of 4 seconds
- Proposed chemiresistive sensor shows high sensitivity with fast response characteristics as compared to similar reported PANI nanocomposites based sensors

7.2 Future scope of work

PdO nanoparticles based sensing elements have been studied extensively in this thesis work for both electrochemical and chemiresistive sensing of H_2 gas at room temperature. Pristine PdO nanoparticles exhibit good H_2 sensitivity at room temperature, only when they are used as working electrodes in liquid electrolyte based amperometric sensing setup; but, the increase in magnitude of sensitivity is limited in nature. Additionally, pristine PdO nanoparticles do not exhibit room temperature sensitivity in solid state H_2 chemiresistive sensor as already reported in published research work by different research groups working in this area. It has been reported by various researchers that sensors based on one dimensional (1D) and two dimensional (2D) nanostructures of other MOX, demonstrate reversible room temperature sensing towards H_2 gas with fast response characteristics at room temperature. These nanostructures provide fast charge carriers transport and high surface to volume ratio

for adsorption of H_2 gas compared to their three dimensional (3D) counterparts. Hence, the following research work is currently under process and will be accomplished in future:

- The enhanced reversible sensing response along with fast response characteristics will be achieved by employing 1D, 2D nanostructures of pristine PdO as sensing element in amperometric and chemiresisitve H_2 sensors at room temperature.
- Heterostructure of 1D, 2D nanostructures of PdO with catalytically active metals such as platinum (Pt), copper (Cu) and gold (Au) along with other 2D nanomaterials such as graphene, molybdenum disulfide (MoS_2) and boron nitride (BN) would also be synthesized and used as sensing element in amperometric and chemiresistive sensors, to achieve comprehensive increase in the sensitivity towards H_2 gas at room temperature.
- Additionally, fabricated sensing elements consisting of pristine 1D, 2D nanostructures of PdO and their composites will be irradiated by UV-Vis electromagnetic radiation to enhance their sensitivity and reversibility of response for H_2 gas due to catalysis by generation of plasmons.

With this proposed research work, we would be able to fabricate sensitive, selective and stable nanostructured sensing element which could detect H_2 gas at room temperature. Further, these solid state elements would also be integrated with the electronic circuits to produce hand held sensors for household and industrial applications.

INTERNATIONAL JOURNAL OF HYDROGEN ENERGY XXX (2016) 1–7

Available online at www.sciencedirect.com

ScienceDirect

journal homepage: www.elsevier.com/locate/he

Effect of low pressure hydrogen environment on crystallographic properties of PdO nanoparticles

*Kamal Arora, Deepika Sandil, Gaurav Sharma, Saurabh Srivastava, Nitin K. Puri**

Advanced Sensor Laboratory, Department of Applied Physics, Delhi Technological University, Main Bawana Road, Shahbad Daulatpur, Delhi, 110042, India

ARTICLE INFO

Article history:
Received 16 June 2016
Received in revised form
6 September 2016
Accepted 7 September 2016
Available online xxx

Keywords:
In-situ X-ray
Palladium oxide
Palladium hydride
Low pressure
Hydrogen sensing

ABSTRACT

Palladium oxide (PdO) nanoparticles (~20–130 nm) are synthesized using sol–gel method. The crystal structure of PdO is determined using X-ray diffraction (XRD) whereas surface morphology, shape and size of PdO nanoparticles are analyzed using scanning electron microscopy and transmission electron microscopy. The optical band gap is estimated as 1.8 eV using UV–Vis spectroscopy. The effect of hydrogen gas at low pressure (25, 50, 75 and 100 mbar) on palladium oxide nanoparticle is studied using In-situ X-ray diffraction at room temperature. It is found that face centered cubic (fcc) palladium hydride (PdH_x) crystal structure is formed and the intensity of peaks representing tetragonal PdO (t-PdO) crystal structure almost vanished as the pressure increased to 100 mbar. Also, it is found that the value of lattice constant increased significantly, when the pressure becomes equivalent to 100 mbar due to phase transition (α-β) in PdH_x lattice. It shows that PdO nanoparticles can be used for storage and sensing of hydrogen gas at ambient atmosphere.

Introduction

Hydrogen gas is the lightest, odorless and colorless gas having calorific value three times greater than that of carbon based fuel [1]. These properties makes it best candidate to be used as fuel or energy source in various applications. At present, hydrogen is being used in nuclear reactors, fuel cells and space industries. It is difficult to store hydrogen as it can permeate through materials easily; Furthermore, hydrogen gas becomes flammable and explosive if its concentration becomes greater than 4 percent within the atmosphere [2]. Thus, monitoring and sensing of hydrogen gas in the area of its application is of prime importance.

Detection of hydrogen gas leak through human sensory organs is not possible because it is colorless and odorless in nature. There are various types of sensors on the basis of sensing mechanism. Metal oxide resistive type sensor has gained wide importance over others due to their high stability, selectivity, sensitivity and long life. A good amount of research work has been conducted over years on hydrogen sensing with various nanostructure metal oxides such as Tin oxide (SnO_2), Zinc oxide (ZnO), Tungsten oxide (WO_3), Nickel oxide (NiO), Vanadium oxide (VO_2), Copper oxide (CuO), Titanium oxide (TiO_2), Niobium oxide (Nb_2O_5) and Magnesium oxide (MgO) [3–11]. Nanostructures of these metal oxides show efficient hydrogen sensing characteristics than their bulk counterparts because they have high area to volume ratio, lower working temperature and doping of these metal oxides with suitable catalyst such as palladium (Pd), platinum (Pt) increased their sensitivity towards hydrogen [12]. Palladium doped metal oxide has been extensively explored for hydrogen sensing due

* *Corresponding author.*
E-mail address: nitin.phy@dce.edu (N.K. Puri).

http://dx.doi.org/10.1016/j.ijhydene.2016.09.040
0360-3199/

Please cite this article in press as: Arora K, et al., Effect of low pressure hydrogen environment on crystallographic properties of PdO nanoparticles, International Journal of Hydrogen Energy (2016), http://dx.doi.org/10.1016/j.ijhydene.2016.09.040

to their high selectivity, low activation barrier, high diffusion coefficient & high adsorption coefficient for hydrogen gas [13].

Effects of hydrogen environment on pure Pd nanoparticles and nanoclusters have been studied extensively. It has been reported that Pd forms Palladium hydride (PdH_x) instantly due to high affinity of Pd towards hydrogen. When the hydrogen concentration (x) is low, $0.1 < x < 0.7$, a solid Pd–H solution known as α-phase PdH_x is formed, whereas for $x > 0.7$, hydride phase, known as β-phase comes into existence. Adsorption of hydrogen is maximum in α-phase as compared to hydrogen rich β-phase. There is a phase transition (α-β), as the hydrogen pressure increases which results in lattice expansion of PdH_x crystal structure. The storage of hydrogen in interstitial sites takes place at grain boundaries into subsurface region (0.7–1.1 nm) from surface and within the lattice depending on the concentration of hydrogen [14,15]. Pd readily reacts with hydrogen to form palladium hydride which results in an expansion of 6% in system lattice. The lattice coefficient increases linearly until the H/Pd ratio becomes equal to 0.7 and becomes constant thereafter [16]. In Pd–H system, hydrogen gets stored into octahedral interstitial voids within face centered cubic lattice of Pd [17]. Suleiman et al. showed that lattice expansion in β-phase PdH_x depends strongly on size of their nanostructures. The large Pd nanoclusters shows high lattice expansion in contrast to smaller nanoclusters which do not experience any expansion in their crystal structure and this data is in complete accordance with other types of Pd nanostructures too. Additionally, as the hydrogen pressure is increased from 18 mbar to 100 mbar, there is an abrupt lattice expansion from 3 Å to 4 Å at 100 mbar in large nanoclusters [18]. The difference between the lattice constant of α and β PdH_x crystal structure decreases as the Pd particle size decreases, i.e. lattice expansion reduces in smaller Pd nanoparticles [19]. Okazaki et al. showed that the annealed Pd crystal nanostructures have higher hydrogen adsorption permittivity in comparison to unannealed structures [20]. Baldi et al. studied the phase transition of individual Pd nanocrystals using Insitu electron energy loss spectroscopy and find it in good accordance with literature reported observations for group of Pd nanocrystals [21].

However, at low temperature and high hydrogen pressure, pure Pd gets damaged by hydrogen due to a phenomenon known as hydrogen embrittlement. Also, pure Pd gets irreversibly poisoned due to the poisoning by deposition of sulfur from sulfur containing gases present in the atmosphere [22]. On the other hand, PdO nanoparticles are less prone to these contaminations as they have high operating temperatures and are covered with the protective oxide layer [23]. Thus, palladium oxide (PdO) nanoparticles would be more favorable for sensing and storage of hydrogen than pure Pd.

Few research works has been reported regarding hydrogen sensing mechanism of PdO nanostructures thin film but PdO nanostructures has not been studied for its hydrogen storage characteristics. The first work is reported in 2010 by Lee et al. who studied PdO thin film grown by sol–gel method for hydrogen sensing application via resistive sensing mechanism and observed that it showed good efficiency for sensing 2% hydrogen gas at room temperature [24]. Chiang et al. investigated hydrogen gas sensing study of PdO nanoflakes thin film at temperatures below 250 °C, it is found that thin film showed good sensing behavior at temperature above 200 °C which accords with oxygen vacancy model [25].

Palladium oxide (PdO) converts irreversibly into Pd on reduction and can be used as active catalyst in various applications. The band gap of PdO is experimentally found to be equal to 1.5 eV using electrical conductivity measurements [26].

To the best of our knowledge, the effect of hydrogen environment on tetragonal palladium oxide (t-PdO) nanoparticles has not been explored before. We report the effect of low pressure (25, 50, 75 & 100 mbar) hydrogen gas on crystal structure and lattice constants of palladium oxide nanoparticles using In-situ X-ray diffraction study. Palladium oxide (PdO) nanoparticles are synthesized using simple and cost effective sol–gel method.

Experimental details

Sol–gel synthesis of PdO nanoparticles

All the procured chemicals belong to AR grade with purity of ~99.9%. 1.56 g of palladium chloride ($PdCl_2$) powder (procured from Fisher) is dissolved in 90 ml solution containing 40 ml Hydrochloric acid (HCl) and 50 ml Ethanol (C_2H_5OH) (procured from Sigma Aldrich). The molarity of final solution is calculated to be equal to 0.1 M. Initially, $PdCl_2$ is added to C_2H_5OH directly, but the powder could not dissolve in the solution. However, on addition of HCl, a clear brown solution is obtained. The following chemical formulas could be the possible explanation of complete reaction.

$$PdCl_2 + HCl \rightarrow PdCl_4 + HCl$$

$$PdCl_4 + C_2H_5OH \rightarrow Pd(OH)_2 + C_2H_5Cl + HCl$$

$$Pd(OH)_2 \rightarrow PdO$$

The final solution is kept for 24 h to complete the total reaction as a part of ageing process. The resultant brown colored solution is kept in oven at 80 °C for 24 h to obtain brown powder particles. The powder is divided into three samples 'a', 'b' & 'c', each annealed respectively at three different temperatures 600 °C, 800 °C & 1000 °C in tubular furnace. All three samples are analyzed to study their crystal structure, surface morphology, optical band gap and crystallographic changes in presence of hydrogen gas by characterizing them through X-ray diffraction experiment, scanning electron microscopy (SEM), Transmission electron microscopy (TEM), UV–Vis spectroscopy and In-situ X-ray diffraction experiment.

X-ray diffraction experiment (XRD)

Fig. 1(i–iii) shows XRD spectra of sample 'a', 'b' & 'c' respectively. On comparison of the intensity peaks with the published data (CAS number: 88-2434 & 88-2335), the corresponding peaks belongs to (002), (110), (112), (103), (200) and (202) planes, indicating the formation of tetragonal palladium oxide crystal structure (t-PdO). It can be seen that peaks

Please cite this article in press as: Arora K, et al., Effect of low pressure hydrogen environment on crystallographic properties of PdO nanoparticles, International Journal of Hydrogen Energy (2016), http://dx.doi.org/10.1016/j.ijhydene.2016.09.040

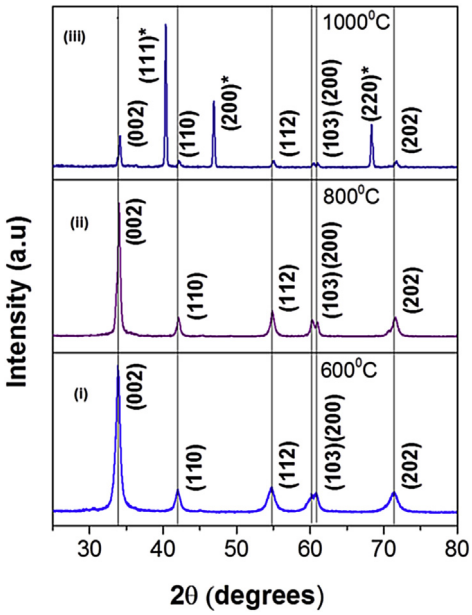

Fig. 1 – XRD spectra comparison of (i) sample 'a', (ii) sample 'b' & (iii) sample 'c'.

becomes narrower and shifted towards right side as temperature increased due to the increase in lattice parameters as a result of temperature induced strain. In Fig. 1(ii), the peaks are less broad and peak splitting is clearly visible in comparison to Fig. 1(i), which defines the good crystalline nature of sample b. Whereas in Fig. 1(iii), three additional peaks come into existence along with regular t-PdO characteristic peaks. Intense peak seen at 40° along with two new peaks arising at 46° and 68° defines (111)*, (200)* and (220)* planes respectively of face centered cubic (fcc) Pd crystal. Thus, t-PdO lattice starts to decompose into fcc Pd lattice as the temperature is raised from 800 °C to 1000 °C. Annealing at high temperature results in the formation of PdO crystal phase as the rate of formation of PdO is compatible with its rate of decomposition into Pd crystal [27]. The results obtained from XRD analysis are found to be in accord with the reported literature [20].

Using Debye Scherrer formula (Eq. (1)) [28], the crystallite size of tetragonal crystal structure was found to be equal to 24.02 nm.

$$D = \frac{0.9\lambda}{\beta \cos\theta} \quad (1)$$

where, D represent crystallite size, λ is wavelength, β is the FWHM (Full width half maxima) and θ is the angle having maximum intensity.

Scanning electron microscopy

Fig. 2(i–iii) represents the scanning electron micrographs of samples 'a', 'b' and 'c'. In Fig. 2(i), no defined particle boundaries can be seen in SEM images of sample 'a' due to agglomeration. In Fig. 2(ii) of sample 'b', particles with more defined particle boundaries are visible. Also, some voids on the surface can be observed in this image. Whereas, rod like crystalline pattern could be observed in SEM image of sample 'c' (Fig. 2(iii)), boundaries and individual particles are non-visible in this image. Thus, it is visible from SEM images, that sample 'a' has particles in nanometer range but no surface uniformity can be observed, whereas sample 'c' comprises non-uniform rod like structure on the surface. Comparatively, sample 'b' has better surface uniformity and distinguishable particle geometry.

UV–Vis spectroscopy

Fig. 3(i) denotes the UV–Vis transmission spectra of sample 'b', there is a strong absorption at 186 nm and gradually, transmission curve becomes constant and decays steadily with wavelength. Sample 'b' has a direct band gap of 1.84 eV, as visible in Fig. 3(ii) containing Tauc plot based on UV–Vis spectral analysis. Several research papers reported direct band gap of PdO to be equivalent to 2 eV [26]. Thus, our study fits the reported data approximately.

Transmission electron microscopy

Fig. 4 represents the Transmission electron microscopy (TEM) and Selected area electron diffraction (SAED) images of samples 'a', 'b', and 'c'. The SAED images show the various Bragg reflection planes of tetragonal palladium oxide which is calculated using relation of reciprocal lattice with interplanar spacing [29]. It can be seen in Fig. 4(i.a) that sample 'a' contains small particles which are grouped together to form clusters of size (20–50 nm). Fig. 4(ii.a) (SAED) shows amorphous nature of sample 'a', with a fainted ring formation due to reflection from highly Bragg reflection favored (101) plane. Fig. 4(i.b) denotes particle size in the range of 10–125 nm, but the respective SAED pattern (Fig. 4(ii.b)) reflects the pure crystalline nature of sample 'b' which is annealed at 800 °C and presence of t-PdO phase can be observed in this sample. The SAED image contains the ordered continuous ring as well as dot patterns due to the presence of single and poly-crystals respectively.

The presence of characteristics (101) plane of tetragonal PdO crystals complements the XRD spectra of the sample 'b'. Sample 'c' contains purely single crystal structure which can be observed in the SAED image (Fig. 4(ii.c)) that contains sporadic ring like structure formed by various dots. Also, it shows the additional peaks (200) & (220) of fcc Pd crystal structure along with (100) peak of t-PdO crystal, thus confirming the presence of both Pd and PdO nanoparticles in sample 'c'. The TEM image in Fig 4(i.c) shows the presence of agglomerated particles which are difficult to distinguish from one another and their size ranges from 20 to 50 nm. TEM also confirms the highly ordered and nano structured formation in sample 'b' along with the presence of interstitial sites which may aid in the adsorption of other atoms, thus sample 'b' would be more favorable for In-situ XRD studies due to its well defined surface morphology, composition as well as crystal structure among other samples.

Results and discussions

In-situ XRD measurements

PdO nanoparticles annealed at 800 °C (sample 'b') are introduced into In-situ XRD spectroscopy vacuum chamber in form of a

Please cite this article in press as: Arora K, et al., Effect of low pressure hydrogen environment on crystallographic properties of PdO nanoparticles, International Journal of Hydrogen Energy (2016), http://dx.doi.org/10.1016/j.ijhydene.2016.09.040

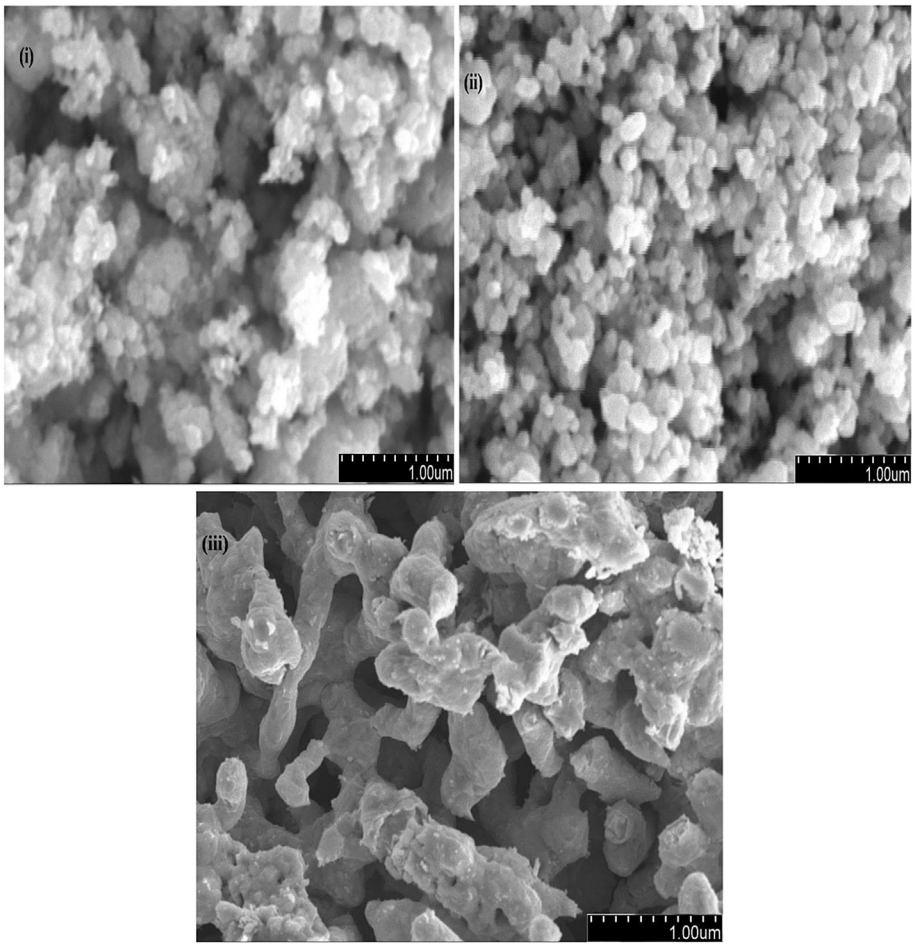

Fig. 2 – SEM images of (i) sample 'a', (ii) sample 'b', (iii) sample 'c'.

pellet. Hydrogen gas is introduced into the chamber at different pressures. When the hydrogen gas comes into contact with surface of PdO, the oxygen atoms are detached from the surface and form water molecules resulting in vacant sites for adsorption. These vacant sites are filled with hydrogen atoms. PdO has high affinity toward hydrogen as compared to water, thus hydrogen react with Pd on the surface to form Palladium hydride (PdH_x). As, the pressure increases, hydrogen gas absorbs inside the pellet and gets stored into the interstitial sites of PdO nanoparticles [30]. Fig. 5 represent In-situ XRD spectroscopy studies of sample 'b' with variable hydrogen gas environmental pressure (25, 50, 75, 100 mbar). In Fig. 5(i), the peaks present in this spectra correspond to same planes [(100), (002), (110), (112), (103), (200) & (202)], as observed in XRD spectra in presence of air, hence confirming the tetragonal crystal structure of sample 'b'. Fig. 5(ii) denotes the XRD spectra of sample 'b' in presence of

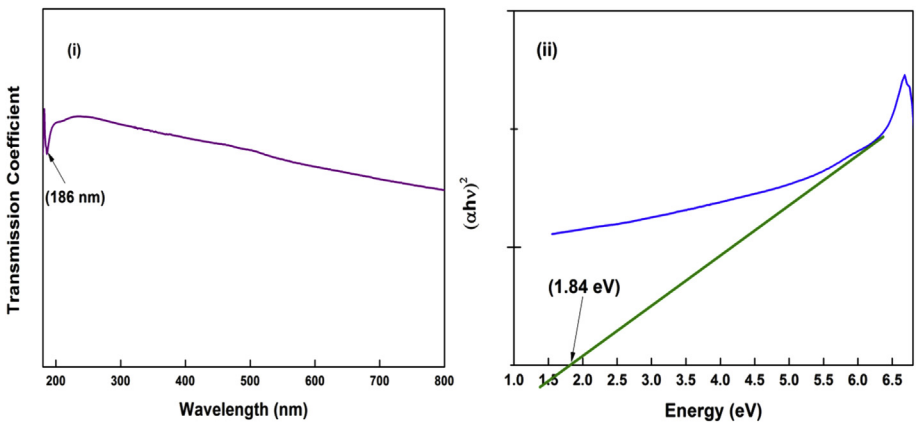

Fig. 3 – (i) UV–Vis transmission spectra and (ii) Band gap estimated from Tauc plot.

Please cite this article in press as: Arora K, et al., Effect of low pressure hydrogen environment on crystallographic properties of PdO nanoparticles, International Journal of Hydrogen Energy (2016), http://dx.doi.org/10.1016/j.ijhydene.2016.09.040

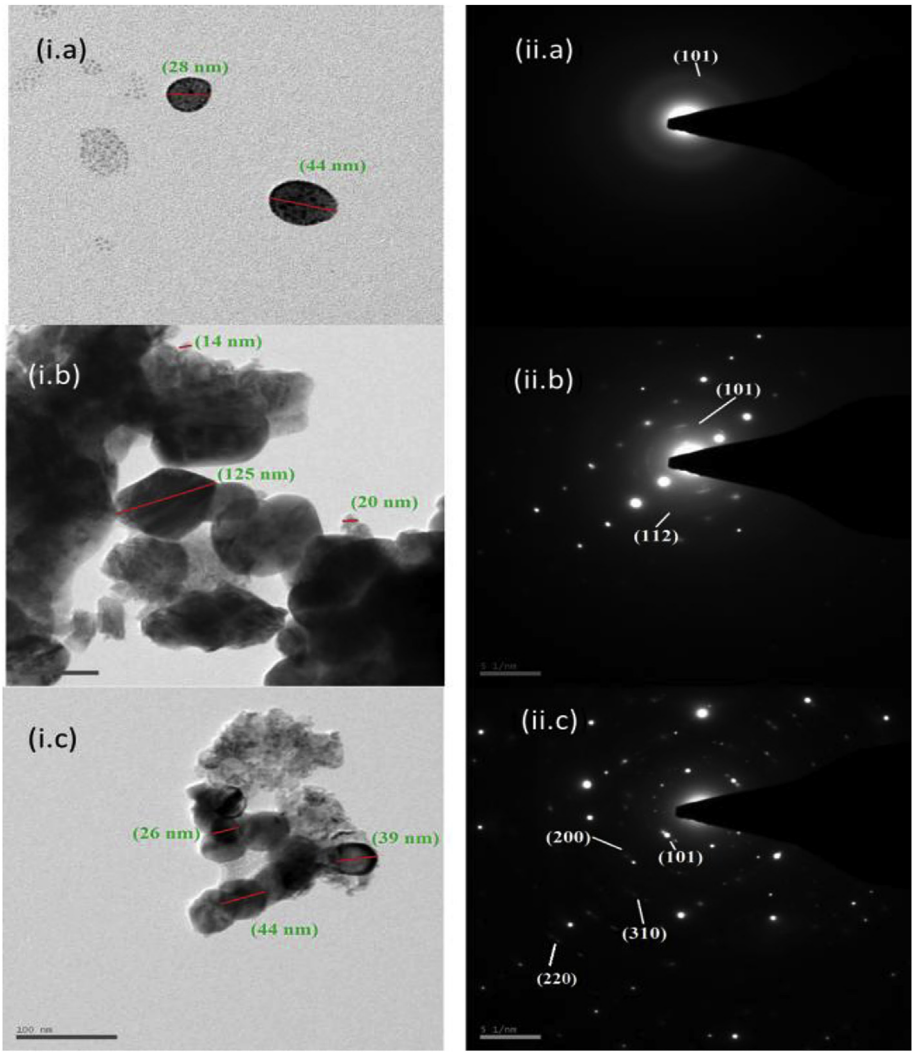

Fig. 4 – (i) TEM images, (ii) SAED images of Sample 'a', Sample 'b' and Sample 'c'.

hydrogen gas at 25 mbar pressure, new planes such as (111)*, (101)*, (110*), (200)* and (211)* along with palladium oxide crystal planes have been formed, describing the formation of face centered cubic (fcc) palladium hydride crystal structure along with tetragonal palladium oxide crystal structure. Whereas, at 50 mbar hydrogen pressure (Fig. 5(ii)), mixed planes of palladium oxide as well palladium hydrides are observed, but the intensity of peaks belonging to palladium oxide tetragonal structure planes has reduced significantly. On the other hand, intensity of peaks representing fcc palladium hydride structure planes has risen comprehensively.

As the pressure escalates from 50 mbar to 100 mbar, all the peaks corresponding t-PdO disappears, except (002) plane revealing that sample mainly consist of fcc PdH_x crystal structure.

Effect of H_2 pressure on lattice constants

In Fig. 6, the lattice parameters for t-PdO ($x = y \neq z$) lattice is calculated for different pressures, where x, y and z are longitudinal and transverse axis respectively [20]. It is observed that at 0 mbar pressure, the transverse axis (z) lattice constant is calculated to be approx. (4.01 ± 0.002) Å, while for longitudinal (x, y) is (3.06 ± 0.0005) Å. As pressure increased gradually from 25 to 100 mbar the value of x, y decreases slightly from (3.06 ± 0.0005) Å to (3.03 ± 0.0009) Å, but increased sharply to (4.06 ± 0.004) Å as approaches 100 mbar, while z remains constant. This slight decrement in lattice constant (3.06 ± 0.0005 Å to 3.03 ± 0.0009 Å) may be attributed to contraction of lattice on being surrounded by hydrogen atoms, but as the pressure reaches 100 mbar, there is a phase transition from α-PdH_x to hydrogen rich β-PdH_x, which results in expansion of lattice in the crystal structure. The result obtained is in good accordance with the work done on Pd nanoparticles [18]. The t-PdO nanoparticles behave similar to Pd nanoparticles in the presence of hydrogen and presence of oxide layer does not hamper its hydrogen absorption characteristics. Gurlo et al. reported that substitution of the hydrogen atoms in the gaps present in between the Pd nanoparticles, result in decrease of its electrical resistance which is the working principle of Pd based highly sensitive hydrogen gas sensing devices [14]. However, in case of Pd

Please cite this article in press as: Arora K, et al., Effect of low pressure hydrogen environment on crystallographic properties of PdO nanoparticles, International Journal of Hydrogen Energy (2016), http://dx.doi.org/10.1016/j.ijhydene.2016.09.040

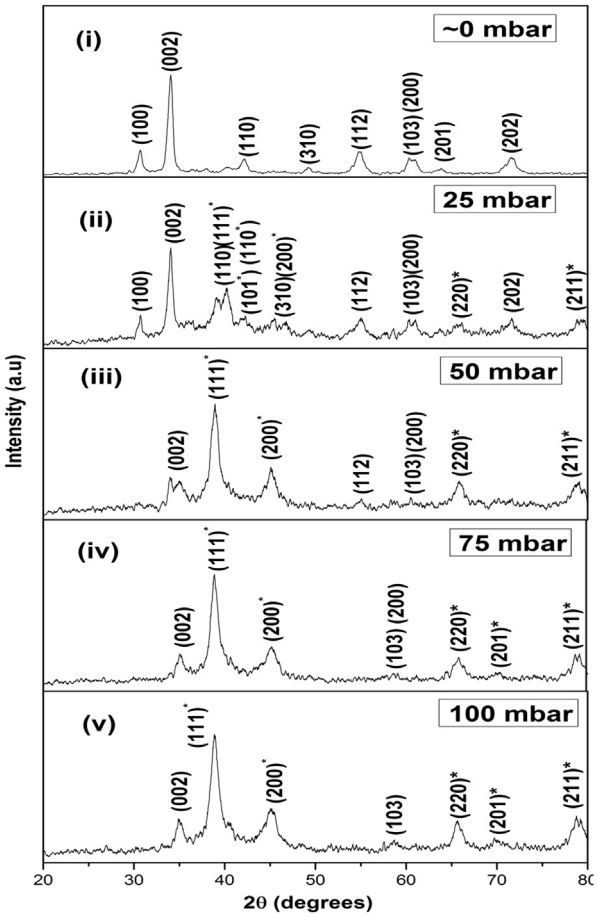

Fig. 5 – XRD spectra of sample b at (i) 0 mbar (ii) 25 mbar (iii) 50 mbar (iv) 75 mbar (v) 100 mbar hydrogen pressure.

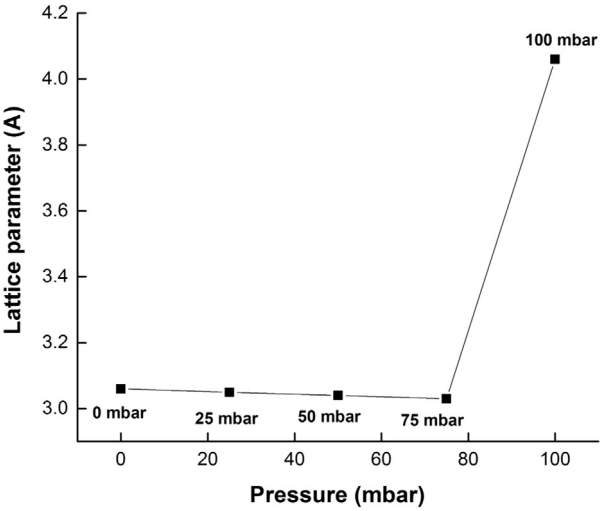

Fig. 6 – Effect of hydrogen gas environment pressure on lattice constants.

nanoclusters, both volume expansion along with resistivity change contributes towards sensing mechanism. The fabricated sensor exhibits good transient response and more efficiency as compared to other sensing devices [30].The lattice expansion due to the phase transition to hydrogen rich β-PdH_x (Fig. 6) implies that the synthesized t-PdO has high affinity towards hydrogen which makes it an efficient candidate for hydrogen storage applications.

Conclusion

PdO nanoparticles of dimension ~20 nm have been grown using sol–gel chemical method, the synthesized samples is annealed at three different temperatures. It is observed that PdO crystal structure starts decomposing to Pd crystal structure at 1000 °C.These samples are characterized with XRD, SEM, UV–Vis, TEM to determine their crystal structure, surface morphology, particle size, and band gap. It is found that PdO nanoparticles annealed at 800 °C shows the best characteristics out of others and hence is subjected to In-situ XRD study in presence of hydrogen gas at low environmental pressure. It is observed that PdO crystal structure has transformed into PdH_x crystal structure gradually with increase in the pressure. There is a phase transition (α-β) in PdH_x crystal structure as hydrogen pressure reached 100 mbar resulting in significant lattice expansion. The PdO nanoparticles demonstrate similar characteristics compared to Pd nanoparticles in the presence of hydrogen gas at low pressure.

Results of the study indicate that the PdO nanoparticles annealed at 800 °C can be used efficiently in hydrogen gas sensors and storage devices. The efforts will be made to utilize this sample for hydrogen gas sensing and solid state hydrogen gas storage at ambient condition.

Acknowledgement

The authors thank Prof. Yogesh Singh, Vice Chancellor, Delhi Technological University, Delhi, India for providing the research facilities. We are grateful to Inter-University Accelerator center (IUAC), and University of Delhi, Delhi, India for providing X-ray diffractometer and transmission electron microscope respectively to carry out necessary studies during this research experiment. The financial supports received from IUAC sponsored project (Grant No. IUAC/XIII.7/UFR-56324) and Department of Science and Technology, India (Grant No. DST/INSPIRE/04/2014/002540) are gratefully acknowledged.

REFERENCES

[1] Broom D. Hydrogen storage materials, green energy and technology. London: Springer-Verlag; 2011.
[2] Khanuja M, Kala S, Mehta B, Kruis F. Concentration-specific hydrogen sensing behavior in monosized Pd nanoparticle layers. Nanotechnology 2008;20(1):015502.
[3] Shen Y, Yamazaki T, Liu Z, Meng D, Kikuta T, Nakatani N, et al. Microstructure and H_2 gas sensing properties of

undoped and Pd-doped SnO_2 nanowires. Sens Actuators B Chem 2009;135(2):524–9.
[4] Kashif M, Ali M, Ali SMU, Hashim U. Sol–gel synthesis of Pd doped ZnO nanorods for room temperature hydrogen sensing applications. Ceram Int 2013;39(6):6461–6.
[5] Boudiba A, Roussel P, Zhang C, Olivier M-G, Snyders R, Debliquy M. Sensing mechanism of hydrogen sensors based on palladium-loaded tungsten oxide (Pd–WO_3). Sens Actuators B Chem 2013;187:84–93.
[6] Fasaki I, Giannoudakos A, Stamataki M, Kompitsas M, György E, Mihailescu I, et al. Nickel oxide thin films synthesized by reactive pulsed laser deposition: characterization and application to hydrogen sensing. Appl Phys A 2008;91(3):487–92.
[7] Baik JM, Kim MH, Larson C, Yavuz CT, Stucky GD, Wodtke AM, et al. Pd-Sensitized single vanadium oxide nanowires: highly responsive hydrogen sensing based on the metal – insulator transition. Nano Lett 2009;9(12):3980–4.
[8] Hoa ND, Van Quy N, Jung H, Kim D, Kim H, Hong S-K. Synthesis of porous CuO nanowires and its application to hydrogen detection. Sens Actuators B Chem 2010;146(1):266–72.
[9] Wen Z, Tian-mo L. Hydrogen sensing characteristics and mechanism of nanosize TiO 2 dope with metallic ions. Phys B Condens Matter 2010;405(2):564–8.
[10] Wang Z, Hu Y, Wang W, Zhang X, Wang B, Tian H, et al. Fast and highly-sensitive hydrogen sensing of Nb_2O_5 nanowires at room temperature. Int J Hydrogen Energy 2012;37(5):4526–32.
[11] Callini E, Pasquini L, Piscopiello E, Montone A, Antisari MV, Bonetti E. Hydrogen sorption in Pd-decorated Mg–MgO core-shell nanoparticles. Appl Phys Lett 2009;94(22):221905.
[12] Hübert T, Boon-Brett L, Black G, Banach U. Hydrogen sensors–a review. Sens Actuators B Chem 2011;157(2):329–52.
[13] Khanuja M, Mehta B, Agar P, Kulriya P, Avasthi D. Hydrogen induced lattice expansion and crystallinity degradation in palladium nanoparticles: effect of hydrogen concentration, pressure, and temperature. J Appl Phys 2009;106(9):093515.
[14] Gurlo A, Clarke DR. High-sensitivity hydrogen detection: hydrogen-induced swelling of multiple cracked palladium films on compliant substrates. Angew Chem Int Ed 2011;50(43):10130–2.
[15] Yamauchi M, Ikeda R, Kitagawa H, Takata M. Nanosize effects on hydrogen storage in palladium. J Phys Chem C 2008;112(9):3294–9.
[16] Fukai Y, Ōkuma N. Formation of superabundant vacancies in Pd hydride under high hydrogen pressures. Phys Rev Lett 1994;73(12):1640.
[17] Narehood D, Kishore S, Goto H, Adair J, Nelson J, Gutierrez H, et al. X-ray diffraction and H-storage in ultra-small palladium particles. Int J Hydrogen Energy 2009;34(2):952–60.
[18] Suleiman M, Jisrawi N, Dankert O, Reetz M, Bähtz C, Kirchheim R, et al. Phase transition and lattice expansion during hydrogen loading of nanometer sized palladium clusters. J Alloys Compd 2003;356:644–8.
[19] Akiba H, Kofu M, Kobayashi H, Kitagawa H, Ikeda K, Otomo T, et al. Nanometer-size effect on hydrogen sites in palladium lattice. J Am Chem Soc 2016;138(32):10238–43.
[20] Okazaki J, Ikeda T, Tanaka DAP, Suzuki TM, Mizukami F. In situ high-temperature X-ray diffraction study of thin palladium/α-alumina composite membranes and their hydrogen permeation properties. J Membr Sci 2009;335(1):126–32.
[21] Baldi A, Narayan TC, Koh AL, Dionne JA. In situ detection of hydrogen-induced phase transitions in individual palladium nanocrystals. Nat Mater 2014;13(12):1143–8.
[22] Khanuja M, Mehta B, Shivaprasad S. Two approaches for enhancing the hydrogenation properties of palladium: metal nanoparticle and thin film over layers. J Chem Sci 2008;120(6):573–8.
[23] Penner S, Wang D, Jenewein B, Gabasch H, Klötzer B, Knop-Gericke A, et al. Growth and decomposition of aligned and ordered PdO nanoparticles. J Chem Phys 2006;125(9):094703.
[24] Lee YT, Lee JM, Kim YJ, Joe JH, Lee W. Hydrogen gas sensing properties of PdO thin films with nano-sized cracks. Nanotechnology 2010;21(16):165503.
[25] Chiang Y-J, Li K-C, Lin Y-C, Pan F-M. A mechanistic study of hydrogen gas sensing by PdO nanoflake thin films at temperatures below 250°C. Phys Chem Chem Phys 2015;17(5):3039–49.
[26] Nilsson P. Optical properties of PdO in the range of 0.5–5.4 eV. J Phys C Solid State Phys 1979;12(7):1423.
[27] Gabasch H, Unterberger W, Hayek K, Klötzer B, Kleimenov E, Teschner D, et al. In situ XPS study of Pd (111) oxidation at elevated pressure, Part 2: palladium oxidation in the 10–1 mbar range. Surf Sci 2006;600(15):2980–9.
[28] Cullity BD, Weymouth JW. Elements of X-ray diffraction. Am J Phys 1957;25(6):394–5.
[29] Wahab MA. Solid state physics: structure and properties of materials. Alpha Science Int'l Ltd; 2005.
[30] Gupta D, Dutta D, Kumar M, Barman P, Sarkar C, Basu S, et al. A low temperature hydrogen sensor based on palladium nanoparticles. Sens Actuators B Chem 2014;196:215–22.

Please cite this article in press as: Arora K, et al., Effect of low pressure hydrogen environment on crystallographic properties of PdO nanoparticles, International Journal of Hydrogen Energy (2016), http://dx.doi.org/10.1016/j.ijhydene.2016.09.040

Vacuum 154 (2018) 302–308

Contents lists available at ScienceDirect

Vacuum

journal homepage: www.elsevier.com/locate/vacuum

Electrophoretically deposited nanostructured PdO thin film for room temperature amperometric H_2 sensing

Kamal Arora, Nitin K. Puri*

Advanced Sensor Laboratory, Department of Applied Physics, Delhi Technological University, Bawana Road, 110042, Delhi, India

ARTICLE INFO

Keywords:
Electrochemical sensor
Hydrogen sensor
Amperometry
Palladium oxide nanoparticles
Metal oxides

ABSTRACT

In the present work, economical and facile hydrothermal sol-gel method is employed for the synthesis of palladium oxide (PdO) nanoparticles. Uniform thin film of PdO nanoparticles are fabricated using Electrophoretic deposition (EPD) set-up. The crystal structure, surface framework, shape and size of PdO nanoparticles are determined using X-ray diffraction spectroscopy (XRD), Transmission electron microscopy (TEM) and scanning electron microscopy (SEM) respectively. An optical band-gap of 1.9 eV is observed using UV-Visible (UV-Vis) spectroscopy. Amperometric sensing of hydrogen gas is studied using PdO thin film as working electrode and characteristics properties have been obtained for different hydrogen (H_2)/Argon (Ar) gas concentrations using potentiostat/galvanostat Autolab instrument at room temperature. The PdO nanoparticles based amperometric hydrogen gas sensor shows high sensitivity of 0.222 μA/%H_2 with fast response and recovery time.

1. Introduction

H_2 is a clean and renewable energy carrier which is used extensively in several petrochemical, medical and aerospace industries. It is highly flammable in nature and could be devastating for the surrounding if its concentration exceeds 4% in air. Thus, it is necessary to fabricate a highly stable, selective and sensitive sensor which can trace H_2 even in small concentrations at room temperature [1].

Out of different types of sensors available in the market today, two sensors have attracted a widespread attention of the researchers and industries due to their peculiar merits over others i.e. conductometric and electrochemical sensors. Conductometric sensors works on the principle of change in conductivity on adsorption of gases on its surface with time, but low relative humidity (RH) and high temperature are required for its efficient working which is in contrast with electrochemical sensors which can detect with high sensitivity and selectivity at room temperature [2,3]. Amperometric and potentimetric are the two classifications of electrochemical sensors which differ in their working and sensing response. Potentiometric sensors show logarithmic response that lacks accuracy, whereas, amperometric sensor demonstrates precise and calibrated linear sensing response [4].

Many wide band-gap metal oxides such as Tin oxide (SnO_2), Indium oxide (In_2O_3) and Zinc oxide (ZnO) have been extensively researched in application for Hydrogen (H_2) gas sensing along with other transition metal oxide elements, as they have distinctive as well as favorable electronic and physical properties [5–8].

Nevertheless, these pristine metal oxides sensor works optimally only at high temperatures and low relative humidity. Also, standalone metal oxides sensor have low sensitivity for hydrogen, but the adsorption rate of H_2 on their surface can be enhanced by doping them with highly electroactive elements such as palladium (Pd) and platinum (Pt) due to the process of hydrogen spillover [9–11]. Pure Pd metal is irreversibly poisoned by gases present in the atmosphere and also it gets damaged by hydrogen embrittlement process on exposure to H_2. On the other hand, palladium oxide (PdO) is protected by the cover of oxide layer and it does not get contaminated due to its high working temperature [12,13]. Hence, PdO nanoparticles are more favorable candidates for H_2 sensing as compared to pure Pd. PdO is a hole majority carrier (p-type) semiconductor and its band-gap lies in range of visible light. Okamoto et al. found that the optical band-gap of PdO lies in the range of 1–2 eV with a hole mobility of about 17 cm V^{-1} s^{-1} [14].

The electrophoretic deposition (EPD) is a versatile and economical technique for the fabrication of uniform coatings or films of metal oxides, graphene along with their composites on conductive substrates as compared to other conventional methods because it consists of simple, low cost apparatus and allows the usage of desired shape of the substrate [15]. EPD gives control over thickness of the film by varying the deposition time and applied potential. Yet, deposition of films depends on two factors i.e. characteristics of the liquid suspension and EPD processing parameters. The thickness and uniformity depends not only on deposition time and applied potential but also on the dielectric constant, viscosity, conductivity and stability of colloidal suspension

* Corresponding author.
E-mail addresses: nitinkumarpuri@dtu.ac.in, nitinpuri2002@yahoo.co.in (N.K. Puri).

https://doi.org/10.1016/j.vacuum.2018.04.023
Received 15 December 2017; Received in revised form 8 April 2018; Accepted 12 April 2018
Available online 13 April 2018
0042-207X/

[16,17]. Thus, these parameters need to be adjusted to achieve desired thickness of the film.

Nanostructured PdO and its composite with other metal oxides have been used as a sensing element for methane, toluene, ethanol and carbon monoxide conductometric gas sensing. They showed high sensitivity on comparison with pristine metal oxides, but the working temperature of the sensors exceeds 200 °C [18–24].

Few research works have been reported using nanostructured PdO and its thin films for sensing H_2 though conductometric sensor. They demonstrated high selectivity and sensitivity for H_2, but the working temperature of these sensors are high [25,26]. Sipra Choudhury et al. showed room temperature H_2 sensing using Langmuir-Blodgett precursor synthesized PdO nanoparticles layered thin film by employing sophisticated and costly KSV 5000 instument [27]. However, room temperature amperometric H_2 sensing by PdO nanoparticles synthesized by cost effective sol-gel hydrothermal method has not been reported yet.

In the present work, PdO nanoparticles have been synthesized using economical and facile hydrothermal sol-gel method. Thin film of PdO nanoparticles have been fabricated on ITO glass substrates by electrophoretic deposition process. PdO/ITO thin film is employed as working electrode (WE) in indigenously fabricated electrochemical cell which is used for amperometric H_2 gas sensing at 25 °C.

2. Experimental work

2.1. Materials used

Palladium chloride ($PdCl_2$), ethanol (C_2H_5OH) and hydrochloric acid (HCl) are purchased from Sigma Aldrich, Merck and Fisher Scientific respectively. These chemicals are used in the synthesis of PdO nanoparticles and they belong to AR grade purity (~99.9%).

2.2. Synthesis of PdO nanoparticles

$PdCl_2$ is dissolved in C_2H_5OH to form 0.1 Molar solution, 1 v/v % HCl is added to solution drop wise to enhance the solubility of $PdCl_2$ in the solution and a transparent brown colored solution is obtained after stirring for 30 min. The resultant solution is allowed to age for 24 h. The solution is transferred to Teflon hydrothermal vessel and allowed to be heated at 200 °C. Thereafter, brown colored powder is obtained which is consequently washed with D.I. water and annealed at 600 °C to remove organic as well chloride ions impurities that yielded a black colored fine powder. X-ray diffraction (XRD), transmission electron microscopy (TEM), and ultraviolet-Visible (UV-Vis) absorption spectroscopy is used to detect crystal structure, shape, size and optical band-gap of synthesized black powder. Data obtained from these analytical studies of as synthesized black powder confirmed the creation of PdO nanoparticles.

2.3. Fabrication of PdO thin film

Thin films of PdO nanoparticles are deposited on (5 mm × 10 mm) ITO coated glass substrates using electrophoretic deposition (EPD) process at various constant electrophoretic deposition potential (10, 15, 20, 25, 30 and 35 V) respectively with deposition time of 2 min. ITO substrate and platinum (Pt) rod serves the role of anode and cathode respectively, these electrodes are placed in a 20 mL glass beaker at separation of 1 cm. 0.1 g of PdO powder is dispersed in 10 mL of ethanol to obtain electrolyte solution. Consequently, 100 μL of magnesium nitrate [$Mg(NO_3)_2{\cdot}6H_2O$] is added to the solution as a dispersant to improve the conductivity and mobility of the ions present in the electrolyte. These processing parameters are experimentally calibrated to obtain uniform coating of 1 μm thick film on the surface of the substrate. Also, uniformity of the film gets distorted on modifying the deposition time and applied potential for the given concentrations of colloidal suspension.

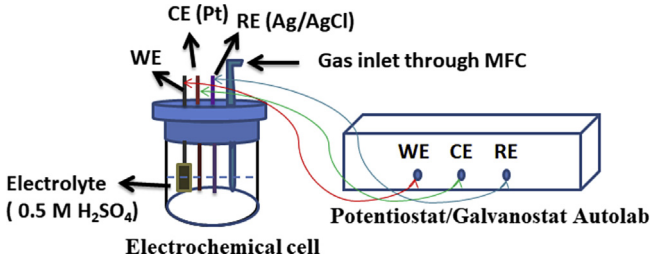

Fig. 1. Electrochemical gas sensing setup.

2.4. Amperometric sensing setup

The Amperometric sensing setup contains an indigenously fabricated three electrodes electrochemical cell which is connected to Potentiostat Autolab instrument (Fig. 1).

PdO thin film/ITO substrate is used as working electrode (WE), whereas platinum rod act as a counter electrode (CE) and Nafion coated Silver/Silver chloride (Ag/AgCl) rod is employed as reference electrode (RE). These three electrodes are dipped into 0.5 M Sulphuric acid (H_2SO_4) electrolyte and placed inside a 30 mL glass beaker. The electrochemical cell is sealed with Teflon cylindrical disk which consist of circular inlets for introduction of electrodes and gas. The cell is attached to the ALICAT gas mix mass flow controller (MFC) through Teflon pipes.

3. Results

3.1. X-ray diffraction study

XRD spectroscopy is performed using PANalytical (Germany), X-ray diffractometer. It can be inferred after comparing with published JCPDS data (CAS number: 750584) that the most intense peak at 33.8° corresponds to (101) plane, whereas other moderately intense peaks at 42°, 54.7°, 60.12°, 61° and 71.3° represent (110), (112), (103), (200) and (202) of tetragonal PdO (t-PdO) respectively (Fig. 2). The average crystallite size of t-PdO can be calculated using Scherrer's formula [Eq. (1)] [15] and it is found to be equal to 14 nm.

$$t = \frac{0.9\lambda}{\beta \cos\theta} \quad (1)$$

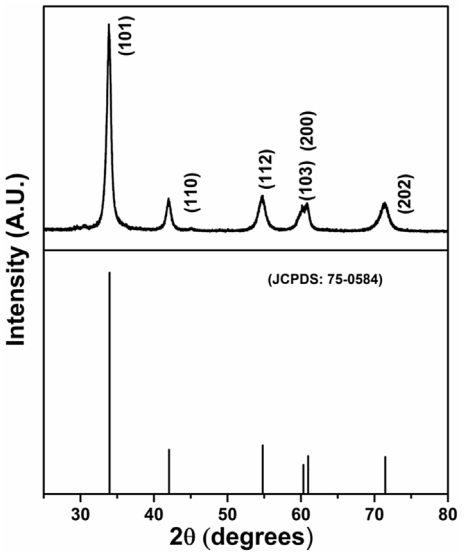

Fig. 2. XRD graph of PdO nanoparticles.

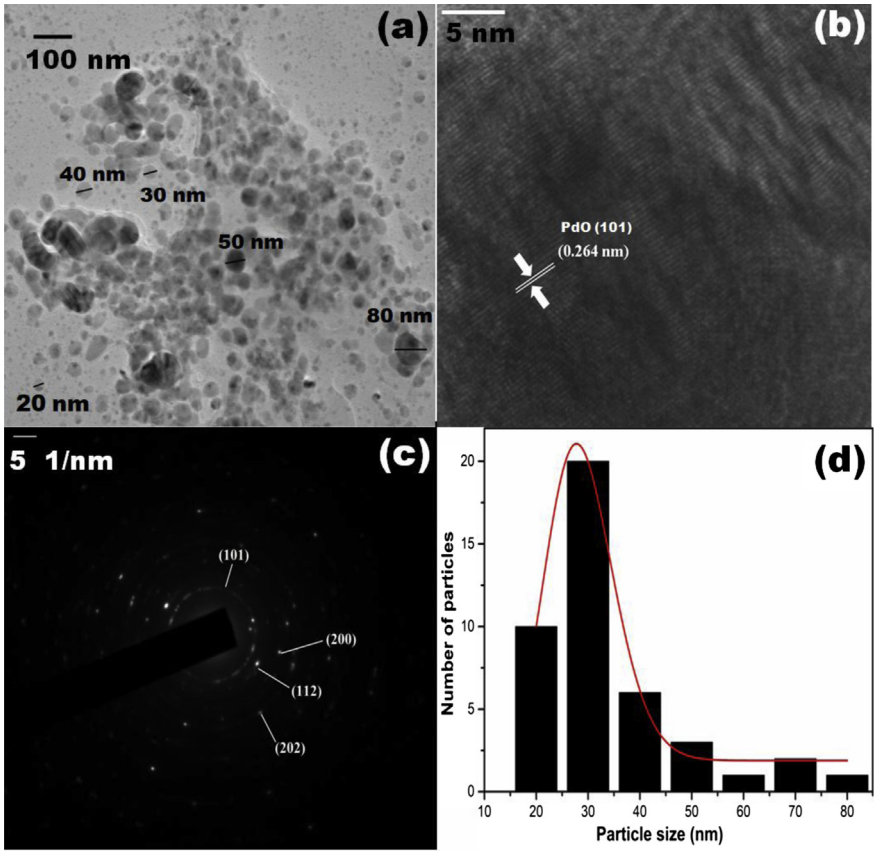

Fig. 3. (a) TEM image (b) HRTEM image (c) SAED image (d) Particle size distribution.

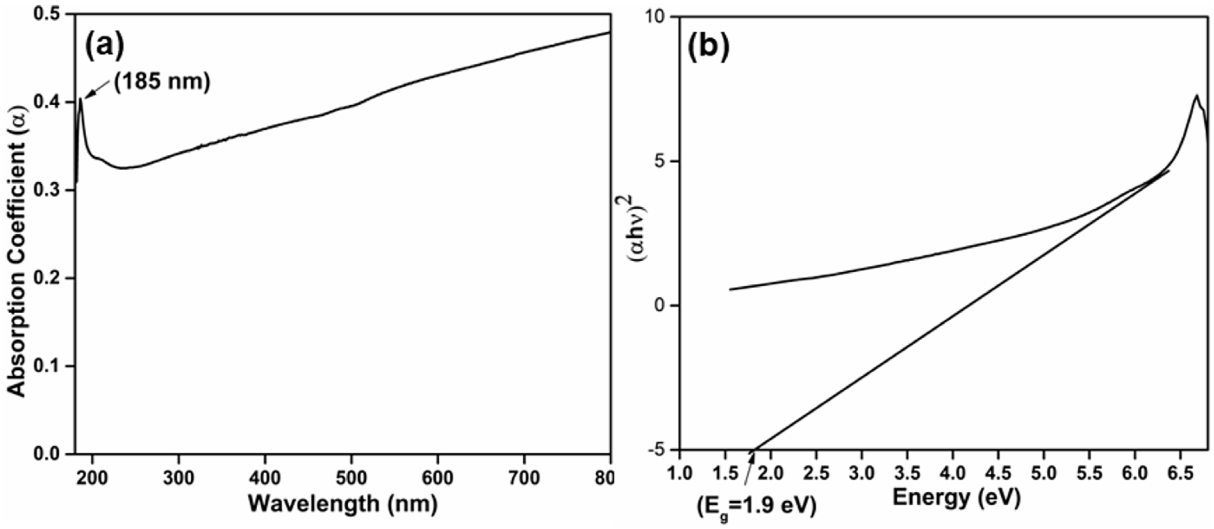

Fig. 4. (a) UV-Vis absorption spectra (b) Tauc plot.

where, β is the FWHM (Full width half maxima), t is average crystallite size, λ is wavelength and θ is the angle having maximum intensity.

Thus, the XRD analysis confirms the formation of t-PdO crystal structure with average crystallite size of 14 nm.

3.2. Transmission electron microscopy

The size and shape of the particles has been observed by TEM images using JEOL (USA) 2100F, Transmission electron microscope (Fig. 3). The particles size ranges from 20 to 80 nm are visible in TEM image (Fig. 3(a)), with high density of nanoparticles with size 20–40 nm comparatively (Fig. 3(d)). HRTEM image shows the presence of parallel crystallographic planes with interplanar spacing of 0.264 nm which represents the (101) planes of t-PdO (Fig. 3(b)), whereas presence of concentric rings formed by dots correspond to (101), (112), (200) and (202) planes of polycrystalline t-PdO (CAS number: 750584). Thus, TEM validates the presence of t-PdO in as-synthesized black powder and coincides with the XRD study.

3.3. UV-Vis spectroscopy

In UV-Vis absorption spectra obtained using LAMBDA 950 UV/Vis

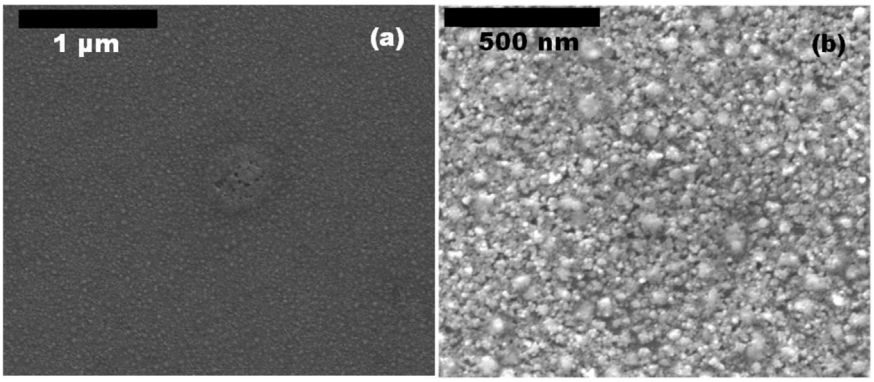

Fig. 5. SEM images with resolutions (a) 1 μm (b) 500 nm.

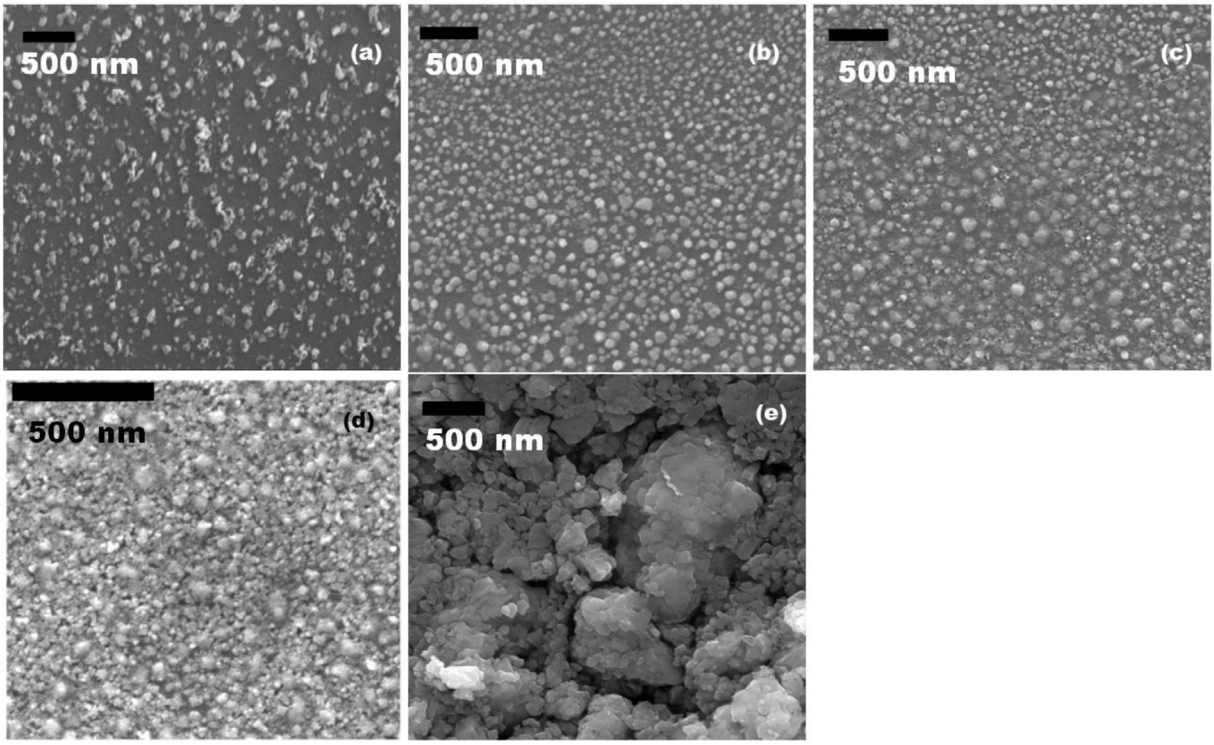

Fig. 6. SEM images of working electrodes deposited at Electrophoresis deposition potential of (a) 10 V, (b) 20 V, (c) 25 V, (d) 30 V and (e) 35 V.

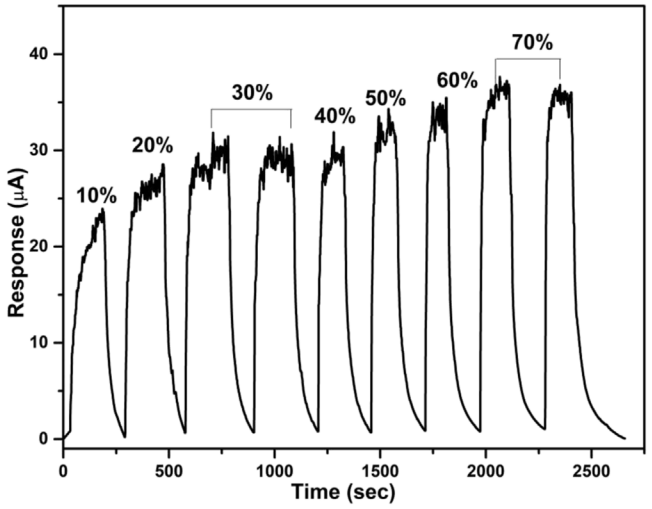

Fig. 7. Response curve.

Spectrophotometer, PerkinElmer (USA), an absorption peak can be observed at 185 nm, which corresponds to absorption of ultraviolet wavelength absorbed by PdO nanoparticles (Fig. 4(a)) [13].

The optical band-gap of PdO nanoparticles is found to be 1.9 eV by plotting $(\alpha h\nu)^2$ versus $h\nu$ (energy) (Fig. 4(b)), i.e. Tauc plot, where α is absorption coefficient, h is Planck's constant and ν is frequency of radiation.

3.4. Scanning electron microscopy

Fig. 5 shows SEM images of PdO nanoparticles thin film deposited on the surface of the ITO glass substrate at deposition voltage of 30 V, captured using MIRA II LMH from TESCAN (Czech Republic). The surface morphology is uniform and continuous with no visible cracks on the surface of the thin film. However, small voids can be seen on the surface within the particles which aid in adsorption of gas molecules. Particles are visible in 500 nm resolution images, but due to agglomeration, particles shape and size cannot be defined distinctly using SEM (Fig. 5(b)). Nevertheless, TEM images confirm the formation of spherical PdO nanoparticles with particle size ranging from 20 to 80 nm.

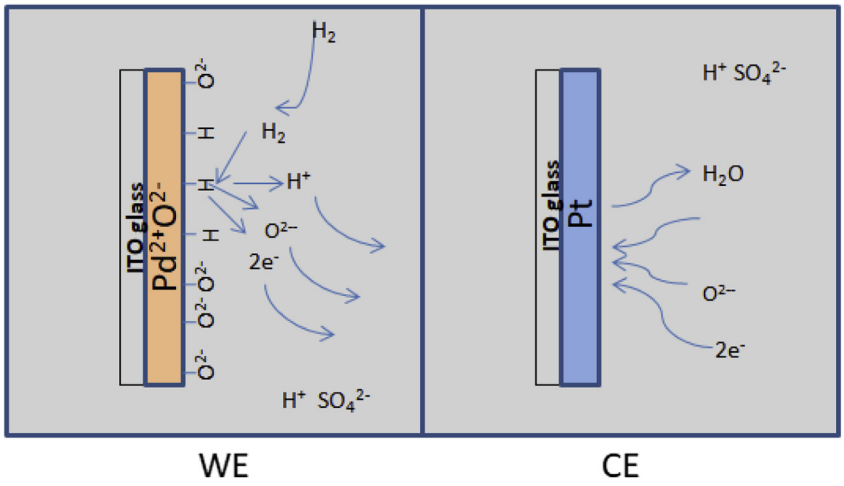

Scheme 1. Schematic representation of Amperometric H_2 sensing by PdO thin film.

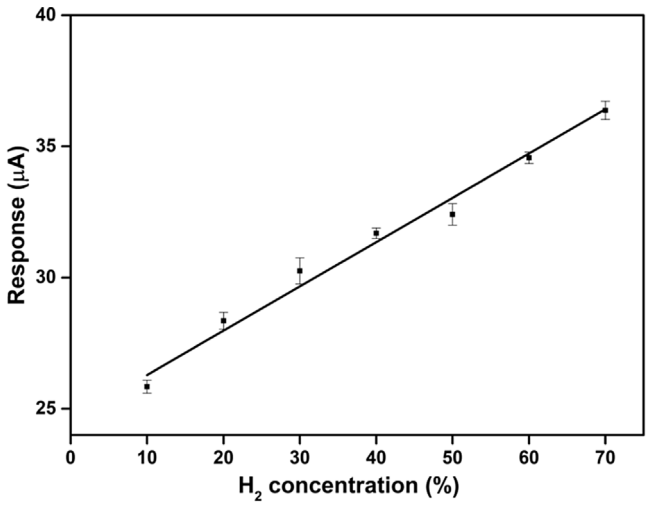

Fig. 8. Calibration plot of response curve.

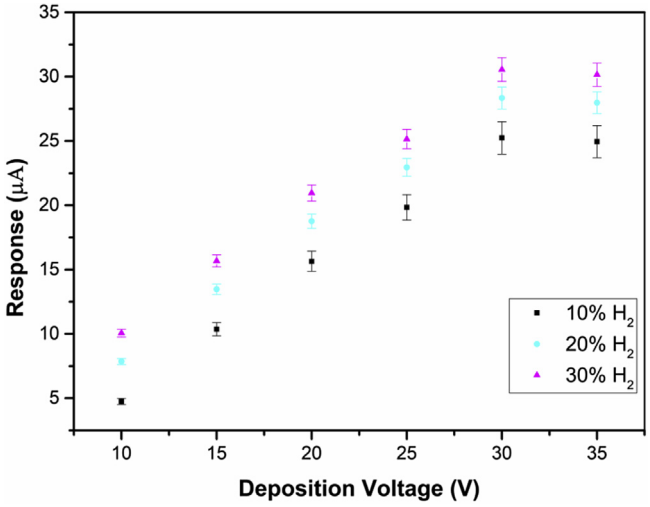

Fig. 9. Relationship between Sensing response and deposition potential.

Fig. 6 (a), (b), (c) and (d) represents the high resolution SEM images of PdO thin film deposited on ITO glass substrates at 10 V, 20 V, 25 V, 30 V and 35 V deposition voltages respectively with deposition time of 2 min. The particle density on surface of thin film deposited at 10 V is sparse, separated and randomly distributed. However, density increases comprehensively and surface gets more uniformly distributed with less separation as the deposition potential rises to 35 V (Fig. 6.). As the deposition potential rises, the concentration of nanoparticles increases which results in linking of nanoparticles, identical to the process of nanojoining [28]. The aggregation of particles takes place at deposition potential of 30 V and number of gaps present on surface decreases with higher surface uniformity.

However, there is large amount of agglomeration present on surface of working electrode deposited at 35 V, which has resulted in the formation of large nanoclusters leading to less homogeneity and uniformity of surface morphology.

Additionally, the particles size changes on modifying the deposition potential; the particles are smaller in size at 10 V deposited electrode, whereas the particles gets bigger in nature as deposition potential reaches 30 V. This variation in the size of the nanoparticles may be explained by the process of recrystallization of Pd^{2+} ions in the electrolyte solution. Also, there is a possibility that electrochemical reaction occurs simultaneously with electrophoretic process which leads to reduction of Pd^{2+} ions into Pd atoms which are then attached to nanoparticles present on the surface of working electrode [29].

3.5. Amperometric sensing study

H_2/Argon gas with different percentage concentrations is allowed to flow at rate of 80 mL/min into the Teflon sealed electrochemical gas sensing setup (Fig. 1) by passing it through mass flow controller (MFC) at 25 °C. The inlet for the gas is covered with fluorinated ethylene propylene (FEP) H_2 gas permeable membrane.

The amperometric sensing is performed by passing H_2 gas into the cell for 200 s and then stopped to allow it to recover. A constant potential of 1 V is applied across the electrodes through Metrohm (Netherland) Potentiostat Autolab instrument. The sensing response for 10–70% H_2 gas is recorded and plotted using response curve (Fig. 7). There is fast rise in the magnitude of current during the duration of the flow of gas, which decays exponentially on gas cut off. Also, the magnitude of current increases as the percentage concentration of H_2 gas increases. This can be attributed to the redox reactions occurring at WE and CE as gas starts diffusing into the electrolyte [Eqs. (2)–(4)] [27].

$$PdO(s) \rightarrow Pd(s) + \frac{1}{2}O_2^{2-} \text{ (Reduction of PdO at WE)} \quad (2)$$

$$H_{2ads} - Pd(s) \rightarrow 2H^+ + 2e^- \text{ (Oxidation of hydrogen at WE)} \quad (3)$$

$$\frac{1}{2}O_2^{2-} + 2H^+ + 2e^- \rightarrow H_2O(l) \text{ (Reduction of oxygen at CE)} \quad (4)$$

Table 1
Amperometric H_2 sensors based on liquid electrolytes.

Gas	Sensing Electrode	Electrolyte	LOD (%H_2)	References
H_2	Pt/Carbon	5 M H_2SO_4	–	[32]
H_2	Gold	9 M H_2SO_4	–	[33]
H_2	Pt-Ag/AgCl	1 M H_2SO_4	< 1%	[34]
H_2-Air	Pt-Ag/AgCl	H_2SO_4	< 0.2%	[35]
H_2-Nitrogen	Pt-Ag/AgCl	H_2SO_4	< 0.4%	[35]
H_2-Ar	PdO	0.5 M H_2SO_4	< 0.2%	Present work

where 's' is solid phase, 'l' is liquid phase and 'ads' is adsorbed species respectively.

In the vicinity of H_2, PdO gets reduced to Pd which binds itself with H atom which results in release of peroxide ions and free electrons at the WE. The hydrogen ion (H^+) present in the electrolyte travels toward the CE and reacts with the peroxide ions on consuming free electrons resulting in water molecules. The exchange of free electrons from WE to CE completes the circuit and gives rise to increase in current at different concentration of hydrogen gas (Scheme 1). Electrochemical sensing response of PdO nanoparticles thin film deposited electrophoretically at deposition potential of 30 V is linearly calibrated and shows high sensitivity (S) of (0.222 ± 0.008) μA/%H_2 with variance of 0.98602 (Fig. 8).

Limit of detection (LOD) of the fabricated sensor is defined as equal to (3S/N), where S is net sensitivity of the sensor and N is the noise and it is estimated to be equal to 0.1% H_2 for this sensor. The fitting is done using linear regression equation y = 24.59 + 0.222x, where x is H_2 gas concentration percentage and y is response current (μA) respectively. The response is fast and stable with quick recovery time. The steady state current time (t_{90}) ranges from 15 to 60 s for various percentage of H_2 gas.

3.6. Effect of deposition voltage on sensing response

The sensing response of working electrodes (WE) deposited electrophoretically at 10, 15, 20, 25, 30 and 35 V deposition potential respectively has been obtained for 10, 20 and 30% H_2 gas concentration correspondingly (Fig. 9.). It can be observed that the sensing current rises linearly as the deposition potential is increased from 10 V to 30 V, thereafter it decreases as deposition voltage reaches 35 V. This increase in sensitivity may be attributed to increase in nanoparticles density and uniformity of thin film as deposition potential rises from 10 V to 30 V.

As the deposition potential reaches to 30 V, the aggregation within the particles enhances (Fig. 6.), which yields in formation of interstitial gaps and voids on the surface that favors as adsorption sites for H_2, thus leads to rise in the sensing response of WE.

When the deposition potential is increased to 35 V, the rate of deposition becomes too rapid which hinders the order and homogeneity of the film due to formation of large size nanoparticles that result in decrease in the sensitivity of the working electrode [30,31]. Additionally, at higher deposition voltage, there is reduction in porosity due to high packing density of deposited particles which drops the amount of voids present on the surface which may result in low sensing response [31].

The sensing characteristic of the proposed room temperature hydrogen gas sensor has been compared with the similar work reported in literature (Table 1).

4. Conclusion

Room temperature amperometric hydrogen gas sensing by PdO nanoparticles have been demonstrated in this paper. PdO nanoparticles are synthesized using economical and facile hydrothermal sol-gel process. XRD spectra show formation of tetragonal crystal structure of PdO which also agrees with the results reflected by SAED and HRTEM images. The size of nanoparticles ranges from 20 to 80 nm as observed from TEM images. Electrophoretic deposition technique is used to fabricate thin film of PdO nanoparticles on ITO glass substrate. PdO/ITO electrode deposited electrophoretically at deposition potential of 30 V shows high sensitivity of 0.222 μA/%H_2 at 25 °C with 0.1% H_2 limit of detection (LOD), sensing response ranging from 15 to 60 s and fast recovery time for 10 to 70 percent concentration of H_2. These studies show application of this sensor for low as well as high concentration H_2 sensing at room temperature. Pristine PdO nanoparticles can be doped or composited with hydrogen philic materials and various nanostructures of PdO can be employed to enhance the sensitivity and selectivity of the sensor.

Acknowledgements

We would thank Prof. Yogesh Singh, Vice chancellor, Delhi Technological University, Delhi, India for arranging the research facilities. We are grateful to Jawahar Lal University (JNU), New Delhi for assisting in characterization of materials. The financial support received from Department of Atomic Energy -Board of Research in Nuclear Sciences (DAE-BRNS), India, SERB, DST, India (EMR/2016/007479), IUAC sponsored project (Grant No. IUAC/XIII.7/UFR-56324), and DST, India (Grant No. IFA14-MS-34) are gratefully acknowledged.

References

[1] G. Korotcenkov, S.D. Han, J.R. Stetter, Review of electrochemical hydrogen sensors, Chem. Rev. 109 (3) (2009) 1402–1433.
[2] J.R. Stetter, J. Li, Amperometric gas sensors a review, Chem. Rev. 108 (2) (2008) 352–366.
[3] W.J. Buttner, M.B. Post, R. Burgess, C. Rivkin, An overview of hydrogen safety sensors and requirements, Int. J. Hydrogen Energy 36 (3) (2011) 2462–2470.
[4] X. Lu, S. Wu, L. Wang, Z. Su, Solid-state amperometric hydrogen sensor based on polymer electrolyte membrane fuel cell, Sensors and Actuators B: Chemical 107 (2) (2005) 812–817.
[5] N. Shirahata, W. Shin, N. Murayama, A. Hozumi, Y. Yokogawa, T. Kameyama, Y. Masuda, K. Koumoto, Reliable monolayer-template patterning of SnO2 thin films from aqueous solution and their hydrogen-sensing properties, Adv. Funct. Mater. 14 (6) (2004) 580–588.
[6] A. Qurashi, T. Yamazaki, E. El-Maghraby, T. Kikuta, Fabrication and gas sensing properties of in 2 O 3 nanopushpins, Appl. Phys. Lett. 95 (15) (2009) 153109.
[7] L.-J. Bie, X.-N. Yan, J. Yin, Y.-Q. Duan, Z.-H. Yuan, Nanopillar ZnO gas sensor for hydrogen and ethanol, Sensor. Actuator. B Chem. 126 (2) (2007) 604–608.
[8] T. Hübert, L. Boon-Brett, G. Black, U. Banach, Hydrogen sensors–a review, Sensor. Actuator. B Chem. 157 (2) (2011) 329–352.
[9] H.-T. Wang, B. Kang, F. Ren, L. Tien, P. Sadik, D. Norton, S. Pearton, J. Lin, Hydrogen-selective sensing at room temperature with ZnO nanorods, Appl. Phys. Lett. 86 (24) (2005) 243503.
[10] T. Samerjai, N. Tamaekong, C. Liewhiran, A. Wisitsoraat, A. Tuantranont, S. Phanichphant, Selectivity towards H 2 gas by flame-made Pt-loaded WO 3 sensing films, Sensor. Actuator. B Chem. 157 (1) (2011) 290–297.
[11] V.V.e. Rozanov, O.V. Krylov, Hydrogen spillover in heterogeneous catalysis, Russ. Chem. Rev. 66 (2) (1997) 107–119.
[12] M. Khanuja, B. Mehta, S. Shivaprasad, Two approaches for enhancing the hydrogenation properties of palladium: metal nanoparticle and thin film over layers, J. Chem. Sci. 120 (6) (2008) 573–578.
[13] K. Arora, D. Sandil, G. Sharma, S. Srivastava, N.K. Puri, Effect of low pressure hydrogen environment on crystallographic properties of PdO nanoparticles, Int. J. Hydrogen Energy 41 (47) (2016) 22155–22161.
[14] P. Nilsson, Optical properties of PdO in the range of 0.5-5.4 eV, J. Phys. C Solid State Phys. 12 (7) (1979) 1423.
[15] S. Srivastava, V. Kumar, M.A. Ali, P.R. Solanki, A. Srivastava, G. Sumana, P.S. Saxena, A.G. Joshi, B. Malhotra, Electrophoretically deposited reduced graphene oxide platform for food toxin detection, Nanoscale 5 (7) (2013) 3043–3051.
[16] L. Besra, M. Liu, A review on fundamentals and applications of electrophoretic deposition (EPD), Prog. Mater. Sci. 52 (1) (2007) 1–61.
[17] P. Sarkar, P.S. Nicholson, Electrophoretic deposition (EPD): mechanisms, kinetics, and application to ceramics, J. Am. Ceram. Soc. 79 (8) (1996) 1987–2002.
[18] G. Xie, P. Sun, X. Yan, X. Du, Y. Jiang, Fabrication of methane gas sensor by layer-by-layer self-assembly of polyaniline/PdO ultra thin films on quartz crystal microbalance, Sensor. Actuator. B Chem. 145 (1) (2010) 373–377.
[19] M. Yuasa, T. Masaki, T. Kida, K. Shimanoe, N. Yamazoe, Nano-sized PdO loaded SnO 2 nanoparticles by reverse micelle method for highly sensitive CO gas sensor, Sensor. Actuator. B Chem. 136 (1) (2009) 99–104.
[20] M. Tong, G. Dai, D. Gao, Gas-sensing properties of PdO-modified SnO 2–Fe 2 O 3 double-layer thin-film sensor prepared by PECVD technique, Vacuum 59 (4) (2000) 877–884.
[21] I.J. Kim, S. Do Han, I. Singh, H.D. Lee, J.S. Wang, Sensitivity enhancement for CO gas detection using a SnO 2–CeO 2–PdO x system, Sensor. Actuator. B Chem. 107

(2) (2005) 825–830.
[22] Z. Lou, J. Deng, L. Wang, L. Wang, T. Fei, T. Zhang, Toluene and ethanol sensing performances of pristine and PdO-decorated flower-like ZnO structures, Sensor. Actuator. B Chem. 176 (2013) 323–329.
[23] Y.-J. Chiang, F.-M. Pan, PdO nanoflake thin films for CO gas sensing at low temperatures, J. Phys. Chem. C 117 (30) (2013) 15593–15601.
[24] L. Wang, Z. Lou, R. Wang, T. Fei, T. Zhang, Ring-like PdO–NiO with lamellar structure for gas sensor application, J. Mater. Chem. 22 (25) (2012) 12453–12456.
[25] Y.-J. Chiang, K.-C. Li, Y.-C. Lin, F.-M. Pan, A mechanistic study of hydrogen gas sensing by PdO nanoflake thin films at temperatures below 250° C, Phys. Chem. Chem. Phys. 17 (5) (2015) 3039–3049.
[26] Y.T. Lee, J.M. Lee, Y.J. Kim, J.H. Joe, W. Lee, Hydrogen gas sensing properties of PdO thin films with nano-sized cracks, Nanotechnology 21 (16) (2010) 165503.
[27] S. Choudhury, C. Betty, K. Bhattacharyya, V. Saxena, D. Bhattacharya, Nanostructured PdO thin film from Langmuir–Blodgett precursor for room-temperature H2 gas sensing, ACS Appl. Mater. Interfaces 8 (26) (2016) 16997–17003.
[28] X.-Y. Zhang, F. Shan, H.-L. Zhou, D. Su, X.-M. Xue, J.-Y. Wu, Y.-Z. Chen, N. Zhao, T. Zhang, Silver nanoplate aggregation based multifunctional black metal absorbers for localization, photothermic harnessing enhancement and omnidirectional light antireflection, J. Mater. Chem. C 6 (5) (2018) 989–999.
[29] S.-Q. Zhu, T. Zhang, X.-L. Guo, Q.-L. Wang, X. Liu, X.-Y. Zhang, Gold nanoparticle thin films fabricated by electrophoretic deposition method for highly sensitive SERS application, Nanoscale research letters 7 (1) (2012) 613.
[30] S.K. Dondapati, P. Lozano-Sanchez, I. Katakis, Controlled electrophoretic deposition of multifunctional nanomodules for bioelectrochemical applications, Biosens. Bioelectron. 24 (1) (2008) 55–59.
[31] R. Zhang, Y. Zhu, J. Huang, S. Xu, J. Luo, X. Liu, Electrochemical sensor coating based on electrophoretic deposition of Au-Doped self-assembled nanoparticles, ACS Appl. Mater. Interfaces 10 (6) (2018) 5926–5932.
[32] V. Nikolova, I. Nikolov, P. Andreev, V. Najdenov, T. Vitanov, Tungsten carbide-based electrochemical sensors for hydrogen determination in gas mixtures, J. Appl. Electrochem. 30 (6) (2000) 705–710.
[33] K. Okamura, T. Ishiji, M. Iwaki, Y. Suzuki, K. Takahashi, Electrochemical gas sensor using a novel gas permeable electrode modified by ion implantation, Surf. Coating. Technol. 201 (19) (2007) 8116–8119.
[34] Y.C. Liu, B.J. Hwang, Y.L. Chen, Nafion based hydrogen sensors: Pt/Nafion electrodes prepared by takenata-torikai method and modified with polypyrrole, Electroanalysis 14 (7–8) (2002) 556–558.
[35] Y. Chao, S. Yao, W.J. Buttner, J.R. Stetter, Amperometric sensor for selective and stable hydrogen measurement, Sensor. Actuator. B Chem. 106 (2) (2005) 784–790.

Electrochemical Hydrogen Gas Sensing Employing Palladium Oxide/Reduced Graphene Oxide (PdO-rGO) Nanocomposites

Kamal Arora, Saurabh Srivastava, Pratima R. Solanki, and Nitin Kumar Puri

Abstract— **This research work aims at proposing cheap, facile, sensitive, and selective assembly of three electrode electrochemical hydrogen (H_2) gas sensor which operates on room temperature in ambient conditions. Palladium oxide-reduced graphene oxide (PdO-rGO) nanocomposite have been synthesized using insitu chemical sol-gel method and modified Hummer's method. The phase, structure, particle size, and bonding information have been obtained using X-ray diffraction (XRD) analysis, transmission electron microscopy (TEM), Fourier Transform Infrared (FTIR) spectroscopy, and Ultraviolet-Visible (UV-Vis) absorption spectroscopy. Palladium oxide (PdO) nanoparticles of size ranging from 30 to 35 nm have been successfully attached with uniform 2D network of reduced graphene oxide (rGO) sheets which offers a large surface area for H_2 adsorption. The thin film of nanocomposite have been fabricated on conducting Indium tin oxide (ITO) glass substrates using electrophoretic deposition (EPD) process and is employed as working electrode (WE) in indigenously developed three-electrode cell. Thin film surface morphology have been observed using Scanning Electron Microscopy (SEM) and it shows agglomerates of PdO nanoparticles with multiple randomly stacked rGO nanosheets uniformly spread across the surface of the film. The amperometric response of the assembled electrochemical sensor has been recorded for the detection of 10 to 80 percent concentration of hydrogen gas using potentiostat/galvanostat autolab. The sensitivity of the sensor is found out to be 0.462 μA/% H_2 concentration and sensing calibration curve shows a uniform linear response. The stability and selectivity of the sensor has been enhanced using H_2 insensitive reference electrode (RE) and solid polymer electrolyte gas permeable membrane, respectively, which will aid new dimensions in designing robust H_2 sensor at room temperature.**

Index Terms— **Amperometry, hydrogen gas sensor, metal oxide, graphene, nanocomposite.**

I. Introduction

HYDROGEN (H_2) gas is reducing in nature and employed in aerospace, energy, medical, aerospace and petrochemical industries [1]. Its highly flammable and combustible characteristics lead to explosion on leakage and it causes hydrogen embrittlement on its penetration into metal and alloy systems. Additionally, hydrogen evolution results into corrosion of metals [2]. Thus, there is a significant need for highly sensitive, selective and stable hydrogen gas sensors which can detect even the order of parts per million of this gas i.e. lower explosive limit (LEL, 4% H_2 in air). These hydrogen sensors should operate in ambient, low temperature and even high temperature surroundings. The most effective sensors should also possess fast response towards the physically undetectable hydrogen gas accompanied with high sensitivity and selectivity [3].

Various types of sensors based on their mechanism have been used for hydrogen sensing application, but electrochemical and conductometric types of sensors have been researched more due to their peculiar merits. However, conductometric sensors require higher working temperature and low relative humidity (RH) for efficient working and it becomes difficult to detect gases in ambient condition, whereas electrochemical sensors can sense gases at room temperature with high degree of sensitivity and selectivity at cheaper cost [3], [4]. Electrochemical sensors are divided into types i.e. potentiometric & amperometric. Although, former provides extensive dynamic range, but lacks accuracy towards its logarithmic response. On the other hand, latter provides highly linear and accurate sensing response [5]. In amperometric sensing, a constant potential is achieved across the circuit using variable resistor and relationship between current versus time is obtained [6].

Carbon based materials such as carbon nanotubes (CNT) and graphene received a lot of attention over others due to their remarkable physical, chemical and electrical properties. Graphene has been the source of major research work in developing new catalysts over other carbon allotropes due to its exceptional properties. Theoretical specific surface area of graphene is 2600 $m^2\ g^{-1}$ which is double to that of CNT and much higher than other allotropes of carbon comprehensively. On comparison to carbon nanotubes, graphene especially pure chemically modified graphene (CMG) can be synthesized at large scale in much cheaper cost using graphite oxide as precursor without support of metallic catalysts. The inclusion of these catalysts leads to impurities in CNT, which affect its electrochemical properties. Graphene electronic structure contains free localized π electron which imparts it high electron mobility and conductivity as well as high catalytic activity. Graphene is highly stable in nature both physically and

Manuscript received April 3, 2019; accepted May 6, 2019. Date of publication May 22, 2019; date of current version August 15, 2019. This work was supported in part by the Inter University Accelerator Center (IUAC) Sponsored Project under Grant IUAC/XIII.7/UFR-56324, in part by the Department of Atomic Energy-Board of Research in Nuclear Sciences *(DAE-BRNS)*, India, in part by Science and Education Research Board (SERB), Department of Science and Technology (DST), India, under Grant EMR/2016/007479, and in part by DST, India, under Grant IFA14-MS-34. The associate editor coordinating the review of this paper and approving it for publication was Dr. Chirasree Roychaudhuri. *(Corresponding author: Nitin Kumar Puri.)*

K. Arora, S. Srivastava, and N. K. Puri are with the Advanced Sensor Laboratory, Department of Applied Physics, Delhi Technological University, New Delhi 110042, India (e-mail: nitinkumarpuri@dtu.ac.in).

P. R. Solanki is with the Special Centre for Nanoscience, Jawaharlal Nehru University, New Delhi 110067, India.

Digital Object Identifier 10.1109/JSEN.2019.2918360

chemically, which provides it with longer lifetime in catalytic activities [7], [8]. Method adopted for synthesis of graphene determines the level of purity, however pure graphene is not electroactive towards hydrogen gas in nature, graphene extracted through chemical method leaves behind some chemical impurities and defects which gives them enhanced catalytic activity as compared to pure graphene, known as chemically modified graphene (CMG) i.e. graphene oxide (GO) and reduced graphene oxide (rGO) [9]. Graphene oxide (GO) owing to large number of oxygenated functional groups and defects, is insulating in nature and shows poor electrochemical properties. To restore the conductivity of pristine graphene, its conversion to reduced graphene oxide (RGO) is essential for most of the electrochemical applications. High surface-to volume ratio and abundant surface defects provides rGO larger surface area for adsorption and other catalytic activity as compared to graphene oxide (GO) [10]. The electroactivity of rGO for hydrogen gas can further be enhanced by doping it with superior catalytic metals such as palladium (Pd) or platinum (Pt) or by forming their composites with other electroactive materials [11]. These doped or composite graphene materials can be used as working material in sensors and fuel cells [12].

Pd nanoparticles is most researched hydrogenation catalyst as it is a good initiator of hydrogen spillover over desired material [13], [14], Pd-rGO nanocomposites has been used as sensing element in hydrogen conductometric sensor and it was found that Pd-rGO composite shows good sensitivity as compared to rGO [15], [16]. Also, It has been found that Pd doped rGO and Pt doped rGO shows high hydrogen sensitivity and selectivity, but former reflects more sensitivity as compared to latter [17]. Nevertheless, pure Pd is costly material and over the time, it is poisoned due to the deposition of sulphur on being in contact with the atmosphere. Whereas, palladium oxide (PdO) is secured from the contamination as it has high operating temperature and protective sheath of oxide layer [18]. Thus, PdO nanoparticles can be substituted for pure Pd for hydrogen gas sensing. Pristine PdO nanoflakes and nanoparticles thin films have been used for conductometric hydrogen gas sensing application and it has been found that they showed high sensitivity and selectivity towards hydrogen gas [19]–[21]. Nanostructured PdO particles and their composites have been studied for carbon monoxide (CO) and other organic volatile gas sensing application [22]–[30]. In our preceding research work, PdO nanoparticles have been studied for amperometric hydrogen gas sensing at room temperature and they showed good sensitivity for H_2 gas among other similar sensors [31]. Nanocomposites of PdO with rGO will enhance the sensitivity of amperometric sensor towards hydrogen gas and moreover they have not been studied before to the best of our knowledge.

In the current work, PdO-rGO nanocomposite and rGO have been synthesized using simple and cost effective insitu chemical sol-gel method and improved modified Hummer's method respectively. PdO-rGO nanocomposite thin film has been fabricated on ITO glass substrate using electrophoretic deposition process. Consequently, PdO-rGO/ITO has been used as working electrode (WE) in indigenously developed three electrode cell for amperometric hydrogen gas sensing at room temperature.

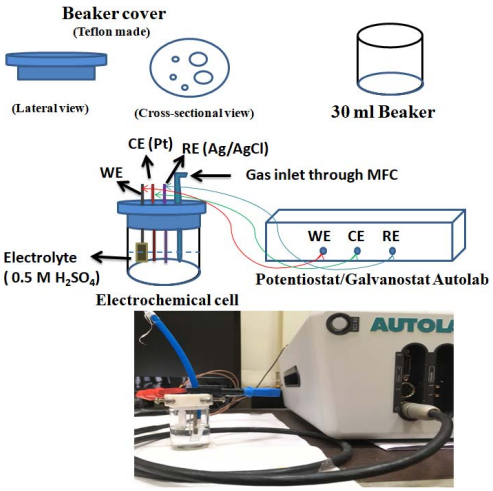

Fig. 1. Electrochemical sensing setup.

II. Experimental

A. Electrochemical Sensing Setup

The setup consist of three electrodes (working electrode (WE), Counter electrode (CE) & Reference electrode (RE)) placed in a electrochemical cell attached to Potentiostat/galvanostat autolab instrument for amperometric (current (i) vs time (t)) measurement (fig. 1).

The CE is made up of (4 cm × 1 mm) Platinum (Pt) cylindrical rod because of its lower oxygen reduction overpotential and less hydrogen solubility in comparison to palladium (Pd) [1]. Reference electrode (RE) is made up of Nafion coated (5 cm × 3 mm) silver/silver chloride (Ag/AgCl) cylindrical rod, because Ag/AgCl remains stable and maintains zero potential shift throughout the reaction between the WE and CE and coating of Nafion polymer allow only hydrogen ion to diffuse to the RE while restricting diffusion of other ions [1]. Silver chloride (AgCl) is deposited onto silver (Ag) electrode by its chloridization in $FeCl_3$/0.1 M HCl solution for 24 hours. The traces of $FeCl_3$ are removed by rinsing electrode with DI water and immersing the electrode in saturated AgCl solution, which results in uniform gray black layer on the electrode. Consequently, Ag/AgCl electrode is coated with uniform Nafion coating by dipping it several times in 5% Nafion 117 polymer solution [32], [33].

Working electrode consist of PdO-rGO nanocomposite thin film as a hydrogen sensing material placed inside electrochemical cell. The electrochemical cell has been fabricated using 30 mL glass beaker sealed with Teflon made beaker cover containing three electrode inlets, a gas inlet as depicted in fig. 1. The electrochemical cell is attached to potentiostat/galvanostat autolab using crocodile connectors and it is filled with 0.5 Molar concentration of sulphuric acid (0.5 M H_2SO_4). The use of proton conducting liquid electrolyte permits setup to be operated at room temperature in ambient conditions and mitigate the problem of relative humidity (RH) in sensor, whereas although solid polymer electrolyte are more

stable and less corrosive, but they are strongly affected by humidity in the surrounding and have low conductivity at room temperature [34]. Also, the ionic liquid (IL) electrolytes which have the best traits of both liquid and solid polymer are not readily used in electrochemical gas sensors because they generate slower response time due to their low conductivity and high viscosity in ambient conditions [35]. The proposed electrochemical sensing setup is attached to the Alicat scientific MC standard series gas mix mass flow controller (MFC) using Teflon pipes.

B. Fabrication of Working Electrode

The chemicals used in synthesis of Palladium oxide-reduced graphene oxide (PdO-rGO) nanocomposite are sulphuric acid (H_2SO_4), phosphoric acid (H_3PO_4), potassium permanganate ($KMnO_4$), graphite powder, distilled water (H_2O), hydrazine hydrate ($N_2H_4.H_2O$), palladium chloride ($PdCl_2$), ethanol (C_2H_5OH) and hydrochloric acid (HCl).All the chemicals used are procured from Fisher and Sigma Aldrich and belongs to AR grade purity (∼99.9 %).

1) Synthesis of rGO: GO is synthesized using improved Hummer's method as suggested by Marcano et al., 26.7 mL of concentrated H_3PO_4 is added to 240 mL of concentrated H_2SO_4 in 9:1 ratio in a conical flask. 2 g graphite powder is added to the H_2SO_4/H_3PO_4 solution. 12 g of $KMnO_4$ is added to the resultant solution slowly as the reaction is highly exothermic. The addition of $KMnO_4$ is followed by stirring of solution at 50° C for 12 hours. The solution is mixed with 270 mL of ice along with slow addition of 2 mL H_2O_2. The resultant brown colored solution in the conical flask is filtered, washed with HCl and subsequently added with distilled water until pH value of 7 is obtained. The resultant solution is dried off at 70° C to obtain brown powder of GO [36].

Park et al. successfully produced high purity rGO using hydrazine hydrate ($N_2H_4.H_2O$) as reducing agent. 300 mg of GO is added to 300 mL of distilled water through continuous stirring in a 500 mL glass beaker. 100 μL of $N_2H_4.H_2O$ is dissolved into the beaker slowly and solution is left for 12 hours under continuous stirring. The final solution turns black colored which is filtered, washed with distilled water to remove traces of $N_2H_4.H_2O$ and is dried at 70° C to obtain black powder of rGO [37].

2) Synthesis of PdO-rGO Nanocomposites: PdO-rGO nanocomposites have been synthesized using insitu chemical solution method. $PdCl_2$ is dissolved in 30 mL solution of rGO and ethanol (1μg/mL) such that their molar ratio remains (1:1) respectively. The solution is continuously stirred for 1 hour to mix uniformly. The resultant solution is kept untouched for 24 hours as a process of ageing. Thereafter, the solution is heated at 80° C for 24 hours to extract brown colored powder. The powder is washed and filtered with DI water several times. Subsequently, the filtered powder is annealed at 600° C to remove organic and chloride ions impurities which yields a black colored powder. The structure, morphology and nature of bonds of the black powder is determined through X-ray diffraction (XRD), Transmission electron microscopy (TEM), Scanning electron microscopy (SEM), Fourier Transform Infrared Spectroscopy and Ultraviolet-Visible (UV-Vis) absorption spectroscopy processes. The analysis of the data obtained from these processes shows the formation of PdO-rGO nanocomposites in the insitu as-synthesized black powder.

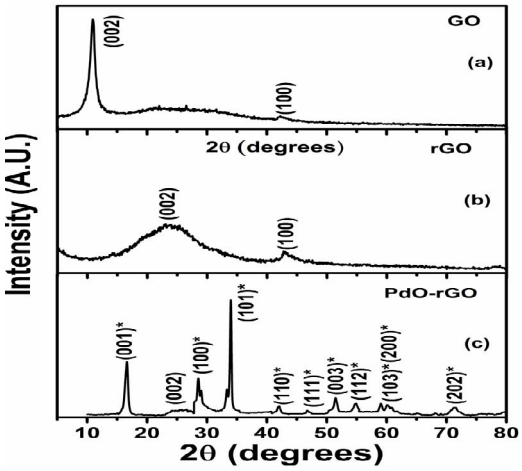

Fig. 2. XRD plot of (a) GO, (b) rGO, (c) PdO-rGO nanocomposite.

Subsequently, 1 μm thick uniform PdO-rGO nanocomposite thin film is deposited onto the conductive (5 mm × 10 mm) ITO coated glass substrate using electrophoretic deposition (EPD) process by applying a constant potential of 40 V for 2 minutes. These fabricated thin films of PdO-rGO are used as working electrode in electrochemical cell for hydrogen gas sensing.

III. Results and Discussions

A. X-Ray Diffraction Analysis (XRD)

The graphs presented in fig. 2(a), (b) and (c) represent the XRD plot of GO, rGO and PdO-rGO nanocomposite respectively. Sharp peak at 11.01° in fig. 2(a) shows the formation of characteristics (002) plane of GO whereas a broad peak at 23.78° in fig. 2(b) confirms the formation of featured (002) plane of rGO. On comparison of intensity of peaks shown in fig. 2(c) with the published JCPDS data (CAS number: 750200 and 850624), it can be deducted that the intensity peaks (001)*, (100)*, (101)*, (110)*, (111)*, (003)*, (112)*, (103)*, (200)* and (202)* corresponds to tetragonal PdO (t-PdO), whereas small hump (002) at 25° belongs to rGO.

Maximum sharp intensity peak at 34° and weaker broad peak at 25.45° belongs to (101) plane of t-PdO and (002) plane of rGO correspondingly. Hence, XRD analysis shows the formation of crystal structure which contains composite of both t-PdO and rGO collectively.

The average size of the t-PdO crystallites and number of rGO layers can be obtained using Scherrer and Bragg's formula. [Eq. 1 and 2] [38], [39]. The d-value of GO for (002) plane is found to be 8.02 Å, whereas d-value of rGO for (002) plane is found to be 3.74 Å respectively. Tetragonal PdO crystallite size is calculated to be 23.72 nm and number

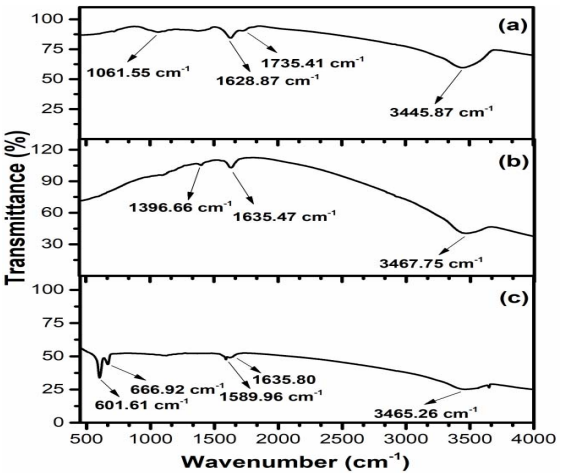

Fig. 3. FTIR spectroscopy plot of (a) GO, (b) rGO, (c) PdO-rGO nanocomposite.

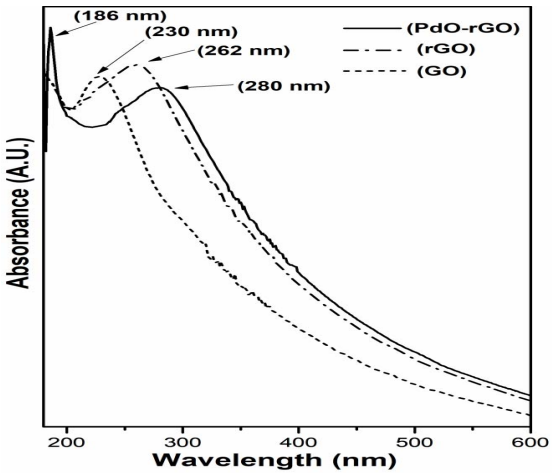

Fig. 4. UV-Vis Spectra of GO, rGO and PdO-rGO nanocomposite.

of rGO layers is found to be equal to three.

$$t = \frac{0.9\lambda}{\beta cos\theta} \tag{1}$$

$$2dsin\theta = n\lambda \tag{2}$$

d is interplanar spacing, n is order of principal maxima, β is the FWHM (Full width half maxima), λ is wavelength, θ is the angle having maximum intensity and t represent crystallite size.

B. Fourier Transform Infrared (FTIR) Spectroscopy

Fig. 3(a), (b) and (c) shows the FTIR plot of GO, rGO and PdO-rGO nanocomposite respectively. The graphs depicted in fig. 3(a) and (b) represent the FTIR spectra of GO and rGO respectively, the absorption bands generated at 1061.55 cm^{-1}, 1628.87 cm^{-1} and 1735.41 cm^{-1} correspond to -C-O- stretching, -C–O–H- deformation and C=O stretching of -COOH- group respectively [40]. The broad absorption band arising at wavenumber 3445.87 cm^{-1} denotes the existence of -O-H- functional groups. Nevertheless, on reduction of GO with hydrazine monohydrate, the oxygen functional groups present in GO FTIR spectra, reduced significantly in case of rGO, the new band at 1396.66 cm^{-1} arises due to the vibration of the graphene sheets skeletal (fig. 3(b)) [41].

In fig. 3(c), the bands arising at 601.61 cm^{-1} and 666.92 cm^{-1} correspond to formation of the -Pd-O- and -Pd-C- vibrational bonds respectively. Other absorption bands appearing in this plot are identical to that of rGO, (fig. 3(b)), but there is an apparent right shift and splitting in the bands, now appearing at 1589.96 cm^{-1}, 1635.80 cm^{-1} and 3465.26 cm^{-1}, due to formation of bonds between PdO and carboxylic as well as hydroxyl groups present in the rGO sheets.

C. Ultraviolet Visible (UV-Vis) Spectroscopy

UV-Vis spectra of GO, rGO and PdO-rGO nanocomposite are shown in fig. 4 through dotted, dashed and solid line respectively. The reduction of GO can be easily observed through this spectra as the absorption peak arising at 230 nm

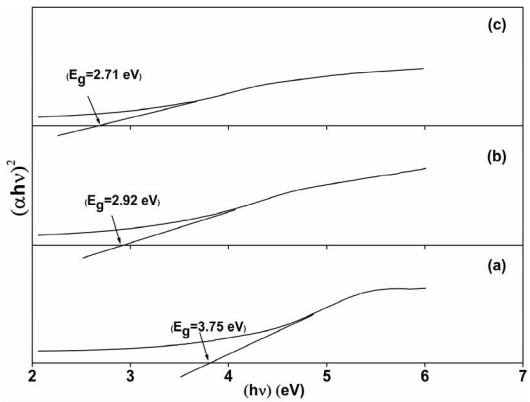

Fig. 5. Tauc plot of (a) GO, (b) rGO and (c) PdO-rGO.

due to $\pi - \pi^*$ transition of C-C bond shifted towards higher wavelength of 262 nm, indicating removal of oxygen containing functional groups present in GO structure which increased the concentration of π electron and restored the sp^2 C-C conjugated structure [42].

There is an apparent red shift in absorption peak of rGO towards 280 nm from 262 nm in UV-Vis spectra of PdO-rGO nanocomposite. It can be attributed towards increase in the π electron concentrations and relaxation of the composite structure due to its doping with PdO nanoparticles [43]. Moreover, there is also an absorption peak present at 186 nm which affirms the formation of PdO in the PdO-rGO nanocomposite [18].

The Tauc plot of the UV-Vis absorption spectra (Fig. 4) is represented by Fig. 5 which demonstrates the value of optical band gap of GO, rGO and PdO-rGO respectively.

It can be observed in Fig, 5(a) that band gap of GO turns out to be 3.75 eV which gets minimized to 2.92 eV on its chemical reduction by hydrazine hydrate to form rGO (Fig. 5(b)), these computed values coincides with the already reported range of values [44], [45]. On the other hand, formation of PdO-rGO nanocomposite further drops the band gap of material to 2.71 eV as visible in Fig. 5(c).

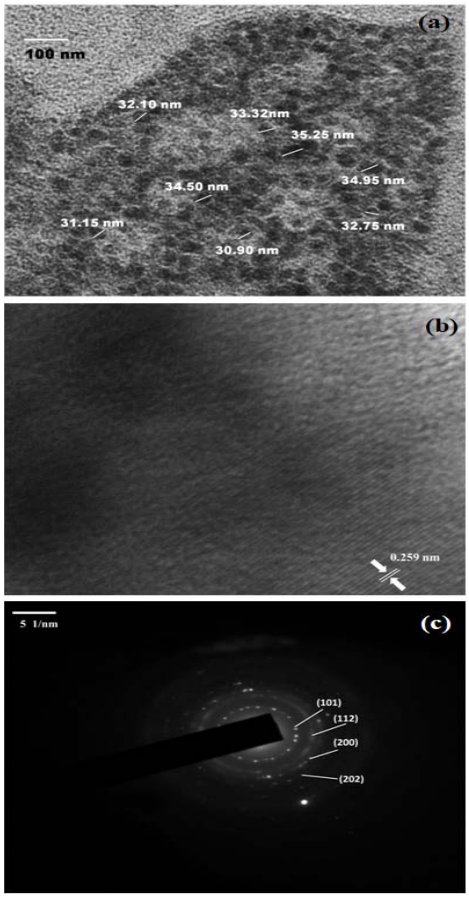

Fig. 6. (a) TEM image, (b) HRTEM image, (c) SAED image of PdO-rGO nanocomposite.

D. Transmission Electron Microscopy (TEM)

Fig. 6(a), (b) and (c) show the images of TEM, high resolution TEM (HRTEM) and selected area electron diffraction (SAED) for PdO-rGO nanocomposite. In fig. 6(a), nanoparticles of size of the order of 30 to 35 nm, with uniform shape and boundaries, can be seen embedded into the transparent 2D rGO sheet like structure. Fig. 6(b) shows the well-defined uniform parallel planes with spacing of 0.225 nm, which corresponds to the interplanar spacing of (101) plane of t-PdO crystal structure on comparison with published JCPDS data (CAS number 750200).

Rings formed by bright dots together with the presence of fused rings are visible in SAED pattern (Fig. 6(c)), which suggests the formation of polycrystalline (101), (112), (200) and (202) planes of t-PdO structure and amorphous rGO sheets.

Hence, TEM analysis agrees with the initial recommendation of XRD analysis about the formation t-PdO-rGO nanocomposite.

E. Scanning Electron Microscopy (SEM)

Fig. 7 illustrates the low resolution (1μm) and high resolution (500 nm) images of surface of thin film of PdO-rGO nanocomposite deposited on ITO glass substrate. Randomly blended and uniformly aggregated multiply stacked

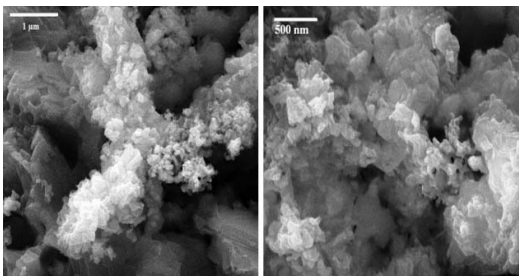

Fig. 7. Scanning electron microscopy (SEM) images of PdO-rGO nanocomposite thin film.

2D nanosheets of rGO can be seen on the surface of the sample in form of dark grey area of the images. However, the bright clusters of spots in images represent the agglomerates of PdO nanoparticles within rGO nanosheets.

These wrinkled 2D nanosheets of rGO are folded at the edges and spread homogeneously along the surface of the sample offering large surface area to the clusters of PdO nanoparticles.

Shape of nanoparticles along with the boundaries between particles and sheets are not visible, since the actual size of particles ranges from (30 to 35 nm), which are clearly visible in TEM image (fig. 6(a)).

F. Electrochemical H_2 Amperometric Sensing Study

Various percentage concentration ratio of H_2/Argon gas is introduced into the electrochemical gas sensing setup (fig. 1.) by composing gas mixture through MFC under ambient condition at room temperature.

There are several factors which affect the sensing efficiency of electrochemical sensors; (a) Flow rate and (b) Selectivity. The flow rate determines the diffusion of gas into the electrolyte and since electrochemical reaction is diffusion limited process, thus, it is important to select suitable flow rate to achieve good sensing response from the sensor. The presence of other gases in surrounding could deter the selectivity of WE toward sensing of H_2 gas and hence would affect the efficiency of the electrochemical sensor [5]. Fig. 8 represents the plot between sensing response current (μA) and different flow rate (mL/min) in presence of 80% H_2 gas.

This plot has been fitted using non-linear curve fit with equation $y = 39.23^{*}\ln(1.31\ln(x))$ with R^2 value of 0.99128, where ln stands for natural logarithm, y indicate the electrochemical sensing current in μA and x represent the flow rate of H_2 gas in mL/min. It can be seen that current raises steeply from flow rate of 10 mL/min to 60 mL/min and then increases steadily onwards upto 200 mL/min. Thus, flow rate of 60 mL/min has been selected as constant flow rate for obtaining amperometric sensing response of electrochemical sensor for various percentage concentration of H_2 gas.

The electrochemical sensor is sealed with cylindrical Teflon cover and inlets with white Teflon tape to protect it from atmospheric gases. Although, Argon is an inert and non-reactive gas, but an 50 μm thick fluorinated ethylene propylene (FEP) selective gas permeable polymer membrane is placed in front of gas inlet to allow only H_2 gas out of

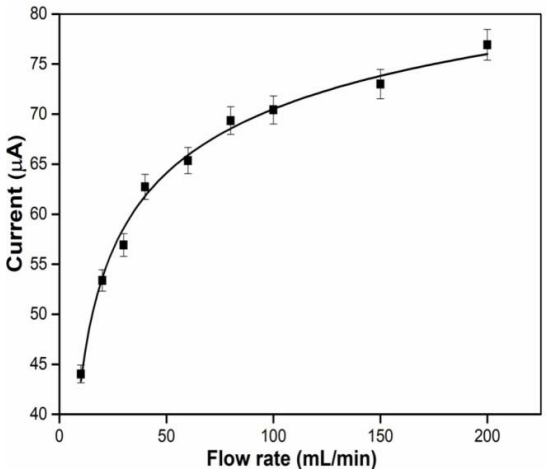

Fig. 8. Flow rate (mL/min) v/s current (μA) relation for 80% H_2 gas.

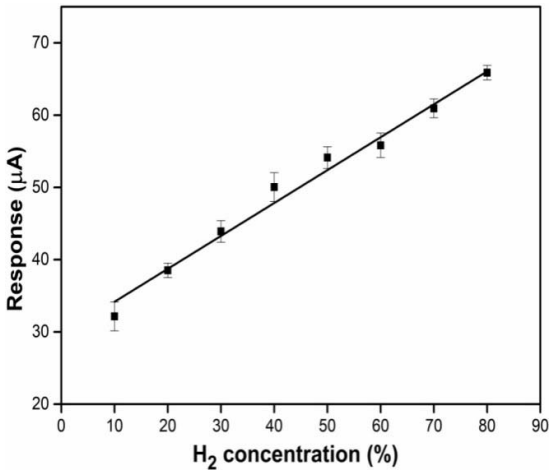

Fig. 10. Calibration plot of response current (μA) vs H_2 concentration (%).

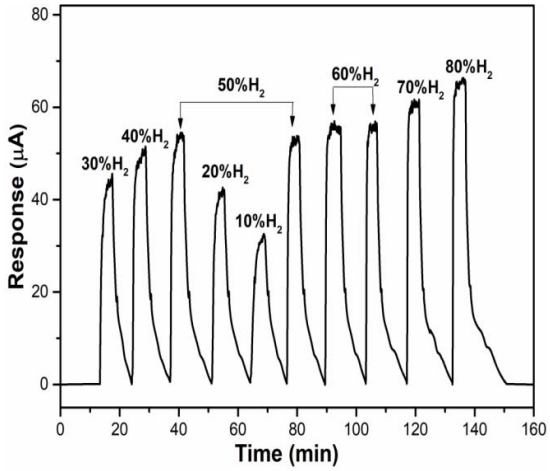

Fig. 9. Response curve for different percentage concentration of H_2 gas.

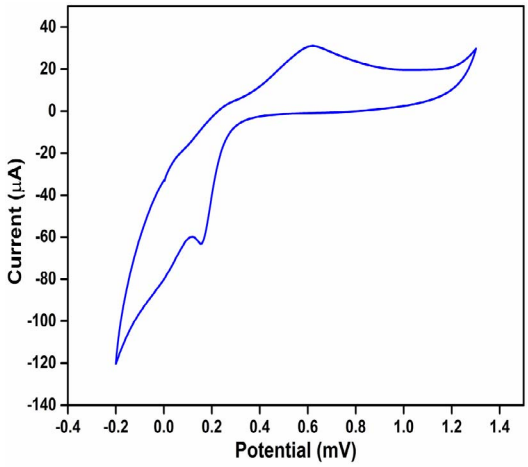

Fig. 11. Cyclic voltammetry study of PdO thin film.

H_2/Argon gas mixture to flow into the electrochemical cell to enhance its selectivity and efficiency.

The H_2 gas is allowed to flow into the electrochemical cell for 5 minutes and thereafter the flow is cutoff to measure the amperometric sensing response by maintaining a fixed potential of 1 V using potentiostat/galvanostat autolab.

Fig. 9 illustrates the amperometry of electrochemical sensor for various percentage (10-80) % of H_2 gas. Steep increase in current is observed on introduction of the gas which becomes constant after reaching a plateau and thereafter decays quickly as soon as gas is cutoff from flowing into the electrochemical cell.

The amperometric response of electrochemical sensor for different percentages of H_2 concentration is illustrated in fig. 9. It shows high sensitivity, stable and fast sensing response with quick recovery time. The time taken by the sensor to reach 90% of steady state current (t_{90}) ranges from 30 to 60 seconds for different percentage of H_2.

The calibration plot of sensor response is depicted in Fig. 10; it shows linear increase in current on raising the percentage concentration of H_2 gas from 10 to 80%. The sensitivity (S) of electrochemical sensor is found out to be (0.462 ± 0.023) μA/%(H_2) with R^2 variance of 0.98229 and fitted by linear regression equation $y = 29.38 + 0.462x$, where x and y represent the percentage concentration (%) of H_2 gas and the response current (μA) of the electrochemical sensor respectively.

Thus, the sensitivity of amperometric sensor towards H_2 gas is enhanced on using PdO-rGO nanocomposite as WE in comparison to pristine PdO nanoparticles [31]. The Limit of detection (LOD) of the fabricated amperometric sensor is calculated to be equal to 0.13% H_2 [32].

The catalytic behavior of palladium oxide (PdO) in presence of 0.5 M sulphuric acid (H_2SO_4) in a electrochemical reaction has been experimentally studied using cyclic voltammetry (CV) (fig. 11). The voltammerty study has been conducted using potential range from -0.2 mV to $+1.3$ mV with a scan rate of 100 mV s^{-1}. It is observed that the reoxidation of PdO occurs during anodic sweep and the maximum anodic oxidation current arises at 0.62 mV, whereas in the cathodic sweep, the reduction of PdO takes place with maximum cathodic reduction current appears at 0.15 mV. This confirms the redox catalytic behavior of PdO and also agrees with the already published similar research work [46], [47].

The cyclic voltammetry (CV) study of PdO-rGO thin film in 0.5 M Sulphuric acid (H_2SO_4) electrolyte has also been

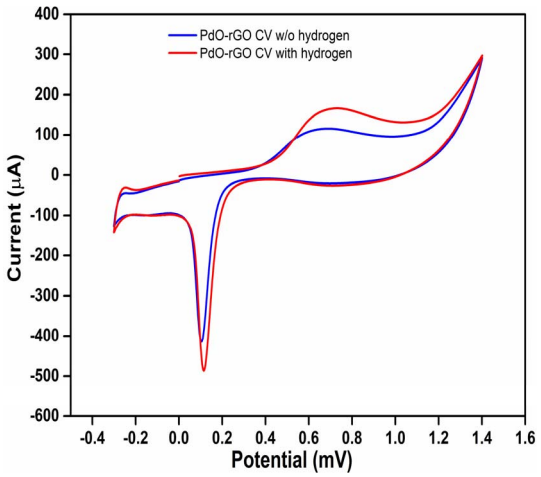

Fig. 12. Cyclic voltammetry study of PdO-rGO nanocomposite thin film.

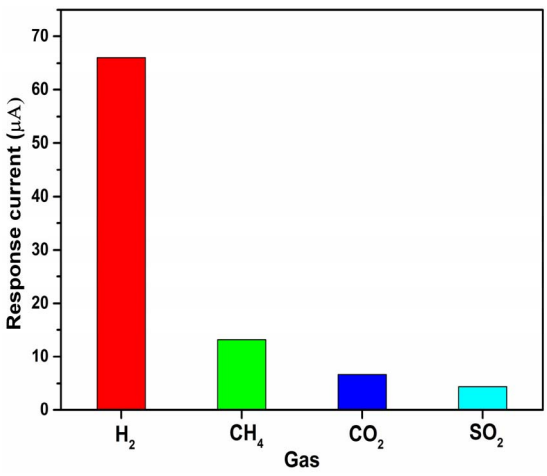

Fig. 13. Response of PdO-rGO nanocomposite based amperometric sensor to various gases.

carried out before and after flowing hydrogen gas, with scan rate of 100 mV s^{-1}. Fig. 12 depicts the CV study of PdO-rGO nanocomposite thin film including both before and after flow of hydrogen gas for 5 minutes (Gas on time is same as used during amperometric H_2 sensing study).

It can be seen that both CV curve coincides with each other perfectly (fig. 12). However, the maximum current value in both reduction as well as the oxidation peaks rises appreciably after the flow of hydrogen gas. The maximum oxidation current in cathodic cycle occurs at 0.65 mV, whereas the maximum reduction current during anodic cycle appears at 0.10 mV and after flow of hydrogen gas, the reduction potential shift towards 0.12 mV and oxidation potential moves towards 0.72 mV respectively.

This shift towards higher potential can be attributed to the high concentration of hydrogen ions within the electrolyte; the population of H^+ ions reaching the electrolyte-WE surface region rises to the point that it creates a barrier for other incoming H^+ ions to participate in the electrochemical reactions.

Hence, CV study affirms that PdO act as an electrocatalytic material towards H_2 gas and returns to its initial state after completion of electrochemical reaction. Wen et. al. showed the mechanism for probable redox reaction taking place on introducing PdO WE in H_2SO_4 electrolyte [47]. Also, after the flow of hydrogen gas in the electrochemical cell, the oxidation of H_2 takes place at the sensing electrode by which it ionizes itself and releases two electrons [1], [3], [5].

Thus, the possible redox mechanism explaining this electrochemical reaction may be as follows:

(Before Hydrogen gas flow)

$$PdO + H_2O \leftrightarrows PdO_2 + 2H^+ + 2e^-$$

$$2PdO_2 \leftrightarrows 2PdO + O_2$$

(After Hydrogen gas flow)

$$PdO + H_2O + H_2 \leftrightarrows PdO_2 + 4H^+ + 4e^-$$

$$2PdO_2 + 4H^+ + 4e^- \leftrightarrows 2PdO + 2H_2O$$

The selectivity of PdO-rGO nanocomposite based amperometric sensor towards various gases has been studied using similar parameters as in H_2 gas sensing and comparison of their sensing response is depicted in Fig. 13. 80 % concentration of Methane (CH_4), Carbon dioxide (CO_2) and Sulphur dioxide (SO_2) gas is introduced into electrochemical cell at flow rate of 60 mL/min and their sensing response is measured in terms of sensing current (μA) at room temperature. It is observed that PdO-rGO/ITO WE shows significant change in current for H_2 gas in comparison to other gases. Although, it shows sensitivity for CH_4 gas too, but it is comprehensively smaller in comparison to H_2. On the other hand, sensing response for CO_2 and SO_2 is negligibly minute, to be considered insensitive.

When SO_2 gas is introduced into the electrochemical cell containing PdO-rGO nanocomposite as WE and H_2SO_4 as electrolyte, the mechanism of its interaction can be divided into following steps, (a) Diffusion or Physical dissolution of SO_2 molecules to sulphite ions (SO_4^{2-}) within the electrolyte, (b) transport of dissolved SO_4^{2-} ions to surface of WE, (c) Diffusion of SO_4^{2-} ions by WE, (d) electro-oxidation of SO_4^{2-} ions at PdO-rGO nanocomposite thin film surface, (e) simultaneous reduction of protons released during physical dissolution of SO_2 at CE to restore the ionic content of the system [6], [48]–[51]. The mechanism can also be understood using following electrochemical reactions:

$$SO_2 + 2H_2O \rightarrow SO_4^{2-} + 4H^+ + 2e^-$$

$$PdO + SO_4^{2-} + 2H^+ \leftrightarrow PdSO_4 + H_2O$$

$$\frac{1}{2}O_2 + 2H^+ + 2e^- \rightarrow H_2O$$

The mechanism of interaction of CO_2 gas inside the electrochemical cell containing H_2SO_4 as electrolyte can be explained by following steps and electrochemical equations, (a) ionization of H_2SO_4 to release H^+ ions (a) transport of dissolved H^+ ions and CO_2 molecules to surface of WE, (c) absorption of CO_2 molecules by WE, (d) electro-oxidation at PdO-rGO nanocomposite thin film surface, (e) simultaneous reduction of protons at CE to restore the ionic content of the

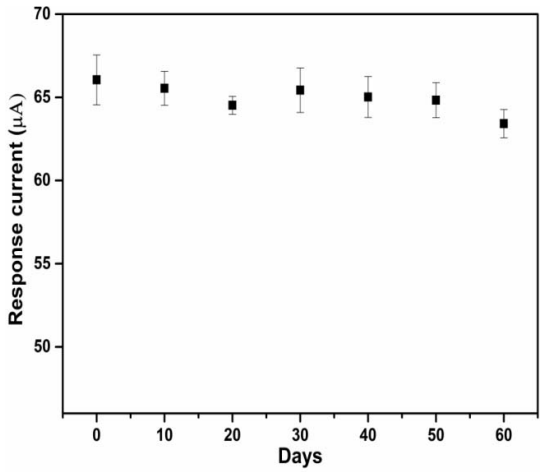

Fig. 14. Stability study of working electrode.

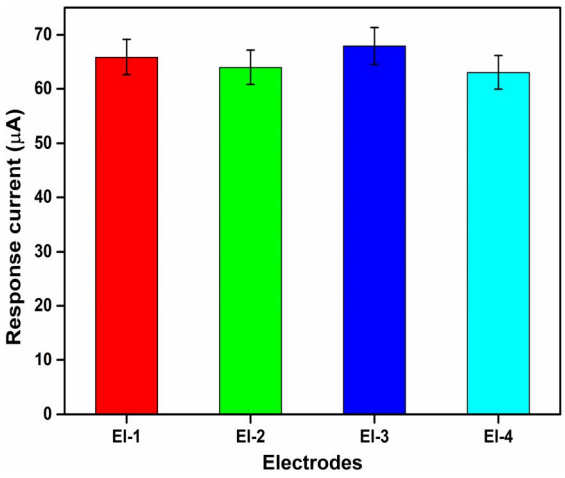

Fig. 15. Reproducibility study of working electrodes.

system [52]–[54].

$$PdO + CO_2 + 2H^+ \leftrightarrow PdCO_3 + H_2O + 2e^-$$
$$\frac{1}{2}O_2 + 2H^+ + 2e^- \rightarrow H_2O$$

These results confirm that fabricated PdO-rGO nanocomposite based amperometric sensor is highly sensitive and selective towards H_2 gas and thus can be utilized for hydrogen gas sensing application in the environment.

The stability of PdO-rGO thin film WE used for the electrochemical sensing of H_2 has been determined using same set of parameters for 60 days (fig. 14). It has been found that there is no significant change in the response current of WE from day 1 to day 60. The current obtained on day 1 is found to be 65.89 μA which decrease to 63.42 μA on day 60. Thus, the results suggest that the fabricated WE is stable and aptly suited for electrochemical sensing of H_2 gas.

Four sets of electrodes of PdO-rGO nanocomposite thin film have been fabricated by electrophoretic deposition method using same deposition parameters as mentioned in experimental details. These electrodes are then employed as WE for electrochemical sensing of H_2 in similar environmental conditions and the sensing currents are obtained respectively. It can be seen in fig. 15 that there is no considerable variations in the response current of the synthesized electrodes and relative standard deviation (RSD) of the reproducibility study is found to be 3.31% which indicates good reproducibility and precision.

TABLE I
LIQUID ELECTROLYTE BASED AMPEROMETRIC HYDROGEN SENSORS

Gas Analyte	Working Electrode	Liquid Electrolyte	Limit of Detection (%H_2)	Sensitivity (μA/% or (ppm)H_2)	References
H_2	Pt/Carbon	5M H_2SO_4	-	-	[55]
H_2	Gold	9M H_2SO_4	-	-	[56]
H_2	Pt-Ag/AgCl	1M H_2SO_4	<1%	0.0305	[57]
H_2-Air	Pt-Nafion	1 M H_2SO_4	<0.2%	0.008	[58]
H_2-Ar	PdO/ITO	0.5M H_2SO_4	<0.2%	0.222	[31]
H_2-Ar	**PdO-rGO/ITO**	**0.5 M H_2SO_4**	**<0.2%**	**0.462**	**Present work**

Some of the similar amperometric sensors working on liquid electrolyte towards hydrogen sensing application along with their characteristics are reported in table 1.

IV. CONCLUSION

In the present research work, PdO-rGO nanocomposite is synthesized using in-situ chemical sol-gel method and modified Hummer's method. The structure, morphology, nature of bonds and its optical band gap are studied using XRD spectroscopy, FTIR transmission spectroscopy, UV-Vis absorption spectroscopy, TEM, HRTEM, and SAED images. TEM images confirm the formation of nanoparticles embedded on the 2D nanosheet, with particles size ranging from 30 to 35 nm. XRD analysis recommends the formation of t-PdO crystals structure in chemically synthesized PdO-rGO composite. HRTEM and SAED studies, also agree with the XRD regarding formation of t-PdO crystal structure along with amorphous rGO in form of PdO-rGO nanocomposite. The optical band gap of the nanocomposite is found to be 2.71 eV as computed by UV-Vis absorption spectroscopy and its Tauc plot.

The thin films of PdO-rGO nanocomposite is fabricated on ITO glass substrate using electrophoretic deposition process. These thin films are used as WE in the proposed assembled electrochemical setup for H_2 sensing application. Different concentration (10 to 80%) of H_2 is introduced at 60 mL/min into electrochemical cell containing PdO-rGO nanocomposite thin film as WE and sensing response is measured using amperometry. The response curve shows good sensing response time ranging from 30-60 seconds and fast recovery time. The proposed electrochemical sensor shows high sensitivity of 0.462 μA/%(H_2) at room temperature in ambient atmospheric conditions. Moreover, the sensor is highly selective towards hydrogen gas compared to other environment pollutant gases. Thus, it can be employed for sensing low as well high concentration H_2 gas present in the surroundings. Further, different nano-hierarchal structures of PdO and its composites will be used to enhance sensitivity and selectivity of electrochemical H_2 sensor.

ACKNOWLEDGMENTS

The author would like to thank Prof. Yogesh Singh, Vice chancellor, Delhi Technological University, Delhi, India for

providing the research facilities. The first author is thankful to Council of Scientific and Industrial Research (CSIR), India for providing the SRF-Direct fellowship as financial assistance.

REFERENCES

[1] G. Korotcenkov, S. Do Han, and J. R. Stetter, "Review of electrochemical hydrogen sensors," *Chem. Rev.*, vol. 109, no. 3, pp. 1402–1433, Feb. 2009.

[2] J. Song and W. Curtin, "A nanoscale mechanism of hydrogen embrittlement in metals," *Acta Mater.*, vol. 59, no. 4, pp. 1557–1569, Feb. 2011.

[3] T. Hübert, L. Boon-Brett, G. Black, and U. Banacha, "Hydrogen sensors—A review," *Sens. Actuators B, Chem.*, vol. 157, no. 2, pp. 329–352, Oct. 2011.

[4] W. J. Buttner, M. B. Post, R. Burgess, and C. Rivkin, "An overview of hydrogen safety sensors and requirements," *Int. J. Hydrogen Energy*, vol. 36, no. 3, pp. 2462–2470, Feb. 2011.

[5] X. Lu, S. Wu, L. Wang, and Z. Su, "Solid-state amperometric hydrogen sensor based on polymer electrolyte membrane fuel cell," *Sensors Actuat. B, Chem.*, vol. 107, no. 2, pp. 812–817, Jun. 2005.

[6] J. R. Stetter and J. Li, "Amperometric gas sensors—A review," *Chem. Rev.*, vol. 108, no. 2, pp. 352–366, Jan. 2008.

[7] C. Huang, C. Li, and G. Shi, "Graphene based catalysts," *Energy Environ. Sci.*, vol. 5, no. 10, pp. 8848–8868, 2012.

[8] M. J. Allen, V. C. Tung, and R. B. Kaner, "Honeycomb carbon: A review of graphene," *Chem. Rev.*, vol. 110, no. 1, pp. 132–145, Jul. 2010.

[9] D. R. Dreyer, S. Park, C. W. Bielawski, and R. S. Ruoff, "The chemistry of graphene oxide," *Chem. Soc. Rev.*, vol. 39, no. 1, pp. 228–240, 2010.

[10] S. Stankovich *et al.*, "Synthesis of graphene-based nanosheets via chemical reduction of exfoliated graphite oxide," *Carbon*, vol. 45, no. 7, pp. 1558–1565, Jun. 2007.

[11] A. Esfandiar *et al.*, "The decoration of TiO_2/reduced graphene oxide by Pd and Pt nanoparticles for hydrogen gas sensing," *Int. J. Hydrogen Energy*, vol. 37, no. 20, pp. 15423–15432, Oct. 2012.

[12] P. A. Russo *et al.*, "Room-temperature hydrogen sensing with heterononostructures based on reduced graphene oxide and tin oxide," *Angew. Chem. Int. Ed.*, vol. 51, no. 44, pp. 11053–11057, Oct. 2012.

[13] V. V. E. Rozanov and O. V. Krylov, "Hydrogen spillover in heterogeneous catalysis," *Russian Chem. Rev.*, vol. 66, no. 2, p. 107, 1997.

[14] H. L. Tierney, A. E. Baber, J. R. Kitchin, and E. C. H. Sykes, "Hydrogen dissociation and spillover on individual isolated palladium atoms," *Phys. Rev. Lett.*, vol. 103, no. 24, Oct. 2009, Art. no. 246102.

[15] P. A. Pandey, N. R. Wilson, and J. Covington, "Pd-doped reduced graphene oxide sensing films for H_2 detection," *Sens. Actuators B, Chem.*, vol. 183, pp. 478–487, Jul. 2013.

[16] U. Lange, T. Hirsch, V. M. Mirsky, and O. S. Wolfbeis, "Hydrogen sensor based on a graphene–palladium nanocomposite," *Electrochimica Acta*, vol. 56, no. 10, pp. 3707–3712, Apr. 2011.

[17] R. Ghosh, S. Santra, S. K. Ray, and P. K. Guha, "Pt-functionalized reduced graphene oxide for excellent hydrogen sensing at room temperature," *Appl. Phys. Lett.*, vol. 107, no. 15, Oct. 2015, Art. no. 153102.

[18] K. Arora, D. Sandil, G. Sharma, S. Srivastava, and N. K. Puri, "Effect of low pressure hydrogen environment on crystallographic properties of PdO nanoparticles," *Int. J. Hydrogen Energy*, vol. 41, no. 47, pp. 22155–22161, Dec. 2016.

[19] Y.-J. Chiang, K.-C. Li, Y.-C. Lin, and F.-M. Pan, "A mechanistic study of hydrogen gas sensing by PdO nanoflake thin films at temperatures below 250 °C," *Phys. Chem. Chem. Phys.*, vol. 17, no. 5, pp. 3039–3049, 2015.

[20] Y. T. Lee, J. M. Lee, Y. J. Kim, J. H. Joe, and W. Lee, "Hydrogen gas sensing properties of PdO thin films with nano-sized cracks," *Nanotechnology*, vol. 21, no. 16, Mar. 2010, Art. no. 165503.

[21] S. Choudhury, C. A. Betty, K. Bhattacharyya, V. Saxena, and D. Bhattacharya, "Nanostructured PdO thin film from Langmuir–Blodgett precursor for room-temperature H_2 gas sensing," *ACS Appl. Mater. Interfaces*, vol. 8, no. 26, pp. 16997–17003, Jun. 2016.

[22] C. Wang, P. Zhao, and S. Liu, "PdO/SnO_2 hollow nanospheres for carbon monoxide detection," *Phys. Status Solidi A*, vol. 212, no. 8, pp. 1789–1794, Aug. 2015.

[23] L. Wang, Z. Lou, R. Wang, T. Fei, and T. Zhang, "Ring-like PdO–NiO with lamellar structure for gas sensor application," *J. Mater. Chem.*, vol. 22, no. 25, pp. 12453–12456, 2012.

[24] Y.-J. Chiang and F.-M. Pan, "PdO nanoflake thin films for CO gas sensing at low temperatures," *J. Phys. Chem. C*, vol. 117, no. 30, pp. 15593–15601, Jul. 2013.

[25] Z. Lou, J. Deng, L. Wang, L. Wang, T. Fei, and T. Zhang, "Toluene and ethanol sensing performances of pristine and PdO-decorated flower-like ZnO structures," *Sens. Actuators B, Chem.*, vol. 176, pp. 323–329, Jan. 2013.

[26] I. J. Kim, S. D. Han, I. Singh, H. D. Lee, and J. S. Wang, "Sensitivity enhancement for CO gas detection using a SnO_2–CeO_2–PdO_x system," *Sens. Actuators B, Chem.*, vol. 107, no. 2, pp. 825–830, Jun. 2005.

[27] M. S. Tong, G. R. Dai, and D. S. Gao, "Gas-sensing properties of PdO-modified SnO_2–Fe_2O_3 double-layer thin-film sensor prepared by PECVD technique," *Vacuum*, vol. 59, no. 4, pp. 877–884, Dec. 2000.

[28] M. Yuasa, T. Masaki, T. Kida, K. Shimanoe, and N. Yamazoe, "Nano-sized PdO loaded SnO_2 nanoparticles by reverse micelle method for highly sensitive CO gas sensor," *Sens. Actuators B, Chem.*, vol. 136, no. 1, pp. 99–104, Feb. 2009.

[29] G. Xie, P. Sun, X. Yan, X. Du, and Y. Jiang, "Fabrication of methane gas sensor by layer-by-layer self-assembly of polyaniline/PdO ultra thin films on quartz crystal microbalance," *Sens. Actuators B, Chem.*, vol. 145, no. 1, pp. 373–377, Mar. 2010.

[30] G. De *et al.*, "Sol–gel derived pure and palladium activated tin oxide films for gas-sensing applications," *Sens. Actuators B, Chem.*, vol. 55, nos. 2–3, pp. 134–139, May 1999.

[31] K. Arora and N. K. Puri, "Electrophoretically deposited nanostructured PdO thin film for room temperature amperometric H_2 sensing," *Vacuum*, vol. 154, pp. 302–308, Aug. 2018.

[32] Y. Chao, S. Yao, W. J. Buttner, and J. R. Stetter, "Amperometric sensor for selective and stable hydrogen measurement," *Sens. Actuators B, Chem.*, vol. 106, no. 2, pp. 784–790, May 2005.

[33] S. Yao and M. Wang, "Electrochemical sensor for dissolved carbon dioxide measurement," *J. Electrochem. Soc.*, vol. 149, no. 1, pp. H28–H32, Jan. 2002.

[34] R. S. Jayashree, M. Mitchell, D. Natarajan, L. J. Markoski, and P. J. Kenis, "Microfluidic hydrogen fuel cell with a liquid electrolyte," *Langmuir*, vol. 23, no. 13, pp. 6871–6874, Jan. 2007.

[35] M. C. Buzzeo, C. Hardacre, and R. G. Compton, "Use of room temperature ionic liquids in gas sensor design," *Anal. Chem.*, vol. 76, no. 15, pp. 4583–4588, Jul. 2004.

[36] D. C. Marcano *et al.*, "Improved synthesis of graphene oxide," *ACS Nano*, vol. 4, no. 8, pp. 4806–4814, Jul. 2010.

[37] S. Park, J. An, J. R. Potts, A. Velamakanni, S. Murali, and R. S. Ruoff, "Hydrazine-reduction of graphite-and graphene oxide," *Carbon*, vol. 49, no. 9, pp. 3019–3023, Aug. 2011.

[38] B. D. Cullity and J. W. Weymouth, "Elements of X-ray diffraction," *Amer. J. Phys.*, vol. 25, no. 6, p. 394, 1957.

[39] S. Srivastava *et al.*, "Electrophoretically deposited reduced graphene oxide platform for food toxin detection," *Nanoscale*, vol. 5, no. 7, pp. 3043–3051, 2013.

[40] M. E. Uddin, R. K. Layek, N. H. Kim, D. Hui, and J. H. Lee, "Preparation and properties of reduced graphene oxide/polyacrylonitrile nanocomposites using polyvinyl phenol," *Compos. B, Eng.*, vol. 80, pp. 238–245, Oct. 2015.

[41] D.-T. Phan and G.-S. Chung, "P–n junction characteristics of graphene oxide and reduced graphene oxide on n-type Si(111)," *J. Phys. Chem. Solids*, vol. 74, no. 11, pp. 1509–1514, Nov. 2013.

[42] A. K. Das *et al.*, "Iodide-mediated room temperature reduction of graphene oxide: A rapid chemical route for the synthesis of a bifunctional electrocatalyst," *J. Mater. Chem. A*, vol. 2, no. 5, pp. 1332–1340, 2014.

[43] S. Gurunathan, J. W. Han, A. A. Dayem, V. Eppakayala, and J.-H. Kim, "Oxidative stress-mediated antibacterial activity of graphene oxide and reduced graphene oxide in *Pseudomonas aeruginosa*," *Int. J. Nanomed.*, vol. 7, pp. 5901–5914, Nov. 2012.

[44] M. A. Velasco-Soto, S. A. Pérez-García, J. Alvarez-Quintana, Y. Cao, L. Nyborg, and L. Licea-Jiménez, "Selective band gap manipulation of graphene oxide by its reduction with mild reagents," *Carbon*, vol. 93, pp. 967–973, Nov. 2015.

[45] Y. Shen *et al.*, "Evolution of the band-gap and optical properties of graphene oxide with controllable reduction level," *Carbon*, vol. 62, pp. 157–164, Oct. 2013.

[46] T.-C. Wen and C.-C. Hu, "Cyclic voltammetric investigation of PdO-coated titanium electrode in H_2 SO_4," *J. Electrochem. Soc.*, vol. 140, no. 4, pp. 988–995, Apr. 1993.

[47] C. C. Hu and T. C. Wen, "Voltammetric investigation of hydrogen sorption/desorption at/within oxide-derived Pd electrodes in NaOH and H_2 SO_4," *J. Electrochem. Soc.*, vol. 141, no. 11, pp. 2996–3001, Nov. 1994.

[48] C.-Y. Chiou and T.-C. Chou, "Amperometric SO_2 gas sensors based on solid polymer electrolytes," *Sens. Actuators B, Chem.*, vol. 87, no. 1, pp. 1–7, Nov. 2002.
[49] A. W. E. Hodgson, P. Jacquinot, and P. C. Hauser, "Electrochemical sensor for the detection of SO_2 in the low-ppb range," *Anal. Chem.*, vol. 71, no. 14, pp. 2831–2837, Jun. 1999.
[50] E. T. Seo and D. T. Sawyer, "Electrochemical oxidation of dissolved sulphur dioxide at platinum and gold electrodes," *Electrochimica Acta*, vol. 10, no. 3, pp. 239–252, Mar. 1965.
[51] G. Belanger, "Determination of sulfur dioxide by anodic oxidation on lead dioxide electrodes," *Anal. Chem.*, vol. 46, no. 11, pp. 1576–1577, Sep. 1974.
[52] Z. Cao, W. J. Buttner, and J. R. Stetter, "The properties and applications of amperometric gas sensors," *Electroanalysis*, vol. 4, no. 3, pp. 253–266, Mar. 1992.
[53] J. W. Fergus, "A review of electrolyte and electrode materials for high temperature electrochemical CO_2 and SO_2 gas sensors," *Sens. Actuators B, Chem.*, vol. 134, no. 2, pp. 1034–1041, Sep. 2008.
[54] J. F. Currie, A. Essalik, and J.-C. Marusic, "Micromachined thin film solid state electrochemical CO_2, NO_2 and SO_2 gas sensors," *Sens. Actuators B, Chem.*, vol. 59, nos. 2-3, pp. 235–241, Oct. 1999.
[55] V. Nikolova, I. Nikolov, P. Andreev, V. Najdenov, and T. Vitanov, "Tungsten carbide-based electrochemical sensors for hydrogen determination in gas mixtures," *J. Appl. Electrochem.*, vol. 30, no. 6, pp. 705–710, Jun. 2000.
[56] K. Okamura, T. Ishiji, M. Iwaki, Y. Suzuki, and K. Takahashi, "Electrochemical gas sensor using a novel gas permeable electrode modified by ion implantation," *Surf. Coat. Technol.*, vol. 201, nos. 19–20, pp. 8116–8119, Aug. 2007.
[57] Y. C. Liu, B. J. Hwang, and Y. L. Chen, "Nafion based hydrogen sensors: Pt/Nafion electrodes prepared by takenata-torikai method and modified with polypyrrole," *Electroanalysis*, vol. 14, nos. 7–8, pp. 556–558, Apr. 2002.
[58] F. Opekar, "Detection of hydrogen in air with a detector containing a nafion membrane metallized on both sides," *J. Electroanal. Chem. Interfacial Electrochem.*, vol. 260, no. 2, pp. 451–455, Mar. 1989.

Kamal Arora received the B.Sc. (Hons.) degree in physics from University of Delhi, New Delhi, India, in 2010, and the M.Sc. degree in engineering physics from Amity Institute of Applied Sciences (AIAS), Amity University, Noida, India, in 2012. He is currently pursuing the Ph.D. degree with the Department of Applied Physics, Delhi Technological University, New Delhi.

He is currently a Research Scholar with a research group in the Advanced Sensor Laboratory (ASL), under the supervision of Dr. N. K. Puri.

Saurabh Srivastava received the Ph.D. degree in physics from Banaras Hindu University/CSIR-National Physical Laboratory, New Delhi, India, in 2015.

He is currently an Assistant Professor (Physics) with the Department of Applied Science and Humanities, Rajkiya Engineering College, India. He has published over 30 research papers in peer-reviewed journals. His research interests are 2-D nanomaterials, electrochemical biosensors, and cancer. He has been a recipient of the DST-INSPIRE Faculty Award and the UGC-Dr. D.S. Kothari Postdoctoral Research Fellowship.

Pratima R. Solanki received the master's and Ph.D. degrees from Maharishi Dayanand University, Rohtak, Haryana.

She has worked at the Biomedical Instrumentation Section, National Physical Laboratory, Council of Scientific Industrial Research, New Delhi. She is Assistant Professor with the Special Centre for Nanoscience, Jawaharlal Nehru University, New Delhi. She has published around 140 research papers in national and international journals, eight international book chapters, and has filed eight Indian patents. She is actively engaged in the research and development of biosensors utilizing nanostructured materials for healthcare and environmental monitoring.

Nitin Kumar Puri received the Ph.D. degree in experimental atomic physics from Cyclotron Laboratory, Panjab University, Chandigarh.

He has worked as an Engineer at the R&D Division, HongHua Company Ltd., China. He has been awarded various sponsored research projects from different funding agencies, including SERB-DST, BRNS, and UGC-DAE (Government of India). He is currently an Associate Professor of Engineering Physics with the Department of Applied Physics, Delhi Technological University (DTU). He is associated with DTU for the last 8.5 years and has teaching and research experience of more than 14 years. He has supervised about 25 M.Tech. students and five Ph.D. students. Currently, six Ph.D. students are pursuing their research under his supervision. He has delivered many invited talks and has over 100 research publications in peer-reviewed journals and conferences of national and international repute. He has worked as the Vice-Chairman and Chairman of working group-III for International Nuclear Security Education Network (INSEN) as one of the Indian Representative at the International Atomic Energy Agency (IAEA), Vienna. His current research interests include accelerator physics, 2D-nanomaterials-based sensors, biosensors, hydrogen sensing, and storage.

Materials Chemistry and Physics 247 (2020) 122850

Contents lists available at ScienceDirect

Materials Chemistry and Physics

journal homepage: www.elsevier.com/locate/matchemphys

Chemiresistive sensing platform based on PdO-PANI/ITO heterostructure for room temperature hydrogen detection

Kamal Arora , Nitin K. Puri *

Advanced Sensor Laboratory, Department of Applied Physics, Delhi Technological University, Shahbad Daulatpur, Bawana Road, Delhi, 110042, India

HIGHLIGHTS

- PANI and PdO-PANI nanocomposites are synthesized using wet chemical process.
- PANI/ITO and PdO-PANI/ITO thin film heterojunction are used as sensing elements.
- Proposed heterostructure device shows high sensitivity for 1%, 3%, 10% and 20% H_2.
- Sensitivity increases with increasing percentage concentration of PdO and H_2.
- Chemiresisitve H_2 sensor demonstrates enhanced sensing response at room temperature.

ARTICLE INFO

Keywords:
Hydrogen sensor
Palladium oxide
Polyaniline
Chemiresistor
Composites

ABSTRACT

Heterostructure of palladium oxide (PdO)-polyaniline (PANI)/indium tin oxide (ITO) have been used to enhance the sensitivity of chemiresistive sensors towards hydrogen (H_2) gas at room temperature. The fabricated sensor assembly is facile and economical as it uses direct metallic electrical contact with the sensing element, which eliminates the need of expensive interdigitated electrodes (IDE). Pristine PANI, 5 wt%, and 10 wt% PdO-PANI nanocomposites are synthesized using one pot in-situ wet chemical polymerization method. Pristine PANI, 5 wt%, and 10 wt% PdO-PANI composites thin film are uniformly interfaced over sputtered indium tin oxide (ITO) layer coated glass substrate using spin coating process. Solid state sensing element consisting of PANI/ITO, 5 wt %, and 10 wt% PdO-PANI/ITO heterojunction has been used for detection of (1, 3, 10, and 20) % H_2 concentration at room temperature. Two folds increase in the sensitivity of PdO-PANI nanocomposite towards 1% H_2 gas concentration has been observed in comparison to pristine PANI based sensing element and further the sensitivity also increases as the percentage concentration of PdO within nanocomposite increases from 5 wt% to 10 wt% respectively. It has been observed that the proposed heterostructure based sensing assembly is highly sensitive towards H_2 gas compared to similar previously reported sensors. With the onset of the hydrogen economy, this research work will pave the way in large scale production of sensitive and responsive handheld H_2 gas sensors that can be used in common households along with industries.

1. Introduction

Several conducting polymers have been studied over the years in field of gas sensing applications; Polypyrrole and Polyaniline (PANI) have been extensively researched including their properties as well as their applications in varied scientific fields due to their favorable electronic and molecular properties among other types of conducting polymers [1]. The peculiar physical properties of hydrogen gas (H_2) make it difficult for human nose to sense it in the surrounding. Also, it's flammable range of 4% and above in environment makes it catastrophical in case of leakage during storage and transportation. But still, it is used as source of fuel in different industries such as nuclear, fuel cell, petrochemical, automobile and space industries because it is a clean combustible energy source with three times calorific value as compared to other energy sources. Thus, there is a dire need for fabrication of highly sensitive, selective and stable H_2 sensor [2].

Pristine standalone PANI nanofibers as well as PANI nanofibers deposited on gold and platinum electrodes have been used for detection of hydrogen gas at room temperature [3,4]. PANI nanofibers have been also used to sense hydrogen gas at room temperature by (Surface

* Corresponding author.,
E-mail addresses: nitinkumarpuri@dtu.ac.in, nitinpuri2002@yahoo.co.in (N.K. Puri).

https://doi.org/10.1016/j.matchemphys.2020.122850
Received 11 December 2019; Received in revised form 19 February 2020; Accepted 24 February 2020
Available online 2 March 2020

Acoustic Wave) SAW based sensing mechanism [5]. However, pristine PANI based room temperature hydrogen gas sensors showed higher response and recovery time which inhibits their application in this field. It has been observed that synthesis of PANI combined with hydrogen-philic and electro-catalytically active materials enhanced the sensitivity towards hydrogen gas and reduced the response and recovery time of the sensor.

Heterostructure based materials have sparked interest among researchers for gas sensing applications due to their unique chemical and electronic properties which enhances the sensitivity and response characteristics of sensing device. Heterostructure material contains two dissimilar constituents (A and B) forming a physical interface between them known as heterojunction. The heterostructures have been classified in three categories consisting of simple mixture or composite (A-B), distribution of one material over other (A@B) and interface between two materials (A/B). The sensors based on these heterostructures display high sensitivity and fast response characteristics because the sensing mechanism of these devices are based on charge separation, development of charge depletion region, Fermi level mediated charge transfer and formation of potential barrier (Schottky barrier) between their heterojunction [6,7].

S. Srivastava et al. used pristine as well ion beam irradiated tantalum-PANI, carbon nanotubes (CNT)-PANI and Titanium dioxide (TiO_2)-PANI nanocomposites for sensing hydrogen gas at room temperature [8–10]. S. Nasirian et al. fabricated composites of PANI with anatase titania as well as TiO_2 and Tin oxide (SnO_2) for hydrogen sensing application at ambient conditions [11,12]. Wei Li et al. combine PANI with Chitosan to use its filtration technique to enhance the sensitivity for hydrogen gas [13]. Platinum oxide-PANI nanocomposite has also been used for fabrication of selective hydrogen sensor at room temperature [14]. P. C. Wang et al. demonstrated enhanced conductometric hydrogen sensing response in various degree of HCl doped PANI [15]. H.M. Moghaddam et al. synthesized composites of Titania and PANI to enhance the recovery as well response time of hydrogen sensor [16]. A. M. More fabricated a low temperature hydrogen sensor using Silver (Ag)-Tin oxide (SnO_2)-PANI nanocomposite as active material [17]. Composite of PANI nanofibers with SnO_2 as well as Aluminum (Al)–SnO_2 is synthesized using electrospinning method for hydrogen sensing application [18,19]. Y. Zou demonstrated palladium (Pd)/PANI-reduced graphene oxide (rGO) nanocomposite to fabricate hydrogen sensor operatable at room temperature [20]. A. Z. Sadek et al. proposed a room temperature SAW sensor based on ZnO/64^0 YX $LiNbO_3$ mixed with Polyaniline/SnO_2 Nanofiber [21]. PANI nanofibers deposited on Lithium tantalate ($LiTaO_3$) has been synthesized to demonstrate SAW based hydrogen sensor [22]. PANI-Platinum oxide nanocomposite has also been synthesized for fabrication of chemiresistive hydrogen sensor which showed higher sensitivity and selectivity towards hydrogen gas as compared to other gases [14].

Numerous research studies have been performed using various pre-transition, transition and post transition semiconductor metal oxide nanostructures for their hydrogen gas sensing application due to their favorable physical and electrical properties [23–32]; however their high temperature operation makes them unsuitable to be pristinely used as active element in H_2 gas sensing operations. It has been found that synthesis of a composite between two or more metal oxides or hydrogen-philic electroactive metals such as palladium (Pd) and platinum (Pt) enhanced the sensitivity of metal oxides composites towards H_2 gas and lowered their operation temperature. However, cost of fabrication, hydrogen embrittlement and poisoning by sulfur containing gases in environment makes pure Pd unsuitable to be used directly for hydrogen sensing application. The platinum group family in the periodic table consists of palladium (Pd), Platinum (Pt), Ruthenium (Ru), Rhodium (Rh), Osmium (Os) and Iridium (Ir). Among these members, Pd is one of the three elements including Pt and Rh whose oxides exhibit semiconducting properties; whereas oxides of remaining members of the family show conducting properties like metals [33]. The building block of palladium oxide (PdO) crystal is a tetragonal unit cell made up of palladium (Pd^{2+}) ions tetrahedrally coordinating the oxygen ions.

Y. J. Chiang et al. published a mechanistic study on H_2 sensing by PdO nanomaterial; they reported that PdO decomposes to Pd in presence of H_2 gas molecule, resulting in formation of Pd nanoislands on the surface of PdO, simultaneously with dissociation of H_2 into hydrogen (H^+) ions at room temperature. Thereafter, H^+ ions adsorb on the surface after reacting with superoxide (O^{2-}) ions and diffuse inside the octahedral interstitial sites of face centered cubic (fcc) Pd crystal present on the nanoisland, leading to the decrease in conductivity of PdO. However, re-oxidation of Pd does not takes place at room temperature and occurs only after temperature rises above 150 °C. The mechanism of interaction with H_2 at temperatures below 150 °C has been explained using oxygen ionosorption model [34]. Additionally, XPS spectra of PdO collected after its exposure from H_2 gas show decrease in curve area of Pd^{2+} intensity peak with significant increase in Pd^0 peak, which confirms the reduction of PdO to Pd in contact with H_2 gas [35]. It has been found using in-situ x-ray diffraction (XRD) spectroscopy that both Pd and PdO nanoparticles form fcc PdH_x crystal structure in presence of H_2 environment and demonstrate phase transition along with lattice expansion at room temperature. The diffused H^+ ions present inside the octahedral interstitial sites of fcc PdH_x act as electron scattering center and decrease the conductivity of Pd nanomaterials [2,36]. Nevertheless, due to high activation energy for desorption of H_2 gas and irreversible sensing behavior, pristine PdO is not a suitable candidate for conductometric H_2 sensing at room temperature. Thus, sensing element consisting of composite materials with PdO nanoparticles would be a suitable substitute for H_2 sensing application [37]. Nanocomposites of PdO with metal oxides such as Titanium dioxide (TiO_2), Tungsten trioxide (WO_3), reduced graphene oxide (rGO) and Zinc oxide (ZnO) shows high sensitivity towards H_2 gas compared to their pristine counterparts through conductometric as well as electrochemical sensing mechanisms [31,38–40].,

PANI/ITO, 5 wt% and 10 wt% PdO-PANI heterostructure based room temperature H_2 sensors have not been studied before up to the best of our knowledge. In the present work, we have synthesized composites of PdO and PANI using one pot in-situ wet chemical assembly process. The as-synthesized material is coated as thin film on sputtered Indium Tin oxide (ITO) layer coated glass substrate using facile spin coating method forming a PdO-PANI/ITO heterojunction. The fabricated thin film is employed as solid state sensing material using direct metallic electrical contacts without employing expensive interdigitated electrodes (IDE) for chemiresistive hydrogen gas sensing in indigenously assembled gas sensing setup. The proposed heterostructure based sensing device exhibits enhanced sensitivity with fast response characteristics for 1%, 3%, 10% and 20% concentrations of H_2 gas and the sensitivity increases as the percentage concentration of PdO increases within the nanocomposite from 5 wt% to 10 wt%.

2. Experimental details

2.1. Chemical profile

All the chemicals used in synthesis process of PANI and its composites with 5 wt% and 10 wt% PdO belong to AR grade and are 99.9% pure. Aniline, Ammonium peroxide sulfate (APS), 10-Camphor sulfonic acid (CSA) and PdO nanoparticles are purchased from Sigma Aldrich. Hydrochloric (HCl) acid (35% concentrated) is purchased from Qualigens Fine chemicals, India. Chloroform and ammonia solution (25% concentrated) are purchased from Fisher Scientific.

2.2. Synthesis procedure

Emeraldine salt (ES) form of PANI and PdO-PANI nanocomposite have been synthesized using one pot in-situ wet chemical polymerization process. 0.1 Molar (M) aniline and APS are dissolved in 100 ml 1 M

HCl solution simultaneously with continuous stirring for 1 h. Adjacently, 5 wt% and 10 wt% PdO nanoparticles powder in comparison to aniline is dispersed in 1 M HCl solution through ultrasonication treatment for 1 h. PANI (ES) and PdO-PANI (ES) nanocomposite has been synthesized using oxidative polymerization reaction between precursor aniline or dispersed PdO nanoparticles-aniline solution and APS solution as oxidizing agent. APS solution is added dropwise to both precursor solutions at a temperature of 0–5 °C under continuous stirring for 2 h as color of the solution turns dark green from transparent. The resultant dark green colored solution is left undisturbed overnight for completion of reaction. Subsequently, it is filtered and washed with 1 M HCl solution as well as deionized (D.I.) water, several times till pH of solution becomes equivalent to 7. The washed precipitates are dried in oven at 60 °C to obtain ES powder of PANI and PdO-PANI nanocomposite.

ES powder of PANI and PdO-PANI nanocomposite are conducting in nature but they are insoluble in most organic solvents. Hence, PANI (ES) and PdO-PANI (ES) composites are converted to emeraldine base (EB) form by dissolving them with 0.1 M ammonia solution through continuous stirring for 6 h. The obtained precipitates are washed with D.I. water several times and dried in oven. The resulting powder of PANI (EB), 5 wt% PdO-PANI (EB) and 10 wt% PdO-PANI (EB) composite are then protonated with CSA powder by grinding it in agate mortar to obtain protonated conducting form of Pristine PANI [CSA doped PANI (EB)] and PdO-PANI [CSA doped PdO-PANI (EB)] nanocomposite which are comparatively easy to cast into thin films [10].

2.3. Thin film fabrication

0.3 g of Pristine PANI, 5 wt%, and 10 wt% PdO-PANI powder is dissolved in 30 ml chloroform and continuously stirred for 4 days to prepare uniform conducting solution. The respective solutions are printed uniformly on to conducting surface of 0.1 μm thin layer of ITO coated glass substrate using spin coating process (Metrex instruments) at 2000 rpm for 20 s, while covering 0.1 cm of its surface from which a direct electrical metallic contact has been achieved (Fig. 1). Henceforth, the obtained 0.2 μm thin films of pristine PANI, 5 wt%, and 10 wt% PdO-PANI nanocomposite are dried in oven at 60 °C for 24 h.

2.4. Sensing device schematic and configuration

The setup consists of indigenously constructed stainless steel (SS) chamber with volume of 3.099 L, attached to rotary vacuum pump along with two gas mass flow controllers (MFC). The SS chamber contains a substrate holder attached to heater with the assistance of heating microcontroller (Fig. 2). The probes are made up of 2 cm long, 0.18 mm thin pins made up of Molybdenum (Mo) metal connected to the assembled source meter for providing constant current supply. 0.2 μm thin films of Pristine PANI/ITO and PdO-PANI/ITO heterojunctions are connected with probe pins through surface of conducting ITO glass substrate to measure the change in electrical characteristics of the thin film (Fig. 1).

The schematic of proposed device is depicted in Fig. 3(a), in which

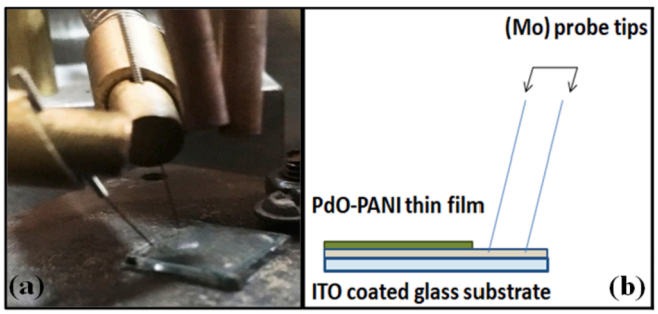

Fig. 1. Probes contact (a) Front view, (b) Side view schematic.

two heterojunctions are formed simultaneously, one between a p-type PANI or p-type PdO-PANI thin film and n-type ITO and the other between Mo metal probe pins and n-type ITO. The work function (Φ) of CSA doped PANI is found to be 4.941 ± 0.035 eV and a band gap of 2.52 eV [4]; whereas work function of ITO is assumed to be 4.7 eV with a band gap of 3.7 eV. Hence, a Schottky contact is formed between p-type PANI or p-type PdO-PANI thin film and n-type ITO substrate as $\Phi_{PANI/PdO\text{-}PANI} > \Phi_{ITO}$ (Fig. 3(b)) [41]. On the other hand, an ohmic contact is created between n-type ITO substrate and Mo metal probe pins as $\Phi_{ITO} > \Phi_{Mo}$, which is observed to be 4.5 eV.

2.5. Sample characterization

The crystallographic structure of pristine PANI and its composite with PdO nanoparticles has been analyzed using PANalytical X'pert PRO X-ray diffractometer. The nature of bonds and the inter-bond interactions of synthesized structure has been observed using PerkinElmer FTIR spectrometer. The optical characteristics of PANI and its composites has been evaluated using PerkinElmer UV–Visible (UV–Vis) spectrometer. The structure and nature of the surface of thin film has been viewed using Zeiss EVO 40 scanning electron microscope.

3. Results and discussions

3.1. X-ray diffraction study

The characteristic peaks of pristine PANI, 5 wt%, and 10 wt% PdO-PANI composites are plotted in Fig. 4. Broad peak at 15.2^0 along with low intensity peaks at 19.5^0 and 25.3^0 corresponds to amorphous as well as crystalline nature of synthesized pristine PANI (ES) powder. The low intensity diffraction peaks at 19.5^0, 25.3^0 belongs to (110) and (003) crystal planes respectively as compared with published data (JCPDS no. 531717). The peaks arising at 15.2^0 and 19.5^0 are originating due to scattering between interplanar spacing of PANI conjugated chains whereas low intensity peak at 25.3^0 is the periodicity characteristics of PANI structure at room temperature.

The narrow well defined high intensity peaks arising at 34.3^0 together with comparatively low intensity peaks at 42.2^0, 55.1^0, 60^0, 61^0 and 72^0 corresponds to (101), (110), (112), (103), (200) and (202) planes of tetragonal (t)-PdO respectively. It can be observed in Fig. 4 that XRD graph of 5 wt%, 10 wt% PdO-PANI powder shows combined peaks of PANI as well as t-PdO, validating the successful synthesis of composite structure. As, the percentage concentration of PdO increases from 5 wt% to 10 wt% in the nanocomposite, the XRD peaks of t-PdO become more intense while intensity of broad peaks representing PANI crystal structure decreases and eventually diminish for 10 wt% PdO-PANI nanocomposite [11]. The decrease in intensity peaks of PANI is due to interaction of PdO nanoparticles with polarons present on amine units in PANI conjugated chain like structure, which inhibit the growth of PANI chain and hamper with the crystalline behavior of PANI matrix [42]. However, the crystalline behavior of PdO nanoparticle remains unperturbed in the presence of PANI matrix [10]. The average crystallite size of the t-PdO in the composite structure is found to be 6.702 nm using Scherrer formula [equation (1)].

$$t = 0.9\,\lambda/\beta\,cos\theta \quad (1)$$

β is the FWHM (Full width half maxima), $\lambda = 1.54$ Å is wavelength of Cu-K_α source, θ is the angle having maximum intensity and t represent crystallite size.

The strain induced by PdO nanoparticles within PANI matrix can be calculated using equation (2) and it can be observed that as the percentage concentration of PdO increases from 5 wt% to 10 wt%, the lattice strain (ε) also increases significantly which leads to broadening of PANI intensity peaks (Table 1). Also, the interchain separation (R) between PANI matrix corresponding to $\theta = 15.2^0$ is calculated to be 3.671

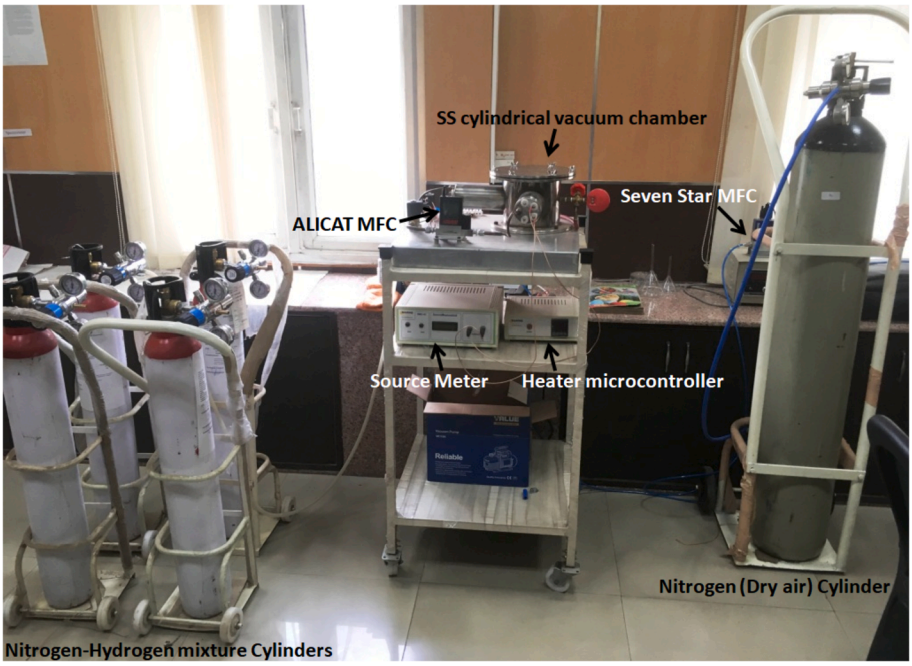

Fig. 2. Resistance based gas sensing setup.

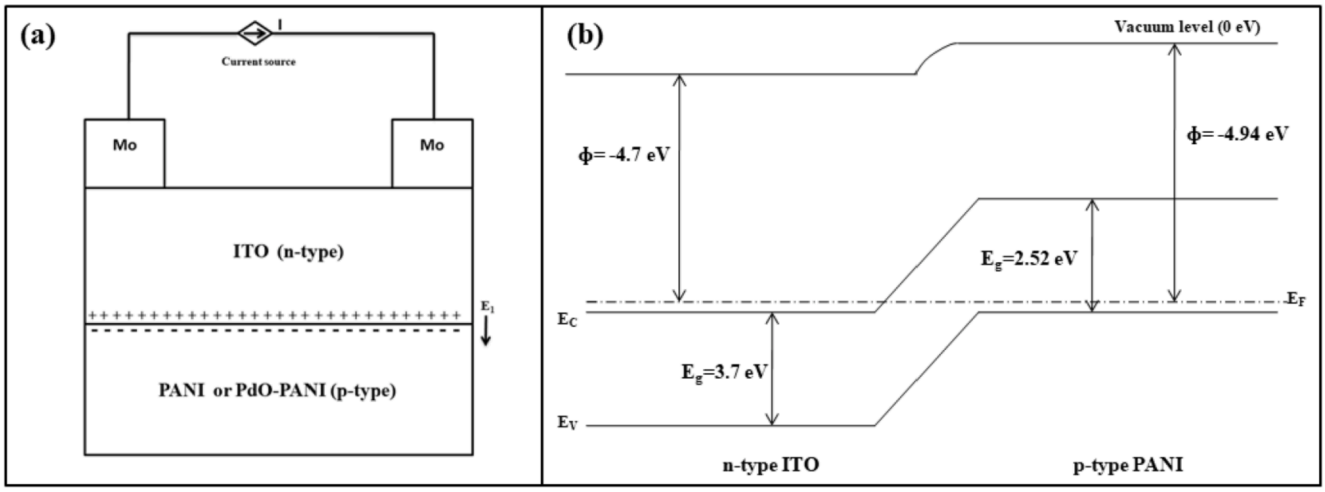

Fig. 3. (a) Device schematic and (b) Band diagram of CSA doped PANI/ITO heterojunction.

Å (equation (3)) [43].

$$\varepsilon = \beta \tan\theta \quad (2)$$

$$R = 5\,\lambda/8\,\sin\theta \quad (3)$$

3.2. Transmission electron microscopy (TEM)

Fig. 5(a) and (b) depicts the transmission electron microscopy (TEM) images of pristine PANI and 10 wt% PdO-PANI nanocomposite respectively. Transparent sheet like structure containing dark thin lines is observed in TEM image of pristine PANI suggesting the formation of disordered amorphous PANI nanofibers matrix (Fig. 5(a)). Adjacently, TEM image of 10 wt% PdO-PANI nanocomposite consists of dark circular dots in bright mesh background, which shows the presence of PdO nanoparticles within the PANI matrix and confirms the formation of composite structure (Fig. 5(b)) [10,44,45].

3.3. Ultraviolet–visible (UV–Vis) absorption spectroscopy

Pristine PANI, 5 wt% PdO-PANI and 10 wt% PdO-PANI nanocomposite are dispersed in chloroform solution to obtain their ultraviolet–visible (UV–Vis) absorption spectra (Fig. 6). Absorption peaks at 348 nm, 430 nm and 769 nm can be observed in UV–Vis spectra of pristine PANI which can be originated from π-π* bond interactions, polaron-π* and π-polaron transitions respectively [46]. These transitions peak shows good conductivity of pristine PANI powder. As the percentage of PdO in PdO-PANI composite increases from 5 to 10 wt%, the intensity of absorption peaks corresponding to pristine PANI decreases and eventually vanishes along with visible red shift in wavelength of absorbed spectrum. These changes in spectra are due to interaction of PdO nanoparticles with PANI aromatic structure leading to change in polaron density within PANI chains of the composite [11].

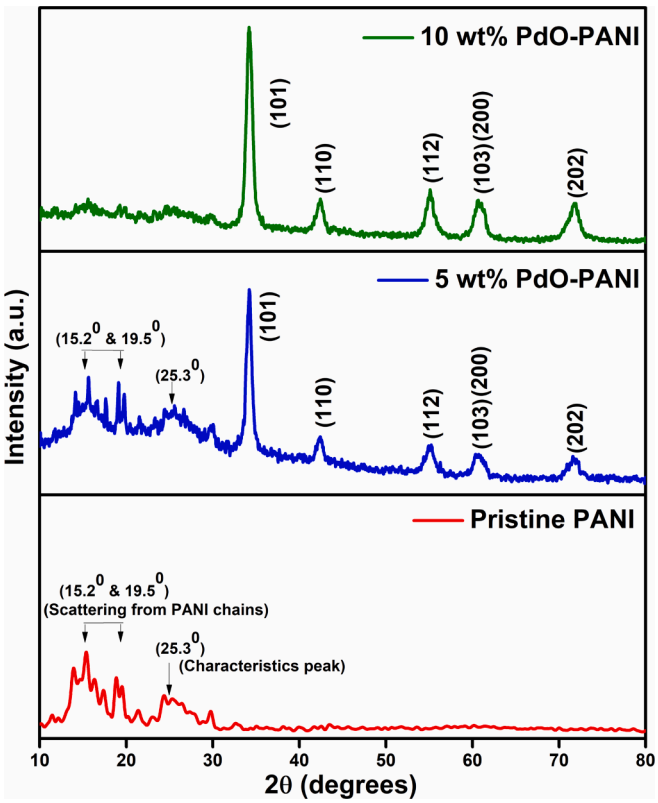

Fig. 4. X-ray diffraction plot.

Table 1
Lattice strain within crystal structure of PANI matrix.

Sample	Diffraction peak (2θ)	Lattice strain (ε)
PANI	15.2^0	0.047
5 wt% PdO-PANI	15.2^0	0.099
10 wt% PdO-PANI	15.2^0	0.120

3.4. Fourier transform infrared (FT-IR) transmission spectroscopy

The nature of bonds and type of interaction between elements of pristine PANI and its composites with PdO has been characterized by FT-IR transmission spectra (Fig. 7). The major broad intense peak arises at wavenumber of 3447 cm^{-1} which is the outcome of N–H bond stretching mode. The transmission peak present at 2885 cm^{-1} and 2960 cm^{-1} belongs to NH_2^+ and N–H bond of aromatic amines respectively. On the other hand, transmission occurring at 1635 cm^{-1},1738 cm^{-1} is due to C–N imine stretching vibrations, whereas peak at 1384 cm^{-1} corresponds to C═C bonds of benzenoid ring. The formation of bands at 1049 cm^{-1},1173 cm^{-1} and 1003 cm^{-1} is a result of quinoid unit of pristine PANI, in-plane bending vibrations of C–H resulting from protonation of PANI (EB) and C–C bond of benzene ring respectively [12]. Synthesis of 5 wt% PdO-PANI and 10 wt% PdO PANI nanocomposite does not yield any new transmission peaks in FT-IR spectra (Fig. 7), however it leads to shifting of bands due to interaction between PdO nanoparticles and amine bonds of benzenoid ring. Also, there is a significant increase in the intensity of transmission peaks as the percentage of PdO increases from 5 to 10 wt% comparatively as a result of uniform distribution of PdO

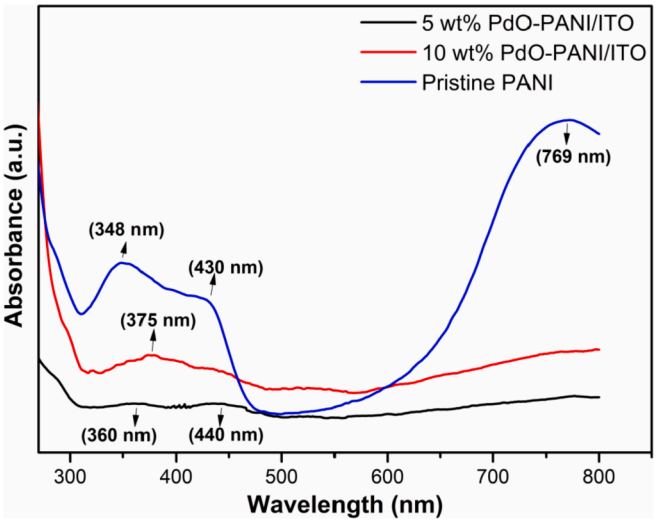

Fig. 6. UV–Vis absorption spectra.

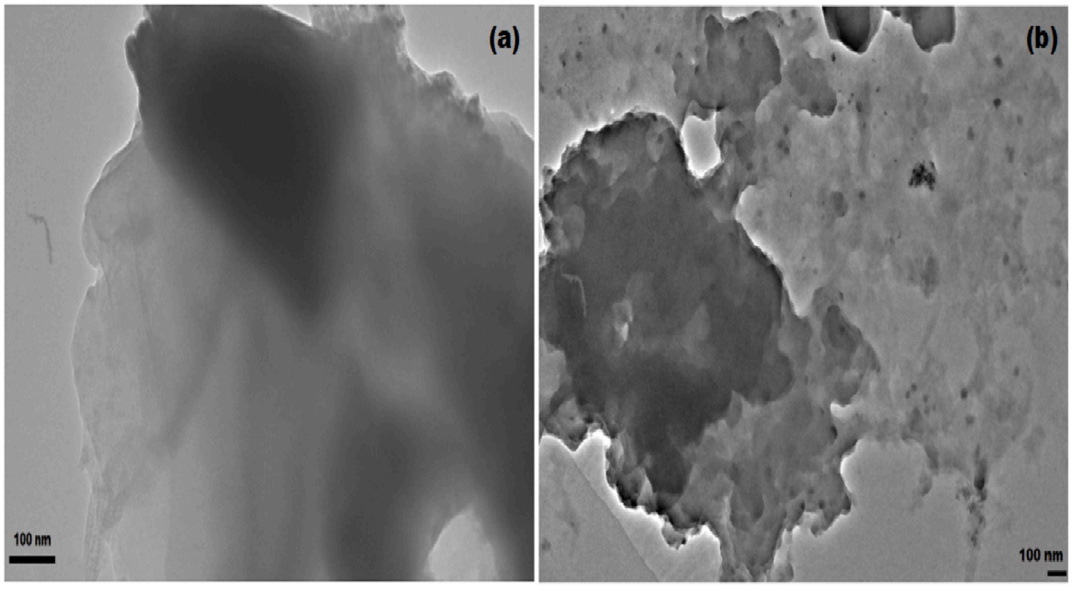

Fig. 5. TEM image of (a) Pristine PANI, (b) 10 wt% PdO-PANI nanocomposite.

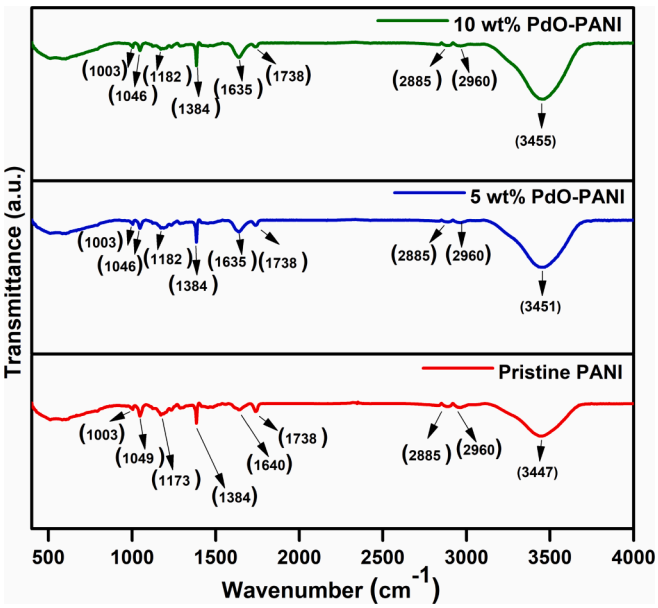

Fig. 7. FT-IR transmission spectra.

nanoparticles in PANI aromatic structure [47].

3.5. Scanning electron microscopy (SEM)

PANI can exist in various nano size shapes such as flakes, tubes, fibers and spheres. Surface morphology of thin film of pristine PANI/ITO, 5 wt% PdO-PANI/ITO and 10 wt% PdO-PANI/ITO coated glass substrate can be seen in Fig. 8(a), (b) and (c) respectively. Thin film surface of prisitne PANI shows uniformly distributed flakes like structure with non uniform shape and size (Fig. 8(a)). As the percentage of PdO nanoparticles increases from 5 to 10 wt%, the size of flakes decreases due to agglomeration of PdO nanoparticles with PANI (Fig. 8(b) and (c)) which can yield in improvement in capacitance of thin film [47].

The surface of pristine PANI thin film shows uneven surface defects consisting of lumps and holes which can aid in absorption of H_2 gas. However, the presence of defects on the surface decreases with increase in percentage of PdO nanoparticles as a result of stacking of flakes with nanoparticles on the surface. During polymerization process, increasing the concentration of PdO nanoparticles result in formation of rod like network in PdO-PANI nanocomposite structure. This enhances the porosity and surface area of thin film which makes it favorable for gas sensing applications [10].

3.6. Chemiresistive H_2 gas sensing study

The H_2 gas sensing study is performed using pristine PANI/ITO, 5 wt % PdO-PANI/ITO and 10 wt% PdO-PANI/ITO heterojunction as sensing platform in indigenously assembled chemiresistive gas sensing setup (Fig. 2). H_2 gas sensing is performed in presence of dry nitrogen (N_2) in order to simulate the true environmental conditions at a temperature of 28 °C. Various (1, 3, 10 and 20) % H_2/dry N_2 mixtures are introduced inside SS vacuum chamber at flow rate of 200 (standard cubic centimeter per minute) sccm for 20 s. The sensing response towards different H_2 gas mixtures is recorded in term of change in resistance (ΔR) (Ohms) and Sensitivity (S) versus time (seconds) as graphical plot and is calculated using equations (4) and (5) (Fig. 9(a), (b), (c) and (d)).

$$\Delta R = R_g - R_a \tag{4}$$

$$S = \Delta R/R_a \tag{5}$$

where R_a, R_g represents value of thin film resistance in presence of dry N_2 and H_2 gas mixtures respectively and it is observed that $R_g > R_a$.

3.6.1. Sensing response

Fig. 9(a), (b) and (c) display the sensing response graphs of pristine PANI/ITO, 5 wt% and 10 wt% PdO-PANI/ITO heterojunction sensing element towards 1%, 3%, 10% and 20% H_2 concentration at room temperature respectively. The resistance of the heterostructures attains a constant base value (R_a) as dry N_2 is introduced inside the vacuum chamber. The base resistance rises swiftly to attain a gas resistance value (R_g) as the H_2 gas enters the chamber and remains constant throughout the duration of flow. Thereafter, R_g falls back to R_a as soon as H_2 gas flow cuts off displaying pulsed sensing response of fabricated heterostructure. It is observed that the value of ΔR increases comprehensively with increasing concentration of H_2 gas. Fig. 10(a), (b), (c) and (d) represent the sensing response comparison plot of PANI/ITO, 5 wt% and 10 wt% PdO-PANI/ITO heterojunction for 1%, 3%, 10% and 20% H_2 gas individually.

The R_a value of PdO-PANI/ITO heterostructure is observed to decrease significantly as compared to pristine PANI/ITO. This reduction is attributed to increase in the conductivity with reduction in the Schottky barrier of heterojunction due to increase in the holes concentration of p-type nanocomposite. However, there is no further significant decrease in the value of R_a on increasing the concentration of PdO from 5 to 10 wt% because of the low barrier height and saturation of the heterojunction [48]. There is small but considerable increase in value of R_g in 5 wt% PdO-PANI/ITO in contrast to pristine PANI/ITO for all concentrations of H_2; however, significant increase in R_g is observed in 10 wt% PdO-PANI/ITO comparatively (Fig. 10). 10 wt% PdO-PANI nanocomposite create effectively large charge carrier separation and depletion along with elevation of potential barrier at ITO

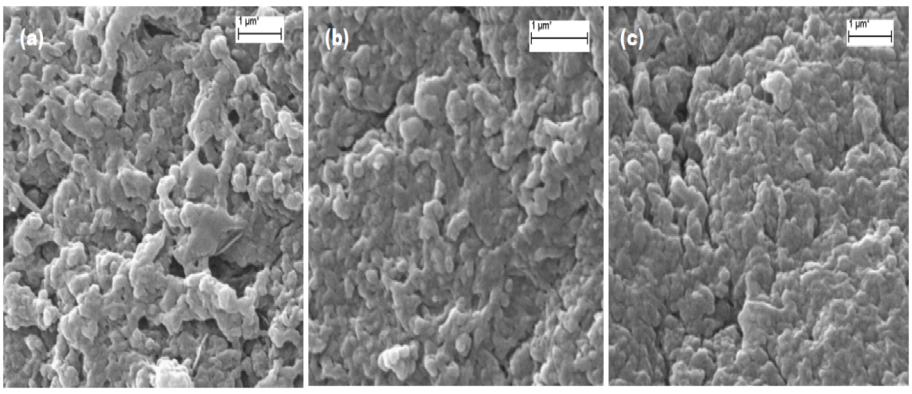

Fig. 8. SEM images of thin film (a) Pristine PANI, (b) 5 wt% PdO-PANI and (c) 10 wt% PdO-PANI.

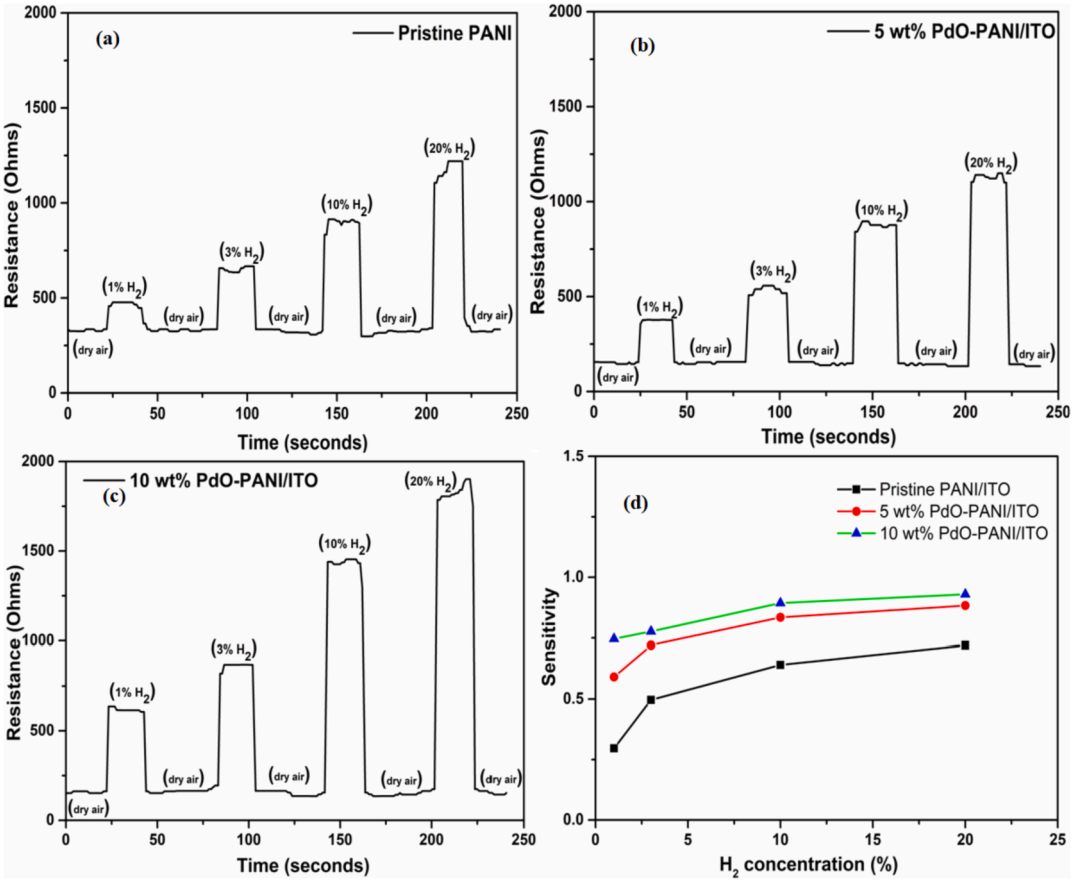

Fig. 9. Sensing response (a) Pristine PANI/ITO, (b) 5 wt% PdO-PANI/ITO, (c) 10 wt% PdO-PANI/ITO and (d) Sensitivity comparison plot.

heterojunction, resulting in comprehensive increase in the resistance on injection of electrons on its surface. The proposed heterostructure based sensing device demonstrates enhanced sensitivity with fast response and recovery time of 3–4 s respectively for all concentrations of H_2 gas.

3.6.2. Sensing mechanism

The sensing mechanism of this heterojunction based sensing device is governed by protonation of amine-imine sites of PANI conjugated structure, chemical sensitization by PdO nanoparticles, charge carrier separation and depletion within nanocomposites, Fermi level mediated charge transfer and formation of potential barrier between interfaces which can be explained using similar published research work.

H_2 gas reacts with pristine polaronic emeraldine PANI through its dissociation to H^+ ion by donating two electrons, followed by its substitution on semiquinone amine nitrogen (-NH^+-) sites and partial protonation of some imine (-N =) units too, resulting in formation of new N–H bonds. The transfer of ionic charges and release of H^+ ions within adjacent amine nitrogen allow PANI to revert back to its original polaronic emeraldine form [49].

Interaction of PdO with H_2 gas molecule can be explained using models suggested by Lee et al. and Y.J. Chiang that suggest reduction of PdO to Pd atoms occur in presence of H_2 gas followed by dissociation of H_2 molecule into H^+ ions as H_2 molecule gets adsorbed on surface of Pd atoms. These H^+ ion diffuses inside the face centered cubic structure of Pd occupying the octahedral sites resulting in formation of palladium hydride (PdH_x), these interstitial sites act as scattering center for electrons by reducing their mobility and therefore decreasing the conductivity [20,50]. Moreover, these dissociated H^+ ions are physisorbed on surface of PANI by process of spillover which results in increase of electrons concentration and thus increase in barrier width at heterojunction. The injection of electrons inside p-type pristine PANI or PdO-PANI thin film layer on interaction with H_2 gas leads to increase in the Schottky barrier between PANI/ITO or PdO-PANI/ITO heterojunction (Fig. 3), which results in increasing the net resistance of the device. Also, substitution of H^+ ions on semiquinone amine (-NH^+-) sites of emeraldine PANI leads to formation of protonated amine (-NH_2^+-) units within the structure and it has been observed that protonated amines offer barrier towards intrachain conduction of electrons (Fig. 11) [51]. Thus, net increase in the resistance of pristine PANI thin films/ITO on interaction with H_2 gas is a result of increase in Schottky barrier at heterojunction (Fig. 3(a)) and formation of insulating protonated amines (-NH_2^+-) inside PANI structure, whereas comprehensive increase in resistance of PdO-PANI thin film/ITO is overall combined effect of net increase in Schottky barrier, formation of protonated amines, chemical sensitization of PANI matrix and increase in scattering centers for electrons with increasing percentage concentration of PdO in nanocomposite respectively.

The sensitivity of pristine PANI/ITO, 5 wt% and 10 wt% PdO-PANI/ITO heterostructure based sensing device is plotted in Fig. 9(d). The sensitivity of all three fabricated heterostructures increase as the percentage concentration of H_2 gas increase, but this increase is more prominent in pristine PANI/ITO compared to others. It is due to increase in number of electrons which reaches the heterojunction and increase the width of potential barrier. However, significant increase in sensitivity with H_2 concentration is restricted in PdO-PANI nanocomposite because of reduction in polaron density in PANI structure, required for transport of electrons towards heterojunction [10]. Moreover, there is a comprehensive increase in the sensitivity for 5 wt% PdO-PANI compared to pristine PANI for same concentrations of H_2; but it is considerably low in 10 wt% PdO-PANI. It is attributed to chemical and electronic sensitization of PANI by PdO nanoparticles towards H_2,

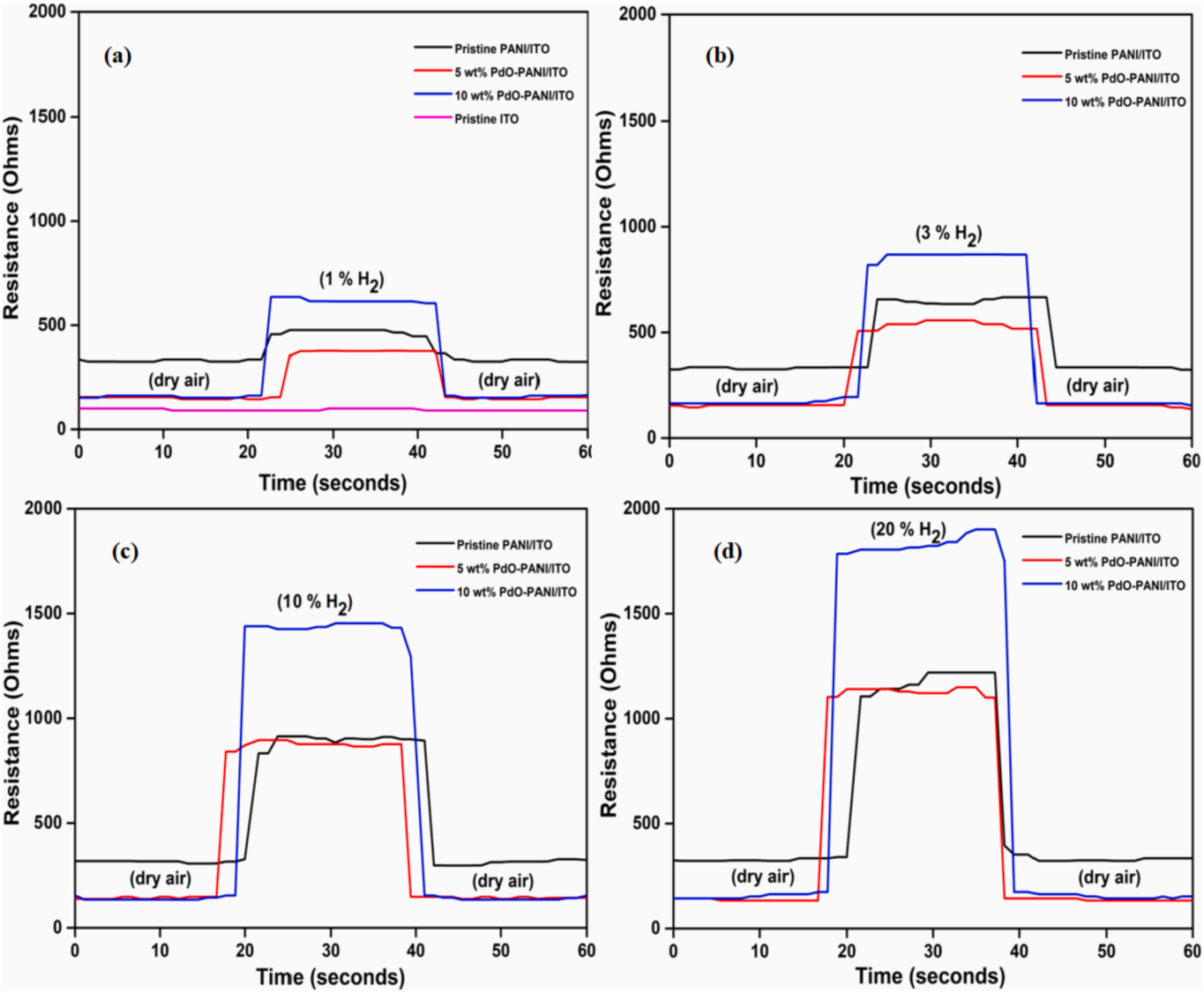

Fig. 10. Sensing response comparison of Pristine PANI/ITO, 5 wt% and 10 wt% PdO-PANI/ITO towards (a) 1% H_2, (b) 3% H_2, (c) 10% H_2 and (d) 20% H_2.

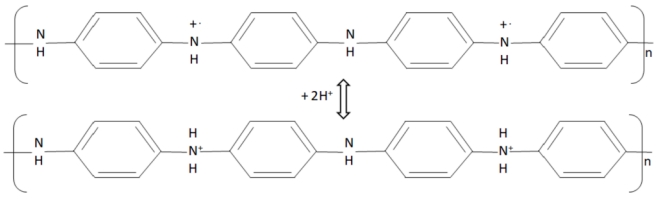

Fig. 11. Hydrogenation of polaronic form.

involving dissociation into H^+ ions followed by their spillover onto PANI matrix, resulting in high electron density and large barrier width. Further, increase in PdO nanoparticles concentration, saturates the PANI conjugated chain structure by reducing the available amine units and thus inhibits their electron transport mechanism.

Some of the recent research work employing various composites of PANI for hydrogen sensing application and their comparison with metal oxide based H_2 sensors has been reported in Table 2. It has been found that proposed sensor shows best response towards low concentration (1%) of H_2 gas at room temperature with fast response characteristics.

4. Conclusions

Pristine PANI, 5 wt%, and 10 wt% PdO-PANI composites have been synthesized using cheaper and facile one pot in-situ wet chemical polymerization process. The crystallographic structure, geometry of heterostructure, optical characteristics, nature of bonds and type of inter-bond interactions of pristine PANI and their composites with PdO has been observed using x-ray diffraction (XRD), transmission electron microscopy (TEM), ultraviolet–visible (UV–Vis) absorption spectroscopy and Fourier transform infrared (FT-IR) transmission spectroscopy. The results suggest that synthesized pristine PANI exists in its emeraldine form and it has successfully formed composite with tetragonal PdO. Thin film of pristine PANI, 5 wt%, and 10 wt% PdO-PANI nanocomposites are deposited over sputtered ITO layer coated glass substrate forming PANI/ITO and PdO-PANI/ITO heterojunction which is used as sensing element. H_2 sensing response has been studied using low cost indigenously constructed chemiresistive gas sensing setup with direct contact of metallic probes without using expensive interdigitated electrodes (IDE) and sensitivity response has been recorded in terms of change in resistance in presence of (1, 3, 10, and 20) % H_2 gas concentrations. The resistance is found to increase with increase in content of PdO and also with percentage concentration of H_2 gas. The net

Table 2
A comparison between various PANI composites and metal oxides based chemiresistive hydrogen sensors.

S.No.	Sensing element	H_2 concentration	Response	Response time (seconds)	Recovery time (seconds)	Operating Temperature (^{0}C)	References
1.	**PdO-PANI/ITO**	**1%**	**1.75**	**3**	**4**	**28**	**Present work**
2.	Ag–SnO_2/PANI	500 ppm	1.9	16	24	42	[17]
3.	Pd-rGO doped PANI	1%	1.25	20	50	25	[20]
4.	SnO_2/PANI	1000 ppm	1.5	3	4	50	[19]
5.	PANI/anatase TiO_2	0.8%	1.63	83	130	27	[12]
6.	PANI/rutile TiO_2	0.8%	1.54	152	170	27	[16]
7.	TiO_2:SnO_2/PANI	0.8%	1.25	75	117	27	[11]
8.	ZnO thin film	0.5%	1.48	150	170	100	[25]
9.	TiO_2 thin film	1%	1.24	250	300	225	[52]
10.	ZnO–SnO_2 composite	10 000 ppm	1.9	60	75	150	[53]

increase in the resistance is a combined effect of increase in Schottky barrier at heterojunction, formation of protonated amines (-NH_2^+-) units within conjugated PANI chain structure and increase in number of scattering centers for electrons with increase in doping percentage of PdO respectively. It has been observed that sensitivity of PdO-PANI nanocomposites is two folds higher than that of pristine PANI towards 1% H_2 gas concentration and it enhances comprehensively as the percentage concentration of PdO nanoparticles increase from 5 to 10 wt%. Hence, a highly sensitive room temperature H_2 gas sensor has been successfully fabricated which can wide range concentrations of H_2 gas in the environment. Moreover, heterostructures of other hierarchal nanostructures of PdO with emeraldine PANI conjugated structure can be fabricated to elevate the sensitivity and responsiveness of the proposed chemiresistive H_2 sensor.

CRediT authorship contribution statement

Kamal Arora: Conceptualization, Data curation, Formal analysis, Investigation, Methodology, Writing - original draft. **Nitin K. Puri:** Project administration, Resources, Supervision, Validation, Writing - review & editing, Funding acquisition.

Acknowledgements

The Authors are grateful to Prof. Yogesh Singh, Vice chancellor, Delhi Technological University, Delhi, India for providing the ambient environment and facilities for conducting fruitful research work. We are thankful to Advanced Instrumentation Research Facility (AIRF), Jawahar Lal Nehru University (JNU) and Inter University Accelerator Center (IUAC) for providing the characterization and imaging facilities. The first author is obliged to Council of Scientific and Industrial Research (CSIR), India for providing the SRF-Direct fellowship as financial assistance. The financial support received by IUAC sponsored project (Grant No. IUAC/XIII.7/UFR-56324), Department of Atomic Energy -Board of Research in Nuclear Sciences (DAE-BRNS), India, SERB, DST, India (EMR/2016/007479) and DST, India (Grant No. IFA14-MS-34) for successful completion of this research work is sincerely acknowledged.

References

[1] M. Rozemarie, B. Andrei, H. Liliana, R. Cramariuc, O. Cramariuc, Electrospun Based Polyaniline Sensors–A Review, IOP Conference Series: Materials Science and Engineering, IOP Publishing, 2017, 012063.
[2] K. Arora, D. Sandil, G. Sharma, S. Srivastava, N.K. Puri, Effect of low pressure hydrogen environment on crystallographic properties of PdO nanoparticles, Int. J. Hydrogen Energy 41 (2016) 22155–22161.
[3] S. Virji, R.B. Kaner, B.H. Weiller, Hydrogen sensors based on conductivity changes in polyaniline nanofibers, J. Phys. Chem. B 110 (2006) 22266–22270.
[4] J.D. Fowler, S. Virji, R.B. Kaner, B.H. Weiller, Hydrogen detection by polyaniline nanofibers on gold and platinum electrodes, J. Phys. Chem. C 113 (2009) 6444–6449.
[5] A. Sadek, A. Trinchi, W. Wlodarski, K. Kalantar-Zadeh, K. Galatsis, C. Baker, R. Kaner, A room temperature polyaniline nanofiber hydrogen gas sensor, Sensors (2005) 4, 2005 IEEE, IEEE.
[6] D.R. Miller, S.A. Akbar, P.A. Morris, Nanoscale metal oxide-based heterojunctions for gas sensing: a review, Sensor. Actuator. B Chem. 204 (2014) 250–272.
[7] Z. Yuan, R. Li, F. Meng, J. Zhang, K. Zuo, E. Han, Approaches to enhancing gas sensing properties: a review, Sensors 19 (2019) 1495.
[8] S. Srivastava, S. Kumar, Y. Vijay, Preparation and characterization of tantalum/polyaniline composite based chemiresistor type sensor for hydrogen gas sensing application, Int. J. Hydrogen Energy 37 (2012) 3825–3832.
[9] S. Srivastava, S. Sharma, S. Agrawal, S. Kumar, M. Singh, Y. Vijay, Study of chemiresistor type CNT doped polyaniline gas sensor, Synth. Met. 160 (2010) 529–534.
[10] S. Srivastava, S. Kumar, V. Singh, M. Singh, Y. Vijay, Synthesis and characterization of TiO_2 doped polyaniline composites for hydrogen gas sensing, Int. J. Hydrogen Energy 36 (2011) 6343–6355.
[11] S. Nasirian, H.M. Moghaddam, Polyaniline assisted by TiO_2: SnO_2 nanoparticles as a hydrogen gas sensor at environmental conditions, Appl. Surf. Sci. 328 (2015) 395–404.
[12] S. Nasirian, H.M. Moghaddam, Hydrogen gas sensing based on polyaniline/anatase titania nanocomposite, Int. J. Hydrogen Energy 39 (2014) 630–642.
[13] S. Park, J. An, J.R. Potts, A. Velamakanni, S. Murali, R.S. Ruoff, Hydrazine-reduction of graphite-and graphene oxide, Carbon 49 (2011) 3019–3023.
[14] C. Conn, S. Sestak, A.T. Baker, J. Unsworth, A polyaniline-based selective hydrogen sensor, Electroanalysis: An Int. J Devoted Fund. Practical Aspects Electroanal. 10 (1998) 1137–1141.
[15] P.-C. Wang, Y. Dan, L.-H. Liu, Effect of thermal treatment on conductometric response of hydrogen gas sensors integrated with HCl-doped polyaniline nanofibers, Mater. Chem. Phys. 144 (2014) 155–161.
[16] H.M. Moghaddam, S. Nasirian, Hydrogen gas sensing feature of polyaniline/titania (rutile) nanocomposite at environmental conditions, Appl. Surf. Sci. 317 (2014) 117–124.
[17] S.B. Kondawar, A.M. More, H.J. Sharma, S.P. Dongre, Ag-SnO_2/Polyaniline composite nanofibers for low operating temperature hydrogen gas sensor, J. Mater. NanoSci. 4 (2017) 13–18.
[18] H.J. Sharma, D.V. Jamkar, S.B. Kondawar, Electrospun nanofibers of conducting polyaniline/Al-SnO_2 composites for hydrogen sensing applications, Procedia Mater. Sci. 10 (2015) 186–194.
[19] H.J. Sharma, N.D. Sonwane, S.B. Kondawar, Electrospun SnO_2/polyaniline composite nanofibers based low temperature hydrogen gas sensor, Fibers Polym. 16 (2015) 1527–1532.
[20] Y. Zou, Q. Wang, C. Xiang, C. Tang, H. Chu, S. Qiu, E. Yan, F. Xu, L. Sun, Doping composite of polyaniline and reduced graphene oxide with palladium nanoparticles for room-temperature hydrogen-gas sensing, Int. J. Hydrogen Energy 41 (2016) 5396–5404.
[21] A.Z. Sadek, W. Wlodarski, K. Shin, R.B. Kaner, K. Kalantar-zadeh, A Room temperature Polyaniline/SnO_2 nanofiber composite based layered ZnO/64 YX $LiNbO_3$ SAW hydrogen gas sensor, in: 2006 Conference on Optoelectronic and Microelectronic Materials and Devices, IEEE, 2006, pp. 208–211.
[22] R. Arsat, X. Yu, Y. Li, W. Wlodarski, K. Kalantar-Zadeh, Hydrogen gas sensor based on highly ordered polyaniline nanofibers, Sensor. Actuator. B Chem. 137 (2009) 529–532.
[23] M. Hübner, R. Pavelko, N. Barsan, U. Weimar, Influence of oxygen backgrounds on hydrogen sensing with SnO_2 nanomaterials, Sensor. Actuator. B Chem. 154 (2011) 264–269.
[24] M. Alvarado, È. Navarrete, A. Romero, J. Ramírez, E. Llobet, Flexible gas sensors employing octahedral indium oxide films, Sensors 18 (2018) 999.
[25] K.-S. Choi, S.-P. Chang, Effect of structure morphologies on hydrogen gas sensing by ZnO nanotubes, Mater. Lett. 230 (2018) 48–52.
[26] Y. Zou, J. He, Y. Hu, R. Huang, Z. Wang, Q. Gu, Room-temperature hydrogen sensing performance of Nb_2O_5 nanorod arrays, RSC Adv. 8 (2018) 16897–16901.
[27] A. Sanger, A. Kumar, A. Kumar, J. Jaiswal, R. Chandra, A fast response/recovery of hydrophobic Pd/V_2O_5 thin films for hydrogen gas sensing, Sensor. Actuator. B Chem. 236 (2016) 16–26.
[28] F. Annanouch, S. Roso, Z. Haddi, S. Vallejos, P. Umek, C. Bittencourt, C. Blackman, T. Vilic, E. Llobet, p-Type PdO nanoparticles supported on n-type WO_3 nanoneedles for hydrogen sensing, Thin Solid Films 618 (2016) 238–245.
[29] N.D. Hoa, C.M. Hung, N. Van Duy, N. Van Hieu, Nanoporous and crystal evolution in nickel oxide nanosheets for enhanced gas-sensing performance, Sensor. Actuator. B Chem. 273 (2018) 784–793.
[30] S.M. Hamidi, A. Mosivand, M. Mahboubi, H. Arabi, N. Azad, M.R. Jamal, New generation of α-MnO_2 nanowires@ PDMS composite as a hydrogen gas sensor, Appl. Phys. A 124 (2018) 253.

[31] U.T. Nakate, G.H. Lee, R. Ahmad, P. Patil, Y.-B. Hahn, Y. Yu, E.-k. Suh, Nano-bitter gourd like structured CuO for enhanced hydrogen gas sensor application, Int. J. Hydrogen Energy 43 (2018) 22705–22714.
[32] Y. Zhang, W. Zeng, Y. Li, Theoretical and experimental investigations on H_2 sensing properties of flower-like titanium dioxide, Mater. Res. Bull. 107 (2018) 139–146.
[33] D. Rogers, R. Shannon, J. Gillson, Crystal growth and semiconductivity of palladium oxide, J. Solid State Chem. 3 (1971) 314–316.
[34] Y.-J. Chiang, K.-C. Li, Y.-C. Lin, F.-M. Pan, A mechanistic study of hydrogen gas sensing by PdO nanoflake thin films at temperatures below 250° C, Phys. Chem. Chem. Phys. 17 (2015) 3039–3049.
[35] Y.K. Kim, S.-H. Hwang, S.M. Jeong, K.Y. Son, S.K. Lim, Colorimetric hydrogen gas sensor based on PdO/metal oxides hybrid nanoparticles, Talanta 188 (2018) 356–364.
[36] M. Khanuja, B. Mehta, P. Agar, P. Kulriya, D. Avasthi, Hydrogen induced lattice expansion and crystallinity degradation in palladium nanoparticles: effect of hydrogen concentration, pressure, and temperature, J. Appl. Phys. 106 (2009), 093515.
[37] K. Arora, N.K. Puri, Electrophoretically deposited nanostructured PdO thin film for room temperature amperometric H2 sensing, Vacuum 154 (2018) 302–308.
[38] S. Kabcum, D. Channei, A. Tuantranont, A. Wisitsoraat, C. Liewhiran, S. Phanichphant, Ultra-responsive hydrogen gas sensors based on PdO nanoparticle-decorated WO_3 nanorods synthesized by precipitation and impregnation methods, Sensor. Actuator. B Chem. 226 (2016) 76–89.
[39] O. Lupan, V. Postica, M. Hoppe, N. Wolff, O. Polonskyi, T. Pauporté, B. Viana, O. Majérus, L. Kienle, F. Faupel, PdO/PdO_2 functionalized ZnO: Pd films for lower operating temperature H_2 gas sensing, Nanoscale 10 (2018) 14107–14127.
[40] K. Arora, S. Srivastava, P. Solanki, N.K. Puri, Electrochemical hydrogen gas sensing employing palladium oxide/reduced graphene oxide (PdO-rGO) nanocomposites, IEEE Sensor. J. 19 (18) (2019) 8262–8271.
[41] A. Bera, K. Deb, V. Kathirvel, T. Bera, R. Thapa, B. Saha, Flexible diode of polyaniline/ITO heterojunction on PET substrate, Appl. Surf. Sci. 418 (2017) 264–269.
[42] S. Kotresh, Y. Ravikiran, P.H. Raj, K.S. Vijaya, Polyaniline-Titanium dioxide composite as humidity sensor at room temperature, НаносистеМы: физика, хиМия, МатеМатика (2016) 7.
[43] B. Butoi, A. Groza, P. Dinca, A. Balan, V. Barna, Morphological and structural analysis of polyaniline and poly (o-anisidine) layers generated in a DC glow discharge plasma by using an oblique angle electrode deposition configuration, Polymers 9 (2017) 732.
[44] R. Li, C. He, X. Han, Y. Yang, Carbon-Based Polyaniline Nanocomposites for Supercapacitors, Carbon-Based Polymer Nanocomposites for Environmental and Energy Applications, Elsevier, 2018, pp. 489–535.
[45] T. Sen, S. Mishra, N.G. Shimpi, Synthesis and sensing applications of polyaniline nanocomposites: a review, RSC Adv. 6 (2016) 42196–42222.
[46] C.-L. Zhu, S.-W. Chou, S.-F. He, W.-N. Liao, C.-C. Chen, Synthesis of core/shell metal oxide/polyaniline nanocomposites and hollow polyaniline capsules, Nanotechnology 18 (2007) 275604.
[47] A. Mostafaei, A. Zolriasatein, Synthesis and characterization of conducting polyaniline nanocomposites containing ZnO nanorods, Prog. Nat. Sci.: Mater. Int. 22 (2012) 273–280.
[48] B.G. Streetman, S. Banerjee, Solid State Electronic Devices, Prentice-Hall of India, 2001.
[49] I. Fratoddi, I. Venditti, C. Cametti, M.V. Russo, Chemiresistive polyaniline-based gas sensors: a mini review, Sensor. Actuator. B Chem. 220 (2015) 534–548.
[50] Y.T. Lee, J.M. Lee, Y.J. Kim, J.H. Joe, W. Lee, Hydrogen gas sensing properties of PdO thin films with nano-sized cracks, Nanotechnology 21 (2010) 165503.
[51] A. Ray, A. Richter, A. MacDiarmid, A. Epstein, Polyaniline: protonation/deprotonation of amine and imine sites, Synth. Met. 29 (1989) 151–156.
[52] A. Sadek, J. Partridge, D. McCulloch, Y. Li, X. Yu, W. Wlodarski, K. Kalantar-Zadeh, Nanoporous TiO2 thin film based conductometric H_2 sensor, Thin Solid Films 518 (2009) 1294–1298.
[53] B. Mondal, B. Basumatari, J. Das, C. Roychaudhury, H. Saha, N. Mukherjee, ZnO–SnO_2 based composite type gas sensor for selective hydrogen sensing, Sensor. Actuator. B Chem. 194 (2014) 389–396.

KAMAL ARORA

ORCID ID. : https://orcid.org/0000-0003-2120-7492
LinkedIn ID. : https://www.linkedin.com/in/kamal-arora-bb442418
Email id: kamalarora_2k13@dtu.ac.in, kamal.arora8@hotmail.com
Contact Number: +91-9910886308

Education

2013 – 2020: **Ph. D. Applied Physics** *(Awarded)*, Department of Applied Physics, Delhi Technological University, Delhi, India.
Thesis title: "*Nanostructured metal oxides for hydrogen sensing applications*",
Thesis supervisor: Dr. Nitin K. Puri, Associate Professor

2010 – 2012: **M. Sc. Engineering Physics**, Amity Institute of Applied Sciences, Amity University, Noida, Uttar Pradesh, India. (CGPA): 9.17/10
Thesis title: *"Tin oxide thin film fabrication and its characterization"*
Thesis supervisor: Dr. Pramila Shukla, Associate Professor

2007 – 2010: **B. Sc. (Honors) Physics**, Kirorimal College, University of Delhi, Delhi, India. (Percentage marks: 61.18%)

2006 – 2007: **Diploma in Computer Business Application**, Delhi Institute of Computer Science, Delhi, India

2005 – 2006: **Higher senior secondary school (Grade 12)**, DAV Public school, Delhi, India. (Percentage marks: 79.6%)

2003 – 2004: **Higher secondary school (Grade 10)**, ST. Joseph's Academy, Delhi, India. (Percentage marks: 85.6%)

Publications

1. **Kamal Arora**, Nitin K. Puri. *"Chemiresistive sensing platform based on PdO-PANI/ITO heterostructure for room temperature hydrogen detection."* Materials Chemistry and Physics (2020), 247 122850. (I.F.= 3.408)
2. **Kamal Arora**, Saurabh Srivastava, Prartima R. Solanki, Nitin K. Puri. *Electrochemical Hydrogen Gas Sensing Employing Palladium Oxide/Reduced Graphene Oxide (PdO-rGO) Nanocomposites*. IEEE Sensors Journal (2019), 19(18), 8262-8271. (I.F.= 3.073)
3. **Kamal Arora**, Nitin K. Puri. *Electrophoretically deposited nanostructured PdO thin film for room temperature amperometric H_2 sensing*. Vacuum (2018), 154, 302-308. (I.F.= 2.906)

4. Deepika Sandil, Saurabh Kumar, **Kamal Arora**, Saurabh Srivastava, B. D. Malhotra, S. C. Sharma, Nitin K. Puri. *Biofunctionalized nanostructured tungsten trioxide based sensor for cardiac biomarker detection*. Materials Letters (2017), 186, 202-205. (I.F.= 3.204)

5. **Kamal Arora**, Deepika Sandil, Gaurav Sharma, Saurabh Srivastava, Nitin K. Puri. *Effect of low pressure hydrogen environment on crystallographic properties of PdO nanoparticles*. International Journal of Hydrogen Energy (2016), 41(47), 22155-22161. (I.F.= 4.939)

6. Saurabh Srivastava, Vinod Kumar, **Kamal Arora**, Chandan Singh, M. Azhar Ali, Nitin K. Puri, B. D. Malhotra. *Antibody conjugated metal nanoparticle decorated graphene sheets for a mycotoxin sensor*. RSC Advances (2016), 6(61), 56518-56526. (I.F.= 3.119)

7. **Kamal Arora**, Alpana Goel. *Mechanism of formation Tsunami mega waves*, Indian Association of Physics Teachers (IAPT) Bulletin (2012), 4(8), August, 205-207, 216.

Conference proceedings

1. **Kamal Arora**, Nitin K. Puri. *PdO/Polyaniline nanocomposite for room temperature hydrogen sensing application,* "17th International Meeting on Chemical Sensors – IMCS" 2018 at University of Vienna, Vienna, Austria, (15^{th} – 19^{th} July 2018), Page no. 865, doi: 10.5162/IMCS2018/P2NG.11, ISBN no. 978-3-9816876-9-9

2. **Kamal Arora**, Saurabh Srivastava, Nitin K. Puri. *Room Temperature Amperometric H_2 Sensing using PdO Thin Film,* "17^{th} International Conference on Thin films (ICTF-2017*)"* at National Physical Laboratory, New Delhi, India, (13^{th} November 2017), Indian Vacuum Society, Abstract Id.: 307, Poster ID.: P266-L10, URL: https://drive.google.com/file/d/1Gqx-1bQCluSuOvPxafUiaHhHWzU7IU9z/view

Teaching experience

2020 *(Jan-Mar)*	**Teaching research assistant**, B. Tech. (I^{st} year), Applied Physics Lab-I, Department of Applied Physics, Delhi Technological University, Delhi, India.
2019 (*Aug – Dec*):	**Teaching research assistant**, M. Sc. Physics Lab-I course, Department of Applied Physics, Delhi Technological University, Delhi, India.
2016 – 2018:	**Teaching research assistant**, M. Tech. Nuclear Engineering Lab course, Department of Applied Physics, Delhi Technological University, Delhi, India
2014 – 2016:	**Teaching research assistant**, M. Tech. Nuclear Engineering Lab course, Department of Applied Physics, Delhi Technological University, Delhi, India
2013 – 2014:	**Teaching research assistant**, undergraduate lectures (Applied Physics), B. Tech. (I^{st} year), Department of Applied Physics, Delhi Technological University, Delhi, India.

Research Experience

- Chemiresistive gas sensor
- Amperometric gas sensor
- Electrochemical immunosensors
- Metal oxides nanostructure synthesis
- Nano/micro sensor device fabrication

Training Experience

2012 (*Jan – Jun*): **Research intern**, Solid State Physics Laboratory (SSPL), Defence Research and Development Organization (DRDO), New Delhi, India.

Research supervisors: Dr. S. K. Pandey, Scientist 'D' & Dr. Amita Gupta, Scientist 'G'

Aim: Fabrication of metal oxides based volatile organic gas sensors

Research work:

- Synthesis of tin oxide (SnO_2) nanoparticles using wet chemical process
- Fabrication of gold (Au) patterned interdigitated electrodes (IDE) on quartz glass substrates using laser ablation equipment and ultraviolet (UV) photolithography
- Fabrication of SnO_2 thin films on IDE substrates using spin coating and dip coating techniques
- Performing chemiresistive sensing of Dimethyl methylphosphonate (DMMP)
- Sensor shows good sensing response at 200 – 400 ^{0}C working temperature range

Additional activities

2017 (*1st – 3rd Jul*): **Organizing committee member**, 10th national conference entitled *"Solid State Chemistry and Allied areas (ISCAS-2017")*, Department of Applied Physics, Delhi Technological University, Delhi, India.

2014 – *2016:* **Establishment and development** of Nanomaterials Research Lab (NRL), Department of Applied Physics, Delhi Technological University, Delhi, India

2013 – *2014:* **Establishment and development** of Advanced Sensor Lab (ASL), Department of Applied Physics, Delhi Technological University, Delhi, India

2011 (*19th – 20th May*): **Student organizing committee member**, National conference entitled "Recent Trends in Materials and Devices (RTMD)" at Amity University, Noida, Uttar Pradesh, India.

Awards and Achievements

1. **Review editor**, *Wearable Electronics*, Frontiers in electronics, July 2020
2. **Reviewer**, *Materials Chemistry and Physics*, Elsevier, May 2020
3. **Reviewer**, *International Journal of Hydrogen Energy (IJHE)*, Elsevier, March 2020
4. ***Commendable research award*** *(2019 – 2020)*, Department of Applied Physics, Delhi Technological University, Delhi, India
5. ***CSIR-Direct senior research fellowship*** *(SRF)*,(May 2018 – Present), (Duration: 2 years)
6. ***Commendable research award*** *(2018 – 2019)*, Department of Applied Physics, Delhi Technological University, Delhi, India
7. ***Commendable research award*** *(2017 – 2018)*, Department of Applied Physics, Delhi Technological University, Delhi, India
8. **IUAC sponsored *Project fellowship***, Department of Applied Physics, Delhi Technological University, Delhi, India (November 2015 – March 2018)
9. NASA Great Moon buggy race. ***Best Initial Design Award***, AL, Huntsville, United states (April 2009)
10. NASA Great Moon buggy race. ***System Safety Award***, AL, Huntsville, United states (April 2009)

Conferences and Workshops attended

1. Participated in TEQIP-III sponsored faculty development programme on "*Recent Trends in Material Science and Engineering*", Department of Applied Physics, Delhi Technological University, Delhi, India, (17^{th} – 21^{st} September 2018)
2. Participated in *"17^{th} International Meeting on Chemical Sensors (IMCS-2018)"* at University of Vienna, Vienna, Austria, (15^{th} – 19^{th} July 2018), (poster presentation)
3. Participated in *"17^{th} International Conference on Thin films (ICTF-2017")* at National Physical Laboratory, New Delhi, India, (14^{th} – 17^{th} November 2017), (poster presentation)
4. Participated in Pre-Conference workshop, "17^{th} *International Conference on Thin films (ICTF-2017)"* at National Physical Laboratory, New Delhi, India, (13^{th} November 2017)
5. Participated in UGC sponsored *"National Seminar on Recent Advances in Physics (NSRAP)",* Delhi Technological University, (16^{th} February 2015)
6. Participated in *Climate catalyst workshop*, Indian youth climate network (IYCN), Delhi, India, (27^{th} – 28^{th} September 2014)
7. Participated in *International conference on electron microscopy & XXXV Annual meeting of Electron Microscope Society of India (EMSI)* at University of Delhi, (9^{th} – 11^{th} July 2014)

8. Participated in *Pre-Conference Workshop, Electron Microscope Society of India (EMSI),* in University of Chicago, centre in Delhi and University of Delhi, (7^{th} – 8^{th} July 2014)

9. Participated in *Astrophotography workshop* "The World at Night (TWAN)", Nehru planetarium, New Delhi, India, (3^{rd} – 6^{th} October 2008)

10. Participated in "*Newtonian 2008"*, academic festival organized by physics society, Kirorimal college, University of Delhi, Delhi, India, (15^{th} – 16^{th} February 2008)

Other Professional Experience

1. Worked as an Insurance Policy Advisor in ICICI Prudential Life Insurance Company Ltd, (2008 – 2009)

2. Worked as a Tutor in Tutor vista Pvt Ltd teaching Mathematics to higher grade US/UK students, (2007 – 2008)

Language Proficiency

1. **English**: Advanced (IELTS, 21^{st} March 2015, Band score: 7.5)

2. **German**: Intermediate (Curriculum, M.Sc. Engineering Physics, 2010 – 2012)

References

1. Dr. Nitin K. Puri
   Associate Professor
   Department of Applied Physics
   Delhi Technological University
   Delhi-110042, India
   Email: nitinkumarpuri@dtu.ac.in, nitinpuri2002@yahoo.co.in

2. Prof. B. D. Malhotra
   Professor
   Department of Biotechnology
   Delhi Technological University
   Delhi-110042, India
   Email: bansi.malhotra@gmail.com

3. Dr. Saurabh Kumar
   DST INSPIRE Faculty
   Centre for Nano Science and Engineering (CeNSE),
   Indian Institute of Science (IISc),
   Bangalore, Karnataka, India.
   Email: saurabh2203@iisc.ac.in

4. Dr. Saurabh Srivastava
   Assistant Professor
   Department of Applied Science and Humanities (Physics)
   Rajkiya Engineering College,
   Ambedkar Nagar-24122
   Uttar Pradesh, India
   Email: saurabhnpl@gmail.com